
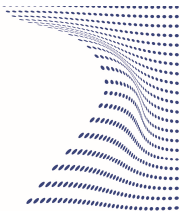

Doctoral Dissertation
Doctoral Program in Electrical, Electronics and Communication Engineering
(31st cycle)

Control of Wireless Power Transfer System for Dynamic Charging of Electric Vehicle

Mojtaba Khalilian
* * * * * *

Supervisor
Prof. Paolo Guglielmi

Doctoral Examination Committee:
Prof. Manuele Bertoluzzo, Università degli Studi di Padova
Prof. Burak Ozpineci, Oak Ridge National Laboratory
Prof. Carlo Concari, Università degli Studi di Parma
Prof. Michele Angelo Pastorelli, Politecnico di Torino
Prof. Gianmario Pellegrino, Politecnico di Torino

Politecnico di Torino
2019

Declaration

I hereby declare that, the contents and organisation of this dissertation constitute my own original work and does not compromise in any way the rights of third parties, including those relating to the security of personal data.

_____

Mojtaba Khalilian
2019

* This dissertation is presented in partial fulfillment of the requirements for Ph.D. degree in the Graduate School of Politecnico di Torino (ScuDo)

.Summary

In order to limit the production of pollutant gases, the transportation sector, both public and private, has turned its attention to Electric Vehicles (EVs). The most important barrier to commercializing and spreading EVs are the issues regarding the battery. The batteries are heavy, bulky, expensive, and have a limited lifetime. Furthermore, frequent charging and limited operating range due to the low energy density are other obstacles to developing EVs worldwide. Dynamic Wireless Power Transfer (WPT) is a possible solution in order to solve the problems related to the battery. In this solution, the battery of the EV can be charged when the vehicle is in motion. In this kind of charging system, the transmitter coils are embedded into the ground and the receiver coil is installed underneath the vehicle. Through a sufficient charging infrastructure large enough to charge the electric vehicle during driving, the size of the battery onboard can be reduced and the driving range of the EV can be extended.

The main goal of this thesis is research on the development and control of a 100-m segmented charging system for dynamic charging of an electric vehicle. The rating power of the charging system is 20 kW at the nominal air-gap of 25 cm. Due to its simple structure and good performance in dynamic charging conditions, series-series compensation topology has been chosen for the compensation of the self-inductances of the coils at a frequency of 85 kHz. One of the major difficulties involved in dynamic WPT systems is the control of the amount of power received by the battery as the vehicles travel along the road with fast speed. One possible solution is the establishment of a communication link between the EV and the ground. However, communication links may cause delays and affect the charging process. Here, two new control strategies for regulating the output power with different power electronics are introduced. These control methods are able to regulate the battery power from the EV and without any establishment of the

communication between vehicle and ground, even in the case of lateral misalignment or variations of the air-gap. Subsequently, the complete simulation of the system in static and dynamic charging conditions is performed and the operation in different charging conditions such as variations of the operating frequency, power demand, lateral misalignment, vehicle speed, and air-gap, is studied. The procedure for the construction of the charging lane with the development of the coils, the embedding procedure and implementation of the power electronic converter is presented. The results obtained by the experimental tests show good coherence with the simulation results.

Acknowledgment

I would like to express my deepest gratitude to my supervisor, Professor Paolo Guglielmi, who contributed immensely to my education and research throughout my studies at Politecnico di Torino. I would also like to thank Prof. Manuele Bertoluzzo and Prof. Burak Ozpineci for their helpful comments and suggestions during the review of my PhD thesis. I am grateful to PhD committee members Prof. Carlo Concari, Prof. Michele Angelo Pastorelli, and Prof. Gianmario Pellegrino.

I would like to express my gratitude to all my friends who helped me throughout my PhD studies. There are too many names to remember; however, I wish to single out Michela Diana, Vincenzo Cirimele, Jacopo Colussi, Alessandro La Ganga, Riccardo Ruffo, and Adel Deriszadeh for their support. I am also thankful for the encouragement from all of my family members.

Contents

List of Tables

List of Figures

Chapter 1

Introduction

Due to several issues such as environmental effects, global warming, oil resources limitations, and energy security, the attentions to the investment, production, and usage of renewable energy and other energy sources as a replacement to the currently used fossil energies are increasing. One of the main consumers of oil and petroleum is the transportation sector. With high energy density and ease of use, petroleum is a suitable source of energy. Furthermore, due to the increase in the vehicle production rate worldwide, the fuel consumption is dramatically increasing. In order to limit and reduce the production of greenhouse gases, the attentions of the transportation sector in public and private parts to the electric vehicle (EV) are developing around the world. With the use of electric powered transportation systems, it is possible to decrease the consumption of fossil fuels. Electric vehicles have many advantages over fuel-powered vehicles. They consumes electricity which can be generated from different sources such as renewable resources. Furthermore, during the movement, CO_2 and other gases emissions of EV are zero which can significantly help the reduction of air pollution in urban areas. In private EVs, vehicles are plugged into the grid and the battery is charged using electricity. Furthermore, by managing the charging process, the charging of EV could be done during the low demand periods such as at night when the stress on the grid is less and the grid has enough capacity for the EV charging.

Different chargers have been proposed for the charging of the EVs at different power levels. According to the power level, the chargers are classified into three levels including level 1, level 2 and level 3 [1]. As shown in Table 1.1, the level 1 charger is a slow charger that is suitable for the charging of the electric vehicle at home during the night. This charger is compatible with the home electrical plug. The level 2 charger is a semi-fast charger which is considered as the main method for both private and public cars. Nowadays, the most attention is on level 2 chargers which can provide sufficient power and can be realized in most locations. Usually, level 1 and level 2 chargers are single phase chargers. The level 3 charger is a high-power fast charger and is used for massive charging of the EVs. Usually, these types

of chargers are three phase chargers and the main purpose for implementation of them is for applications in public and commercial sectors. The level 3 chargers are able to charge the EV battery to 80% in only thirty minutes however they are not compatible in all EVs. At present, there is not any standard for level 3 chargers but this kind of chargers are available commercially. The electric vehicles such as Mitsubishi I and Nissan LEAF can be charged with level 3 charger [2].

Table 1.1: EV charger type classifications.

Charger type	Supply voltage	Phase	Type of use	Energy supply interface	Power level	Charging time
Level 1	120 V	1 phase	Charging at home or office	Conventional outlet	1.4-1.9 kW	17 Hours
Level 2	240 V	1 or 3 phase	Charging at private or public outlets	Dedicated chargers	3.1-19.2 kW	8 Hours
Level 3	300-600 V	3 phase	Charging at station	Dedicated chargers	50-240 kW	30 minutes

1.1 Various wireless charging systems

The main existing chargers for the EVs are conductive chargers. In this kind of chargers, a person is required to connect the charger to the EV. The wireless chargers have been proposed as an alternative solution for charging EVs and plug-in EVs in a contactless manner. In the Wireless Power Transfer (WPT) system, it is possible to send the power from a source (transmitter) to the equipment (receiver) wirelessly and without the use of any wire. In comparison with the conventional charging systems, wireless charging systems provide several advantages. These include reliability, simplicity, user-friendliness, and safety [3]. Due to these advantages, in recent years, WPT concept has been employed widely in many applications from small and low power applications and tools such as household appliances and biomedical implants to medium and high power applications such as the charge of the EVs and trains. Now, different types of WPT systems are presented and according to their operation and characteristics, they can be classified differently. However, depending on the distance between the transmitter and receiver, WPT systems can be classified into two main groups; near field WPT systems and far field WPT systems [4]–[7]. The block diagram of the WPT systems classification is presented in Fig. 1.1. Despite the difference between these wireless solutions, the basic layout of all of them is similar. All of them are composed of the transmitter and receiver circuits. The transmitter is supplied by the transmitter converter and the receiver is connected to the receiver side power electronics.

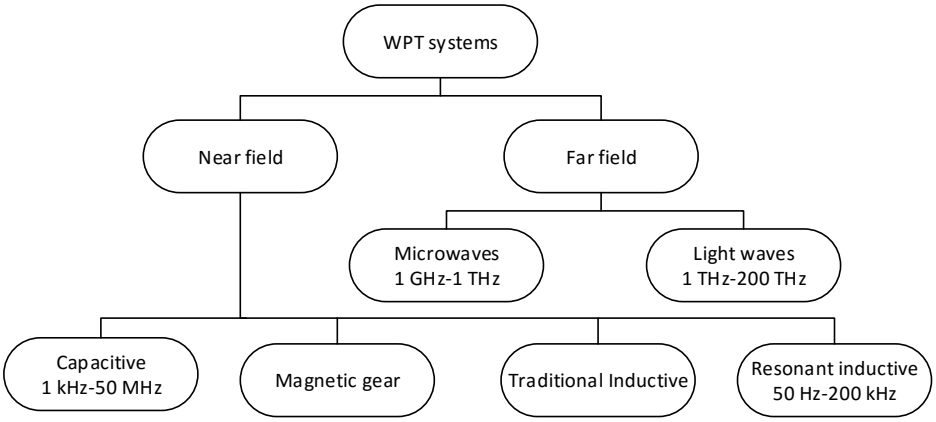

Fig. 1.1: Classification of WPT systems.

In the far field WPT system, the electric and magnetic fields are straight and they are propagated as an electromagnetic wave such as microwaves and light waves. Here, the part of the energy is radiative. The transmitter sends the power regardless of whether there is a receiver to get it or not. The part of the energy which is not received by the receiver is dissipated. At low frequencies, a very little amount of power is radiated and in practical devices, frequencies above 1 GHz are required. This high-frequency operation can cause problems due to human exposure to radiation. Furthermore, shielding this radiation is not an easy task without limiting the performance and range of operation [4].

In near field WPT systems, the power transmission is via magnetic fields by inductive coupling of the transmitter coil and the receiver coil or via electric fields by capacitive coupling between plates. In near field WPT systems, the electric and magnetic fields are not radiative and the energy of the transmitter remains within a short distance from it. The field strength reduces exponentially with distance from the transmitter. For power transmission, the distance between the transmitter and receiver must be short. The distance is related to the shape and size of the transmitter. In the case of no receiver within the range, the amount of power that leaves the transmitter is almost zero. The near field WPT systems can be divided into four types [4]; capacitive power transfer, magnetic gear based wireless power transfer, traditional inductive power transfer (IPT), and resonant inductive power transfer.

One of the solutions for transferring power from the transmitter to the receiver wirelessly is taking advantage of capacitive coupling [8]. The structure of the capacitive power transfer is presented in Fig. 1.2. The DC source voltage is connected to an H-bridge converter. The H-bridge converter generates a high-frequency current passes through coupling capacitors. In order to increase power transfer capability and make the impedance seen from the source purely resistive, additional inductors are added to the circuit and in series with the coupling capacitors. With the help of the inductors, the H-bridge converter can operate in soft switching conditions. The received AC voltage at the receiver side is converted to the DC voltage using a rectifier and finally, the power is received by the battery.

The amount of power that can be sent through the capacitive power transfer depends on the size of the capacitors and the distance between the plates. Capacitive power transfer is efficient in small air-gap and usually uses in low power level devices due to its cost and size such as electronic devices and cell phones.

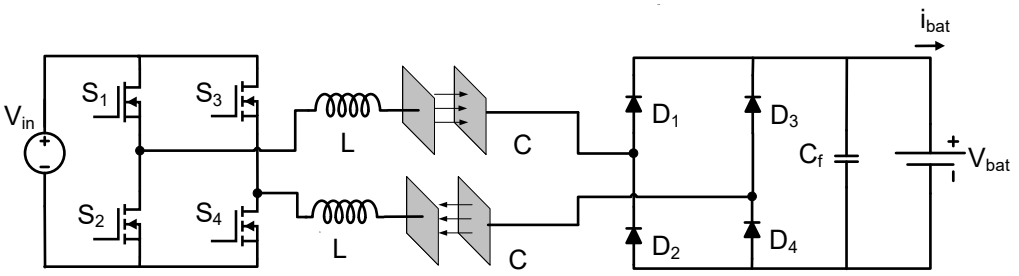

Fig. 1.2: Capacitive power transfer configuration.

The traditional inductive charger is composed of the transmitter coil and the receiver coil which are strongly coupled and form a U-shaped core transformer [9]. Since in this structure the high coupling for the transformer is necessary, the air-gap is very small. In this kind of chargers, the transmitter coil is named charging paddle and it places on the port where the receiver coil is located. This structure is implemented and used for different applications and different power levels from a few milliwatts to kilowatts. The IPT charger was developed at 6.6 kW and 50kW power level as a charger for the Chevrolet S10 electric vehicle in 1996 [7].

Resonant inductive power transfer is the improved version of the traditional inductive power transfer system. In this structure, the air-gap between the transmitter and receiver coils is increased. So, the coils are not strongly coupled but loosely coupled. Since the coupling coefficient of the coupled inductors is very low, the leakage inductances are relatively high. In comparison to the inductive power transfer, additional capacitors are added to the transmitter and receiver. The capacitors can be connected to the coils in different configurations such as series or parallel to form a resonant circuit in the transmitter and receiver. The presence of the capacitors helps to compensate the reactive part and to reduce the losses. Also, it provides the possibility of operating at higher frequency [4]. Fig. 1.3 shows the schematic of the resonant inductive power transfer system. The high-frequency H-bridge converter supplies the transmitter with a high-frequency voltage. A resonant circuit creates and the power is sent to the receiver. Then the power received by the receiver coil is converted to DC and finally, the power is transferred to the battery. When the frequency of the H-bridge converter is equal to the resonant frequency of the transmitter and receiver, the maximum efficiency can be achieved.

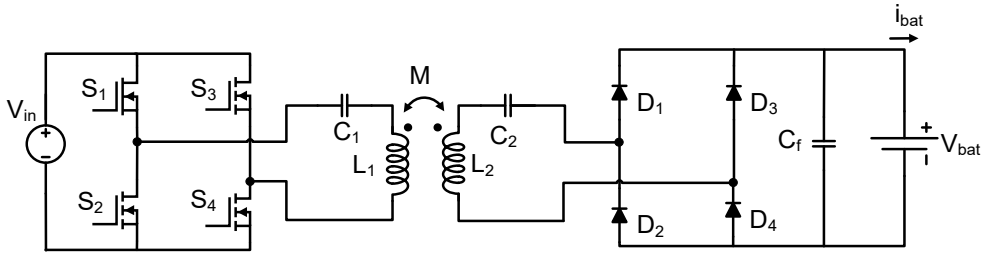

Fig. 1.3: Power circuit configuration of resonant inductive power transfer.

The operation principle of magnetic gear WPT is different from capacitive and inductive power transfer systems. This system is composed of two permanent magnets which build the transmitter and receiver of the system. By supplying the transmitter winding, the transmitter starts rotating. The receiver is placed on the vehicle with a certain distance from the transmitter. According to the coupling of the magnetic field, the receiver rotor tends to rotate at the transmitter rotor speed. Thus, the receiver permanent magnet receives power and then transfers it to the battery of the vehicle. In [7] a 1.6 kW magnetic gear WPT system is implemented and it is able to deliver power through the 15 cm of the air-gap. The controller regulates the speed of the transmitter by the feedback from the battery. The problem of this system is that the received power drops significantly when the air-gap between two permanent magnets increases.

In far field WPT systems, the resonant frequency is in the MHz range. This operating frequency results in severe problems with human exposure to radiation. In Magnetic gear WPT, due to the mechanical components, the size and maintenance cost are high. Furthermore, with the variation of the air-gap, the power significantly reduces. Capacitive power transfer solution is suitable for low power applications with small size and small air-gap. In traditional inductive power transfer, the air-gap is very small and the charging paddle must be placed over the receiver port manually. It can be concluded that of all of the wireless power transfer systems described above, only resonant inductive power transfer system could be a solution for wireless charging of EVs due to the operation at a considerable air-gap of 20-40 cm, high efficiency, and high power required for the vehicle. In the literature, resonant inductive power transfer has been referred with different names such as inductive powered transfer, inductively coupled power transfer (ICPT), wireless power transfer and contactless power transfer (CPT). In this dissertation, the term wireless power transfer will be used hereafter for consistency.

1.2 WPT for EV charging

For the EV application, wireless chargers can be classified into three main categories according to the EV operation, namely static wireless power transfer, dynamic wireless power transfer and quasi dynamic wireless power transfer [10]. In static charging of the EV, when the EV is parked right over the charging pad at the garage or parking, the battery charges. The second type of wireless charging system is dynamic WPT charging. In this charging system, the EV charges during the movement resulting in the increase of the driving range of the EV. Quasi dynamic WPT is another type of WPT charging system which its operating principle is between static and dynamic charging solution. The EV moves and then stops at certain places that are equipped with wireless chargers. The battery of the EV charges when the vehicle is completely stopped over the charging pads. Quasi dynamic WPT system is suitable for public transportation vehicles especially EV buses.

1.2.1 Static charging

Static wireless power transfer provides a safe environment for the consumer and reduces the driver involvement in the charging process as it is not necessary for the consumer to plug in the charger to the vehicle. This would solve safety-related issues for instance hazards and electric shock [11]. The power circuit of a WPT charging system is presented in Fig. 1.4. The charging structure is composed of two parts including ground facility and onboard part. The ground facility is composed of the transmitter converter, transmitter coil, and the compensation network. The onboard part is composed of the receiver coil, compensation network, rectifier, DC-DC converter, and the battery. Normally, the transmitter coil is installed under the ground and the receiver coil is mounted underneath the EVs. By energizing the transmitter coil with the transmitter converter, the energy is sent to the receiver coil. The received energy is converted to DC using a rectifier and then is transferred to the battery. Furthermore, in order to control the amount of the power received by the battery and manage the battery charging process, the DC-DC converter is employed before the battery. Moreover, with a communication line, the status of the battery could be transferred to the ground converter.

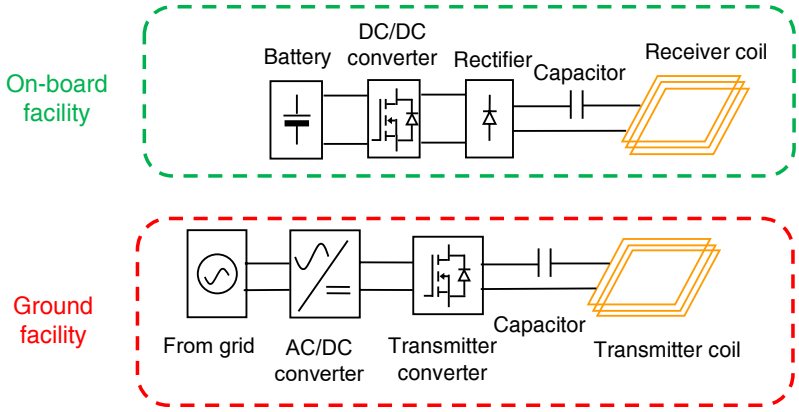

Fig. 1.4: Basic configuration of a wireless charging system.

The static WPT chargers can be installed in different private and public areas such as home, parking areas, and commercial centers. Recently, many prototypes have been implemented and tested by different universities and companies at different power levels [12]. As an example, the wireless power transfer charger for BMW i3 and i8 models has been demonstrated by BMW [13]. Furthermore, wireless charger capable of charging at home for the Tesla Model S can be mentioned. The amount of the power that the WPT charger can transfer and the charging time of the EV depend on many factors including input source power level, the size of the transmitter coil, the size of the receiver coil and the air-gap between them. The air-gap for the light-duty vehicle is approximately between 10 and 30 cm. The prices of the WPT chargers for the power levels between 3.3 and 7.2 kW vary from 2700 to 13000 USD approximately. The power level of the charger

according to the recently published SAE standards (J2954) is defined as 3.7 kW for level 1 charger and 7.7 kW for charger level 2 with at least 85% efficiency at perfect alignment and an operating frequency of 81.9-90 kHz.

1.2.2 Dynamic charging

The most important barrier in commercializing and wide spreading electric vehicle is the issues regarding to the battery [14]. The batteries are heavy, costly, bulky and with a limited lifetime. The size of the battery is very big and it takes up most space of the EV. Furthermore, the frequent charging and limited operating range due to the low energy density are other barriers in developing EVs world widely. The charging time of EV is generally high. The fast chargers available in the market are able to charge the battery in around 30 minutes which is still more than the fueling time in a conventional vehicle. Generally, the batteries are made of lithium. Due to the material and technology used in the construction of the battery, they are very expensive and account for more than one-third of the electric vehicle price. Considering the electrification of the buses, it requires too many battery packs resulting in the increase in the cost, size and charging time. The problem associated with static WPT is that EV can be charged only when it is parked at home or garage. This kind of charging method cannot solve the battery problems such as limited range and big volume. Dynamic WPT could be a solution in order to solve the problems related to the vehicle energy storage system. In this solution, the battery of the EV can be charged when the vehicle is in motion. Thus, the size of the battery onboard can be reduced and the driving range of the EV can be extended [14]. The structure of the dynamic WPT system is similar to the static WPT. The transmitter coils are embedded into the ground and the receiver coil is installed underneath the vehicle. The difference of dynamic WPT with the static counterpart is that in the dynamic charging system, the number of the transmitter coils embedded into the roadbed is increased. Thus, when the EV passes over the transmitter coils, frequent charging of the EV during the movement can be possible.

According to the dynamic WPT topologies presented in the literature, two main dynamic charging solutions namely long track topology [15] and segmented track topology [16], [17] exist. In long track topology or long track coupler, the size of the transmitter coil is much longer in comparison to the receiver coil. The basic diagram of dynamic WPT with long track topology is illustrated in Fig. 1.5. An example of this topology is presented in [18] where the track length reached 240 m long. The main advantage of this topology is that the coupling coefficient is constant along the track and it is not dependent on the position of the vehicle. For the energizing the whole track, only one H-bridge converter is necessary which makes the control much easier. In spite of these interesting merits, there are several drawbacks to long track topology. The size of the transmitter coil is much longer and because of that, the coupling coefficient between the transmitter and receiver coil is very low. Low coupling coefficient results in having high stray magnetic field and low power transfer efficiency. Furthermore, due to the small size of the

receiver coil in comparison to the transmitter coil, when the transmitter coil is energized, some part of it is not covered by the vehicle and the generated magnetic field in these areas causes danger for the nearby peoples and the environment. Due to the use of only one H-bridge converter for supplying the whole track, a very high VA rating H-bridge converter is required. Furthermore, because of high current of the track, considerable compensation capacitor must be added to the circuit. Almost in all of the long track topologies presented in the literature, the operating frequency is 20-40 kHz. The switching frequency is kept at this range in order to limit the voltage stress of the compensation capacitors. As described before, according to the SAE J2945 standard for static WPT chargers, a frequency range of 81.39 - 90 kHz has been proposed. The standard for dynamic WPT chargers is not yet published however due to the interoperability between the static and dynamic chargers, this frequency range must be considered for the dynamic systems too.

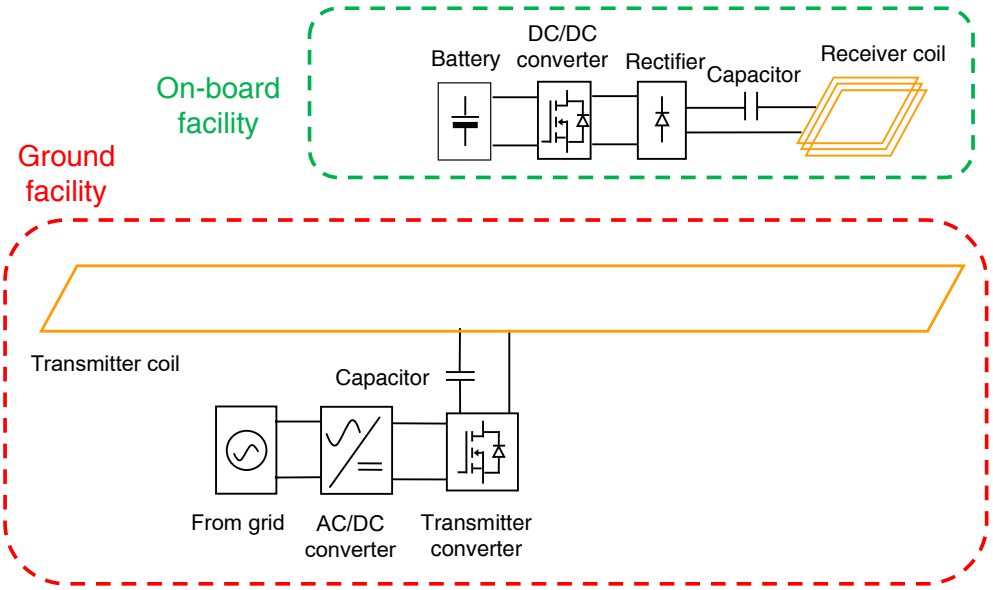

Fig. 1.5: Diagram of dynamic WPT with long track topology.

Another dynamic WPT solution is segmented track topology. The basic diagram of dynamic WPT with segmented track topology is illustrated in Fig. 1.6. In this topology, the length of the transmitter coil is smaller than the size of the vehicle. For energizing each transmitter coil, an independent low VA H-bridge converter is employed [19]. Another method of supplying the transmitter coil is presented in [20]. In this solution, several transmitter coils are embedded into the ground. But instead of supplying the transmitter coils with independent H-bridge converters, they are all connected to a common H-bridge converter and the energizing the coils is managed by a switching device. Each transmitter coil is energized when the presence of the vehicle is identified and EV is exactly on the top of that. Thus, the magnetic field is shielded by the vehicle and problems related to the magnetic field and safety are recovered. In this topology, the value of the coupling topology is higher and for this reason, higher efficiency can be achieved.

One of the biggest challenges of this solution is that the presence of the vehicle must be identified and then the transmitter coil which is covered by the vehicle becomes turned on. The presence of the vehicle can be identified with different solutions such as sensors, communication devices or other auxiliary circuits however this system must be fast enough in order to be able to charge the vehicle even in fast speed of the vehicle.

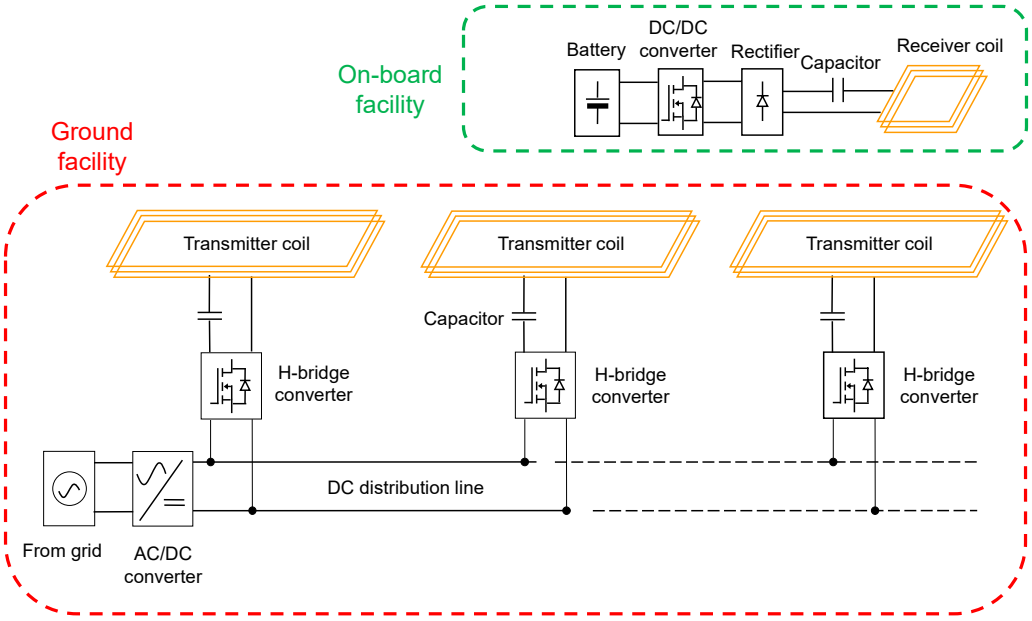

Fig. 1.6: Diagram of dynamic WPT with segmented track topology.

1.3 Research progress of WPT

In recent years, extensive research by universities and companies on dynamic WPT has been performed all over the world. Due to these efforts, many solutions have been presented in the literature and some of them have been developed practically for various transportation applications such as light weight electric vehicle, public buses and rail transport systems. In this section, the review of these systems is presented and the advantages and disadvantages of them are explained in detail. The first prototype of the dynamic charging system was designed by Lawrence Berkeley National Laboratory in 1976 and then an 8 kW prototype was developed and tested but it was not fully working [21]. In 1992 at the University of California Berkeley, advanced transit and highways (PATH) team designed a wireless charging of a bus. The output power of the prototype was 60 kW and the efficiency of 60% with the 7.6 cm air-gap was achieved [22]. Despite great achievements in developing a dynamic WPT system from different aspects such as road construction and installations, this system has many drawbacks that needed to be solved before being commercially developed. Due to the heavy coils supply rail structure, the construction cost was huge. Also, due to the lack of high frequency semiconductor devices, suitable ferret core and wire, the switching frequency of the system was kept as low as 400 Hz which resulted in low efficiency of the power

transmission and creation of audible noises. Low air-gap was another important problem of the PATH system. Korean KAIST institute started working on the dynamic charging of EVs since 2009. Till now, they have developed different prototypes with different structures and specifications for various vehicles specially buses [23]–[27]. The first prototype of KAIST On-Line Electric Vehicle (OLEV) 1G was a golf cart [18]. The working frequency of this system was 20 kHz which was much more than the switching frequency of the PATH prototype. The vehicle was equipped with the pick-up controller in order to improve the alignment. The long track topology with 45 m long and E-type cores was adopted for this system. The maximum efficiency of 80% at the output power of 3 kW was achieved. The Air-gap between the transmitter and receiver was 1 cm which still was very small. In the second generation 2G OLEV, the air-gap improved and reached 17 cm [18]. For improving the air-gap, the U-type shape for the transmitter and I-type shape for the receiver was developed. The cross-section views of transmitter and receiver coils are presented in Fig. 1.7. The second generation was used for the charging of electric buses. The transmitter of the system had 240 m long which was put inside the asphalt and the receiver was composed of ten pick-ups. The maximum efficiency of 72% at the output power of 60 kW was achieved.

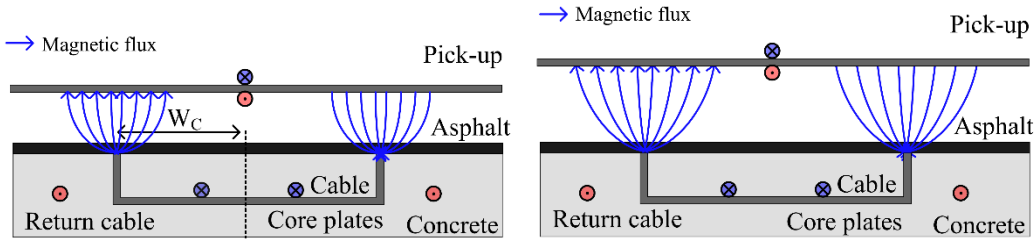

Fig. 1.7: Cross-section of the U-type transmitter and I-type receiver coils in different air-gaps.

For the third generation of OLEV 3G sports car, a W-type coil structure for the transmitter and overlapped double coils with flat shape for the receiver were developed [18]. The cross-section transmitter and receiver coils are presented in Fig. 1.8. The operating frequency of this EV was 20 kHz and with a distance of 17 cm, the system efficiency was measured 71%. The total efficiency of the OLEV 3G was low. So, all of the components of the system including rectifier, inverter, transmitter coil, receiver coil, and regulator were designed again in order to improve the overall efficiency of the system. The new design was named 3G+. It was the improved version of the 3G OLEV and was used for an electric bus [23]. After the test, the efficiency of 83% at 20 cm air-gap was obtained. This electric bus was commercialized and employed in different routes in Korea.

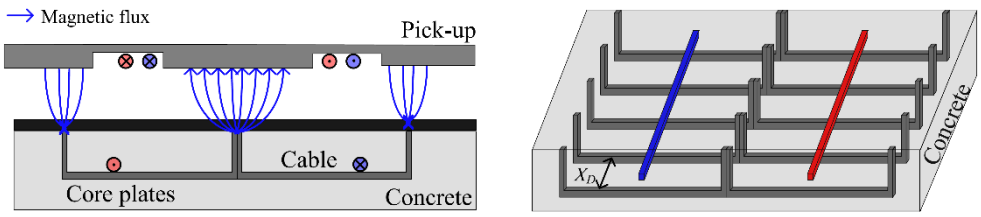

Fig. 1.8: Different views of the W-type transmitter and overlapped double coils with flat for the receiver.

The next generation of the KAIST vehicle was the 4G OLEV bus. The operating frequency of this system was 20 kHz similar to the previous vehicles. For the transmitter of the system, an I-type shape coil was designed as shown in Fig. 1.9 and in comparison to the previous design, the air-gap was improved and reached 20 cm [24]. Furthermore, the amount of EMF was reduced. During the test, the maximum power was 35 kW. At 27 kW power, the efficiency was measured 74%.

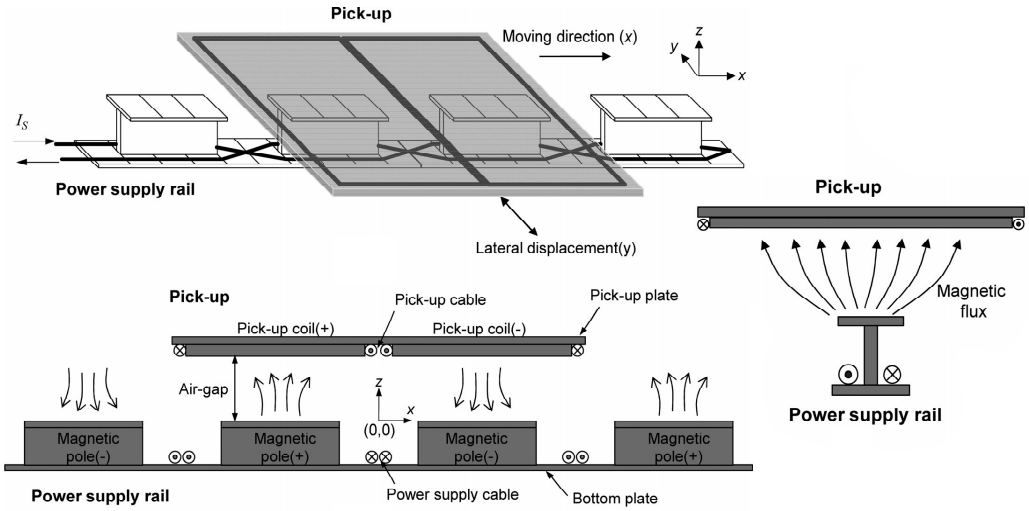

Fig. 1.9: Structure of the coils for 4G vehicle from different views; Top: transmitter and receiver coils, bottom: side view, right: front view.

For the transmitter coil of the fifth OLEV generation 5G, an S-type core with only 4 cm coil width was used which was much less than the I-type one. Thus, the total construction of roadway infrastructure and installation costs was reduced. Furthermore, because of the narrower width of the S-type transmitter coil, the EMF was lower than the I-type transmitter coil [25]. The structure of the coils for the 5G vehicle is presented in Fig. 1.10. As shown in Fig. 1.10, the core has S-shape when seeing the cross-section view of the coil. The air-gap of the system was 20 cm and the working frequency of it was 20 kHz. The efficacy of the system at 22 kW output power was 71%. However, the maximum efficiency of the system without considering the transmitter converter was 91%.

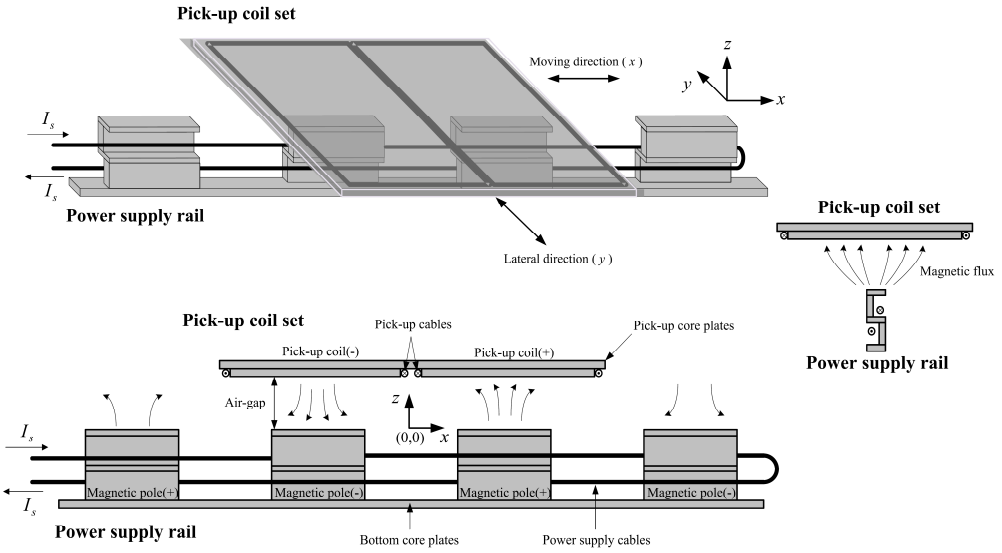

Fig. 1.10: Structure of the coils for the 5G vehicle from different views; Top: transmitter and receiver coils, bottom: side view, right: front view.

In [26], the design and test of a 100 kW WPT system using the OLEV bus are presented. The transmitter inverter converts the 60 Hz power to 20 kHz power and the coil is supplied with 260 A. The receiver is composed of five 20 kW pickups and each pickup has two windings. Thus, the receiver is composed of ten rectifiers and ten DC-DC boost converters and the output of the DC-DC converters is connected to the battery. Ten boost converters are operated with 36-degree phase shift in order to reduce output voltage ripple. The maximum efficiency of 80% at 100 kW output power and 26 cm air-gap was achieved.

The operating frequency of the OLEV vehicles was limited to 20 kHz due to the high leakage inductance of the coil, high current in the coils and high voltage stress of the compensation capacitors. In order to limit the voltage stress of the compensation capacitors, one solution is the use of distributed compensation capacitors and series connection of them. However, for high power application, this solution is not suitable. One answer to this question could be the application of segmented topology instead of long track topology and this is the solution that OLEV 6G follows [27]. By reducing the size of the transmitter coil, and reducing the leakage inductance of the coils, the operating frequency of the system can increase and reach 85 kHz which is the SAE J2954 frequency. This design can also satisfy the interoperability issues between static and dynamic charging systems. The OLEV 6G 3.3 kW coils configuration is presented in Fig. 1.11. The shape of the transmitter coil for OLEV 6G is similar to OLEV 3G but the difference is that in the new design, there is no core in the transmitter. Due to the coreless characteristics, the construction cost and installation time are reduced because there is no need to protect the ferrite cores inside the ground. According to [27], with the coreless transmitter, the system is more tolerant to lateral misalignment compared to the transmitter with core since the variation of the receiver coil is small during lateral misalignment.

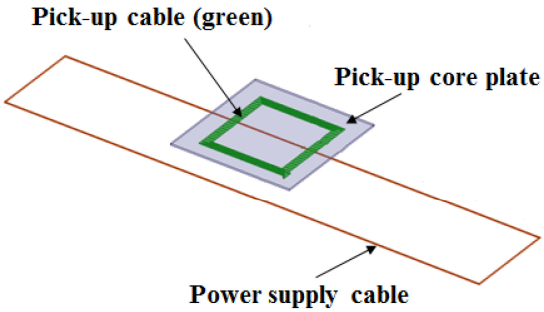

Fig. 1.11: 6G OLEV transmitter and receiver coils configuration.

Auckland University has been working on the design of WPT systems for many years. The segmented coil topology was introduced by the Auckland University team. The transmitter coils have a smaller size and weight which make the installation easily. The main working concentration of Auckland team was the design of the transmitter and receiver coils for static and dynamic wireless chargers and till now, various coil structures have been proposed such as circular coils, single-sided polarized coil, single-sided polarized coil with additional coil, and bipolar coil in order to improve the coupling and tolerance to misalignment [28]–[30]. A 20-kW circular coil with 70 cm diameter and 20 cm air-gap was proposed in [31].

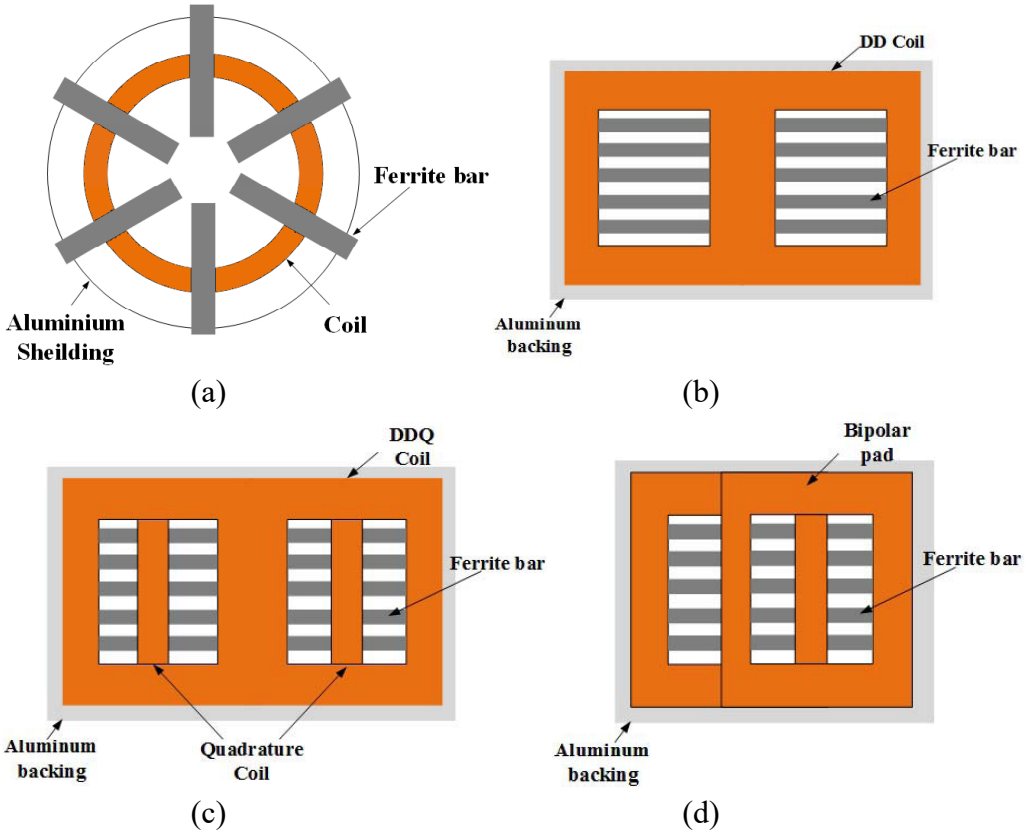

Fig. 1.12: Different coil shapes introduced by the University of Auckland; (a) circular shape coil, (b) Double-D coil (DD), (c) Double D quadrature coil (DDQ), and (d) bipolar coil.

Furthermore, this university has designed a circular coil with more than 90 % efficiency. The shape of a circular shape coil is shown in Fig. 2.12(a). The design guideline and optimization procedures for this coil for having higher efficiency and power density have been reported in the literature [32]. The disadvantage of a circular shape coil is that the power transfer capability is low and in comparison to the rectangular shape coil, it has lower misalignment tolerance. Basically, the lateral misalignment of the circular coil can be increased by choosing a larger diameter for the coil. However, it is not practical due to space and size limitations. Furthermore, the circular shape coil has limited air-gap length. According to the design procedure, with an increase in distance between the transmitter coil and the receiver coil, it is required to increase the diameter of the circular coil four times [33]. Thus, the circular shape coil is not suitable for WPT systems with large air-gap or high lateral misalignment.

In order to solve the problems and limitations of the circular shape coil, a new coil shape namely flux pipe coil was proposed [33]. This coil is implemented by winding the coil along the ferrite bar where two coils are magnetically connected in series and electrically connected in parallel. This structure has a higher coupling factor and higher lateral misalignment with a reduction of the size in comparison to the circular shape coil. In this coil, the magnetic fluxes are created at both sides of the coil. Thus, the generated flux at the back of the coil which is not useful is equal to the flux that is engaged to the coupling. This will cause an increase in the losses in the shield. The 1.5 kW coil with 7.5 cm air-gap and 95% efficiency and 3 kW coil with 20 cm air-gap and 90% efficiency can be mentioned as some example of this coil topology [34].

The picture of the Double D (DD) coil is presented in Fig. 2.12(b). This coil design has the advantages of both circular shape coil and flux pipe. DD coil is built from two rectangular coils [35]. As shown in the figure, the coils are placed on the ferrite bars and the aluminum shield is placed under the ferrite bars. The main advantage of the DD coil is that the flux path is single sided (opposite to the ferrite bars) which results in higher coupling coefficient and quality factor. Furthermore, due to the higher lateral misalignment, this coil design can be used in WPT systems.

The Double D Quadrature (DDQ) coil is an improved type of DD coil and is designed to overcome the problems of the circular coil [36]. The DDQ coil is created by adding the quadrature coil Q to the DD coil. The additional coil is used at the center of the DD coil. The picture of the DDQ coil is shown in Fig. 2.12(c). The coil is designed in such a way that the DD coils catch the flux in the d-axis and the Q coil catches the flux in the q-axis and thus, the tolerance of the DDQ coil to the misalignment is extended. According to the misalignment between the transmitter and receiver, D or Q coil can couple the power. Furthermore, this coil has a single-sided flux path. In this coil structure, the mutual inductances between the coils in the same side are so small and can be neglected. The problem of this coil design is that due to the additional coil and additional power electronic converter, the charger may face additional losses.

Similar to the DDQ coil, the bipolar coil is composed of two coils. These coils which are identical, have mounted on the ferrite bars with overlap [30]. The picture of the bipolar coil is illustrated in Fig. 2.12(d). The advantages of the bipolar coil are that it has good misalignment tolerance and a high coupling coefficient. Furthermore, the construction of a bipolar coil needs less copper in comparison to the DDQ coil.

Based on the Qualcomm Halo™, Qualcomm Technologies has implemented a WPT system for dynamic charging of EV with the power up to 20 kW at highway speeds. Furthermore, this wireless charging solution has been implemented based on a market available static charging system and then was extended to the dynamic charging system. Qualcomm Technologies has also designed and tested simultaneous charging of two vehicles on the charging lane. The dynamic charging lane is a 100-meter test track and the receiver part was mounted on two Renault vehicles. The 100-meter transmission line is composed of 56 coils which are divided into four 25-meter segments. For each segment, an 85 kHz inverter exists. Each segment is divided into elementary modules which are activated when the receiver coils are close enough.

Korea Railroad Research Institute (KRRI) has designed and implemented a 1 MW WPT system for supplying a high-speed train [37]. In order to reduce the size and cost, the operating frequency of 60 kHz has been used for the system. The DC voltage for the supply of the inverter is constructed using silicon controlled rectifier. Since it is difficult to build a 1 MW inverter, for realizing a 1 MW inverter, five 200 kW inverters using IGBT switches were implemented and connected in parallel. The inverter converters the DC power to 60 kHz power and with using five matching transformers, the necessary 300 A output current is constructed. The transmitter was made of Litz wire with a single turn loop and length of 128 m. The receiver was composed of four 200 kW pickups. During the test, the maximum efficiency of 82.7% at 820 kW output power and 5 cm air-gap was obtained.

The Japanese Railway Technical Research Institute (RTRI) has designed a 300 kW wireless charger for railway systems. Furthermore, according to the designed system, a 50 kW downsized prototype has been developed [38]. The transmitter coil has a U-type shape and has 13.2 m long. The receiver is composed of three 16.7 kW pickups in order to build a 50 kW receiver. The configuration of the receiver in full power 300 kW will be composed of 18 pickups. The operating frequency of the system is 10 kHz and with the air-gap of 7.5 cm, the efficiency of 72.6 % was measured.

Bombardier has been working on WPT charging systems (PRIMOVE) since 2010 and till now, many static and dynamic systems for different purposes including buses and trams have been developed [18]. The PRIMOVE system in Augsburg allows charging of the trams over the air-gap wirelessly during the motion and without the use of conventional overhead power lines at the rated power of 250 kW. In this project, the bombardier tram is equipped with two receiver coils

to capture the power from the transmitter coils which are installed under the road. The general structure of this wireless system is presented in Fig. 1.13.

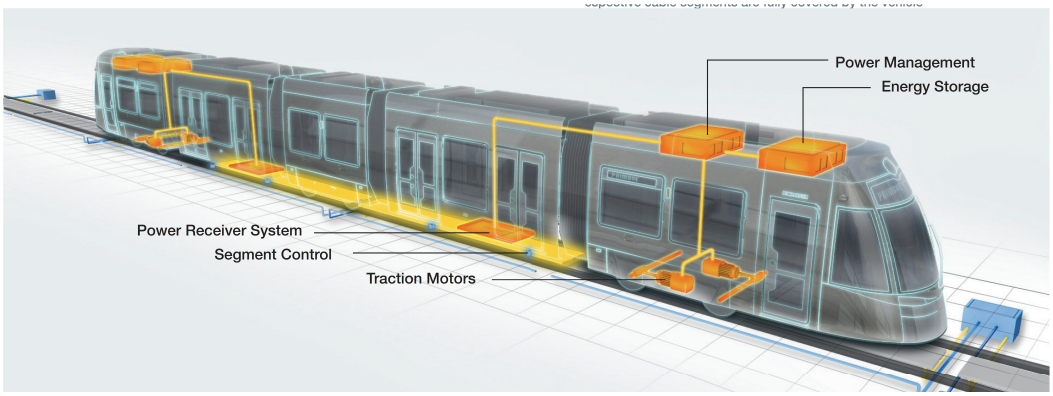

Fig. 1.13: Placement of the coils in Bombardier tram.

A three-phase power system is adopted in order to transfer high power to the receiver. The power line is constructed by 8-meter cable segments which are energized only when they are covered by the tram in order to minimize the electromagnetic field. The inverter is connected to a 750 VDC power supply and operates in 20 kHz. The air-gap between and transmitter and receiver is about 6 cm and as mentioned before, in the rail system, the lateral misalignment is very limited which makes the design much easier. The PREMOVE system is also used for the charging of the electric buses at various bus stops similar to a quasi-dynamic charging system. This system is now operative in some countries including Germany, Sweden, and Belgium. Restricted technical information about this system is available but it is found out that the output power is 200 kW with the efficiency of over 90%.

The dynamic WPT system designed by Nissan Research Center is composed of a rectangular shape 30 cm × 1.6 m transmitter coil, and a 40 cm diameter circular receiver coil as shown in Fig. 1.14. Five transmitter coils have been embedded into the ground [39]. In order to build the road surface without damaging the embedded coils, cement-asphalt (CA) mortar was used. CA mortar can be obtained when the asphalt is emulsified in water with soap. Furthermore, the receiver was mounted on a compact EV. According to the measurement, the coupling coefficient of 0.09 between the transmitter and receiver at the air-gap of 10 cm was obtained. At this air-gap, the maximum efficiency was 90% at the output power of 1 kW.

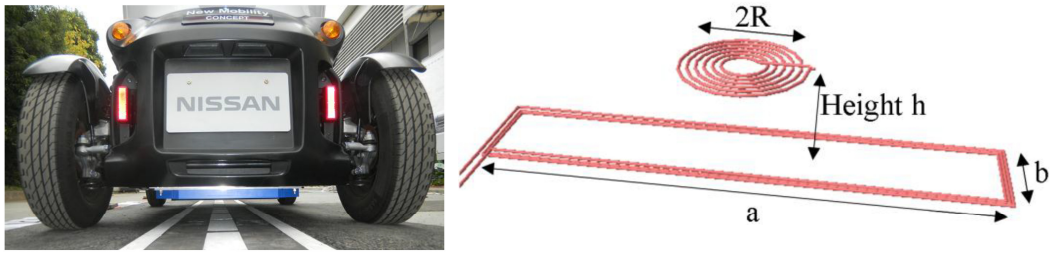

Fig. 1.14: Nissan dynamic WPT prototype; on the left: Photograph of the test EV, and on the right: structure of the coils.

The integrated infrastructure solution (INTIS) has been studying on WPT system for static charging and dynamic charging of EV since 2011. The transmitter of the dynamic solution is a single phase system. The charging lane has a total of 25 m long and it is composed of several coils with different characteristics and lengths [18], [40]. The supping of the transmitter coils is handled through the power electronics boards installed alongside the road. The picture of the charging structure is illustrated in Fig. 1.15. The transmitter coil has a double U-type shape. The transmitter coil layout is designed to be low cost with minimum material that allows for easy installation on road. The activation of the coil sections are done using positioning and communication systems. The operating frequency of the transmitter coil is 30 kHz and with the 10 cm air-gap, the output power of 30 kW is received. However, the obtained efficiency data is not available at this time.

Fig. 1.15: INTIS dynamic charging setup.

VICTORIA project, a project associated with FABRIC and Endesa, has developed different strategies for charging the EV including plug-in, static and dynamic charging systems. In this charging scenario, the EV is charged during the night when it is parked using a plug-in slow charger (3.7 kW). During the day, the EV can be charged wirelessly by static chargers placed at the bus stops and by the dynamic chargers installed in the charging lane at the power rating of 50 kW. The total route is 300 m long and is composed of ten transmitter coils. Of these ten transmitter coils, eight coils build the dynamic charging lane with the 12.5 m intervals and two remaining transmitter coils construct the static charging points as illustrated in Fig. 1.16. In order to reduce the misalignment between the transmitter and receiver during the charging process, an automatic steering wheel control system is used. The rated power of the system is 50 kW with the operating frequency of 23.8 kHz. A. According to [18], the efficiency of the system with 15 cm air-gap is reported 83%. The bus can operate with the speed of 10 km/h and is tolerant to 20 cm of lateral misalignment. The size of the receiver coil with 4 turns is 0.6 m × 2.5 m and the size of the transmitter is 0.6 m × 0.8 m.

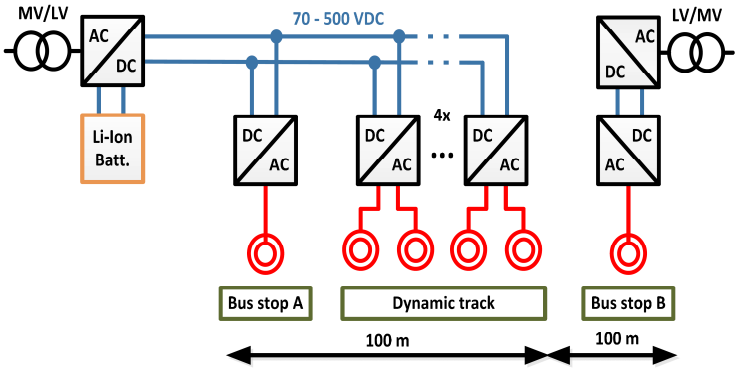

Fig. 1.16: Schematic of the charging lane of VICTORIA project composed of ten transmitter coils.

Utah State University has developed a wireless power transfer system for the dynamic charging of EV. The charging track has 400 m long with 75 m of embedded transmitter coils. The available information regarding Utah state university wireless system is limited however the power level is 25 kW with the air-gap around 15-25 cm. The efficiency of the system has reached approximately 90% [41].

Since 2011, Oak Ridge National Laboratory (ORNL) has been working on the dynamic charging of EV [42], [43]. The picture of the prototype is shown in Fig. 1.17. As shown in this figure, the segmented track topology has been adopted for this system and also the transmitter and receiver coils have a circular shape. The problem of this coil structure is that the system is not tolerant to the lateral misalignment. The operating frequency of the system is near 20 kHz. The output power is 2.2 kW which is used to charge a 72 V battery. The measured coil-to-coil and DC-to-DC efficiencies were 90% and 74% respectively. Besides the dynamic charging, ORNL has developed static wireless charging for various electric vehicle models.

Fig. 1.17: The ORNL dynamic WPT charging of an EV.

In Table 1.2, the important dynamic WPT system has been summarized. It is clear that the range and the research activities in the dynamic charging of EV are quite diverse. However, for most of the industry-oriented projects, limited information has been published. Furthermore, different groups have been working on different aspects of this system. Thus, it is difficult to have a perfect comparison between different dynamic charging systems at this developing stage with currently published information. For example, the efficiency presented in Table 1.2 is not clearly explained. In some of the measurements, AC grid-battery efficiency is presented, and in some other studies, DC-DC efficiency or coil-coil efficiency are performed. However, for a complete system comparison and analysis, the overall AC grid-battery efficiency measurement is necessary. From the current information, KRRI and Bombardier have implemented full-scale charging systems. Now, UTAH and OLEV dynamic charging systems are being utilized but the rating power levels are much lower that KRRI and Bombardier systems. In general, most of the systems have used long track topology except ORNL, INTIS, and Nissan for stable battery power and simple control. The operating frequency of all systems except Qualcomm is not in the range of SAE J2954 standard presented for the static charging system. KAIST OLEV 6G is now being developing a new system with 85 kHz operating frequency to reach the standard range according to the interoperability issues. From the transmitter coil point of view, Bombardier has used a quite different technology with distributed three-phase winding but other technologies have used single phase configuration

Table. 1. 2: Summary and research progress of dynamic WPT.

Prototype name	Vehicle type	Transmitter topology	Operating frequency (kHz)	Air-gap (cm)	Power (kW)	Efficiency (%)
PATH	Bus	Long	0.4	7.6	60	60
KAIST OLEV 1G	Golf cart	Long	20	1	3	80
KAIST OLEV 2G	Bus	Long	20	17	60	72
KAIST OLEV 3G	Car	Long	20	17	15	71
KAIST OLEV 4G	Bus	Long	20	20	25	74
KAIST OLEV 5G	Bus	Long	20	20	22	71
ORNL	Car	Segmented	23	10	1.5	75
Bombardier	Train	Long	20	6	250	90
KRRI Korea	Train	Long	60	5	820	83
Nissan Japan	compact car	Segmented	78	10	1	90
INTIS	Car	Segmented	30	10	30	TBD
Victoria	Bus	Long	23.8	15	50	83
Wave UTAH	Bus	TBD	20	25	25-50	90
Qualcomm	Car	Segmented	85	25	20	-
RTRI Japan	Train	Long	10	7.5	50	72.6

1.4 Research Goals and Objectives

The topic of this thesis is the summary of the activities and results in the project FABRIC [44]. According to the project target, a 100-m charging system for dynamic charging of the electric vehicle has been implemented. The rating power of the charging system is 20 kW at the nominal air-gap of 25 cm. The system is necessary to charge the EV during the movement with the maximum lateral misalignment of 20 cm. The segmented topology with 50 transmitter coils has been chosen. All transmitter coils have been embedded into the ground and covered with cement. Each coil has been connected to one high-frequency converter. Each high-frequency converter was connected to a 650 V DC bus and supplies the related coil with the current at the frequency of 85 kHz. The output power of the receiver has to charge the vehicle battery which its voltage varies between 250-400 V. This thesis is mainly focused on the control of the charging process during the movement of the vehicle. The thesis is composed of seven chapters. A brief description of each chapter is described as follows.

In the second chapter, the basic model of a WPT system is described. Due to the low coupling coefficient between the transmitter and receiver coils in wireless charging systems, the leakage inductance is high which limits the power transmission. In order to increase the power transmission capability and efficiency, some resonant capacitors are added to the transmitter and receiver side of the system. Various compensation topologies are discussed and their merits and weak points are investigated. Among all of these topologies, series-series topology is chosen due to the simple structure and good performance in dynamic conditions. The important equations of the WPT system with this capacitor topology are presented. Furthermore, the behavior of the system under different working conditions is analyzed. Finally, from the simplified model, the complete model of a WPT system is presented.

In chapter 3, the description of the transmitter and receiver coils are presented. The effect of the air-gap and lateral misalignment on the coupling coefficient of the coils is simulated. The rest of this chapter is dedicated to the control of the WPT system. Several control techniques are studied in this chapter. Then, two novel control strategies for the regulation of the output power at the presence of the mutual inductance variations are proposed. In these control strategies, the transmitter converter operates at a definite power level and the receiver can regulate the output power from zero power to the peak power according to the demand using a DC-DC converter or an active rectifier and without communicating with the transmitter converter. Finally, two methods for the identification of the vehicle are proposed.

In the fourth chapter, the simulation of the whole system in static and also in dynamic charging conditions is presented. The operation of the control system in different charging conditions such as variations of the operating frequency, power demand, and lateral misalignment is analyzed. Furthermore, in dynamic charging

the amount of energy that the battery receives in different vehicle speeds, air-gaps, and lateral misalignments is studied.

In chapter 5, the development of the charging lane is presented. The construction of the transmitter and receiver coils and resonant capacitors are provided in this chapter. Furthermore, the embedding procedure of the transmitter coils into the ground are given. Also, the design, implementation, and control of the power electronic converters are described in this chapter.

The results of several experimental tests are presented in the sixth chapter. The results are composed of various tests such as power demand control, operation of the control system with the variation of the air-gap, operation of the control with the presence of the lateral misalignment and the identification procedure.

Chapter 2

Basic theory and operation of WPT

It is more than one hundred years that wireless power transfer systems for different applications are developed however the basic idea can be expressed by Ampere's law and Faraday's law. In this chapter, the basic model of the system based is presented. The application of the resonant capacitors is discussed. Then, from the basic model, the complete model of the system is constructed.

2.1 Theory behind wireless power transfer

As shown in Fig. 2.1, a wireless power transfer system is composed of two coils separated by a large air-gap. The basic operation of the WPT can be expressed according to Ampere's law and Faraday's law [10].

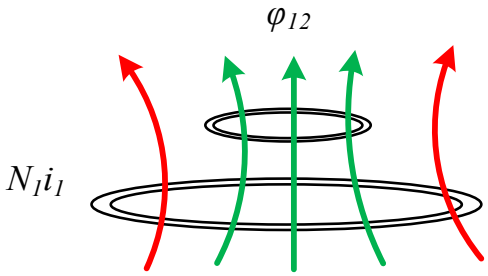

Fig. 2.1: Fundamental principle of WPT.

Based on the Ampere's law, when the AC current is flowing in a conductor, a time-varying magnetic flux will generate. The generated magnetic field is related to the current of the conductor and permeability of free space as

$$\sum B_T \, \Delta l = \mu_0 i_1 N_1 \tag{2.1}$$

Where μ_0 is the magnetic permeability, i_1 is the current flowed the transmitter conductor, N_1 is the number of transmitter conductor turns, l is the length of the

conductor in meters and B_T is the magnetic flux density in Tesla. According to the Faraday's law, if the time-varying magnetic flux generated by the transmitter conductor links the receiver conductor, it induces a voltage in it. If the receiver coil is kind of a closed circuit, an AC current will flow through it. The value of the induced voltage is related to the number of turn of the receiver and the rate of change in magnetic flux as

$$V_2 = -N_2 \frac{d\varphi_{12}}{dt} \tag{2.2}$$

Where N_2 is the number of turns of the receiver, and φ_{12} is the linked flux in the magnetic path in Weber. The portion of the magnetic field generated by the transmitter conductor which is linked with the receiver is determined by the geometry and material of the coils and can be described by the coupling factor as

$$k = \frac{M}{\sqrt{L_1 L_2}} \tag{2.3}$$

Where M is the mutual inductance between the coils and L_1 and L_2 are self-inductances of the transmitter and receiver coils respectively. k is between 0 and 1 because, unlike a conventional transformer, there is no core between the transmitter and receiver coils except air and all of the magnetic fluxes generated by the coil cannot pass to the other conductor. The flux generated by the coil that does not link with the other side is introduced as the leakage. When there is no receiver coil, the mutual inductance is zero and the self-inductance is only consisting of the leakage inductance.

2.2 Application of compensation capacitors

The power circuit of a non-compensated WPT system is presented in Fig. 2.2. L_1 and L_2 are self-inductances of the transmitter and receiver coils, respectively and M is the mutual inductance between the coils. Furthermore, in the WPT circuit, R_1 and R_2 are the resistances of the transmitter and receiver coils respectively. The AC source is for supplying the transmitter coil.

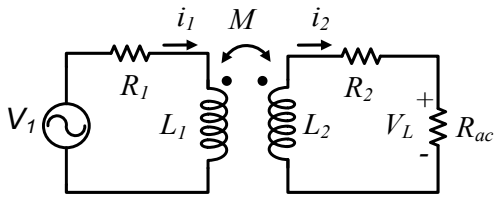

Fig. 2.2: Equivalent model of a non-compensated WPT system.

By writing the voltage equations for the transmitter and receiver circuits, the following equation set is obtained:

$$\begin{cases} V_1 = (R_1 + j\omega L_1)i_1 - j\omega M i_2 \\ j\omega M i_1 = (R_2 + j\omega L_2)i_2 + R_{ac} i_2 \end{cases} \tag{2.4}$$

By solving the above system of equations, the equations of i_1 and i_2 can be obtained as follows:

$$i_1 = \frac{(R_2 + R_{ac} + j\omega L_2)V_1}{(R_1 + j\omega L_1).(R_2 + R_{ac} + j\omega L_2) + (\omega M)^2} \tag{2.5}$$

$$i_2 = \frac{-j\omega M V_1}{(R_1 + j\omega L_1).(R_2 + R_{ac} + j\omega L_2) + (\omega M)^2} \tag{2.6}$$

The equation of the efficiency for the system can be written using the above equations as follows:

$$\begin{aligned} \eta &= \frac{{i_2}^2 R_{ac}}{{i_1}^2 R_1 + {i_2}^2 R_2 + {i_2}^2 R_{ac}} \\ &= \frac{R_{ac}}{(R_{ac} + R_2)\left(1 + \frac{R_1(R_{ac} + R_2)}{(\omega M)^2}\right) + R_1\left(\frac{L_2}{M}\right)^2} \end{aligned} \tag{2.7}$$

The efficiency of the system with the variation of the operating frequency of the input source is shown in Fig. 2.3(a). Due to the large air-gap and lack of core between the transmitter and receiver coils, the uncoupled magnetic flux between the coils increases. This uncoupled magnetic flux is realized as the leakage inductance. Since the coupling coefficient is very low, the value leakage inductance is relatively high. Thus, the system behaves inductively. As shown in this figure, by increasing the working frequency, higher efficiency for power transmission can be obtained. When the operating frequency goes up, the input impedance becomes more inductive naturally. Consequently, by increasing the operating frequency, the power factor reduces. When the power factor reduces, the input converter requires a larger Volt-Ampere (VA) rating. On the receiver side, when the working frequency increases, the receiver impedance extremely reduces the receiver current. In this case, the power transfer capability significantly reduces. These are major disadvantages of using this configuration for power transfer. In order to compensate the leakage inductance effect, some capacitors are added to the transmitter and receiver coils. With the compensation capacitors, the input reactive power becomes zero and the WPT system operates in Zero Phase Angle (ZPA) condition. Thus, the load seen from the output of the H-bridge converter is purely resistive and the VA rating of the converter becomes minimized [45]. Furthermore, the switching losses are minimized and the power transmission to the load is maximized. After the coils are designed and the self-inductance and mutual inductance become known, the next step is to calculate compensation capacitors.

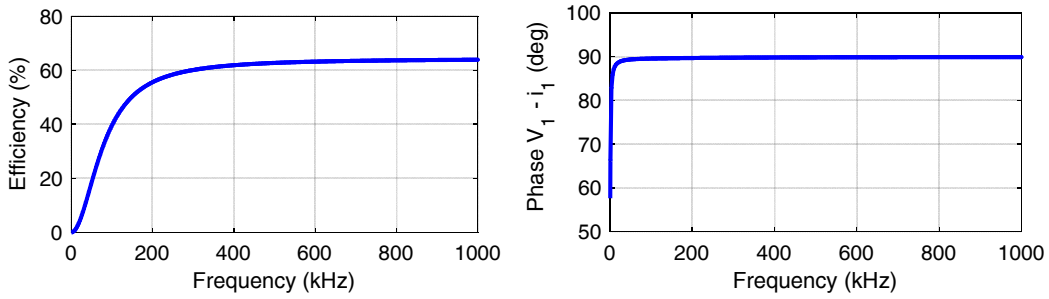

(a) (b)

Fig. 2.3: Simulation of a non-compensated wireless system. (a) Efficacy, and (b) input impedance phase.

2.2.1 Basic compensation topologies

In general, four elementary compensation topologies including series-series (SS) [46]–[48], series-parallel (SP) [49]–[52], parallel-series (PS) [53], [54], and parallel-parallel (PP) [55], [56] are available. Series and parallel represent the way that the capacitor is connected to the coil. Each of these compensation topologies has a specific load characteristic and uses for different applications. The equivalent models of these topologies are shown in Fig. 2.4.

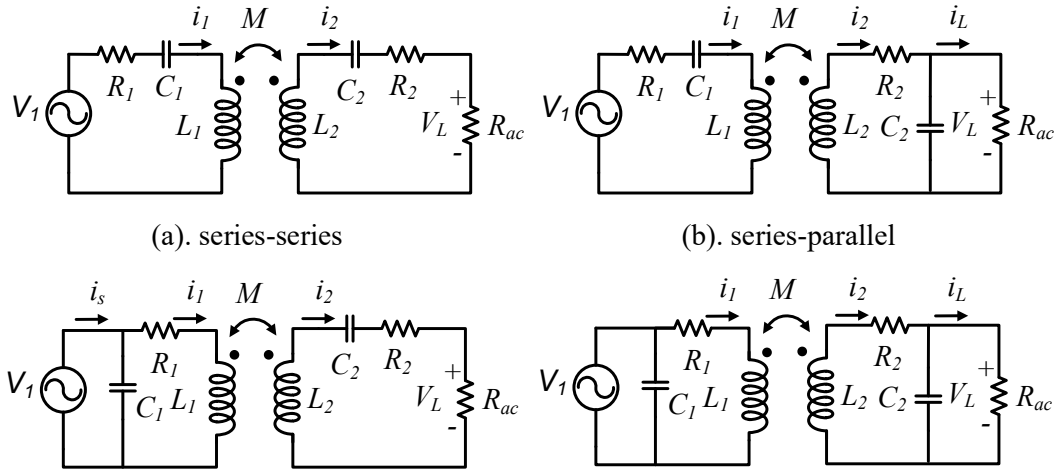

Fig. 2.4: Basic compensation topologies.

2.2.1.1 SS topology

In series-series compensated circuit, as shown in Fig. 2.4(a), capacitors are in series with the transmitter and receiver coils. For the design of the capacitor, the first step is the calculation of the receiver capacitor. For maximizing the power transfer capability, the impedance of the L_2 must be equal to the impedance of the receiver capacitor. Thus, the value of the receiver capacitor is calculated according to the following equation:

$$C_2 = \frac{1}{\omega^2 L_2} \tag{2.8}$$

The input impedance is composed of the transmitter impedance and the receiver impedance referred to the transmitter. By writing the equations of the transmitter and receiver, the input impedance of the circuit can be obtained as follows:

$$Z_{in-SS} = R_1 + j\omega L_1 + \frac{1}{j\omega C_1} + \frac{\omega^2 M^2}{R_2 + R_{ac}} \tag{2.9}$$

It can be seen that the reflected impedance to the transmitter side is zero. This means that the receiver will draw only the active power when the system is operating at the receiver resonance frequency. In order to make the equivalent impedance seen from the transmitter purely resistive, the value of the resonant capacitor in the transmitter side should be equal to:

$$C_1 = \frac{1}{\omega^2 L_1} \tag{2.10}$$

The value of the transmitter capacitor only depends on the transmitter self-inductance and the resonant frequency of the transmitter. By putting (2.10) into (2.9), the value of input impedance can be determined by:

$$Z_{in-SS} = R_1 + \frac{\omega^2 M^2}{R_2 + R_{ac}} \tag{2.11}$$

The input impedance is in opposite relation with the load resistance. This means that if the load resistance increases, the input power and relatively the output power increases.

2.2.1.2 SP topology

The circuit of the SP compensated WPT system is presented in Fig. 2.4(b). In the transmitter side of this topology, a capacitor is placed in series with the transmitter coil. Furthermore, on the receiver side, the compensation capacitor is in parallel with the receiver coil and the load resistance. The receiver compensation capacitor is used to maximize the power transfer capability. If the resistance of the receiver coil is neglected, this goal is fulfilled only if the impedance of the receiver coil is totally compensated by the capacitor and thus, the value of the receiver capacitor is defined by:

$$C_2 = \frac{1}{\omega^2 L_2} \tag{2.12}$$

The total impedance of the system is composed of the transmitter impedance and the receiver impedance referred to the transmitter side as follows:

$$Z_{in-SP} = \frac{V_1}{i_1} = R_1 + j\omega L_1 + \frac{1}{j\omega C_1} + \left[\frac{\omega^2 M^2}{R_2 + j\omega L_2 + \frac{R_{ac}}{1 + jR_L\omega C_2}}\right] \quad (2.13)$$

By neglecting coil resistances and also by putting (2.12) into (2.13) and substituting C_2, (2.13) is simplified as:

$$Z_{in-SP} = j\omega L_1 + \frac{1}{j\omega C_1} + \frac{M^2 R_{ac}}{{L_2}^2} - \frac{jM^2\omega}{L_2} \quad (2.14)$$

According to the above equation, the reflected reactance to the transmitter side is capacitive and is composed of mutual inductance. In order to make the equivalent impedance seen from the transmitter to be purely resistive, the transmitter capacitor must compensate the reactance of the transmitter coil and the reflected reactance from the receiver to the transmitter according to the following equation:

$$C_1 = \frac{L_2}{\omega^2(L_1L_2 - M^2)} \quad (2.15)$$

According to (2.15), the value of the transmitter capacitor depends on the mutual inductance, self-inductances of the coils and the transmitter resonant frequency. By putting (2.15) into (2.14), the value of the input impedance can be calculated as follows:

$$Z_{in-SP} = \frac{M^2 R_{ac}}{{L_2}^2} \quad (2.16)$$

According to (2.16), the input resistance is in relation with the load resistance. If the load resistance increases, the load power decreases and thus, the SP topology is suitable for high voltage low current application.

2.2.1.3 PS topology

The parallel-series compensated circuit is shown in Fig. 2.4(c). In the receiver side, a capacitor is placed in series with the coil. In the transmitter side, the capacitor is in parallel with the coil. The design of the receiver capacitor is similar to the SS topology according to (2.8). For the design of the transmitter capacitor, by considering (2.8) and neglecting the coil resistances, the input impedance of the system is calculated as follows:

$$Z_{in-ps} = \frac{1}{\frac{1}{j\omega L_1 + \frac{\omega^2 M^2}{R_{ac}}} + j\omega C_1} \quad (2.17)$$

The impedance of the receiver referred to the transmitter has only real component and no reactive components and thus, the receiver will draw only active power. Now, for the calculation of the transmitter capacitor, the imaginary part of the input impedance must be equal to zero and thus, C_1 is calculated according to the following equation.

$$C_1 = \frac{L_1 {R_{ac}}^2}{\omega^4 M^4 + {L_1}^2 {R_{ac}}^2 \omega^2} \tag{2.18}$$

It can be seen from (2.18) that the transmitter capacitor depends on the mutual inductance and the load resistance. By substituting C_1 in (2.17) with (2.18), the input resistance value is obtained as:

$$Z_{in-ps} = \frac{{L_1}^2 {R_{ac}}^2 + \omega^2 M^4}{R_{ac} M^2} \tag{2.19}$$

For this topology, the input impedance depends on load resistance, self-inductance of the transmitter, the mutual inductance, and the resonant frequency.

2.2.1.4 PP topology

In parallel-parallel compensated circuits as shown in Fig. 2.4(d), the compensation capacitors both in the transmitter and receiver sides are connected in parallel to the coils. The design of the receive capacitor is similar to the SP topology according to (2.12). For the design of the transmitter capacitor, by considering (2.12) and neglecting the coil resistances, the input impedance of the system is calculated as follows:

$$Z_{in-PP} = \frac{1}{\frac{1}{j\omega L_1 + \frac{M^2 R_{ac}}{{L_2}^2} - \frac{jM^2\omega}{L_2}} + j\omega C_1} \tag{2.20}$$

It can be seen that the receiver impedance referred to the transmitter is capacitive. The transmitter capacitor must be designed in order to compensate the reactance of the transmitter coil and the reflected reactance from the receiver to the transmitter according to the following equation:

$$C_1 = \frac{{L_2}^3 (L_1 L_2 - M^2)}{M^4 {R_{ac}}^2 + {L_2}^2 (L_1 L_2 - M^2)^2 \omega^2} \tag{2.21}$$

It is clear that C_1 is depended on the mutual inductance and the load resistance. By substituting C_1 in (2.20) with (2.21), the input impedance is obtained as:

$$Z_{in-PP} = \frac{{L_1}^2{L_2}^4\omega^2 - 2L_1{L_2}^3M^2\omega^2 + {L_2}^2M^4\omega^2 + M^4{R_{ac}}^2}{{L_2}^2M^2R_{ac}} \quad (2.22)$$

By designing the transmitter and receiver capacitors according to the design procedure described above, for all topologies, the input impedance is purely resistive when working at the resonant frequency. However, only in SS topology, the transmitter capacitor is independent of both mutual inductance and load. The transmitter resonant frequency is only depended on the self-inductances of the coils. For other topologies, the transmitter resonant frequency is depended on the mutual inductance. Furthermore, for the topologies with the parallel compensation capacitor in the transmitter, the transmitter resonant frequency is a function of the load as well. One of the major drawbacks of the topologies with the parallel capacitor in the transmitter side is that when the voltage polarity changes, the voltage of the transmitter capacitor goes up and reaches the source voltage immediately. This causes flowing of high current in the capacitor which leads to reducing the capacitor lifetime. Thus, an additional series inductor is necessary to regulate the current flowing into the parallel circuit. This inductor increases the total size and cost of the system. The SS topology is the best choice for the applications where the mutual inductance variation is considerable.

2.2.2 Higher order compensation topologies

In spite of the great advantages of SS topology, there are some problems associated with this topology that must be considered during the system design. The SS topology is constraint by the parameters of the coils. When the transmitter and receiver coils are designed and constructed, if the input DC source, air-gap, and resonant frequency remain constant, the maximum output power cannot be changed except modifying the coil. In SS topology, when the coupling drops down the transmitter current increases. Thus, it is necessary to protect the circuit of SS topology against overcurrent fault. Furthermore, the high voltage stress on the compensation capacitors makes the construction difficult especially at high-power applications. Thus, several higher order compensation topologies have been introduced in order to improve system performance [57], [58].

2.2.2.1 LCL-LCL topology

In LCL topology, an LC resonant circuit is added to coils to form an LCL resonant circuit in each side [59], [60]. This topology is presented in Fig. 2.5.

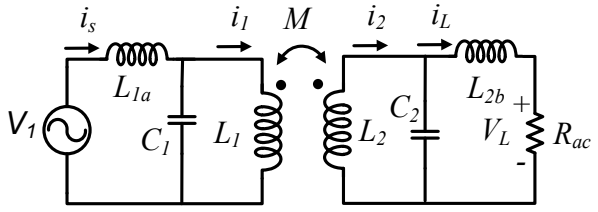

Fig. 2.5: Equivalent model of LCL topology.

The overall impedance of the receiver side (Z_R) is:

$$Z_R = j\omega L_2 + (R_{ac} + j\omega L_{2\mathrm{b}}) \| \frac{1}{j\omega C_2} = j\omega L_2 + \frac{(R_{ac} + j\omega L_{2\mathrm{b}}) \frac{1}{j\omega C_2}}{R_{ac} + j\omega L_{2\mathrm{b}} + \frac{1}{j\omega C_2}} \tag{2.23}$$

The impedance of the receiver becomes purely resistive if the values of the resonant circuit are selected as follows:

$$X_R = j\omega L_2 = j\omega L_{2\mathrm{b}} = -\frac{1}{j\omega C_2} \tag{2.24}$$

Thus, the impedance of the receiver is obtained as follows:

$$Z_R = \frac{-{X_R}^2}{R_{ac}} \tag{2.25}$$

In order to have the resistive impedance seen from the input source and to decrease the VA rating of the source, the values of the resonant elements in the transmitter side must be designed in the same way as the receiver side as follow:

$$X_T = j\omega L_1 = j\omega L_{1\mathrm{a}} = -\frac{1}{j\omega C_1} \tag{2.26}$$

By selecting the resonant elements according to (2.26), the input impedance seen from the source can be expressed as:

$$Z_{in-LCL} = \frac{-{X_T}^2}{\frac{\omega^2 M^2}{Z_R}} = \frac{{X_T}^2 {X_R}^2 R_{ac}}{\omega^2 M^2} = \frac{{L_1}^2 {L_2}^2 \omega^2 R_{ac}}{M^2} \tag{2.27}$$

It is clear from the above equation that the input impedance is purely resistive. Furthermore, the input impedance has an inverse relation with the mutual inductance. In means that, if the mutual inductance increases, the input resistance decreases and thus, the input current goes up. So, there is no need to protect the circuit against overcurrent fault in low coupling conditions. By writing KVL equations for the transmitter side we have:

$$\begin{cases} V_1 = j\omega L_{1\mathrm{a}} i_{\mathrm{s}} + \left(\frac{\omega^2 M^2}{Z_R} + j\omega L_1\right) i_1 \\ \left(\frac{\omega^2 M^2}{Z_R} + j\omega L_1\right) i_1 = \frac{1}{j\omega C_1}(i_{\mathrm{s}} - i_1) \end{cases} \tag{2.28}$$

The transmitter current equation is determined by:

$$i_1 = \frac{V_1}{X_T} \tag{2.29}$$

By obtaining the transmitter coil current, the equation for the load current (i_L) can be calculated by:

$$i_L = \frac{j\omega M i_1}{X_R} = \frac{j\omega M V_1}{X_T X_R} = \frac{M V_1}{j\omega L_1 L_2} \tag{2.30}$$

In can be concluded from (2.30) that the load current is independent of the load resistance and similar to SS topology, LCL topology is a constant current topology.

2.2.2.2 LCC-LCC topology

Despite several merits, LCL topology has some drawbacks. Similar to SS topology, in LCL topology, the maximum output power is constraint by the parameters of the coils. It is possible to control the output power by changing the values of the inductors L_{1a} and L_{2b}. However, in this case, the input impedance would not be purely resistive. Furthermore, in the design of the LCL topology, the values of the additional inductors are the same as the coils inductances which increase the size and cost of the system. The power circuit of the LCC topology is presented in Fig. 2.6.

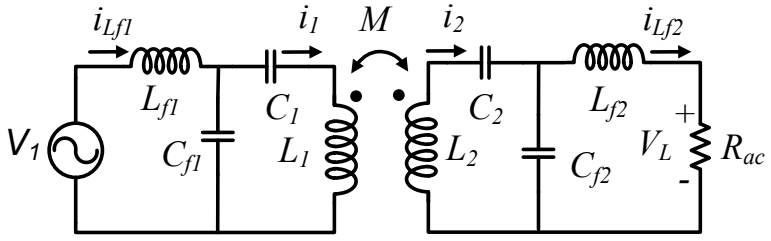

Fig. 2.6: Equivalent model of LCC topology.

In order to reduce the size of the additional inductors, additional resonant capacitors are put in series with the transmitter and receiver coils of LCL topology and LCC topology is formed [61]–[71]. The relation between the additional capacitors and inductors in the transmitter and receiver sides is defined by:

$$X_R = j\omega L_{\mathrm{f2}} = j\omega L_2 + \frac{1}{j\omega C_2} = -\frac{1}{j\omega C_{\mathrm{f2}}} \tag{2.31}$$

$$X_T = j\omega L_{\mathrm{f1}} = j\omega L_1 + \frac{1}{j\omega C_1} = -\frac{1}{j\omega C_{\mathrm{f1}}} \tag{2.32}$$

Similar to LCL, the input impedance can be calculated according to the following equation:

$$Z_{in-LCC} = \frac{-{X_T}^2}{\frac{\omega^2 M^2}{Z_R}} = \frac{{X_T}^2 {X_R}^2 R_{ac}}{\omega^2 M^2} = \frac{{L_{f1}}^2 {L_{f2}}^2 \omega^2 R_{ac}}{M^2} \tag{2.33}$$

Where Z_R is the impedance of the receiver. Similar to LCL topology, in low coupling, the input impedance is very big which limits the input source current. Finally, the load current can be calculated according to the following equation:

$$i_{Lf2} = \frac{j\omega M V_1}{X_T X_R} = \frac{M V_1}{j\omega L_{f1} L_{f2}} \tag{2.34}$$

Similar to SS and LCL topologies, LCC topology has constant current characteristics independent of the load resistance variations. Furthermore, according to the above equation, the load current is depended on the values of the extra inductors. These inductors have added an additional degree of freedom to the design and by modifying these values, it is possible to change the output power without the necessity to replace the transmitter and receiver coils. Considering that SS and LCC topologies are designed to transfer the same amount of power with the voltage gain equal to one, it can be concluded that the voltage and current of stresses over the transmitter and receiver coils (L_1 and L_2) are the same at the aligned situation for both topologies. The peak-peak voltage stress of the series capacitors of the transmitter for SS and LCC topologies can be expressed as

$$\Delta V_{C1-ss} = \frac{i_1 \Delta t}{C_1} = i_1 \Delta t \omega^2 L_1 \tag{2.35}$$

$$\Delta V_{C1-LCC} = \frac{i_1 \Delta t}{C_1} = i_1 \Delta t \omega^2 (L_1 - L_{f1}) \tag{2.36}$$

Where Δt is defined as half of the switching period. Thus, the relation between the voltage stress over the series capacitors of the transmitter is determined by

$$\frac{\Delta V_{C1-LCC}}{\Delta V_{C1-ss}} = \frac{L_1 - L_{f1}}{L_1} \tag{2.37}$$

In the same way, the voltage stresses of the receiver capacitors for both topologies can be defined by

$$\frac{\Delta V_{C2-LCC}}{\Delta V_{C2-ss}} = \frac{L_2 - L_{f2}}{L_2} \tag{2.38}$$

Thus, the voltage stress over the series capacitors in the transmitter and receiver sides for the LCC topology is smaller than the SS topology. As described above, LCC topology has many advantages however the problem of this topology is that

the additional components are needed in comparison to the basic compensation topologies. This increases the size and cost of the system. Furthermore, due to these additional components, the efficiency in the LCC circuit is lower in comparison to the SS system.

Besides these topologies, many new topologies with several interesting characteristics have been generated and used for different applications such as: LCL-S [72], S-LCL [73], LCL-P [74], [75], LCC-S [76]–[79], S-LCC [80], S-CLC [81] and LC-S [82]. The operating principle and important equations of these topologies are based on the previously discussed topologies and for this reason, they are not described here. Furthermore, it should be noted that the hybrid compensation topology is built by the combination of two compensation topologies and switching between them using some semiconductor devices in order to utilize the benefit of two topologies characteristics [83]–[93].

In conclusion, the SS, LCL and LCC topologies have great features that make them suitable for wireless applications. In these topologies, the resonant frequency is independent of the load resistance and mutual inductance. Furthermore, the input source operates in the ZPA condition. SS topology has a simple structure but the voltage stress on capacitors is high. Furthermore, it needs a load detection circuit and overcurrent protection circuit. LCC topology has solved these problems with the expense of extra components and lower efficiency.

2.3 Basic equations and operation of SS topology

Since SS topology is used in the implemented WPT system, the operation and behavior of this topology are analyzed here. The equivalent model WPT system with SS compensation topology is shown in Fig. 2.7.

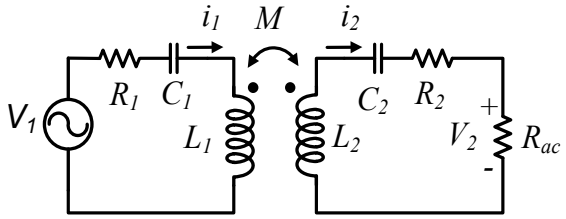

Fig. 2.7: Simplified model of the WPT system with SS compensation topology.

By writing the equations for the transmitter circuit and the receiver circuit, two sides of the system, the following equation set is achieved:

$$\begin{cases} V_1 = \left(R_1 + j\omega L_1 + \dfrac{1}{j\omega C_1}\right) i_1 - j\omega M i_2 \\ j\omega M i_1 = \left(R_2 + j\omega L_2 + \dfrac{1}{j\omega C_2}\right) i_2 + R_{ac} i_2 \end{cases} \tag{2.39}$$

By solving the above system of equations, i_1 and i_2 can be obtained as follows:

$$i_1 = \frac{\left(R_2 + R_{ac} + j\omega L_2 + \frac{1}{j\omega C_2}\right) V_1}{\left(R_1 + j\omega L_1 + \frac{1}{j\omega C_1}\right).\left(R_2 + R_{ac} + j\omega L_2 + \frac{1}{j\omega C_2}\right) + (\omega M)^2} \quad (2.40)$$

$$i_2 = \frac{-j\omega M V_1}{\left(R_1 + j\omega L_1 + \frac{1}{j\omega C_1}\right).\left(R_2 + R_{ac} + j\omega L_2 + \frac{1}{j\omega C_2}\right) + (\omega M)^2} \quad (2.41)$$

Thus, the output power equation can be determined by

$$P_o = R_{ac}|i_2|^2 = R_{ac}\left|\frac{\omega M V_1}{\left(R_1 + j\omega L_1 + \frac{1}{j\omega C_1}\right).\left(R_2 + R_{ac} + j\omega L_2 + \frac{1}{j\omega C_2}\right) + (\omega M)^2}\right|^2 \quad (2.42)$$

Furthermore, the impedance seen from the input is calculated by dividing the input source voltage and current as follows:

$$Z_{in} = \frac{V_1}{i_1} = R_1 + j\omega L_1 + \frac{1}{j\omega C_1} + \left[\frac{\omega^2 M^2}{R_2 + R_{ac} + \frac{1}{j\omega C_2} + j\omega L_2}\right] \quad (2.43)$$

The waveforms of the output power P_o, input impedance Z_{in}, input impedance phase and the efficiency versus the variations of the frequency for different mutual inductances are shown in Fig. 2.8. As shown in Fig. 2.8(a), in the low coupling, the peak of the output power curve relating to the frequency has one peak which occurs exactly at the resonant frequency of the system. In a WPT system, in order to improve efficiency, it is desirable to build a coil with high coupling. The efficiency of the system versus the frequency is shown in Fig. 2.8(b). It can be seen that the efficiency of the system increases if the coupling goes up. Furthermore, the efficiency becomes maximum at the resonant frequency. However, as shown in Fig. 2.8(a), by increasing the coupling coefficient, the output power peak is divided into two and a double-peak waveform is generated. When the coupling coefficient reduces, these two peaks approach each other. This double peak phenomenon is named bifurcation or frequency splitting [94], [95]. This effect is due to the behavior of the input phase of the impedance. The waveforms of the input impedance phase for various mutual inductances are presented in Fig. 2.8(c). In the low coupling coefficient, there is one zero phase angle frequency. However, if the designed coupling coefficient increases, the phase of the input impedance shows three zero crossings instead of one. The input impedance phase is zero in all three ZPA frequencies. However, it is crucial to identify the real ZPA frequency because the maximum efficiency occurs at this frequency. Identifying the ZPA frequency

by tracking of the input voltage and current with PLL controllers is proposed in the literature [94]. However, this control may face instability due to bifurcation phenomena. It can be seen from Fig. 2.8(d) that phase difference between the input voltage and the output current is unique in all mutual inductances and is not affected by bifurcation. This option is studied in [96] to identify the resonant frequency. Appearing of the additional ZPA frequencies when coupling increases are presented in Fig. 2.8(e). The waveforms of the input impedance magnitude versus frequency for different mutual inductance are shown in Fig. 2.8(f). The input impedance of the system is composed of the real part and the imaginary part as presented in (2.43). In order to have only one ZPA frequency, the imaginary part of the input impedance equation must be zero. By writing the input impedance equation and putting the imaginary part of it zero, the limit coupling coefficient for having a unique zero phase angle frequency can be determined by [95]:

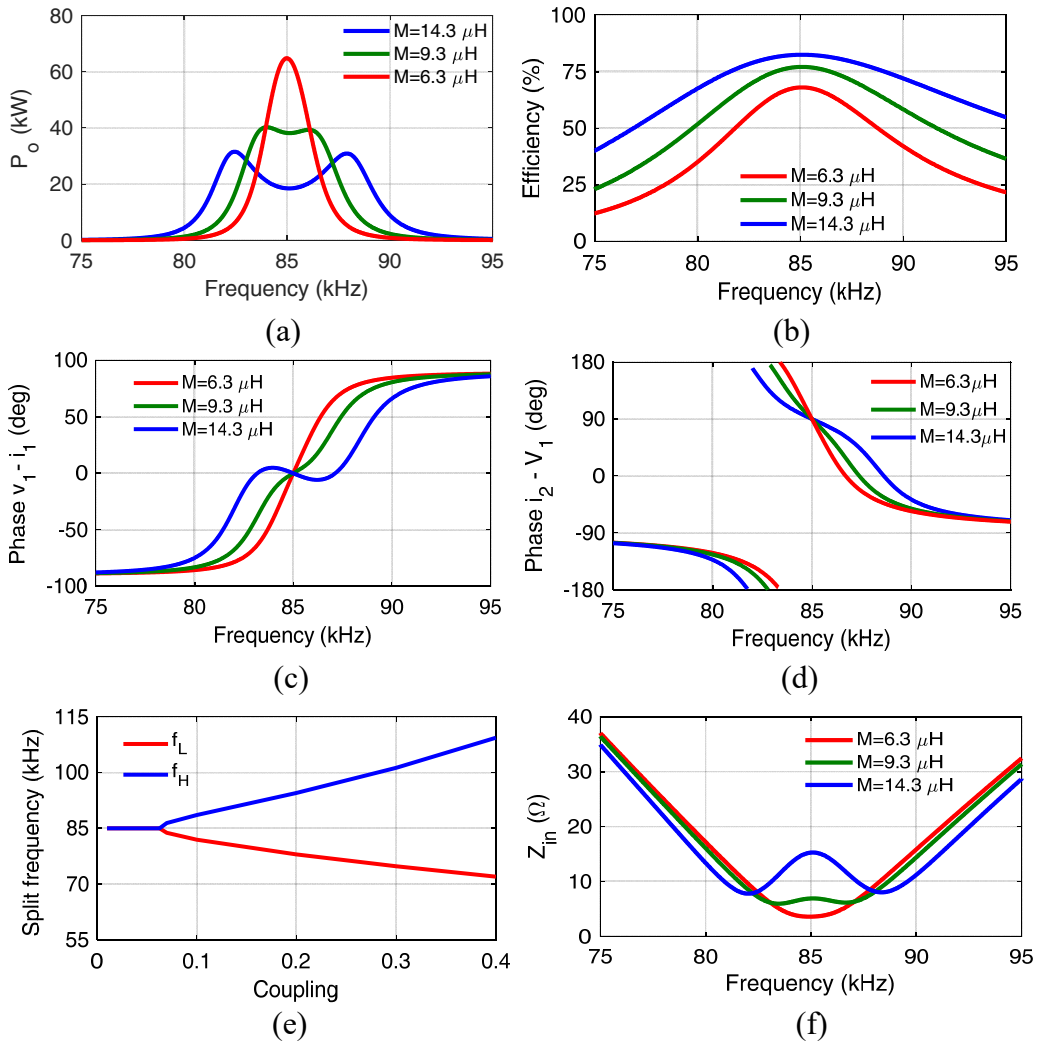

Fig. 2.8: Operation of the system versus frequency variations for different mutual inductances. (a) Output power, (b) efficiency, (c) input impedance phase, (d) phase difference between output current and input voltage, (e) appearing of the two additional ZPA frequencies, and (f) input impedance magnitude versus frequency.

$$k < \sqrt{\frac{4{Q_2}^2 - 1}{4{Q_2}^4}} \cong \frac{1}{Q_2} = \frac{R_{ac}}{\omega L_2} \tag{2.44}$$

The output power and input impedance phase versus frequency for different load resistances are shown in Fig. 2.9(a) and Fig. 2.9(b). It can be seen from Fig. 2.9(b) that if the load resistance decreases, three ZPA frequencies appear again. According to (2.44), the coupling limit is proportional to the load resistance too.

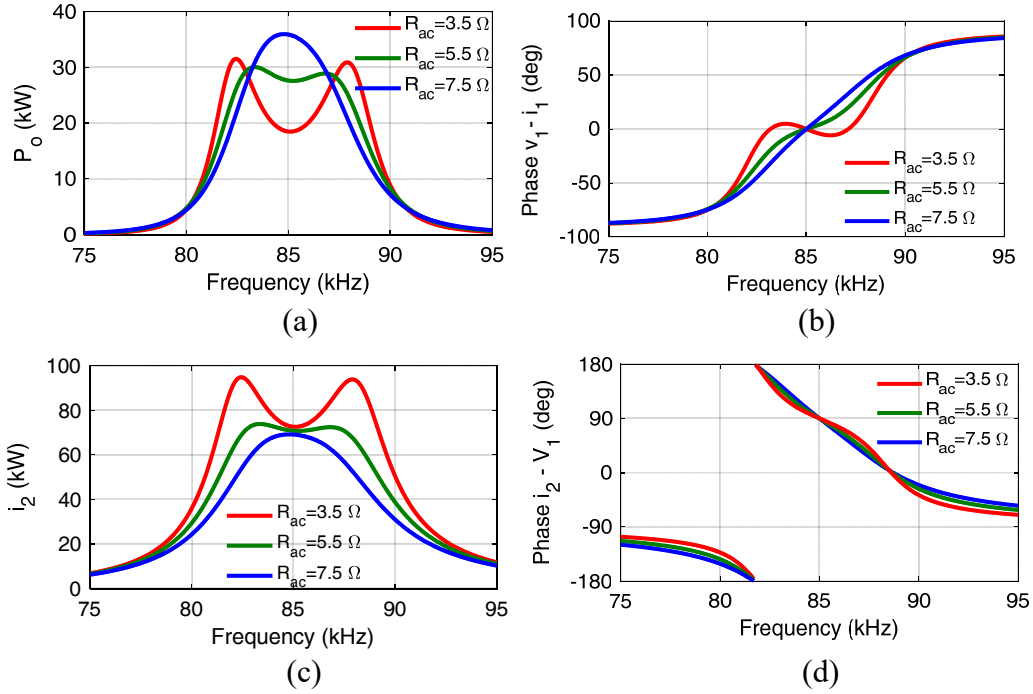

Fig. 2.9: Operation of the system versus frequency variations for different resistances. (a) Output power, (b) input impedance phase, (c) receiver current, and (d) phase difference between output current and input voltage.

Generally, the resonant capacitors C_1 and C_2 are designed in order to compensate the inductance of the coil at resonant frequency ω_0 as follows:

$$\omega_0 = \frac{1}{\sqrt{L_1 C_1}} = \frac{1}{\sqrt{L_2 C_2}} \tag{2.45}$$

By considering that the system operates at the resonant frequency according to (2.45), the equation set (2.39) can be simplified as:

$$\begin{cases} V_1 = R_1 i_1 - j\omega M i_2 \\ j\omega M i_1 = R_2 i_2 + R_{ac} i_2 \end{cases} \tag{2.46}$$

From (2.46), the transmitter and receiver currents equations can be determined by

$$i_1 = \frac{(R_2 + R_{ac})\, V_1}{R_1(R_2 + R_{ac}) + \omega_0^2 M^2} \tag{2.47}$$

$$i_2 = \frac{j\omega_0 M V_1}{R_1(R_2 + R_{ac}) + \omega_0^2 M^2} \tag{2.48}$$

The output power equation can be obtained as:

$$P_o = \frac{{V_1}^2 \omega^2 M^2 R_L}{[\omega^2 M^2 + R_1(R_2 + R_{ac})]^2} \tag{2.49}$$

Furthermore, the efficiency of the system can be defined by:

$$\eta = \frac{{i_2}^2 R_{ac}}{{i_1}^2 R_1 + {i_2}^2 R_2 + {i_2}^2 R_{ac}} = \frac{(\omega M)^2 R_{ac}}{(R_2 + R_{ac})[R_1(R_2 + R_{ac}) + (\omega M)^2]} \tag{2.50}$$

Furthermore, the impedance seen from the input is calculated by dividing the input source voltage and current as follows:

$$Z_{in} = R_1 + R_{\text{ref}} = R_1 + \frac{\omega^2 M^2}{R_2 + R_{ac}} \tag{2.51}$$

Where R_{ref} is the receiver impedance reflected to the transmitter side. One of the main issues in the WPT system is keeping the efficiency maximum. The power which is dissipated in R_{ref} is equivalent to the transferred power to the receiver side of the system. So, it is necessary to increase R_{ref} in order to increase efficiency. In low reflected impedance, most of the energy dissipates in the transmitter resistance and the efficiency reduces. The reflected impedance is proportional to the mutual inductance and load resistance. If the mutual inductance increases, the reflected impedance increases and thus the efficiency of the system becomes higher. In a high value of R_{ac}, the reflected impedance becomes small and the efficiency reduces again. However, a very small value of R_{ac} would not result in an increase in efficiency. In this case, most of the transferred power dissipates in the receiver resistance and the efficiency drops again. The optimal load resistance for having the maximum efficiency can be written as follows:

$$R_{L-opt} = \sqrt{\frac{R_2}{R_1}[R_1 R_2 + (\omega M)^2]} \tag{2.52}$$

According to (2.52), $R_{L\text{-opt}}$ depends on mutual inductance. However, the mutual inductance changes due to the misalignment between coils. By using an additional power electronic converter, it is possible to keep the load resistance equal to optimal resistance and maintain the efficiency of the system at the highest possible value.

The waveforms of i_1, i_2, efficiency, and P_o versus mutual inductance for various load resistances are presented in Fig. 2.10. Transmitter current waveform versus mutual inductance for different load resistances is shown in Fig. 2.10(a). According to (2.47), when mutual inductance increases, the transmitter current reduces. Furthermore, when the load resistance increases, according to (2.51), input impedance decreases and transmitter current increases. Receiver current waveform versus mutual inductance for different load resistances is illustrated in Fig. 2.10(b). The receiver current increases with mutual inductance firstly and then decreases. In low mutual inductance, the receiver current decreases when load resistance increases. On the other hand, when the mutual inductance is high, the receiver current remains constant in spite of load resistance variations. The efficiency of the system versus mutual inductance is presented in Fig. 2.10(c). It is obvious that the efficiency goes up when the mutual inductance increases. The waveforms of the output power for different mutual inductances and load resistances are presented in Fig. 2.10(d). It can be seen that when load resistance increases, for having maximum output power, the increase of the mutual inductance is necessary.

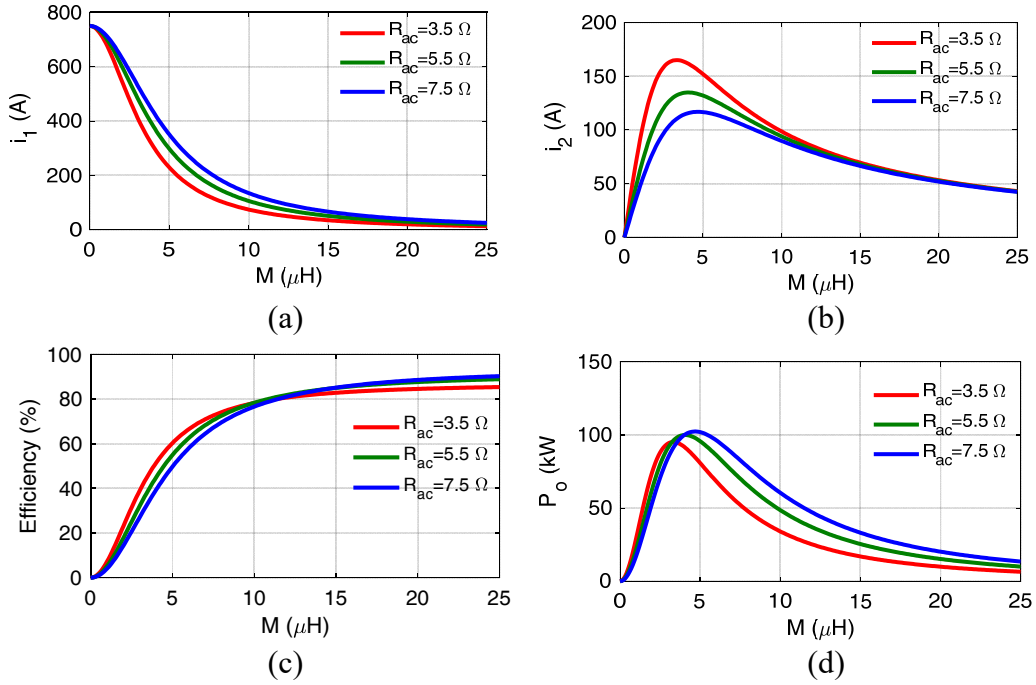

Fig. 2.10: Operation of the system versus mutual inductance variations for different load resistances. (a) Transmitter current, (b) receiver current, (c) efficiency, and (d) output power.

The waveforms of the transmitter current i_1, receiver current i_2, efficiency, and output power P_o versus load resistance for various mutual inductances are presented in Fig. 2.11. According to Fig. 2.11(a) and Fig. 2.11(b), when the mutual inductance decreases, both transmitter and receiver currents increase. Furthermore, when equivalent load resistance increases, the transmitter current increases. However, in the receiver side and when the mutual inductance is high, the receiver current

variations versus load resistance remain almost constant. In high mutual inductances, transmitter and receiver currents are lower. Thus, the voltage drop over the transmitter resistance is smaller and the receiver current variation is not significant. According to Fig. 2.11(c), when mutual inductance increases, the efficiency increases. Furthermore, by variation of the mutual inductance, the optimal load resistance changes based on (2.52). The behavior of the output power is like the current of the transmitter. When the mutual inductance decreases or the load resistance increases, the output power increases as shown in Fig. 2.11(d).

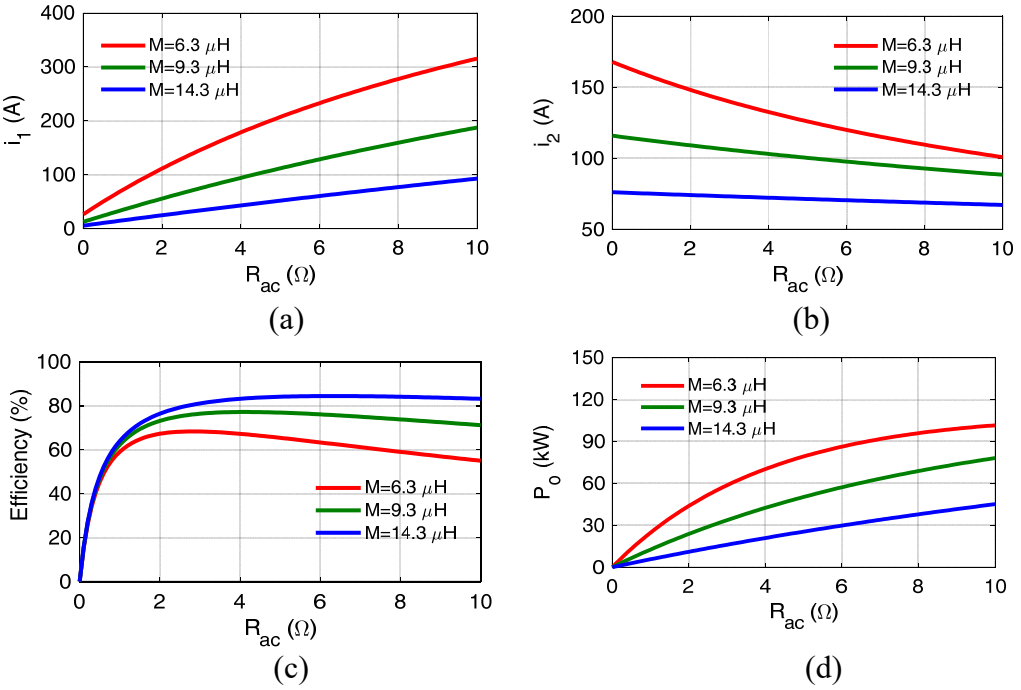

Fig. 2.11: Operation of the system versus load resistance variations for different mutual inductances. (a) Transmitter current, (b) receiver current, (c) efficiency, and (d) output power.

2.4 Complete power circuit of WPT

The equivalent model of the WPT system with SS topology was presented in Fig. 2.7. In this model, the transmitter coil is supplied by an AC source. However, in a real system, the AC voltage is generated by an H-bridge converter. Furthermore, the output of the receiver is connected to a diode rectifier in order to supply the load with DC current. The whole structure of a wireless charging system can be expressed as presented in Fig. 2.12. The transmitter converter is a high-frequency H-bridge converter composed of switches S_1, S_2, S_3 and S_4. The H-bridge converter provides the excitation current to the transmitter coil. Then, the power is transferred to the receiver across a gap. Then, an AC voltage induces to the receiver coil. The induced AC voltage is rectified by a passive rectifier composed of diodes D_1, D_2, D_3 and D_4 and then the DC power is transferred to the load R_L. In this figure, the battery is modeled with a resistance R_L.

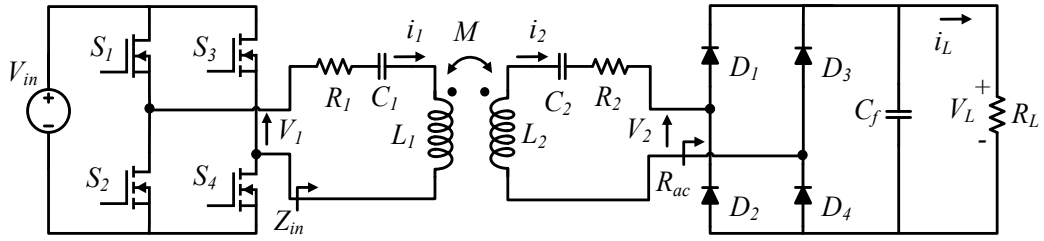

Fig. 2.12: Complete power circuit of a WPT system.

The relation between the equivalent model and the complete model can be expressed according to the First Harmonic Approximation (FOA) analysis [97]. The waveform of the DC-AC converter output voltage is a square wave. The Fourier series of the converter output voltage is equal to:

$$V_1(t) = \frac{4V_{in}}{\pi}\sum_{n=1}^{\infty}\frac{1-(-1)^n}{2n}\sin(n\omega t) \tag{2.53}$$

By neglecting higher order harmonics, the Fourier series of the inverter output voltage can be simplified and the first harmonic equation can be determined by

$$V_1(t) = \frac{4V_{in}}{\pi}\sin(\omega t) \tag{2.54}$$

Now, the H-bridge output voltage can be modeled as an AC voltage source with the RMS value of the first harmonic equation as follows:

$$V_1 = \frac{2\sqrt{2}}{\pi}V_{in} \tag{2.55}$$

The waveform of the voltage at the output of the receiver coil is a square wave and the FOA analysis can be extended to it as well. Therefore, the first-order harmonic of the receiver voltage can be expressed as

$$V_2 = \frac{2\sqrt{2}}{\pi}V_L \tag{2.56}$$

Furthermore, the relation between i_L and the receiver current can be written according to the following equation:

$$i_2 = \frac{\pi\sqrt{2}}{4}i_L \tag{2.57}$$

Based on (2.56) and (2.67), the relation between the load resistance (R_L) and the equivalent resistance seen from the input of the rectifier (R_{ac}) can be determined by:

$$R_{ac} = \frac{8}{\pi^2} R_L \tag{2.58}$$

2.5 Conclusion

In this chapter, the basic operation of the WPT system from a circuit point of view was studied. The basic model of a WPT system was presented. Then, the reflected impedance from the receiver side to the transmitter side of the system was calculated. It was indicated that with the application of the resonant capacitors it is possible to maximize the power transmission and efficiency especially at low coupling coefficients and high distances. Several resonant capacitor topologies were compared and their merits and weak points were presented. Due to simple structure and having great performance in dynamic conditions, series-series compensation topology was discussed and the effect of varying the frequency, load and coupling on the output power was studied. Finally, the complete electric circuit of the WPT system with the transmitter and receiver converters were presented and the relation between the complete model and simplified model was provided.

Chapter 3

Design and control

In this chapter, the design procedure and control of the WPT system is presented. In a wireless system, the most important part is the coil structure which is composed of the transmitter and receiver coils. In the first part of the chapter, the information about the coil structure is presented. Furthermore, the effect of the air-gap and lateral misalignment on the coupling coefficient between the two coils is analyzed. The rest of this chapter is dedicated to the control of the WPT system. Several control techniques are studied in this chapter. Then, two new control strategies for the regulation of the output power at the presence of the mutual inductance variations are proposed. At the end of this chapter, two methods for the identification of the vehicle in dynamic charging are presented.

3.1 Resonant circuit

In the transmitter and receiver side of the WPT system, the self-inductance of the coil resonates with the resonant capacitors in order to transfer the maximum power with high efficiency. In this section, the design procedure of these elements is described.

3.1.1 Structure of the coils

The most important part of a WPT system is the coil structure which is composed of the transmitter and receiver coil. The major characteristics that an efficient coil must have are high coupling coefficient k, high misalignment tolerance, and high-quality factor Q. Parameters of the coils including coil geometry, the distance between the transmitter and receiver coils, type of the ferrite used in the coils determine these factors. The coupling coefficient k has already been described in the text. The quality factor Q of the coils is obtained by the square root of the product of transmitter and receiver quality factors as

$$Q = \sqrt{Q_1 Q_2}\ , \qquad Q_1 = \frac{\omega L_1}{R_1}\ , \qquad Q_2 = \frac{\omega L_2}{R_2} \tag{3.1}$$

Where L_1 and L_2 are self-inductances of the coils and R_1 and R_2 are resistances of the coils. According to these equations, in order to have high coil quality factor Q, at the high operating frequency, the self-inductance of the coil must be high and the series resistance of the coil must be low. However, the operating frequency of the coil must be in the range of 85 kHz according to the SAE standard and cannot go beyond that. According to the self-inductance equation, the self-inductance of the coil is related to the square of the number of turns [98]. However, the series resistance of the coil is related to the number of turns. When the number of turns increases, the self-inductance of the coil increases more than the coil resistance and thus, the coil quality factor goes up.

In order to increase the quality factor, the resistance of the coil must be decreased. The resistance of the coil consists of DC resistance and AC resistance. When the DC current is passed through the coil, the current is distributed uniformly in the cross-section of the coil. Thus, the DC resistance of the coil can be decreased by increasing the cross-sectional area of the coil. By increase of the operating frequency, the efficiency and the maximum power of the wireless power transfer can be increased. However, the eddy losses increase as well which will cause the reduction of efficiency. The skin effect and proximity effect are the cause of the eddy losses and are created due to the inhomogeneous distribution of the current in the wire [99]. In higher frequencies, the current density is higher along the outer surface of the coil. These effects cause an increase in the AC resistance of the wire. The AC resistance of the coil increases with the increase of the frequency. In the construction of the WPT coils, lits wire are used as a solution for the reduction of these losses when the wire carrying AC current at high frequencies. The thin individually insulated strands are twisted together and bundles are created. Then, these bundles are woven again and the bundles in the next layers are formed. The result builds the litz wire. Different litz wires with different conductor materials, insulation layer thicknesses, number of strands, and strand diameters are available in the market.

For a wire carrying AC current, the skin depth is determined as the depth to which AC current penetrates. The skin depth decreases when the frequency goes up. Thus, in order to mitigate the skin effect and reduce the AC resistance of the coil, each thin conductor of the litz wire has to be less than skin-depth. The skin depth of each stand of the lits wire can be determined by [99]

$$\delta_i = \sqrt{\frac{\rho_i}{\pi f \mu_0 \mu_r}} \tag{3.2}$$

Where f is the operating frequency, μ_0 is the permeability of free space, and μ_r is the relative permeability. The permeability of the copper is almost equal to μ_0 and

thus, its relative permeability is 1. ρ_i is the resistivity of the strand and for the copper, this value is equal to 1.72×10^{-8} Ωm. According to (3.2), with the increase of the number of the strands and decrease the strand diameter, the losses reduce. However, fabrication of the thin strands is expensive which will limit the diameter of the strands.

One of the operational solutions for increasing the coupling coefficient is adding ferrite bars to the coil. The ferrite bars guide the flux and help to reduce the leakage flux. Therefore, the ferrite bars increase the self-inductance and mutual inductance between the two coils. However, the losses of the coil such as core losses and copper losses increase if the ferrite bars are used. Choosing of the ferrite cores depends on many factors such as frequency, permeability, shape, and cost. In conclusion, for having an efficient coil, the size, diameter, number of turns of the coil and the application of ferrite bars must be designed optimally.

As previously described in chapter 1, generally two main coil topologies namely long track topology and segmented track topology exist in wireless charging of EV. There are many drawbacks of long track topology such as low coupling coefficient, high stray magnetic field, low power transfer efficiency, high VA rating of H-bridge converter and low operating frequency. For the transmitter coil, the segmented track topology is chosen in order to avoid these problems.

The operating frequency of the system is chosen 85 kHz according to the SAE J2945 standard and due to the interoperability between the static and dynamic chargers. The nominal power of the wireless charger is 20 kW. Furthermore, the supply DC voltage is 630 V and the battery voltage is 300 V. The main parameter in the design of the wireless power transfer system is the design of the mutual inductance since it links transmitter and receiver sides and influences the power transfer. In the condition of maximum voltage at the H-bridge output and for a given battery voltage, there is only one value of mutual inductance that allows the transfer of a certain power. If losses are neglected, the equation of the power at the receiver side can be determined by

$$P_2 = V_2.i_2 = \left(\frac{2\sqrt{2}}{\pi}V_{bat}\right)\frac{\left(\frac{2\sqrt{2}}{\pi}V_{in}\right)}{\omega M} = \frac{8V_{in}V_{bat}}{\pi^2\omega M} \tag{3.3}$$

By choosing the input DC voltage 630 V, the battery DC voltage 300 V, and the receiver power equal to 20 kW, mutual inductance can be derived from (3.3) as

$$M = \frac{8\times630\times300}{\pi^2\times2\times\pi\times85000\times20000} = 14.3\ \mu H \tag{3.4}$$

After the calculation of the mutual inductance, the next step is the design of the transmitter and receiver coil with this mutual inductance at rated air-gap of 25 cm. Different types of coils were investigated in chapter 1. The circular coil has better coupling that square or rectangular shape coils. The circular coil is not enough

tolerant to lateral misalignment. The lateral misalignment of the circular coil can be increased by choosing a larger diameter for the coil but it is not practical due to size limitations. Furthermore, the circular shape coil has limited air-gap length. On the other hand, the rectangular coil has a simpler structure and a lighter weight. Furthermore, the design and construction are easier than the other types of the coils and it shows better misalignment tolerance in comparison to the circular shape coil which is very crucial is dynamic charging applications [98]. Due to these reasons, the rectangular shape coil is chosen for both transmitter and receiver coils. The full estimation of the mutual inductance for the rectangular shape coil can be found in [98]. However, this equation is an approximation of the mutual inductance. A more precise method is the application of the finite element programs.

According to the review of WPT systems in chapter 1, in most of the wireless charging systems such as ORLN, Auckland University, KAIST systems, ferrite cores are used for the development of the coils. However, here for the construction of the transmitter coil, the application of the ferrite core is neglected for some reasons. First of all, the operating frequency of the system is 85 kHz and with a coreless transmitter coil, the losses on the coil can significantly reduce. Furthermore, the ferrite core price remarkably contributes to the overall cost of the charging lane and the application of coreless transmitter coil can significantly reduce the overall cost. Moreover, the ferrite cores are fragile and the installation of them into the ground requires great effort. Furthermore, they are exposed to too much pressure and because of that, it is necessary to protect them against these pressures which result in increasing the construction cost considerably. Also, the transmitter coil without the ferrite cores is more tolerant to lateral misalignment compared to the transmitter with the ferrite core. The size of the transmitter coil is chosen 150 cm × 50 cm in order to be smaller than the size of the vehicle [100]. The transmitter coil is energized when EV is exactly on the top of that. The system is supposed to operate with the lateral misalignment of 30 cm. Thus, the reason for choosing the width of the transmitter 50 cm is that the transmitter coil becomes completely covered by the vehicle even in case of maximum misalignment. In the case of misalignment, the magnetic field is shielded by the vehicle and problems related to the magnetic field and safety are recovered. Furthermore, the power can be transferred at higher coupling and higher efficiency.

By defining the operating frequency equal to 85 kHz, the skin depth limit of the litz stands with the copper material for the mitigation of the skin effect losses can be obtained 0.22 mm from (3.2). Since the operating frequency of the transmitter and receiver is the same, the strand diameter of 0.1 mm is chosen for them which thinner than the skin depth at this frequency. In litz wire, each strand must be insulated otherwise all strands in a bundle could become short together. In this case, it behaves like a normal single wire and the skin effect problem remains. If the thickness of the insulation increases, the distance between the strands changes which will affect the internal magnetic field and thus, the proximity effect losses decrease however the size and weight of the litz wire increases.

The next step is the calculation of the coil section. The current densities in the coils must be below their maximum values. The maximum value for different wire sections and at different operating frequencies can be found in [101]. The wire section for transmitter and receiver coils can be determined by knowing the currents flow through them. A strict current density value recommended in the design manuals is 3 A/mm^2 however in other references [102], the current density value of 6 A/mm^2 is proposed. The value of mutual inductance, operating frequency, input DC voltage and the battery voltage are known and according to (2.46), the transmitter and receiver currents are approximately equal to 35 A and 74 A, respectively. By selecting the section of both coils equal to 16 mm^2, the current density of the transmitter and receiver coils are calculated 2.18 A/mm^2 and 4.6 A/mm^2. The current density of the transmitter coil is selected lower than the receiver current density because unlike the receiver coil, the transmitter coil is buried in the ground and the heat exchange rate is different.

By designing the mutual inductance between the two coils, the size of the transmitter and the cross-section of the coil, the next step is the design of the transmitter and receiver coils. The required mutual inductance of 14.3 μH can be obtained with an infinite number of combinations for the transmitter and receiver turns and with different shapes and dimensions for the receiver coil. However, the optimal design for the transmitter and receiver coils must be considered prior to fabrication. The dimension of the receiver is optimized using finite element analysis (FEA) software. The design procedure is presented in [100].

Table 3.1: Specifications and parameters of the transmitter and receiver coils.

Parameter	**Value**	**Unit**
Transmitter self-inductance, L_1	279.5	μH
Transmitter inner coil length	150	cm
Transmitter inner coil width	50	cm
Transmitter outer coil length	160	cm
Transmitter outer coil width	60	cm
Transmitter coil number of turns	10	-
Receiver self-inductance, L_2	120.8	μH
Receiver inner coil length	30	cm
Receiver inner coil width	52.5	cm
Receiver outer coil length	40	cm
Receiver outer coil width	62.5	cm
Receiver coil number of turns	10	-
Mutual inductance, M	14.3	μH
Wire diameter	5	mm
Wire section	16	mm^2
Operating frequency	85	kHz

For the design of the receiver coil, ferrite cores are employed. The ferrite cores guide the flux and reduce the leakage flux. With the ferrite cores, the self-inductance, the mutual inductance between the two coils and the coupling coefficient increase. Thus, the efficiency of the power transmission increases. The parameters of the transmitter and receiver coils after completing the optimization process are presented in Table 3.1 [100].

The 3D model of the coils at the air-gap of 25 cm and without any aluminum shield is shown in Fig. 3.1. The magnetic Flux lines in the transmitter and receiver coils when both coils are supplied with an equal current of 35 A are illustrated in Fig. 3.2.

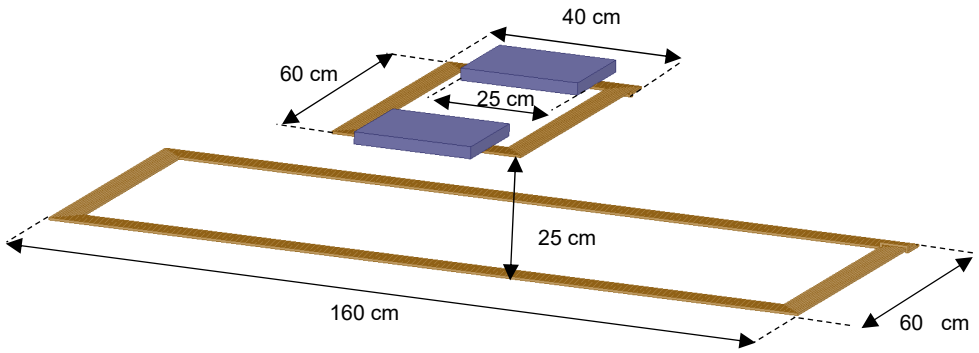

Fig. 3.1: Size and shape of the transmitter and receiver coils.

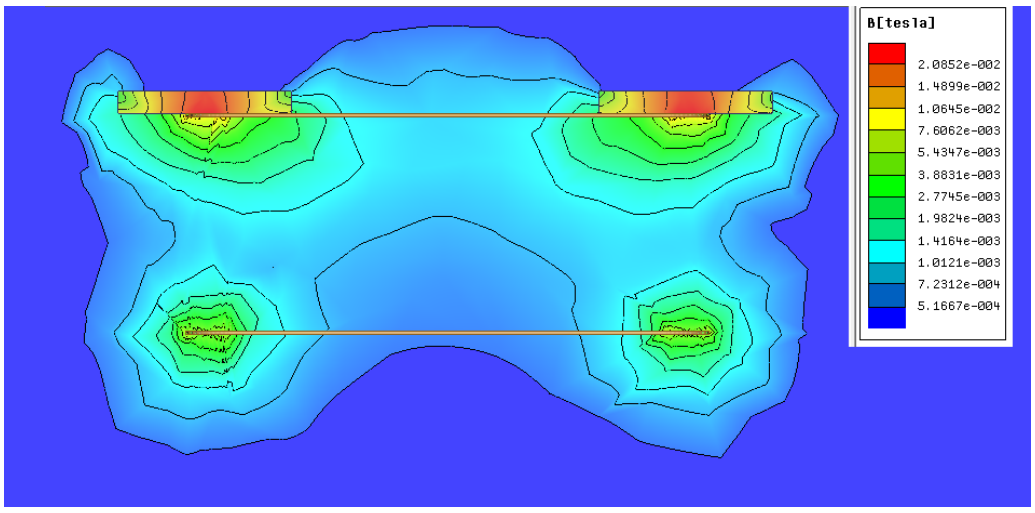

Fig. 3.2: Flux lines in the transmitter and receiver coil.

During the charging of EV, the distance between the transmitter and receiver coils remains constant. However, in dynamic condition, it is difficult to maintain the transmitter and receiver coil perfectly aligned when the vehicle is passing and the misalignment is unavoidable. During the misalignment, the air-gap is constant but the coils are not concentric. Fig. 3.3 and Fig. 3.4 show the coupling coefficient versus x-direction and y-axis misalignments, respectively. The x-direction

misalignment is defined for door-to-door direction and y-direction misalignment is defined for front-to-rear direction. The length of the transmitter coil is bigger than the receiver one and because of that, the coil is tolerant to the y-direction misalignment. As shown in Fig. 3.4, when the y-direction misalignment increases, at first the coupling coefficient changes a little. If y-direction misalignment increases in a big range, the coupling coefficient drops rapidly. The coil is more sensitive to x-direction misalignment. When x-direction misalignment increases, the coupling coefficient drops fast. When x-direction misalignment increases more, the coupling coefficient becomes negative. The negative mutual inductance is due to the magnetic flux cancellation when the coils are far from each other.

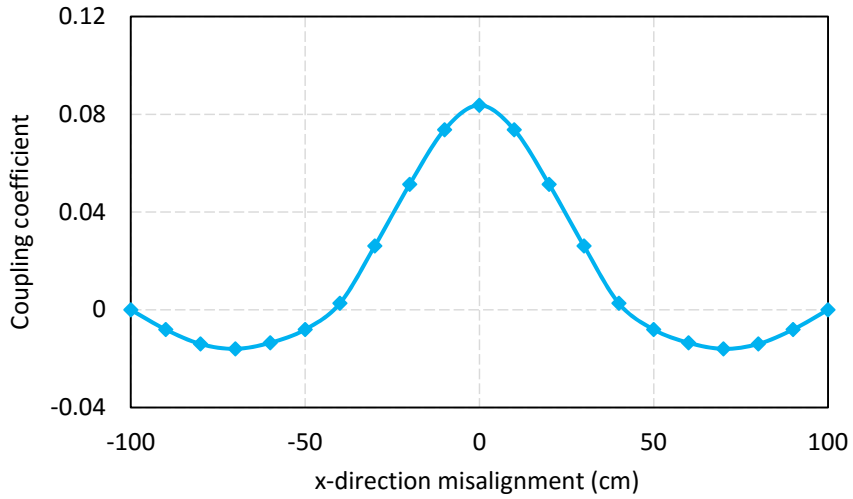

Fig. 3.3: Coupling coefficient versus x-direction misalignment.

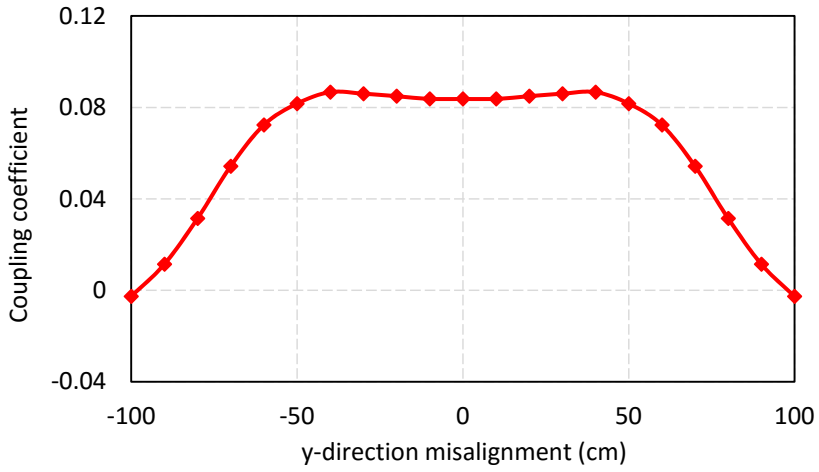

Fig. 3.4: Coupling coefficient versus y-direction misalignment.

The mutual inductance variations with x-direction and y-direction displacements are presented in Fig. 3.5. It can be seen that the mutual inductance value is high when the transmitter and the receiver are concentric. The self-inductances of the coils versus the variations of the misalignment are presented in Fig.3.6 and Fig. 3.7. As shown in these figures, self-inductances of the coils are not

considerably affected by the misalignment between the transmitter and receiver. The variations are less than 2%. The absence of the ferrite cores in the transmitter coil helps to keep the self-inductance constant. It is necessary to have a system with minimum variations of the self-inductance since it is one of the resonant elements. If the self-inductances of the transmitter and receiver changes, the power transfer capability reduces due to the variations of the resonant frequency.

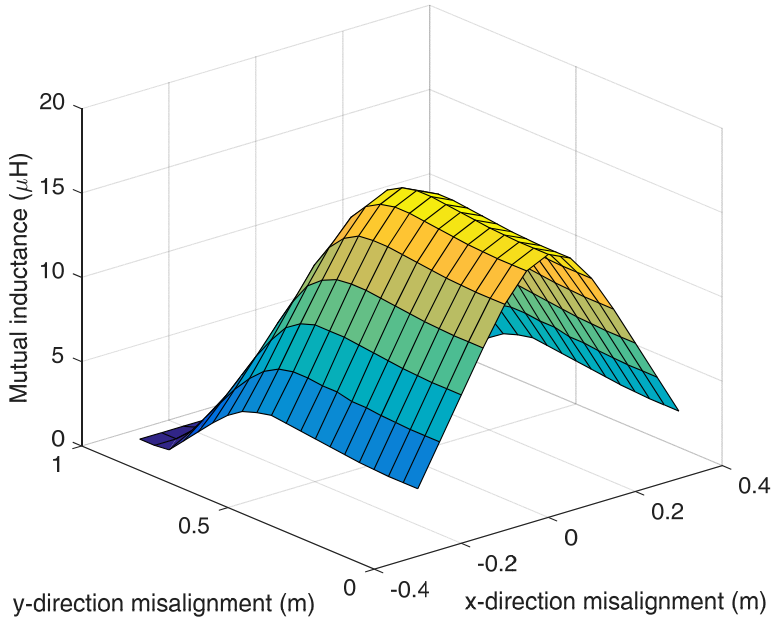

Fig. 3.5: Mutual inductance variations with x-direction and y-direction displacements.

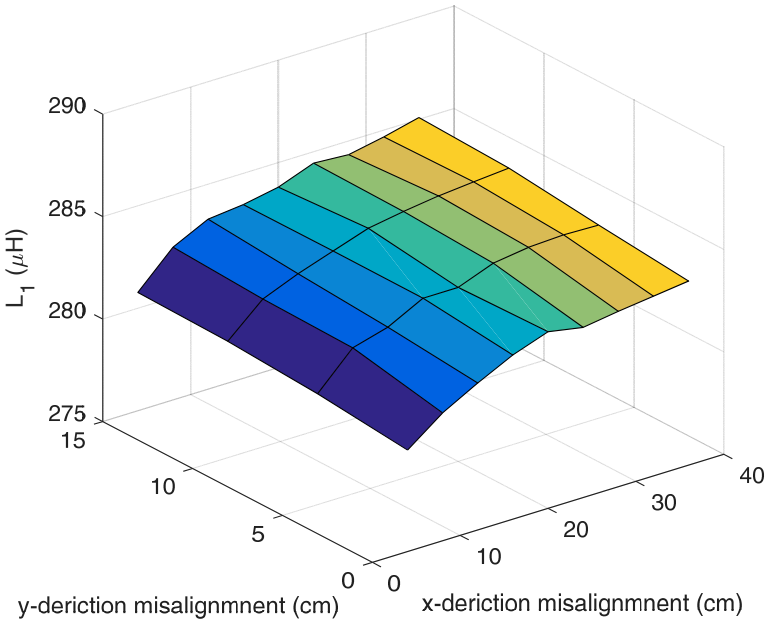

Fig. 3.6: Transmitter self-inductance under variations of x-direction and y-direction misalignments.

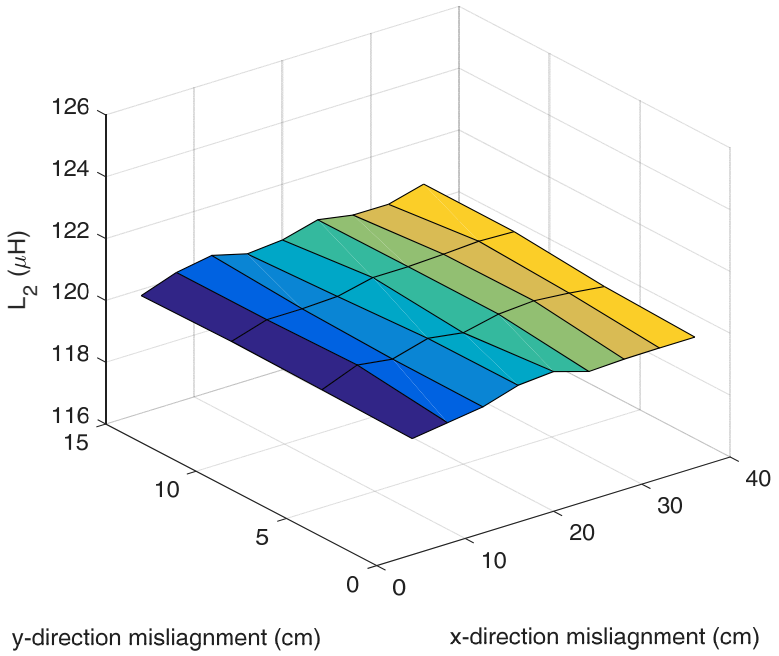

Fig. 3.7: Receiver self-inductance under variations of x-direction and y-direction misalignments.

The behavior of the mutual inductance when the receiver coil is passing over two transmitter coils is illustrated in Fig. 3.8. In the real system, the charging line is composed of several transmitter coils. The distance between two nearby coils is 50 cm. Due to this distance, the mutual inductance between two nearby transmitters is almost zero. When the receiver coil leaves the first transmitter coil, the mutual inductance drops to zero and then by approaching the next transmitter coil, it goes up again. The variations of the mutual inductance when the air-gap varies are presented in Fig. 3.9. According to this figure, the variation is approximately linear. It is clear that when air-gap increases the mutual inductance reduces.

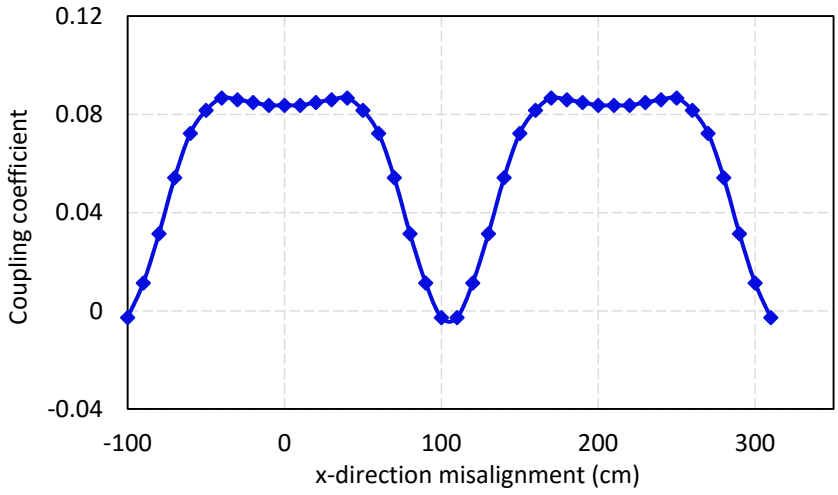

Fig. 3.8: Coupling coefficient versus y-direction misalignment with two transmitter coils.

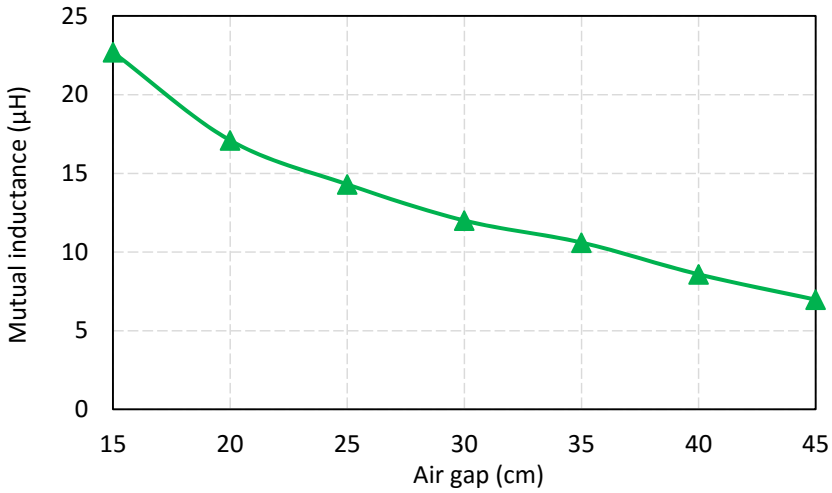

Fig. 3.9: Mutual inductance against the air-gap variations.

3.1.2 Selection of the resonant capacitor topology

According to the analysis in chapter 2, four elementary compensation topologies, SS, SP, PS, and PP, are mostly used for different applications. Besides these topologies, several new topologies such as LCL and LCC are proposed. From the above topologies, SS, LCL and LCC compensation topologies can be used in dynamics charging of the electric vehicle since the resonant frequency is irrelevant with the coupling coefficient and the load variations. Additionally, the system output current is constant independent of the load variations. The design of the LCL circuit usually requires the same value for the two inductors which increases the size and cost of the system. The LCC compensation has a lot of desirable advantages and ZPA and ZVS can be easily achieved at constant switching frequency but the only drawback is that the compensation network is composed of two inductors and four capacitors which increase the construction cost, maintenance cost, size, and losses of the system. It is worth noting that the final charging lane is composed of several transmitter coils. In contrast to SS, in a charging lane with the LCC compensation network, too many extra reactive components are required. So, in order to reduce the total construction cost, SS topology is chosen.

3.2 Control techniques for WPT systems

According to the (2.49), the output power of a WPT system depends on the coupling coefficient and the load resistance. During the charging, the equivalent resistance of the battery changes greatly. In addition, the coupling coefficient depends on the position of the coils and it is not constant. If the mutual inductance changes, the transmitter current would change which effects on the output power significantly. In series-series compensated WPT system, if the coupling coefficient

reduces, the transmitter current increases dramatically causing the increase of the losses on the transmitter side. Therefore, a closed-loop control system for the system is necessary to regulate the output power at varying coupling coefficient and battery resistance.

Extensive research works have been done on the control of WPT systems and several control techniques have been proposed [96], [103]–[120]. The control techniques in WPT systems can be classified into two main groups; transmitter or primary side control techniques and dual-side control techniques [114]. The output power can be controlled by the transmitter control and using a transmitter DC-AC converter or a DC-DC converter. In [115], the output power is controlled with control of the operating frequency of the transmitter converter. However, the maximum efficacy occurs only at the resonant frequency. The efficiency drops down when the system operates at other frequencies. A transmitter side variable frequency control is proposed in [96]. The zero phase angle operation is calculated according to the measurement of the transmitter voltage and receiver current. This control scheme offers a single ZPA. This ZPA is not affected by bifurcation and thus this method can be used in the WPT system in coupling variation conditions. Also, the amount of the output power can be managed by phase shift modulation control [121]. In this control, the H-bridge output voltage is controlled by changing the phase shift angle between the first leg and the second leg of the converter. In this way, the output power can be regulated without changing the operating frequency. The advantage of regulating the output power with the DC-AC converter in the transmitter side control is that electric vehicle has lower power electronics which reduces the size and weight of the EV and has cost-effective benefit. The power circuit structure of transmitter side control with the H-bridge converter is illustrated in Fig. 3.10.

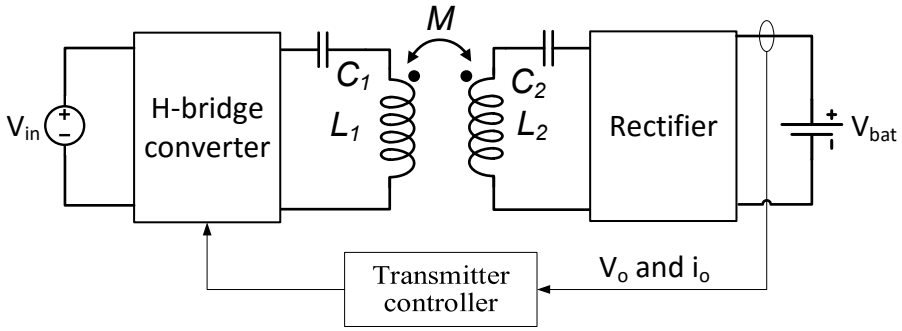

Fig. 3.10: Configuration of the transmitter side control with H-bridge converter.

One way to control the output power from the transmitter side is the application of a DC-DC converter which is placed between the DC source and the H-bridge converter. This DC-DC converter is used for regulating the DC link voltage of the DC-AC converter [116]. In this method, the DC-AC converter switches work in soft switching conditions at various output powers. The structure of the transmitter side control with a DC-DC converter is presented in Fig. 3.11.

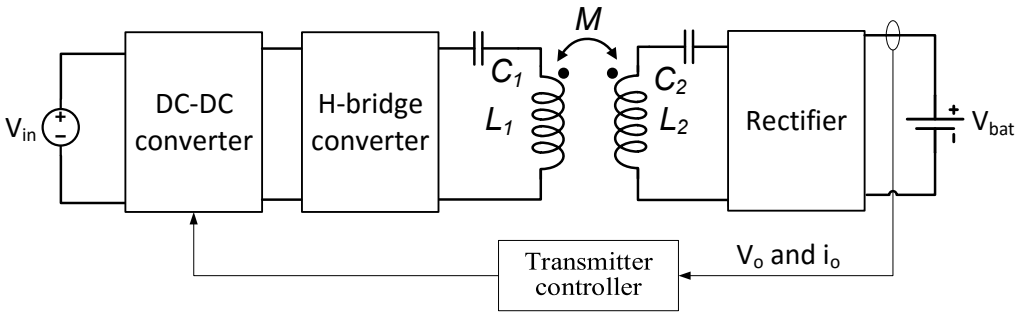

Fig. 3.11: Configuration of the transmitter side control with a DC-DC converter.

The important issue that must be considered in the design of the WPT system with transmitter side control strategies is that in all of the methods, the feedbacks of the receiver variables such as battery current and voltage are necessary to control the entire system. In [117], by estimating the mutual inductance by the control circuit, the output power is controlled from the transmitter and without the information of the output current and voltage. Nevertheless, complex computations are required in order to estimate the value of the mutual inductance. The receiver side control method is used in the applications where multiple receivers are connected. In dual side control, in addition to the transmitter converter, a power electronics converter is used in the receiver. The power electronic converters in the transmitter and receiver sides are controlled simultaneously in order to control the WPT system. The receiver converter can be a DC-DC converter [118], a semi-active rectifier [119], or a full active rectifier [122]. In dual side control with the receiver side DC-DC converter, the output power is regulated by controlling the duty cycle of the DC-DC converter. The power circuit configuration of this control method is shown in Fig. 3.12.

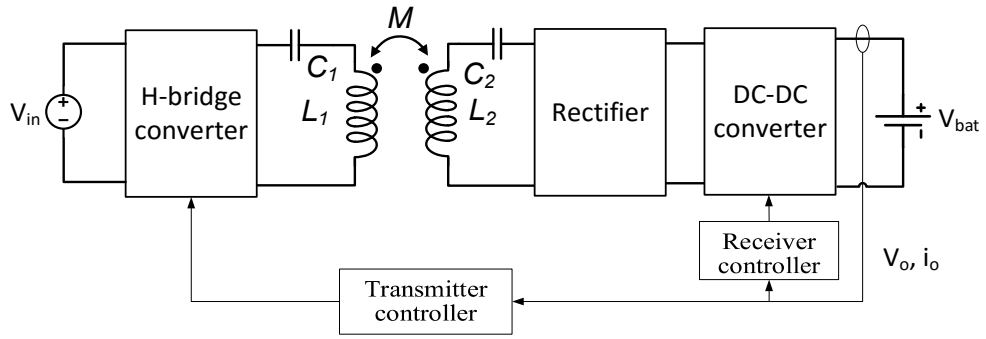

Fig. 3.12: Configuration of the dual side control with DC-DC converter at the receiver side and H-bridge converter at the transmitter side.

By replacing two bottom diodes of the receiver rectifier with two switches, semi-active rectifier topology can be built. This topology can simplify the receiver structure and the output power can be regulated by these switches without the need for the DC-DC converter. In [122], by implementing a bidirectional power transfer with an active rectifier, the receiver DC-DC converter and diode bridge are omitted.

Bidirectional power transfer is employed where the transmission of the power at both sides is necessary such as vehicle-to-grid (V2G) systems and regenerative energy recovery systems. In this control structure, the direction and amount of the power are controlled with an active rectifier. By controlling the phase between the voltage and current at the input of the active rectifier, the direction of the power flow can be controlled. In the bidirectional WPT system reported in [123], a power-frequency control strategy is proposed to regulate the power flow. The configuration of a bidirectional wireless system with a dual side control technique is presented in Fig. 3.13.

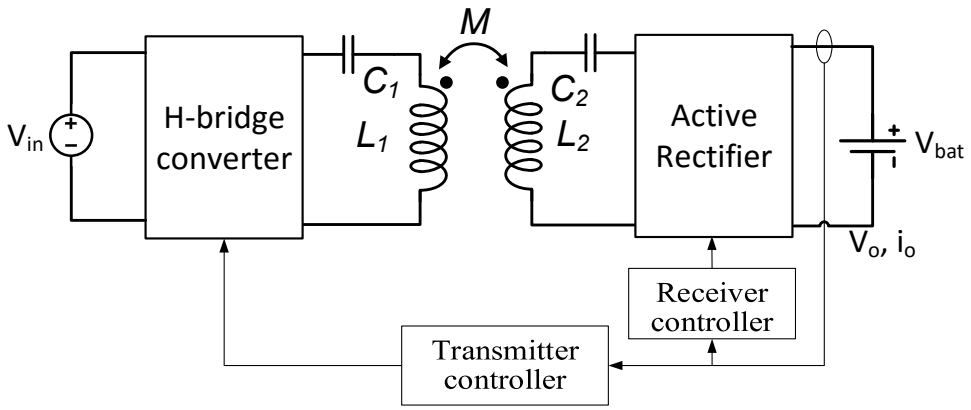

Fig. 3.13: Configuration of the bidirectional wireless system with the control at both sides.

Another advantage of dual side control is that, since two power electronic converters are used, the transmitter converter regulates the output power by receiving the information of the battery and the receiver side converter tracks the maximum efficiency of the system. The Maximum efficiency point tracking strategy is achieved using a converter at the receiver [120]. For the operation of the control system in most of these techniques, the information of the output voltage and output current is necessary to be sent to the transmitter control. However, the establishment of the communication link and transmission of the data will increase the total cost and size of the system and make the construction complicated. The application of dual-side control with the communication link is the most popular control method in static WPT systems however this method cannot be used in the WPT system for charging the EVs moving with fast speed in the highways since the communication like may cause delay and reduce the charging time of the vehicle. Hence, independent controls of the transmitter and receiver and without data transmission are desirable in dynamic WPT systems. The drawback of this method is that conflict between control systems in two sides can cause instability.

3.3 Dual side control with DC-DC converter at the receiver

The idea of the control is to regulate the output power from the receiver and without the need to transmit data between two sides. Fig 3.14 shows the configuration of the wireless charging system composed of transmitter side control and receiver side control. The transmitter control and the receiver control operate jointly and regulate the battery power during the EV movement and even in a possible presence of lateral misalignment but without the need to transmit to each other any data.

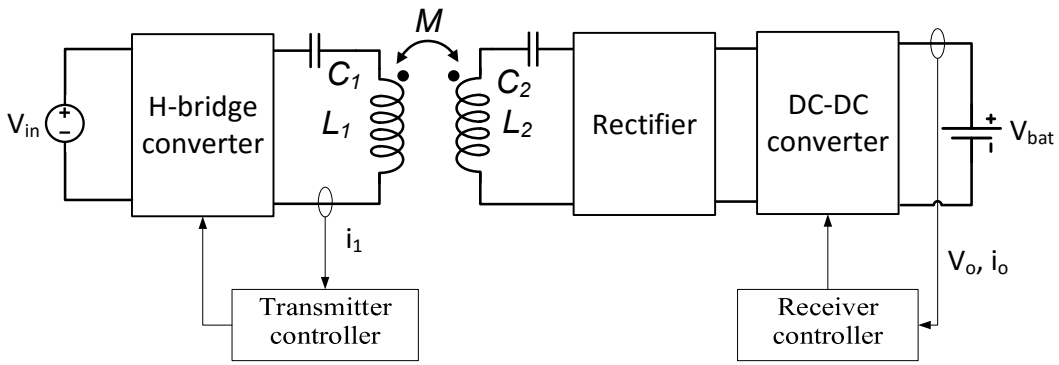

Fig. 3.14: The idea of the dual side control strategy without communication.

The control scheme is divided into two parts. In the transmitter, a current control is developed. This current control is used in order to maintain the current of the transmitter DC-AC converter at peak current capability during the misalignment condition. This is due to the fact that in SS topology, the current of the transmitter goes up when the lateral misalignment increases. In the receiver of the WPT system, a resistance control is implemented. The resistance control is used in order to regulate the battery power using a DC-DC converter at the receiver. The power control is achieved by regulating the equivalent resistance at the input of the DC-DC converter with the variations of the duty cycle of the converter. In this control strategy, the transmitter converter operates at a definite power level and the receiver can regulate the battery power from zero power to the peak power according to the demand without communicating with the transmitter converter. When the battery of the vehicle is nearly full, the receiver control could choose to receive only the power which is necessary for the movement. On the other hand, when the battery of the vehicle is not fully charged, the receiver control modifies the equivalent resistance value for receiving the maximum power.

3.3.1 Transmitter side control

The complete circuit of the system is presented in Fig. 3.15 which is composed of DC-AC converter, coils, rectifier, DC-DC boost converter, output filter, and the battery.

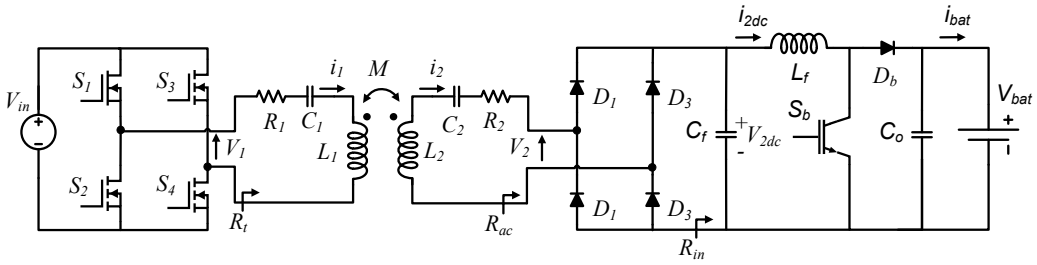

Fig. 3.15: Power circuit configuration of the WPT system.

As shown in this figure, for the compensation of the inductances, series-series topology is chosen. As completely described in chapter two, this topology is simple and the resonant frequency is independent of the load and the mutual inductance variations. In SS compensation topology, when the value of the mutual inductance drops down due to the misalignment or the increase of the air-gap, the transmitter current goes up. Also, when the load resistance increases, the transmitter current increases too. Therefore, it is necessary to protect the transmitter DC-AC converter against overcurrent conditions. Hence, a current control circuit is implemented for the transmitter DC-AC converter. In the dynamic condition when the misalignment occurs, the transmitter control limits the transmitter current at the peak value by controlling the voltage at the output of the DC-AC converter using phase shift control [124], [125]. The switching waveform of the converter with phase shift modulation is illustrated in Fig. 3.16.

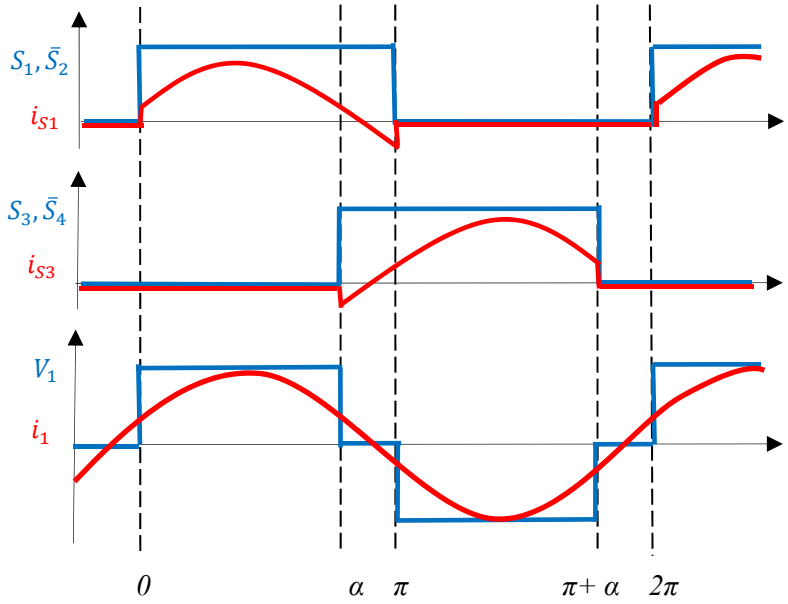

Fig. 3.16: Gating signals of the DC-AC converter controlled with phase shift control scheme and the related output voltage and current.

According to this figure, by changing the phase shift angle α between the two legs of the converter, the shape of the H-bridge output voltage changes. In this control strategy, switches of the first leg (S_1 and S_2) turn off at ZCS conditions but

they turn on at hard switching conditions. On the other hand, switches of the second leg (S_3 and S_4) turn on at ZVS conditions and have only turn-off switching losses.

The modeling of H-bridge output voltage is according to the First Harmonic Approximation (FOA) analysis. This approximation was introduced in chapter 2. The equation of the fundamental harmonic of the DC-AC converter output voltage can be determined by

$$V_1 = \frac{2\sqrt{2}}{\pi} V_{in} \sin\left(\frac{\alpha}{2}\right) \tag{3.5}$$

When the phase shift angle is 180 degrees, the H-bridge output voltage is at its maximum value. By reducing α, the H-bridge output voltage goes down. The schematic of the control circuit in the transmitter side is illustrated in Fig. 3.17.

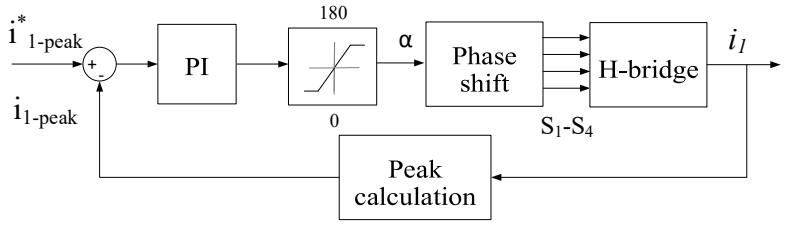

Fig. 3.17: Transmitter current control scheme.

The reference current in Fig. 3.17 is defined as the maximum current capability of the DC-AC converter. In the control, the current of the transmitter is required. This current is measured using a high-frequency current transformer. After the measurement of the transmitter current, the peak current is calculated. The reference current is compared with the current of the transmitter and the difference value is applied to a PI controller which calculates the phase shift angle. PI controller is saturated between 0 and 180°. Finally, according to the phase shift angle, the DC-AC converter is switched. In the nominal mutual inductance, phase shift angle is 180 degrees. When mutual inductance reduces, the transmitter current starts increasing. The PI controller decreases α and the pulse width of the transmitter voltage reduces. In this case, the transmitter current remains at the peak level. In contrast, if the mutual inductance increases, the transmitter current reduces. In this situation, the controller increases the phase shift angle to its maximum value and the DC-AC output voltage becomes a pure square wave similar to rated mutual inductance operating condition.

The transmitter converter works at constant angular frequency ω_0 that is the resonant frequency of the coils as

$$\omega_0 = \frac{1}{\sqrt{L_1 C_1}} = \frac{1}{\sqrt{L_2 C_2}} \tag{3.6}$$

By considering that the system operates at the resonant frequency and using phase shift modulation equation for calculation of the transmitter output voltage, the transmitter and receiver currents equations can be rewritten as

$$i_1 = \frac{(R_2 + R_{ac})}{R_1(R_2 + R_{ac}) + \omega_0^2 M^2} \frac{2\sqrt{2}}{\pi} V_{in} \sin(\frac{\alpha}{2}) \tag{3.7}$$

$$i_2 = \frac{j\omega_0 M}{R_1(R_2 + R_{ac}) + \omega_0^2 M^2} \frac{2\sqrt{2}}{\pi} V_{in} \sin(\frac{\alpha}{2}) \tag{3.8}$$

The output power equation can be obtained as

$$P_o = \frac{(\omega M)^2 R_{ac}}{[R_1(R_2 + R_{ac}) + (\omega M)^2]^2} {V_{in}}^2 \frac{8}{\pi^2} \sin^2(\frac{\alpha}{2}) \tag{3.9}$$

According to (3.9), the output power can be regulated by applying the phase shift modulation technique to the transmitter converter but in this control method, the information of the output voltage and current is required. Thus, it is desired to regulate the battery power without any communication between two sides.

3.3.2 Receiver side control

The idea for the control is that the transmitter DC-AC converter operates at its maximum current specification and any needed power adjustment is carried out using the receiver side converter. According to (2.49), the output power depends on the equivalent AC resistance R_{ac}. Since the values of the coils resistances are much smaller than R_{ac}, by neglecting them it can be concluded that If R_{ac} increases, the output power goes up. According to the first harmonics approximation, the value of R_{ac} depends on the value of the resistance at the input of the DC-DC converter R_{in}. Furthermore, this resistance deepens on equivalent load resistance R_L. Thus, the reflected impedance to the AC side is a function of the duty cycle of the DC-DC converter and load resistance. Therefore, the DC-DC converter behavior is like an impedance matching circuit [126]. As a result, it is possible to regulate output power by control of the DC-DC converter. Different types of DC-DC converters are proposed in the literature to practically control the power such as buck [97], [127], boost [128], and buck-boost [129]. The relations between the load resistance and resistance seen from the input side of the DC-DC converter for these converters are analyzed in the following section.

3.3.2.1 Impendence matching in DC-DC converters

The circuit configuration of three regular DC-DC converters is shown in Fig. 3.18. By neglecting the losses of the DC-DC converters and considering the input and output powers to be equal, the equation for the input impedance of the DC-DC converter can be written as follows:

$$R_{in} = \frac{P_{in}}{{I_{in}}^2} = \frac{P_o}{{I_{in}}^2} = \frac{R_L {I_o}^2}{{I_{in}}^2} \tag{3.10}$$

Where I_{in} is the input current and I_o is the load current. Now, the input resistance can be calculated from the relation between input and output currents.

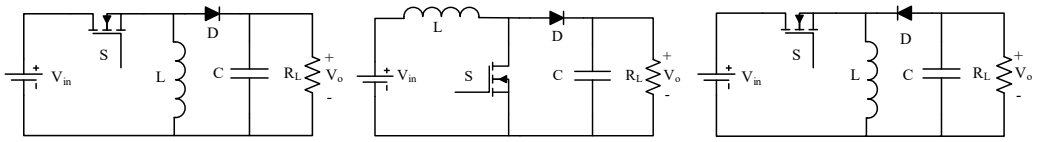

(a) (b) (c)

Fig. 3.18: Circuit configuration of basic DC-DC converters; (a) buck converter, (b) boost converter, and (c) buck-boost converter.

In the buck converter, the relation between the source and the load currents, the relation between input and output voltage and the input resistance in terms of duty cycle D can be written as follows:

$$V_o = DV_{in} \ , \ I_o = \frac{I_{in}}{D} \ , \ R_{in} = \frac{R_L}{D^2} \tag{3.11}$$

The duty cycle D is between 0 and 1 and thus the range of input impedance for the buck converter is between R_L and $+\infty$. It can be seen that, the buck converter converters the load resistance to a resistance greater than the load resistance. The relation between the input and output current, the relation between the input and output voltage, and the input resistance in terms of duty cycle D for boost converter can be expressed as follows:

$$V_o = \frac{V_{in}}{(1-D)} \ , \ I_o = I_{in}(1-D) \ , \ R_{in} = R_L(1-D)^2 \tag{3.12}$$

The range of input impedance for the boost converter is between 0 and R_L and thus the boost converter converters the load resistance to a resistance smaller than the load resistance. For the buck-boost converter, the equations of the output voltage, output current, and the input resistance in term of the duty cycle D can be written as follows:

$$V_o = V_{in}\frac{D}{(1-D)}, \ I_o = I_{in}\frac{(1-D)}{D} \ , \ R_{in} = \frac{(1-D)^2}{D^2} \tag{3.13}$$

The range of input impedance for the Buck-boost converter is between 0 and $+\infty$ and the input impedance can be higher or lower than the load resistance. As seen, each converter has different behavior and generates different impedance range that can be used in different applications. In the proposed method for power control of the electric vehicle, the transmitter converter operates at maximum power level. According to (2.49) and by neglecting coil resistances, for the control of the output

power between zero and maximum power based on vehicle load demand, resistance at the input of the DC-DC converter must be kept at the range between zero and a resistance which is equivalent to the maximum power capability of the transmitter converter. According to the above equations, buck converter converts higher impedance than load resistance. Therefore, the buck converter is not suitable for this power control strategy. The buck-boost converter can provide the desired resistance range. However, the polarity between input and output voltages is the opposite. Furthermore, the power losses can increase especially in high power transmissions. The boost converter is a good candidate for this control scheme since equivalent load resistance can be controlled between zero and the resistance related to the maximum power.

3.3.2.2 Resistance control of the receiver with the boost converter

The block diagram of the control circuit with the resistance control is presented in Fig. 3.19.

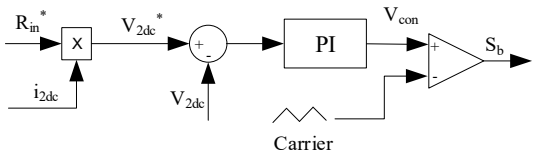

Fig. 3.19: resistance control of the receiver.

R_{in}^* is the reference resistance at the input of the DC-DC boost converter used in the receiver control circuit in order to regulate the received power by the battery. The value of $R_{in\text{-}Pmax}$ is the reference resistance in which the maximum power can be transferred to the battery at the rated coupling. This situation happens when the phase shift angle is maximum and its output voltage is a full square wave. Also, the current of the transmitter is at its maximum value. Thus, the resistance at the output of the transmitter converter R_t is calculated as

$$R_t = \frac{\left(\frac{2\sqrt{2}V_{in}}{\pi}\right)}{i_{1-max}} \tag{3.14}$$

Where $i_{1\text{-}max}$ is the maximum current of the transmitter. Now, the value $R_{in\text{-}Pmax}$ can be determined as

$$R_{in-Pmax} = \frac{\pi^2}{8}\left(\frac{\omega^2 M^2}{\frac{2\sqrt{2}V_{in}}{\pi i_{1-max}} - R_1} - R_2\right) \tag{3.15}$$

The reference input resistance R_{in}^* is multiplied by the measured current at the input of the DC-DC converter i_{2dc}. Now, the reference voltage V_{2dc}^* at the input of

the DC-DC converter is obtained. The duty cycle of the DC-DC converter is obtained by comparing the reference DC voltage V_{2dc}^* and measured voltage at the input of the DC-DC converter V_{2dc} and sending the result to a PI controller. The DC-DC converter by controlling the duty cycle can reach V_{2dc}^* and finally, the desired output power can be achieved. The variations of the different variables of the WPT system for various values of the reference resistance R_{in}^* in nominal mutual inductance are presented in Fig. 3.20. For ease of the description of the control circuit, the values of the transmitter and receiver resistances are neglected. V_1 is a full square wave in rated coupling. In SS topology, i_2 remains constant in load variations. The value of i_2 is depended on the mutual inductance, operating frequency, and the transmitter voltage. By keeping all of these parameters constant, i_2 remains constant in different powers.

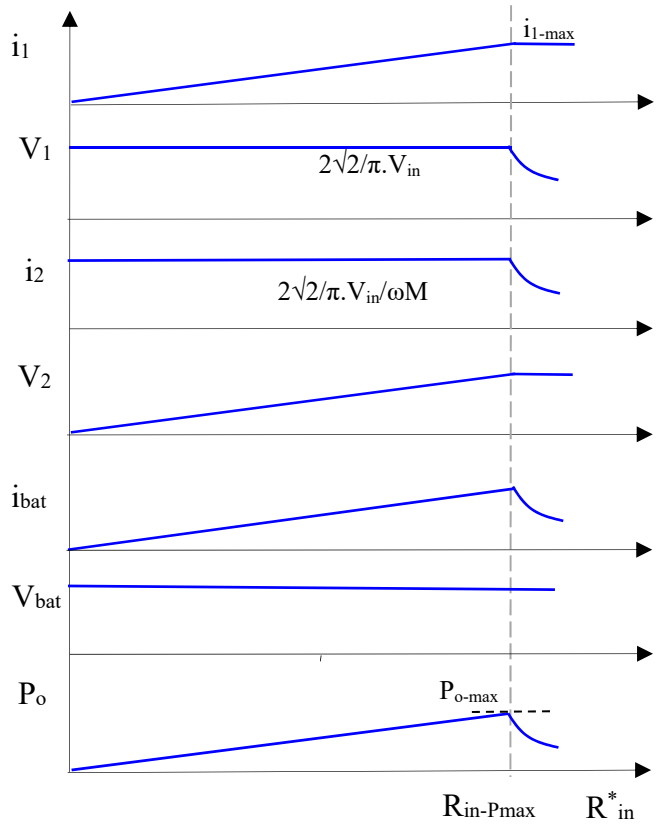

Fig. 3.20: Important variables of the system with the variation of the R^*_{in}.

When R_{in}^* is zero, V_{2dc}^* becomes zero and the control circuit makes the receiver voltage V_2 short-circuit by turning the switch of the boost converter on. In this condition, the amount of power that receives by the battery is zero. When R_{in}^* increases, V_2 increases by the control and output power level goes up. When R_{in}^* reaches $R_{in\text{-}Pmax}$, the battery receives the maximum power. At this point, the current and voltage of the transmitter are at their peak values. If R_{in}^* becomes more than $R_{in\text{-}Pmax}$, the transmitter current tends to increase. However, i_1 is at its peak level and cannot increase more. Thus, the V_1 is reduced in order to maintain the current of the transmitter at the peak value by the transmitter control. In this situation, input power

and consequently the output power decreases. If R_{in}^{*} increases more, the power at the output of the system drops more. In conclusion, by controlling the resistance at the input of the DC-DC converter from zero to $R_{in\text{-}Pmax}$, it is possible to regulate the output power from zero to maximum power just from the receiver.

3.3.2.3 Extension to the multi-phase boost converter

For wireless power transfer applications, the DC-DC converter should work at high efficiency and high power density and be capable of carrying high current. To provide these requirements, one solution is the interleaving of the DC-DC converter. The idea is parallel use of the switches, diodes, and inductors in a way in order to share the input current among the parallel converters or phases and reduce the current rating of each of them. There are many advantages with interleaving; the total efficiency of the system increases due to the reduction of the conduction losses in each switch, the dynamic response of the converter improves and it is possible to build a converter with low heat dissipation, high reliability, and high fault tolerant characteristic. One of the problems of the typical DC-DC converter is the voltage ripple at the output of the converter and at the input of the battery. The high voltage ripple at the input of the battery increases the losses which will lead to an increase in the battery temperature and reduce of the battery lifetime. In order to decrease the output voltage ripple of the DC-DC converter, one possible way is to choose a bigger filter capacitor. However, it will cause an increase in the total weight and size of the converter. The interleaving of the converter makes the output voltage ripple and the input current ripple of the converter lower [130]–[143]. Thus, the size of the input and output filters significantly reduces. Furthermore, the electrolytic capacitors can be replaced with film capacitors with lower series resistances. However, by increasing the number of the phase in the converter, the number of semiconductor devices and inductors increases which will increase the total cost, size and weight of the converter. Thus, proper selection of the number of the phase is essential.

The power circuit configuration of the receiver with the interleaved nine phase boost converter is shown in Fig. 3.21. The nine-phase interleaved converter is created by paralleling nine identical inverter legs in order to share the total current of the receiver coil. The inductors L_{f1}, L_{f2} till L_{f9} are inductors of each phase of the DC-DC converter. The converter structure is a bidirectional converter and can operate in both boost and buck mode. However, in this application, only the converter operates in boost mode and the energy is transferred from the receiver coil to the battery. In this case, the bottom switches of the inverter legs are used to control the boost converter and only body diodes of the upper switches of the inverter legs are utilized for power transmission.

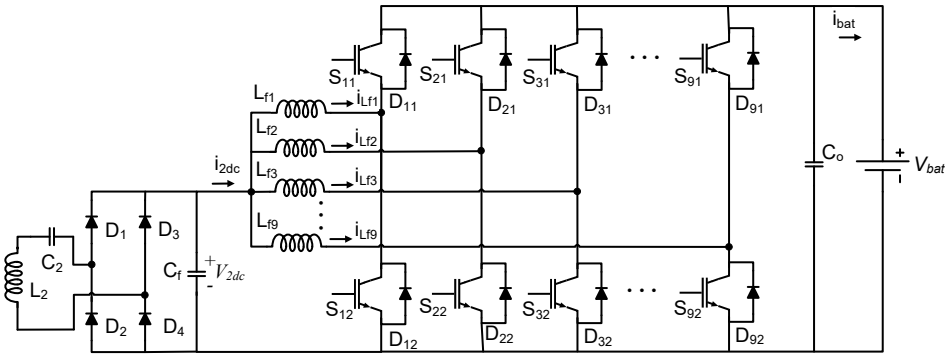

Fig. 3.21: Nine-phase bidirectional interleaved boost/buck converter.

The switches of the interleaved DC-DC converter are controlled with the same switching frequency and are equally shifted with a value of 1/f×N where *N* is the number of phases. The switches of each leg operate in complementary mode and when the lower switch is on, the upper switch is off. The input current, currents of the inductors and the output current waveforms of the nine-phase interleaved boost converter are shown in Fig. 3.22. The input current is the sum of all inductor currents. The currents of the inductors have similar waveforms with a phase shift. The output current is the sum of the currents of the phases whose switches are off. When the bottom switch of the inverter leg turns on for the time period of *DT*, the voltage across the respective inductor is equal to the DC-DC converter input voltage V_{2dc} and the current of the phase inductor increases from $iL_{f\text{-}min}$ to $iL_{f\text{-}max}$. When the switch turns off, the voltage across the inductor is equal to the voltage difference between the input and output of the DC-DC converter. Since the output voltage of the DC-DC converter is greater than the input voltage, the voltage of the inductor becomes negative and the current decreases. During this mode, the current flows through the body diode of the upper switch of the inverter leg.

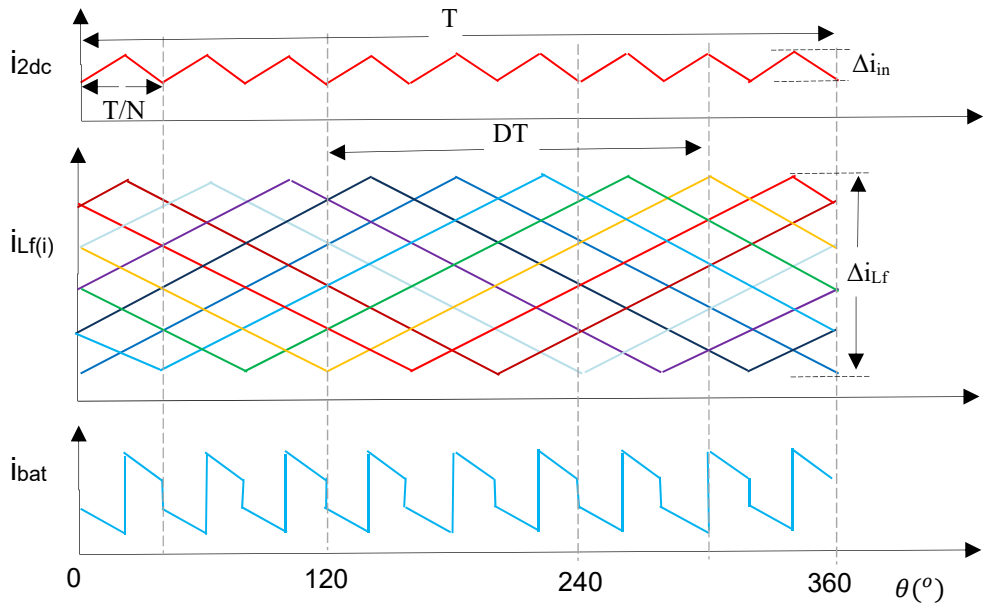

Fig. 3.22: Current waveforms of the interleaved boost converter. Top: input current ripple, middle: inductor currents, and bottom: output current ripple.

For simplifying the analysis, it is considered that the value of all inductors are equal to L_f and the switching frequency and duty cycle for all phases are the same. The peak to peak current ripple of each inductor can be expressed as

$$\Delta i_{Lf} = \frac{V_{2dc}.D}{f_{sw}.L_f} \tag{3.16}$$

Where f_{sw} is the switching frequency of the converter and D is the duty cycle. The ripple of each inductor is always maximum at the duty cycle of 50%. The equation of the current ripple for each inductor can be determined by

$$\Delta i_{Lf} = \frac{V_{2dc}.D}{f_{sw}.L_f} = \frac{V_{bat}.D(1-D)}{f_{sw}.L_f} \tag{3.17}$$

The ripple of each inductor is not depended on the number of the phases and it is only affected by the duty cycle of the switch. The average current of each inductor is given as

$$i_{Lf}(avg) = \frac{i_{bat}}{N} \tag{3.18}$$

If the converter works at CCM, the maximum current of the lower switch can be obtained according to the following equation as

$$i_S(max) = \frac{i_{Lf}(avg)}{N} + \frac{V_{2dc}.D}{2.f_{sw}.L_f} \tag{3.19}$$

3.3.2.3.1 Ripple calculation

The input and the output passive filter of the DC-DC converter play a key role in the total size and weight of it. One of the most major advantages of the interleaved DC-DC converter is the ability to cancel the input and output ripples. The interleaved DC-DC converter is composed of N commutation cells. These commutation cells work in parallel and the input and output currents of the converter operate in a frequency, N times the switching frequency of a single cell. Thus, the input current ripple and the output current ripple are significantly reduced. Furthermore, in some operating points, the variations of the phase currents are exactly opposite of each other and the current ripple is totally canceled. This ability results in a reduction of the filtering requirement for the DC-DC converter [135]–[138].

The input current is the sum of all inductor currents and depends on the duty cycle of the converter. The gating signals of the boost switches have the same duty cycle but are 360/N degrees shifted. The value of the input current ripple based on the duty cycle can be divided into N sub-period. According to the value of the duty cycle and sub-period, the number of ON switches that shares the input current is

different. During the first sub-period (0<D=<1/N), only one switch is ON at the same time. In the second sub-period (1/N<D=<2/N), two switches are ON and share the input current. For the next sub-periods, the number of ON switches that shares the input current changes respectively. The input ripple current equation of the boost converter with respect to the variation of the duty cycle *D* can be written as

$$\Delta i_{in} = \frac{V_{2dc}(N_{sub} - ND)(1 - N_{sub} + ND)}{f_{sw} L_f N (1 - D)} \tag{3.20}$$

Where N_{sub} is the sub-period number. Since the battery voltage is approximately constant, (3.20) can be rewritten according to the battery voltage as

$$\Delta i_{in} = \frac{V_{bat}(N_{sub} - ND)(1 - N_{sub} + ND)}{f_{sw} L_f N} \tag{3.21}$$

It can be concluded from the above equation that by increasing the switching frequency or the value of the inductance, a lower input current ripple can be achieved. However, these methods increase the total losses and decrease efficiency. Furthermore, by increasing the value of inductances, the size and weight of the converter increase. The normalized input current ripple according to the variation of the duty cycle of the converter for different numbers of the interleaved phases is calculated according to (3.21) and is shown in Fig. 3.23. It can be seen from this figure that by maintaining the phase inductors constant, if the number of phase increases, the input current ripple is significantly reduced. Furthermore, if the input current ripple remains constant, the value of the inductors can be selected 1/N compare to the single phase one.

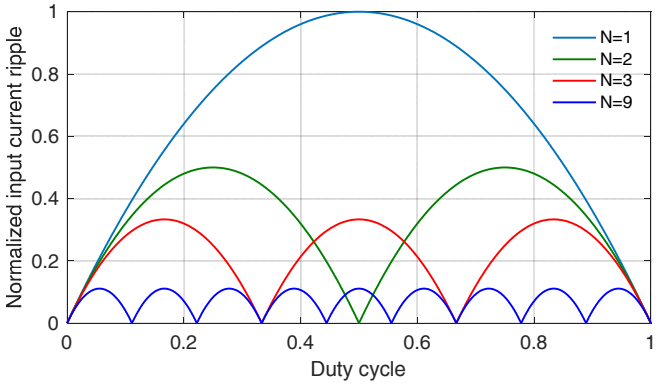

Fig. 3.23: Normalized input current ripple when V_{bat} is constant.

The input current ripple is zero when the duty cycle is *A*/*N* (*A* is an integer from 0 to *N*) and the input current is maximum when the duty cycle is *B*/*2N* (*B* is an odd integer from 1 to *2N*). The maximum input current ripple can be expressed as

$$\Delta i_{in}(max) = \frac{V_{2dc}}{2 f_{sw} L_f (2N - 1)} = \frac{V_{bat}}{4 f_{sw} L_f N} \tag{3.22}$$

In addition, the current ripple cancellation coefficient K is defined as the ratio between the input current ripple and current ripple of each inductor and the equation can be determined by

$$K = \frac{\Delta i_{in}}{\Delta i_{Lf}} = \frac{(N_{sub} - ND)(1 - N_{sub} + ND)}{ND(1 - D)} \tag{3.23}$$

The ripple cancelation coefficient is not depended on the input voltage or the output voltage. The normalized current ripple cancellation coefficient according to the variation of the duty cycle of the converter for different numbers of the interleaved phases is shown in Fig. 3.24.

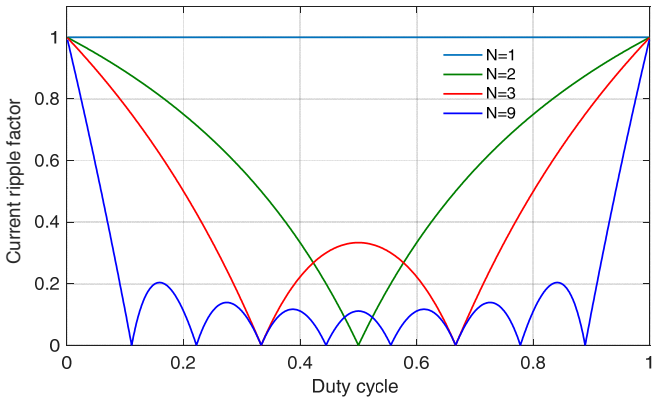

Fig. 3.24: Current ripple cancellation coefficient.

3.3.2.3.2 Difference techniques in control of interleaved converters

Many techniques have proposed for the control of the interleaved DC-DC converters. Most of these techniques have used current control for each phase of the converter in order to share the load current in each phase equally. The most important current control techniques for the interleaved DC-DC converters are hysteresis current control [139], [140], peak current control [141] and average current control [142], [143]. In hysteresis current control method, a lower current reference and a higher current reference are defined for the control of the inductor current. When the current of the inductor becomes less than the lower current reference, the switch turns on. Then, the current of the inductor rises and when it reaches the higher current reference, the switch turns off. The advantages of this control technique are that it has a fast response and the implementation is simple. With hysteresis control, the converter operates at the variable switching frequency. Another technique for the control of the interleaved converter is the peak current control. In this control, a peak reference current is defined for the control circuit. By turning on the switch, the current of the inductor linearly increases. At the moment the current of the inductor reaches the reference peak current, the switch of the converter turns off. Depending on the load condition, the peak current control may operate in DCM or CCM. The advantage of this converter is that it works at the constant switching frequency and due to the reference peak current, the switch

is protected against the overcurrent fault. However, this technique is unstable for duty cycles higher than 50%. In order for the converter to work in duty cycles over 50%, an extra compensator is required in the control loop. The average current control overcomes the problem of the peak current control by introducing a PI controller in the current loop. Similar to peak current control, in average current control, two control loops exist. The outer control loop is the voltage loop. The output voltage of the converter is measured and then compared with the output voltage reference. The difference between the reference voltage and the measured voltage is calculated and the value is applied to a PI controller which defines the reference current for the current loop. This reference current is the average current value of the converter to reach the output voltage reference. In the current control loop, the inductor current is compared with the reference current. The difference value is calculated and applied to a PI controller which calculates the desired duty cycle of the converter. By controlling the duty cycle of the converter, the average current and consequently the output voltage can be regulated. The advantages of the average current control technique are that it works at the fixed switching frequency, it has better stability and can operate in the whole range of the duty cycle variations even above 50% without any compensation.

3.3.2.3.3 Resistance control using the interleaved DC-DC converter

The block diagram of the resistance control of the WPT at the receiver side with the interleaved DC-DC boost converter and with average current control is shown in Fig. 3.25. The control is similar to the single phase boost converter but for sharing the current between the phases of the interleaved converter, an additional current loop is added to the control circuit based on average current control method. V_{2dc}^{*} is constructed similar to the single phase control method by multiplying i_{2dc} and R_{in}^{*}. By controlling the voltage at the input of the DC-DC converter, the output power can be controlled and thus, the voltage control loop is the outer loop of the control. The constructed V_{2dc}^{*} is compared with the measured voltage at the input of the DC-DC converter and the error goes through a PI controller. Unlike single phase DC-DC converter, here in the interleaved DC-DC converter, the output of the PI controller is the average reference current related to the output power. This current is divided by nine in order to build the average reference current for each phase of the interleaved converter. Then, the current is followed by a limiter in order to limit the current of each phase at the maximum current level. The value of i_{min} is selected higher than zero in order to keep the receiver short circuit during the start-up. The inner control loop is the current loop. In the current loop, the reference current is the average current of each phase. The current of the inductor is compared with the reference current and the error is entered to a PI controller. This PI control calculates the desired duty cycle of the converter. The voltage of the battery changes during the charging process and in order to keep the bandwidth of the control independent of the variation of the battery, in the control loop, the output of the PI controller is divided by the voltage of the battery. The obtained duty cycle is

compared with a triangle waveform and the PWM gating signal of the switch is generated. For each phase, one inverter leg is used. Switches of each inverter leg operate in complementary mode. When the bottom switch of the leg turns on, the top switch of the leg turns off and vice versa. The switching frequency of each phase is constant and it is equal to 19.5 kHz. With the proper switching of each leg, the current of the inductor can follow the current reference. Under different load conditions, the DC-DC converter may operate in CCM or DCM however the operating frequency is constant.

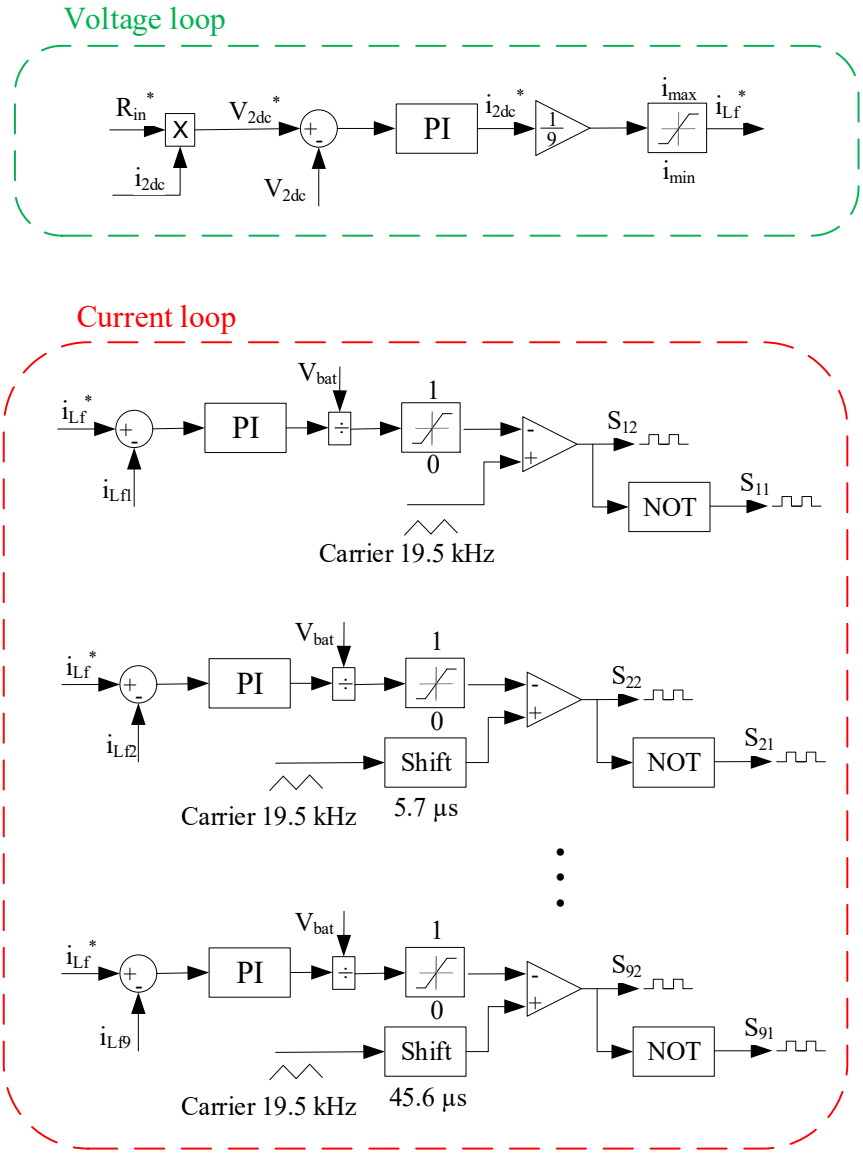

Fig. 3.25: Receiver control with the interleaved boost converter.

3.3.2.3.4 Design considerations for DC-DC converter

After the coils implementation, the resistances of them are measured 0.78 Ω and 0.53 Ω respectively. According to the design of the transmitter, DC source

voltage is 650 V. Thus, the transmitter voltage when the phase shift angle is maximum is equal to

$$V_1 = \frac{2\sqrt{2}}{\pi} V_{in} = \frac{2\sqrt{2}}{\pi} \times 650 = 585.2 \tag{3.24}$$

The maximum current that the H-bridge converter can switch is 35 A. By considering the transmitter and receiver resistances, the receiver voltage and current can be determined using (2.46) as

$$\begin{cases} R_1.i_1 - j\omega M.i_2 = V_1 \\ j\omega M.i_1 = R_2.i_2 + V_2 \end{cases}$$
$$\begin{cases} 0.78 \times 35 - j2 \times \pi \times 85000 \times 14.3 \times 10^{-6} \times i_2 = 585.2 \\ j2 \times \pi \times 85000 \times 14.3 \times 10^{-6} \times 35 = 0.53 \times i_2 + V_2 \end{cases} \tag{3.25}$$

By solving the equation, the values receiver voltage and current are calculated 73 A and 228.9 V, respectively. The receiver DC voltage and current can be calculated as

$$V_{2dc} = \frac{\pi}{2\sqrt{2}} V_2 = \frac{\pi}{2\sqrt{2}} \times 228.9 = 254.2\ V$$
$$i_{2dc} = \frac{2\sqrt{2}}{\pi} i_2 = \frac{2\sqrt{2}}{\pi} \times 73 = 65.7A \tag{3.26}$$

At this condition, the maximum power at the input of the DC-DC converter can be obtained as

$$P_{2dc} = i_{2dc} \times V_{2dc} = 16.7\ kW \tag{3.27}$$

The next step is to calculate the number of phases and the inductor of the DC-DC converter. In the design, important parameters are the maximum input current ripple of the DC-DC converter and the maximum current capability of each single phase of the interleaved DC-DC converter in all duty cycles. The maximum current of each switch of the DC-DC converter depends on the number of the phases which shares the output current and duty cycle. The ripple of the phase inductor is always maximum at the duty cycle of 50%. Battery voltage is considered 400 V, so the maximum current ripple of each phase occurs at input DC voltage of 200 V. The value of the inductor is also depended on the switching frequency of the DC-DC converter. If the switching frequency increases, a smaller inductor can be used. In the experimental set-up, power modules are chosen for the DC-DC converter. The maximum operating frequency of these power modules is 20 kHz. By considering the maximum current of each phase of 10 A and the maximum input current ripple of 1%, an equation set according to (3.19) and (3.22) can be obtained as

$$\begin{cases} \Delta i_{in-max} = \dfrac{V_{bat}}{4 f_{sw} L_f N} \\ i_{L(max)} = \dfrac{iL_i(avg)}{N} + \dfrac{V_{2dc}.D}{2.f_{sw}.L_f} \end{cases} = \begin{cases} 0.66 = \dfrac{400}{4 \times 20 \times 10^3 \times L_f \times N} \\ 10 = \dfrac{65.7}{N} + \dfrac{200 \times 0.5}{2 \times 20 \times 10^3 \times L_f} \end{cases} \quad (3.28)$$

By solving the equations set, two answers are obtained.

$$\begin{cases} N = 20.6 \\ L_f = 0.366mH \end{cases} , \begin{cases} N = 9.7 \\ L_f = 0.786mH \end{cases} \quad (3.29)$$

For the number of phases of the DC-DC converter, nine is selected. Furthermore, the inductance value of each phase is selected 1mH. According to the selected number of phases and value of the inductances, the maximum input current ripple of the DC-DC converter and the maximum current of each phase will be:

$$\Delta i_{in}(max) = \frac{400}{4 \times 20 \times 10^3 \times 1 \times 10^{-3} \times 9} = 0.49A$$
$$i_{Lf}(max) = \frac{65.7}{9} + \frac{200 \times 0.5}{2 \times 20 \times 10^3 \times 1 \times 10^{-3}} = 9.8A \quad (3.30)$$

The value of the phase inductor for operation in BCM (boundary condition) which is between the DCM and CCM versus the input voltage of the DC-DC converter when the battery voltage is 400 V is shown in Fig. 3.26.

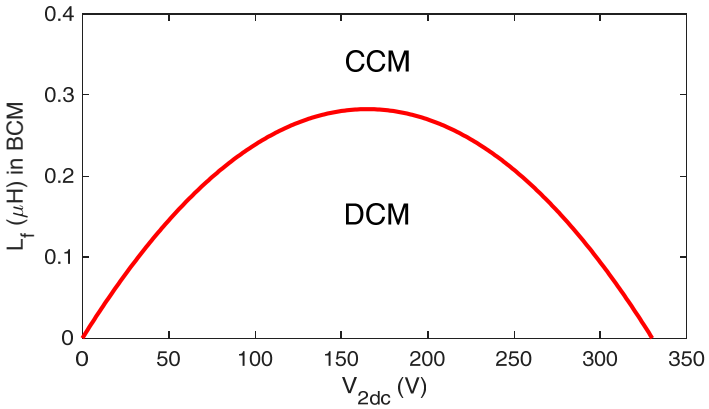

Fig. 3.26: Boundary between CCM and DCM operation for the DC-DC converter.

For the operation of the DC-DC converter in CCM, the phase inductor should be designed bigger than 0.3 mH. Since the phase inductor is selected 1mH, the converter operates in CCM for whole duty cycles.

A comparison between different phase numbers is presented in Table. 3.2. Considering the DC-DC converter operates at the maximum current of 65.7 A and with a similar phase inductor of 1 mH, the peak current of the phase switch is obtained. In the interleaved converter, the input current is divided between each phase. In the case of symmetric current sharing in each inductor, the peak current

of the phase can be reduced when the number of phases increases. One of the advantages offered by the interleaved converter is the ripple cancelation capability as shown in Table 3.2. With a similar phase inductor, when the number of the phase increases, the input current ripple decreases. The values of the phase inductors for having the input current ripple of 1 % are compared in Table 3.2. The ripple cancelation capability of interleaved converter helps the converter to have a reduced value of filtering components. With 9 phase converter, only 0.85 mH is necessary for having 1% of input current ripple. Generally, the IGBT power modules available in the market are single and three phases. Thus, for 3, 6 and 9 phase converter, one or several three phase IGBT power modules can be used. Furthermore, using three phase IPM module helps to simplify the construction process since each module is equipped with the gate driver, overcurrent and short circuit protection. In addition, the operating frequency of the transmitter and receiver coils is equal to 85 kHz and thus, the frequency of the ripple at the output of the diode bridge will be equal to 170 kHz. Furthermore, by considering the operating switching frequency of each module up to 20 kHz, the overall ripple frequency of the converter with 9 phases will be up 180 kHz. This frequency is compatible with the current ripple frequency at the output of the diode bridge rectifier.

Table 3.2: Comparison between different phase numbers.

N	1	2	3	4	5	6	7	8	9
Phase peak current (A) L_f=1 mH	68.2	35.35	24.4	18.92	15.64	13.45	11.88	10.71	9.8
Input ripple current (A) L_f=1 mH	5	2.5	1.67	1.25	1	0.83	0.71	0.625	0.55
L_f with 1% current ripple	7.69	3.85H	2.56	1.92	1.54	1.28	1.1	0.96	0.85
Mudule type	1 single phase	-	1 three phase module	-	-	2 three phase modules	-	-	3 three phase module

The controller in the receiver is designed in a way that the boost converter remains short circuit when the coupling is zero. The design is by adding a minus one gain to the receiver control. However, during absent of the receiver coil, the error of the controller remains nonzero for a long time and even it becomes large. This large error may cause the saturation of the controller and delay to the controller response. Especially, this consideration must be taken into account in the implementation of the controller. For these reasons, the anti-windup strategy is necessary to avoid the saturation of the receiver controller.

The receiver control is composed of the inner current control loop and the outer voltage loop. The inner control loop is realized based on the PI controllers. The parameters of the current loop PI controller can be determined by

$$K_{p-c} = \frac{\omega_c L_f}{V_{bat}} \tag{3.31}$$

$$K_{i-c} = \frac{\omega_c R_f}{V_{bat}} \tag{3.32}$$

Where ω_c is the band of the current control loop and R_f is the resistance of the inductor. A similar way is used for the design of the voltage loop. Since the control consists of the inner loop and the outer loop, the bandwidth of the inner loop is selected larger than the bandwidth of the outer loop in order to avoid instability. The parameters of the voltage loop PI controller can be determined by

$$K_{p-v} = \frac{\omega_v C_f}{N} \tag{3.33}$$

$$K_{i-v} = \frac{\gamma \omega_v C_f}{N} \tag{3.34}$$

Where ω_v is the band of the voltage control loop and γ is a gain for making the system operate with a fast response. By defining the band of the current loop equal to 2 kHz, the parameters of the current loop PI controller $K_{p\text{-}c}$ and $K_{i\text{-}c}$ are selected 0.03 and 30, respectively. Furthermore, by selecting the band of the voltage loop equal to 200 Hz, the parameters of the voltage loop PI controller $K_{p\text{-}v}$ and $K_{i\text{-}v}$ are selected 0.01 and 100, respectively.

3.4 Dual side control with active rectifier at the receiver

One of the control methods in WPT systems is the application of the active rectifier [122], [123], [144]–[154]. In this method, the diode-bridge and DC-DC converter are replaced by an active rectifier. Thus, the battery power can be regulated by the active rectifier from the receiver. By using the H-bridge converter at two sides of the system, it is converted to a bidirectional system that is able to transfer the power to both sides which is necessary is different applications such as vehicle to grid systems. However, bidirectional WPT systems are naturally complex. In these systems, complicated control strategies are necessary two control power flow direction and to provide the synchronization. The controller proposed in [144] is used at the receiver to manage power flow in a bidirectional system by utilizing active and reactive power. Power and frequency regulation methods in the bidirectional WPT system are introduced in [146] and [123]. A synchronization technique for the bidirectional system using an additional coil is proposed in [147].

In [148], the resistance control is used at the receiver for tracking the maximum efficiency point.

In this part, a novel solution is proposed for regulating the output power in dynamic charging of the EV. In the receiver of the system, a power control is implemented. This control loop regulates the output power using an active rectifier. Furthermore, for regulating the transmitter current and maintaining the current at the peak level during the misalignment and coupling variations, a transmitter current control is designed. In this method, the transmitter converter operates at a definite power level and the receiver can control the output power from zero to peak power according to vehicle demand without communicating with the transmitter converter.

3.4.1 Circuit description with the active rectifier

The circuit of the proposed bidirectional system is presented in Fig. 7.1 [154] which is similar to a conventional WPT system but in the receiver, the passive rectifier is changed with an active one. In Fig. 3.27, C_f and L_f are output filters before the connection to the battery.

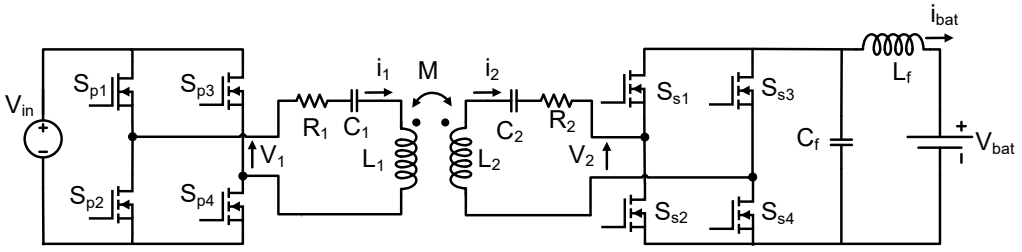

Fig. 3.27: Proposed bidirectional system configuration.

The frequency of the transmitter DC-AC converter is equal to system resonant frequency. The proposed control scheme in this chapter is implemented by two independent control circuits at two sides of the system. A current control loop is used at the transmitter of the system. However, a power control loop is used at the receiver. These control loops operate together for regulating output power during the vehicle movement and also in the presence of misalignment. The receiver control regulates the battery power by controlling the ratio of receiver voltage and current according to the following equation.

$$P_o = \frac{V_2}{I_2}\left(\frac{j\omega_0 M V_1}{R_1\left(R_2 + \frac{V_2}{I_2}\right) + \omega_0^2 M^2}\right)^2 \tag{3.35}$$

The schematic of the control can be seen in Fig. 3.28. DC-AC converter operates at constant frequency ω_0. This frequency is the resonant frequency of the

transmitter and receiver. This converter operates with a phase shift control scheme and regulates the transmitter current according to the mutual inductance variations.

By changing the DC-DC converter and diode rectifier with an active rectifier, it is possible to regulate the voltage of the receiver. The basic operation of the WPT with an active rectifier is similar to a system with passive rectifier and DC-DC converter. Considering a condition when the switch of the boost converter is on and the receiver is short circuit. This condition can be done with the active rectifier when two bottom switches are on. In this case, the receiver voltage becomes zero and the load will receive no power.

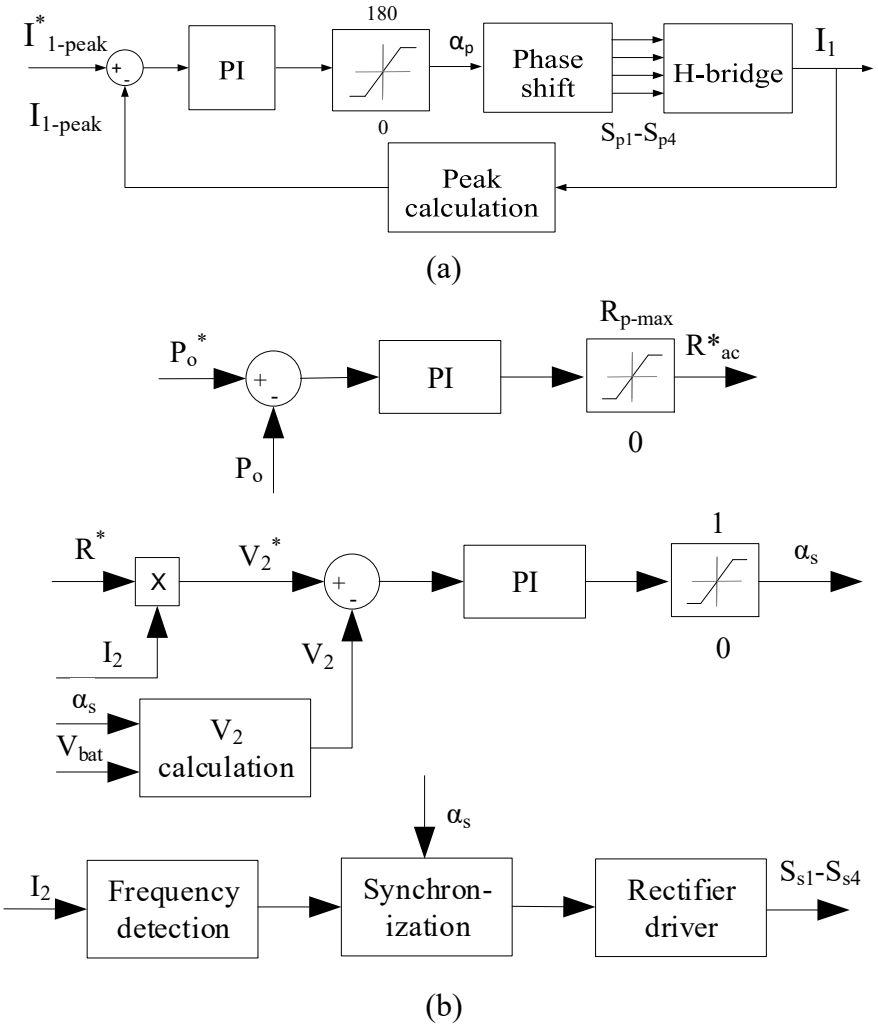

Fig. 3.28: Proposed dual side control scheme. (a) Transmitter control and (b) receiver control.

At the moment that S_{s2} and S_{s4} turn off, the current of the receiver will be transferred to the load. Thus, by controlling the switches of the active rectifier, the battery power can be regulated. For control of the rectifier input voltage, only two bottom switches are enough. But, for having a bidirectional power system, an active rectifier with four switches is employed.

The control scheme that is adopted for the active rectifier is phase shift modulation. The control is like the transmitter control. By this method, the value of V_2 is controlled. Fundamental harmonic of the receiver voltage V_2 controlled by phase shift modulation can be calculated by

$$V_2 = \frac{2\sqrt{2}}{\pi} V_{bat} \cos\left(\frac{\alpha_s}{2}\right) \tag{3.36}$$

The power control has two loops. The power control is the outer loop and the voltage control loop is the inner loop. P_o^* is the reference power equal to demanded power. The output power is calculated and then the obtained value is compared with reference power. The difference value is used in the PI controller. PI controller builds R^*_{ac} according to P_o^*. This value is limited between zero and $R_{p\text{-}max}$. The value of $R_{p\text{-}max}$ is an equivalent resistance where the P_o is maximum at the rated coupling. This resistance can be calculated when the transmitter voltage and current are at their maximum values as:

$$R_{p-max} = \frac{\omega_0^2 {M_n}^2 I_1^*}{\frac{2\sqrt{2}}{\pi} V_{in} - R_1 I_1^*} - R_2 \tag{3.37}$$

The calculated equivalent AC resistance is multiplied by the receiver current. The obtained value is receiver reference voltage V^*_2. The active rectifier must be switched in order to follow this reference voltage. For this reason, firstly, the receiver voltage must be measured. However, it is difficult to measure V_2. Thus, this voltage is calculated based on first-order analysis using phase shift angle α_s and V_{bat}. The receiver reference voltage and the calculated voltage are compared and the difference is calculated. The obtained voltage is applied to a PI controller. This controller constructs the phase shift angle corresponding to V^*_2. The switching frequency of the transmitter DC-AC converter is similar to the transmitter and receiver resonant frequencies. In the control circuit, the transmission of the data of the transmitter frequency to the receiver is avoided. Thus, the switching frequency of the transmitter must be identified by the control circuit of the receiver. Firstly, a unity amplitude square wave is implemented from the receiver current. Then, based on the phase shift angle calculated by receiver control and unity amplitude square wave, the active rectifier is switched.

When the reference power P^*_o is zero, S_{s2} and S_{s4} turn on simultaneously. The receiver voltage becomes short circuit and the output power will be zero. When V^*_2 increases, the reference equivalent AC resistance increases. This causes the receiver voltage to be increased by the active rectifier and consequently, the output power will go up. If the reference power increases more and becomes equal to maximum power, R^*_{ac} reaches its maximum value. At this resistance, i_1 is at the peak value. If P^*_o goes beyond the peak value, the values of R^*_{ac} and subsequently V_2 remains constant.

In rated coupling, the transmitter voltage is a maximum at different output power levels. However, during the misalignment and decrease of the coupling, the V_1 reduces for controlling the transmitter current. During misalignment, output power decreases. The peak output power can be obtained only at the rated coupling.

3.4.2 Design Considerations

The parameters of the simulation are presented in Table. 3.3. When the input DC voltage is 650 V, V_1 is calculated V_1=585.21 V. It is considered that the maximum current of the transmitter is I^*_1=35A. The value of $R_{p\text{-}max}$ will be 3.11Ω using (3.37). Then, according to (2.46), and replacing R_{ac} with $R_{p\text{-}max}$, I_2 and V_2 are calculated 72.05 A and 224.06 V, respectively, using data presented in Table. 3.3. Thus, maximum power will be approximately 16 kW.

Table 3.3: System Specifications.

Parameter	Value	Unit
Transmitter self-inductance, L_1	280	μH
Transmitter resistance, R_1	1	Ω
Transmitter capacitor, C_1	12.5	nF
Receiver self-inductance, L_2	120	μH
Receiver resistance, R_2	0.6	Ω
Receiver capacitor, C_2	29.2	nF
Mutual inductance (nominal), M_n	14.3	μH
Input DC voltage, V_{in}	650	V
Battery voltage, V_{bat}	250-400	V
Nominal transmitter current, I^*_1	35	A
Operating frequency, f_0	85	kHz

3.4.3 Simulation Results

The proposed control scheme is simulated using PSIM. System behavior in variations of P_o^* is shown in Fig. 3.29. When P_o^* becomes more than zero, V_2 and consequently i_1 increases. This will cause an increase in the battery power. When i_1 becomes maximum, the output power reaches its peak. Due to R_1 and R_2, the receiver current is with small variations as Fig. 3.29(b). The efficiency of the system reaches 80% as shown in Fig. 3.29(d).

System behavior in mutual inductance variations is presented in Fig. 3.30. The variations of V_1 and i_1 are presented in Fig. 3.30(a). The rated M is 14.3 μH. When M becomes more than nominal the nominal value, for example when the air-gap decreases, the input impedance increases and the transmitter current reduces. The transmitter voltage in this condition is maximum.

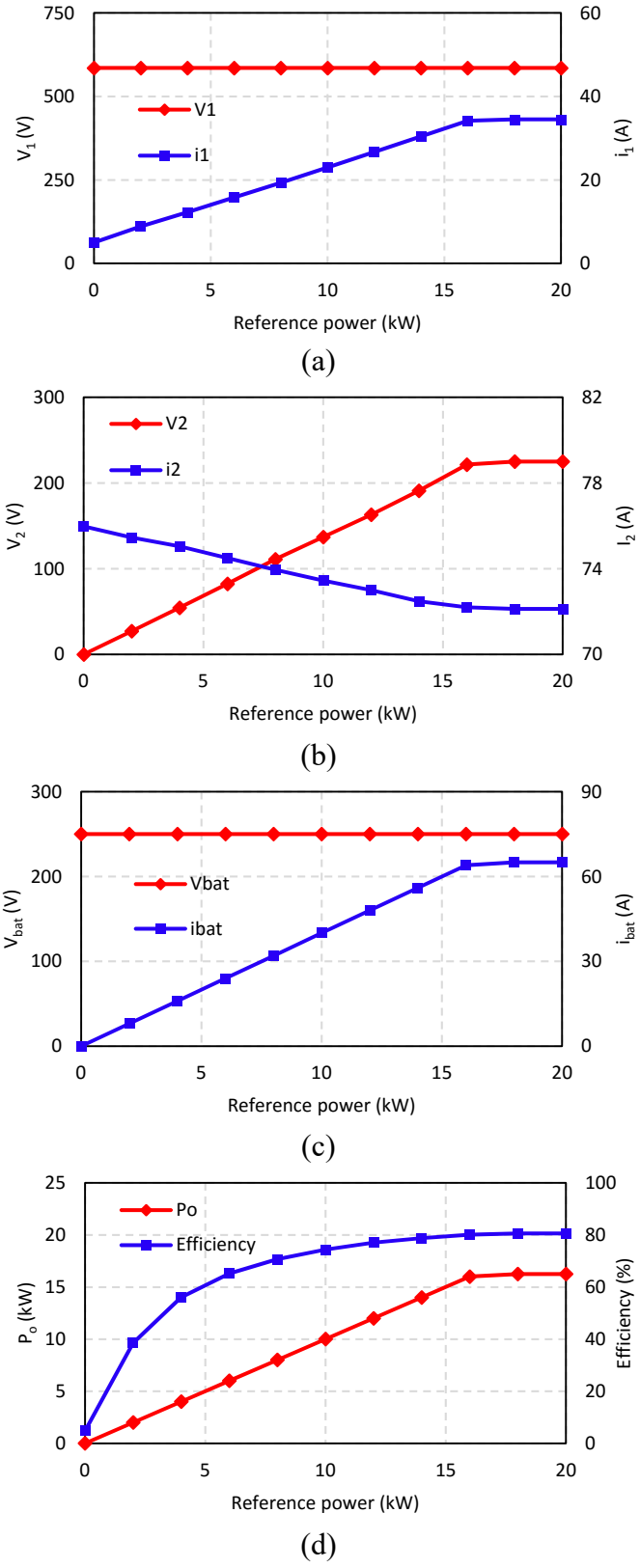

Fig. 3.29: Performance of different parameters of the circuit under variations of the reference output power P_o^*. (a) V_1 and i_1, (b) V_2 and i_2, (c) V_{bat} and i_{bat}, (d) P_o and efficiency.

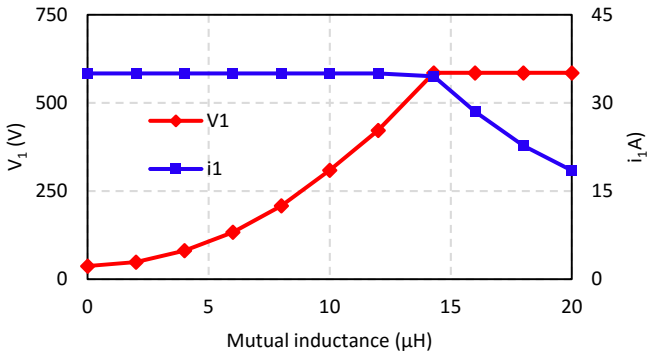

(a)

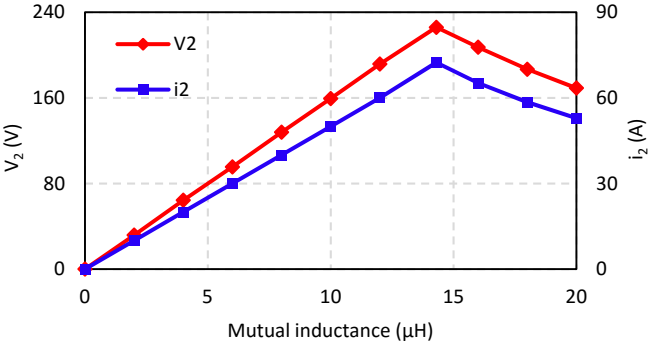

(b)

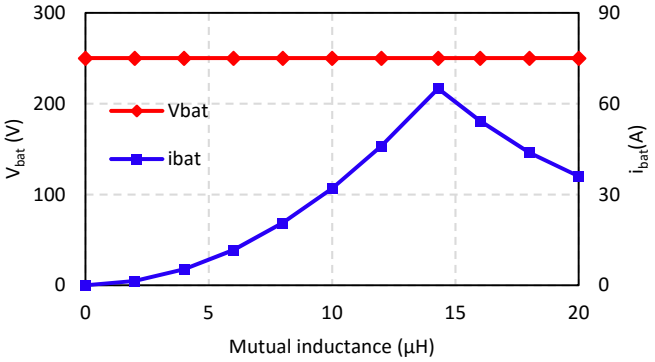

(c)

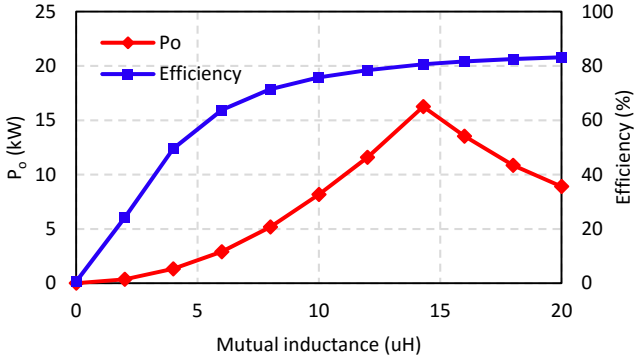

(d)

Fig. 3.30: Performance parameters of the circuit under variations of the mutual inductance. (a) V_1 and i_1, (b) V_2 and i_2, (c) V_{bat} and i_{bat}, (d) P_o and efficiency.

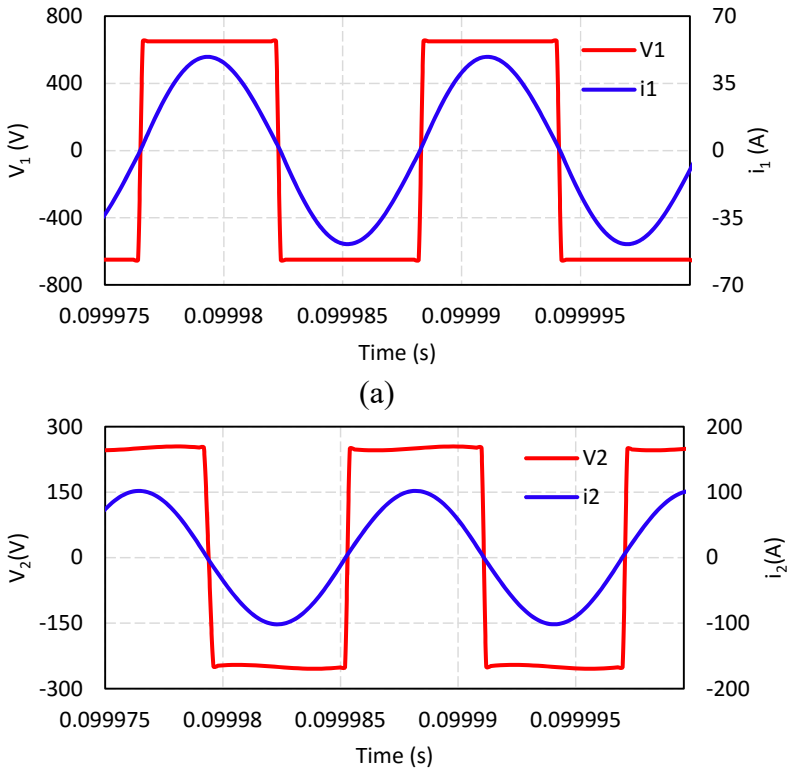

Fig. 3.31: Important waveforms of the system when the output power is maximum. (a) V_1 and i_1, (b) V_2 and i_2.

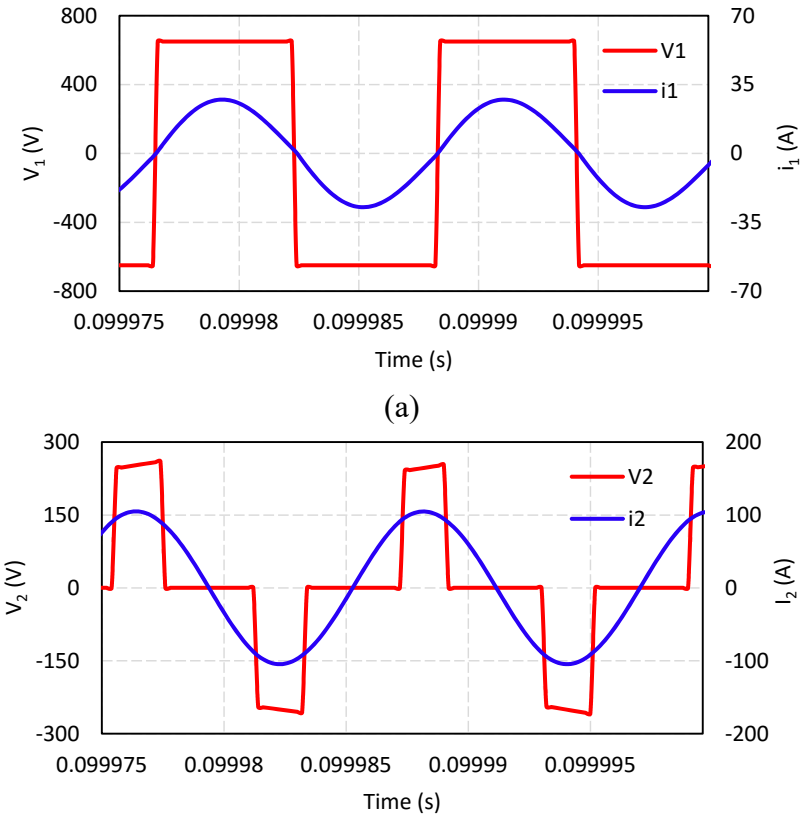

Fig. 3.32: Important waveforms of the system when the output power is reduced. (a) V_1 and i_1, (b) V_2 and i_2.

When M becomes lower than nominal M, the transmitter voltage reduces in order to keep i_1 at peak level. Fig 3.30(b) illustrates V_2 and i_2 versus the variations of M. If M increases, i_2 decreases. But in lateral misalignment and decrease of the mutual inductance, the receiver current decreases. The battery voltage and current versus variations of mutual inductance are presented in Fig. 3.30(c). At nominal M, the battery current is maximum. Output power and efficiency versus M are presented in Fig. 3.30(d). At nominal mutual inductance, peak power is received by the battery since both transmitter current and voltage are maximum.

V_1 and i_1 at the rated power and rated M are shown in Fig. 3.31. At this point, V_1 and V_2 are maximum. The waveforms of the transmitter and receiver at 8 kW output power at rated M are shown in Fig. 3.32. In order to reduce the output power, V_2 is reduced by the receiver control. However, the transmitter voltage has remained unchanged. The transmitter converter switches work in soft switching but active rectifier switches operate in hard switching.

Transmitter and receiver waveforms when a lateral misalignment of 10 cm is present are shown in Fig. 3.33. When the lateral misalignment occurs, the mutual inductance reduces. In this case, the transmitter voltage reduces for limiting the increase of i_1 and thus i_2 reduces too. The value of the equivalent resistance is constant and thus the receiver voltage reduces as well.

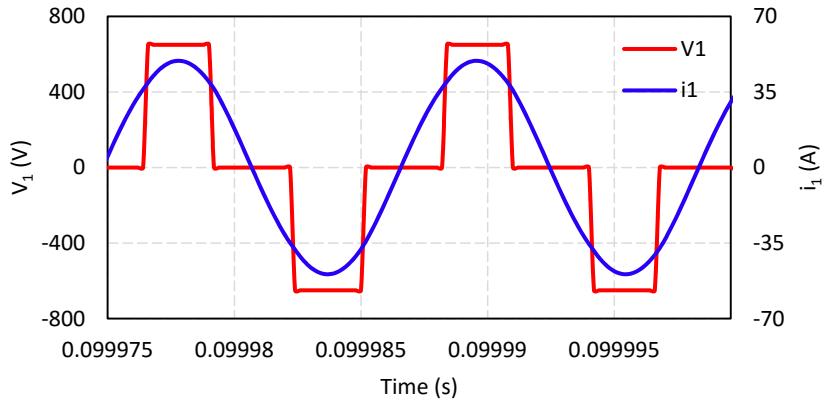

(a)

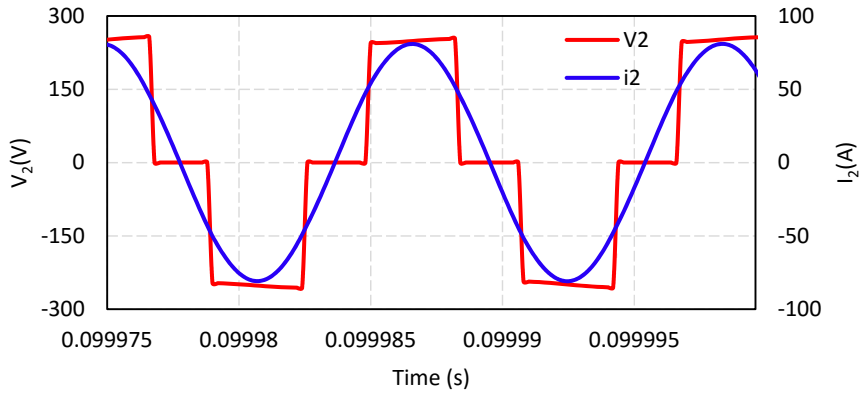

(b)

Fig. 3.33: Operation with 10 cm misalignment. (a) V_1 and i_1, (b) V_2 and i_2.

3.5 Vehicle identification

As mentioned in chapter one, there are two coil topologies for dynamic WPT system including long track topology and segmented track topology. There are several drawbacks with long track topology which can be overcome using segmented track topology. In this topology, several small size transmitter coils are embedded into the ground. Each transmitter coil is equipped with an H-bridge converter which turns on or turns off according to the position of the EV. One of the biggest challenges in segmented track topology is that the presence of the EV must be detected and the transmitter coil must be turned on when the EV is exactly on the top of that. Assuming that the EV is passing in the highway with a speed of 72 km/h, this means that if the length of the coil is 1 m, the EV is on the top of the coil for only 50ms. Thus, this makes the design of the control circuit so difficult because it must be fast enough to detect the EV passing even with fast speed. Furthermore, a small delay in turning the transmitter coil on, will result in a reduction of the power transmission.

Several solutions have been presented in the literature for the detection of the EV [121], [155]–[169]. One solution is the application of radio frequency as a communication link between the transmitter and receiver [160]. However, due to the communication between the two sides, this method has delay and thus, the charging time of the vehicle reduces. The identification of the vehicle in [161] is based on the combination of the RFID (radio frequency identification) technique and the magnetic field coupling method in order to increase the accuracy of the detection. In the dynamic WPT system implemented by KAIST, magnetic sensors are placed at the beginning of the segment to identify the presence of the EV [26]. Furthermore, the static WPT charger designed by ORNL [121], the sensor is employed to detect the EV. However, the application of the sensor increases the overall cost of the charger especially in a charging lane in the highway with several transmitters. In [162] the reactance reflected by the receiver is used to boost the electromagnetic field strength automatically when the coils are coupled and without any communication link. In the system proposed in [163], particle swarm optimization (PSO) algorithm is used to detect the parameters of the load. In [164] by sending energy to the transmitter coil and measuring the decline rate of the current, the parameters of the load are identified in an induction heating application. In works presented by the University of Auckland [165], [166] multiple coils are used in the transmitter and receiver to identify the presence of the EV. In this method, the coil in the receiver side is energized with a 100 kHz AC current. Furthermore, two detection coils are used at the transmitter. When the EV approaches the transmitter coil, a voltage is induced across the detection coils and the control circuit by measuring this voltage can identify the presence of the vehicle. This process can also be employed to turn off the transmitter coil when the vehicle leaves the coil. This solution is robust and simple; however, three extra coils are used in the circuit which two of them are mounted on the transmitter. Thus, the total

construction cost increases when the number of transmitters increases. In [167] the EV is detected without using position sensors. In this system, each coil is connected to two power sources; one is the high power source for power transmission and the other is the low power signal source for the detection purpose. In the detection mode, the low power signal source injects a current to the transmitter coil with a frequency near to the resonant frequency of the coil but not exactly the same as that. The control measures the phase angle between the transmitter voltage and current. When an EV approaches the coil, the phase angle changes and the control detects the presence of the vehicle. The drawback of this system is that two separate sources are necessary for each transmitter coil. In [168] the vehicle is identified with the use of the free resonant currents in the transmitter coil. By designing the transmitter and receiver coils and establishing the coupling between two nearby transmitter coils, when the receiver coil moves over the transmitter coils, a small changes in mutual inductance between two nearby transmitter coils occurs and a free resonance current starts increasing in the nearby transmitter coil. When this current reaches a specific value, the transmitter coil turns on and the power transmission starts automatically. In this detection method, no additional equipment is used however for the detection of the vehicle in the first transmitter coil and at the beginning of the charging lane, a different identification method is necessary.

According to the above discussion, in most of the introduced methods, communication link, sensors, or extra components are used to identify the presence of the vehicle. Position sensor or other extra components increase the overall size and construction cost of the charging lane. Thus, it is desirable to identify the vehicle by the DC-AC converter of the transmitter and without any extra component. In this chapter, two vehicle detection methods are proposed. The first method is the current injection method and measurement of the envelope of the peak current and the second method is the current injection in the transmitter coil and monitoring the phase shift angle. The operating principles of these two methods are discussed in detail in the following sections.

3.5.1. Identification by current injection and free resonant mode

The process of the identification of the vehicle is divided into two parts. The first part is the injection of the energy into the transmitter coil and the second part is monitoring the envelope of the transmitter current in free resonance mode [169]. Fig. 3.34 illustrates the current of the transmitter in both identification modes. The current is injected into the transmitter coil by applying a voltage across it. As shown in Fig. 3.34, at t_0, the current injection starts by switching of the DC-AC converter. At t_1, the free resonant mode begins by short-circuiting the transmitter coil (S_2 and S_4 turn on and S_1 and S_3 turn off). In this case, the transmitter current freewheels in the circuit.

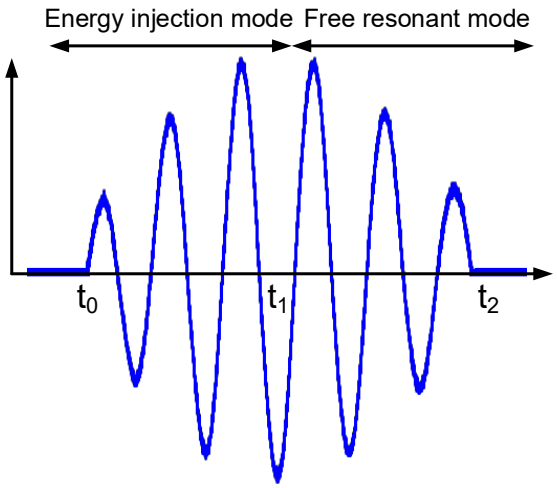

Fig. 3.34: Two operating modes used for the identification.

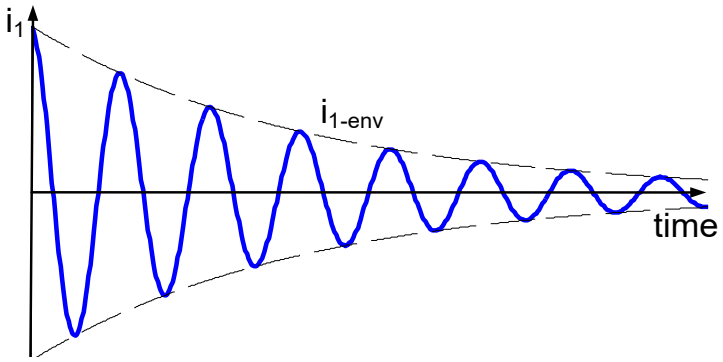

Fig. 3.35: Transmitter current and its envelope in free resonant mode.

As shown in Fig. 3.35, in free resonant mode, the transmitter current gradually decreases due to the resistance of the transmitter coil and DC-AC switches. If the load is present, the energy of the transmitter is transferred to the receiver. The presence of the load can be identified in free resonant mode and for this reason, the peak of the transmitter current is recorded.

The equation of the transmitter current in free resonant mode can be determined by

$$i_1(t) = \frac{\omega_0}{L_1\omega_1} e^{-\alpha t}\cos(\omega_1 t + \theta) \tag{3.38}$$

Where ω_1 is the operating frequency in free resonant mode and ω_0 is the resonant frequency of the transmitter and α is the damping coefficient of the circuit and can be written as follows:

$$\alpha = \frac{\omega_1}{2Q_1} \tag{3.39}$$

$$\theta = \arccos\left(\frac{\omega_1}{\omega_0}\right) \tag{3.40}$$

Q_1 is the quality factor of the coil and is given as

$$Q_1 = \frac{\omega_0 L_1}{R_{eq}} \tag{3.41}$$

R_{eq} is defined as the transmitter resistance and the receiver resistance referred to the transmitter side as

$$R_{eq} = R_1 + \frac{{\omega_0}^2 M^2}{R_2 + R_{ac}} \tag{3.42}$$

According to Fig. 3.35, the current of the transmitter in free resonant mode decreases exponentially according to (3.38). If the transmitter resistance R_1, receiver resistance R_2 and transmitter self-inductance L_1 remain constant, according to (3.39), (3.41), and (3.42), the damping coefficient is depended on R_{ac} and M. The damping coefficient reduces when the equivalent load resistance increases. Thus, the peak current of the transmitter current drops at a slower rate. Furthermore, if the mutual inductance goes up, the damping coefficient becomes higher and for this reason, the peak current drops faster. Fig. 3.36 and Fig. 3.37 show the waveforms of transmitter current under the variations of the mutual inductance M and load resistance R_{ac}, respectively.

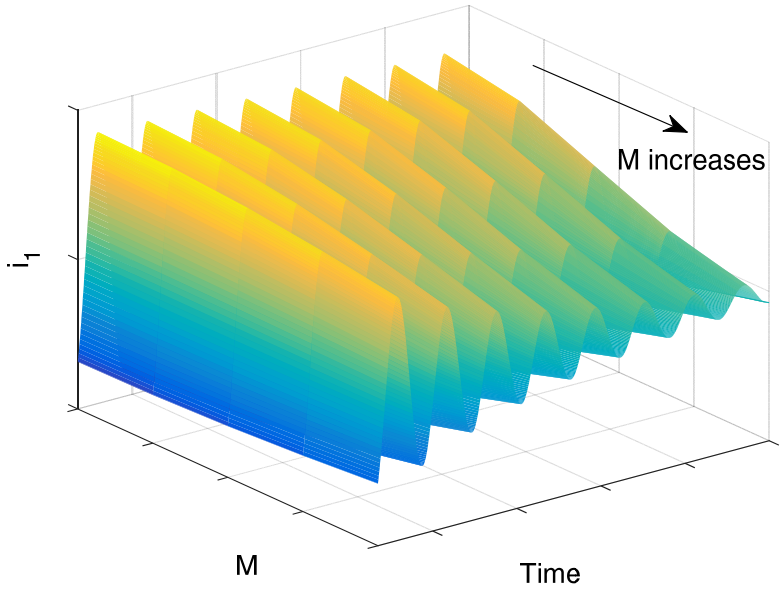

Fig. 3.36: Transmitter current versus M and time in free resonant mode.

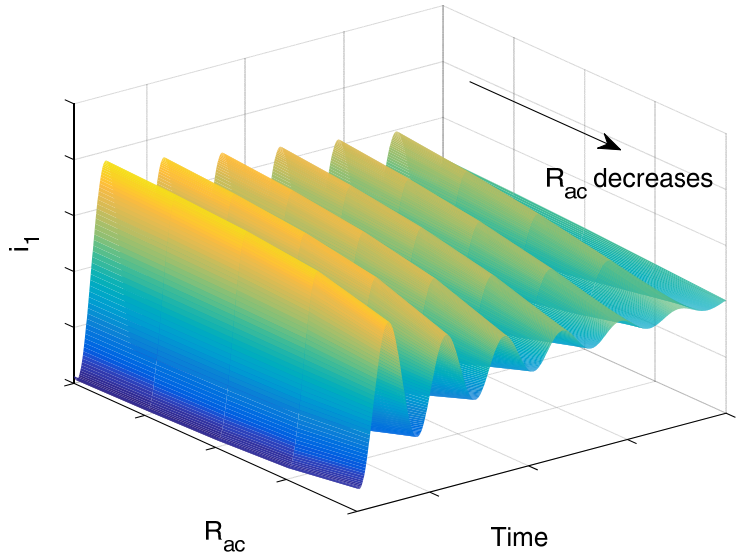

Fig. 3.37: Transmitter current versus R_{ac} and time in free resonant mode.

M is equal to zero when the transmitter coil and the receiver coil are far from each other. In this case, the damping coefficient is low and the envelope waveform of i_1 will decline slower. In this situation, no load is detected. When the receiver coil approaches the transmitter coil, the value of mutual inductance starts increasing. In this case, the damping coefficient value increases and the envelope waveform of i_1 declines faster than without the load condition. The i_1 envelope waveform is used for the identification of the presence of the vehicle. The peak values of the transmitter current can be determined by

$$i_1(n) = \frac{1}{L_1} e^{-\alpha t_n} \quad , \quad t_n = \frac{2\pi(n+1)}{\omega_0} \tag{3.43}$$

Where n is an integer which is defined as the n_{th} oscillation of the transmitter current. By writing the above equation for two different n, we have:

$$\frac{i_1(n_1)}{i_1(n_2)} = \frac{e^{-\alpha\left(\frac{2\pi(n_1+1)}{\omega_0}\right)}}{e^{-\alpha\left(\frac{2\pi(n_2+1)}{\omega_0}\right)}} \tag{3.44}$$

The damping coefficient can be determined by

$$\alpha = \frac{\omega_0 \left(ln\big(i_1(n_1)\big) - ln\big(i_1(n_2)\big)\right)}{2\pi(n_1 - n_2)} \tag{3.45}$$

By putting (3.45) into (3.39) the transmitter quality factor can be obtained. Then, by using (3.41), the equivalent input resistance can be calculated by

$$R_{eq} = \frac{\omega_0 \left(ln\left(i_1(n_1)\right) - ln\left(i_1(n_2)\right) \right)}{\pi(n_1 - n_2)} L_1 \tag{3.46}$$

Obviously, by sampling the peak current of the transmitter according to (3.46), the value of the equivalent input resistance is calculated. When the mutual inductance is zero, the R_{eq} is equal to the value of the transmitter resistance R_1. If the calculated R_{eq} is bigger than R_1, the control can find out that the mutual inductance is increased. By defining a limit for α and R_{eq}, the control can avoid considering a foreign material as a vehicle identification.

3.5.1.1 Results

Some experimental tests have been conducted in order to validate the theoretical analysis. The parameters of the experimental tests can be found in Table 3.4.

Table 3.4: Specifications and parameters of the tested system.

Parameter	**Value**	**Unit**
Input DC voltage, V_{in}	200	V
Transmitter resistance, R_1	0.3	Ω
Transmitter inductance, L_1	240	μH
Transmitter capacitor, C_1	15	nF
Receiver resistance, R_2	0.35	Ω
Receiver inductance, L_2	120	μH
Receiver capacitor, C_2	30	nF
Mutual inductance, M_n	18	μH
Switching frequency, f_0	85	kHz

Two different tests are conducted to evaluate the performance of the identification circuit. In both tests, the transmitter coil is supplied by a voltage for a short time. For the first test, the output of the rectifier at the receiver is short circuit. The waveforms of the i_1 and i_2 for different mutual inductances are presented in Fig. 3.38 and Fig. 3.39, respectively. For the condition that the transmitter coil and receiver coil are far from each other, M is zero. Thus, the transmitter energy is not transferred to the load and the variations of the envelope of the transmitter current are not high. When M increases, the envelope of the transmitter current declines faster after the first oscillations. The behavior of the envelope of the transmitter current depends on the value of the mutual inductance. According to this behavior, the presence of the load can be identified.

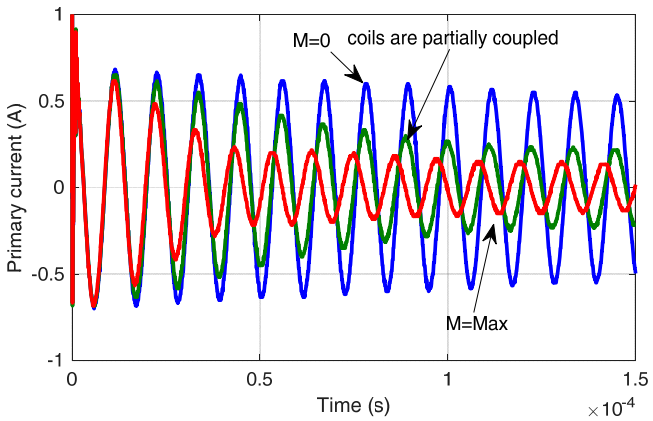

Fig. 3.38: Transmitter current in test one when diode-bridge is connected.

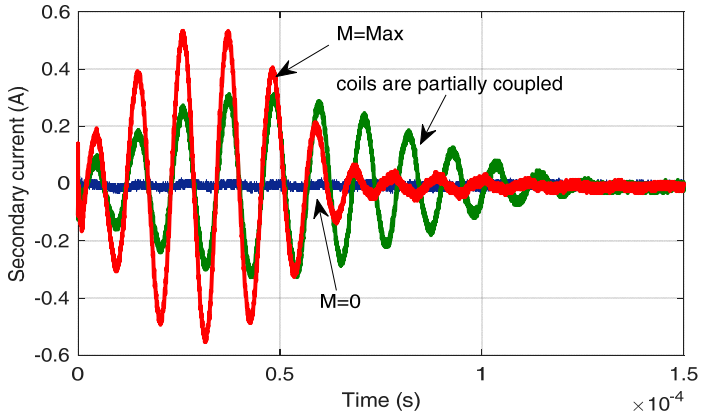

Fig. 3.39: Receiver current in test one when diode-bridge is connected.

For the second test, the rectifier at the receiver side is removed and the receiver coil is short circuit. In this condition, the receiver is only composed of L_2 and C_2. Fig. 3.40 and Fig. 3.41 show the waveforms of the currents of the transmitter and receiver for different mutual inductances. Since the rectifier at the receiver side is removed and the receiver circuit is short circuit, the power in the receiver is transferred again to the transmitter. However, a portion of the receiver power dissipates in the parasitic resistance of the receiver. Similar to the previous test, the envelope of the peak current oscillations depends on the value of the mutual inductance. The waveform used for switching of the DC-AC converter accompanied by the transmitter current is illustrated in Fig. 3.42. As seen in this figure, the top switches of the DC-AC converter are on for a very short period of time.

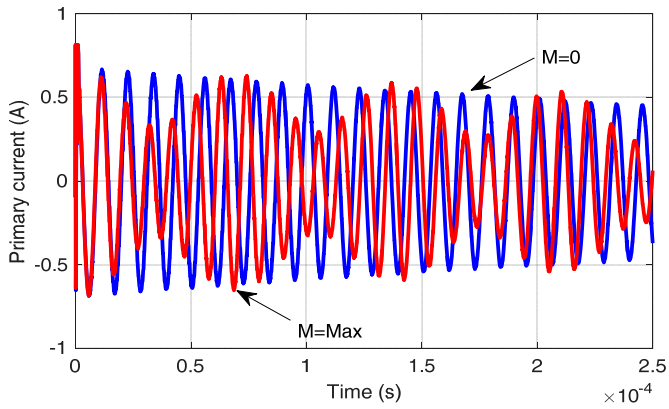

Fig. 3.40: Transmitter current in test two without diode-bridge.

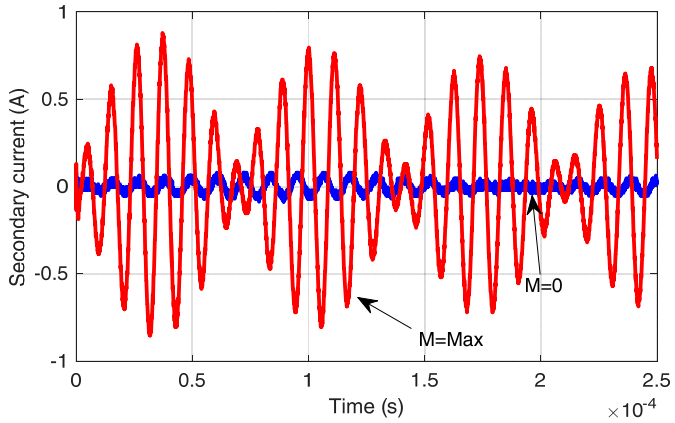

Fig. 3.41: Receiver current in test two without diode-bridge.

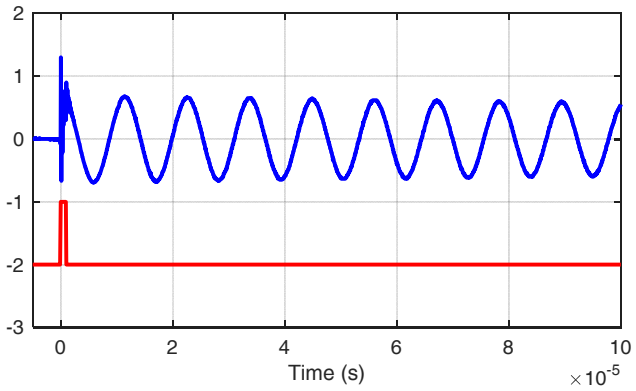

Fig. 3.42: Transmitter current and the signal used for the switching of the converter (shifted by -2).

3.5.2 Identification by the phase shift angle control

The detection of the vehicle with this method is similar to the previous method and a small current is injected in the transmitter coil. However, the difference is that in this method, the peak value of the injected current to the transmitter which is used to identify the vehicle is controlled [170]. By dividing the transmitter voltage to input impedance, the transmitter current equation is determined by

$$i_1 = \frac{1}{R_1 + \frac{(\omega M)^2}{(R_2 + R_{ac})}} \frac{2\sqrt{2}}{\pi} V_{in} \sin(\frac{\alpha}{2}) \tag{3.47}$$

When the distance between the transmitter coil and the receiver coil is too much, M is zero and the impedance seen from the transmitter is only composed of the transmitter resistance R_1. The value of the phase shift angle for having the transmitter current equal to i_d^* can be defined by

$$\alpha = 2sin^{-1}\left(\frac{i_d^* \pi R_1}{2\sqrt{2}V_{in}}\right) \tag{3.48}$$

i_d^* is the transmitter reference current used in the control circuit for the load detection purpose and its value is much lower than the power transmission current. According to the parameters of the coil, the transmitter resistance value is very small and thus, the phase shift angle should be very small in order to maintain the transmitter current at i_d^* level. At the time the receiver coil approaches the transmitter coil, the mutual inductance starts going up. At the condition, the phase shift angle α equation can be expressed as

$$\alpha = 2sin^{-1}\left(\frac{i_d^* \pi \left(R_1 + \frac{(\omega M)^2}{(R_2 + R_{ac})}\right)}{2\sqrt{2}V_{in}}\right) \tag{3.49}$$

The impedance seen from the transmitter increases when the value of the mutual inductance goes up. In this condition, the transmitter current reduces. According to (3.49), when M increases, for maintaining the current of the transmitter constant at the level of i_d^*, the phase shift angle must rise. When the vehicle approaches more, the transmitter current is reduced again and the control must increase the phase shift angle in order to keep i_d^* stable. The transmitter controller monitors the phase shift angle constantly. At the moment that mutual inductance grows enough and the phase shift angle α reaches the threshold angle α_{in}, the controller considers that the vehicle is present and the power transmission must starts. The transmitter control changes the status from the identification mode to power transmission mode by changing the transmitter reference current form i_d^* to i_1^*. The value of i_1^* is the peak current of the DC-AC converter.

In order to keep the efficiency of the charging high and reduce the electromagnetic field exposure, the transmitter coil must be turned off when the vehicle leaves the coil. The turning off procedure of the H-bridge converter is the same as the detection scheme. The mutual inductance is maximum when the receiver coil is above the transmitter coil. At the time the vehicle passes the transmitter coil, M begins decreasing. If the mutual inductance reduces, the total impedance seen from the transmitter reduces and the transmitter current begins

going up. According to (3.49), the transmitter control circuit must reduce the phase shift angle in order to keep the transmitter current at the level of i_1^* constant when mutual inductance reduces. As the vehicle crosses the transmitter coil, the mutual inductance goes down more and therefore, the transmitter controller decreases α again. At the moment that α reaches the threshold angle α_{out}, the controller considers that the mutual inductance is low and the vehicle is leaving the coil and the power transmission must stop.

For the identification, the correct values of the turn-off threshold α_{out}, turn-on threshold α_{in}, and the identification current i_d^* are obtained empirically. Several laboratory measurements have been conducted to search for the minimum identification current for assuring a robust and fast identification. The tests have led to the selection of the identification current i_d^* equal to 3 A. Furthermore, α_{in} and α_{out} are selected independently for each coil. In Fig. 3.43, the phase shift angle variations versus the mutual inductance for two cases are shown. The first case is the normal condition of the system where the resistance seen from the transmitter is equal to the sum of the resistance of the transmitter coil and the reflected resistances of the receiver coil and the load. In the second case, the duty cycle of the DC-DC boost converter is equal to one and the receiver side is short circuit. In this case, the reflected resistance to the transmitter side is only composed of the resistance of the transmitter coil and the reflected resistance of the receiver coil to the transmitter side. According to Fig. 3.43 when the receiver side is short circuit, the input resistance increases much faster as coupling goes up and thus, the phase shift angle increases much more rapidly than the other case. This will help to detect the vehicle faster. From Fig. 3.43, it can be seen that the value of the mutual inductance is about 9 µH for the phase angle equal to 10 degrees.

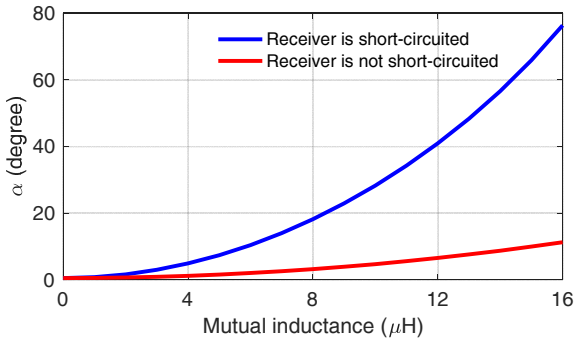

Fig. 3.43: Phase shift angle versus the variations of the mutual inductance when i_1^* is 3 A and V_{in} is 650V.

The advantage of this identification method is that the identification process is performed only with the available power electronics and without the use of any auxiliary components, sensors, or communication link between two sides. This simplifies the system and increases the operation speed. The time period from passing of the coil to detection and turning on the H-bridge converter is less than 10 ms and if the vehicle moves with the speed of 20 km/h, then the vehicle will be above the transmitter coil for about 270 ms. This time is much longer than the

necessary time for vehicle detection. The drawback of this method is that a small current must flow through the transmitter coils for detection function. The power losses during the identification process can be expressed according to the following equation as

$$P_{Loss\ D} = \sum_{i=1}^{N} R_{1i} i_d^{*2} \tag{3.50}$$

Where N is the number of the transmitter coils in the charging lane and R_{1i} are their related transmitter resistances. In order to reduce the identification losses, one solution is that only the first transmitter coil of the charging lane goes to the identification mode and the rest of the transmitter coils remain off. When the first transmitter coil identifies the vehicle, the next transmitter goes to the identification mode. This procedure continues to the end of the charging lane. In this case, the identification losses can be significantly reduced. It is worth noting that, in order to increase the efficiency of the identification process more, the transmitter coil goes to the identification mode with the frequency of 500 Hz. This frequency allows practically identifying the vehicle with a reasonable speed of 100 km/h.

3.6 Design considerations in dynamic charging

For the design of the power converter and control circuit, the steady-state relations can be used for some reasons. The main difference between the static and dynamic charging is the identification of the vehicle for the start and stop of the power transmission and the coupling variations. The time constant of the controller in the transmitter is selected much smaller than the speed of the vehicle. Thus, respect to the control speed, it can be considered as static operation. Furthermore, in the design of the transmitter, the application of the ferrite cores are avoided. For this reason, the variations of the coupling in dynamic charging do not effect on the resonant frequency of the converter. The worst case in dynamic charging is when the coupling is very low. By designing the converter and control in static charging in order to work in this condition, the control will have the same behavior in dynamic charging too. One issue in dynamic charging is that the energy that the battery receives during the dynamic charging depends on the speed of the vehicle. When the speed of the vehicle increases, the time that the vehicle is above the transmitter coil reduces and thus, lower energy will be received by the battery of the vehicle. Thus, the system can be designed for a certain maximum vehicle speed where at this speed, the minimum required energy can be received by the battery. Another issue to be considered for the design of the system during the dynamic charging is that the shape of the coils in segmented coil topology effects on the amount of received energy. There is an interspace between two adjacent coils in this system where the coupling is zero and no power is transferred to the battery. This interspace reduces the average power that the battery can receive during the

movement. For example, in this system, the length of the transmitter coil is 1.5 m and the interspace between two coils is 0.5 m and thus in rating power of 20 kW, the average power that the battery can receive is at most 75% of this power.

3.7 Conclusion

In this chapter, at first, the coil parameters according to the power rating, input voltage, output voltage, and air-gap were determined. The behavior of the coils during the lateral misalignment and air-gap variations is studied. Then, two control strategies for regulating the output power were proposed. Both control schemes were divided into two control circuits composed of the transmitter control and the receiver control. The control was able to regulate battery power from the receiver even in case of lateral misalignment but without the need to transmit the data between two sides. Also, in order to identify the presence of the vehicle, two control strategies were proposed. When the presence of the vehicle is detected, the control begins transferring power. Furthermore, at the moment that the vehicle leaves the transmitter the identification circuit stops transferring power.

Chapter 4

Simulation Results

In this chapter, a complete simulation of the whole WPT system in static and in dynamic charging is presented. The simulation is performed using PSIM software. The whole simulation circuit is composed of the power circuit, control circuit, and the coupling modeling during the movement. The simulation analysis helps to have a better understating of the system and to predict the outcome in a real dynamic charging system.

4.1 Construction of the simulation circuit

The simulated power circuit of the WPT system in PSIM software is presented in Fig. 4.1. For the H-bridge converter, MOSFET switches and for the boost converter IGBT switches are employed similar to the experimental setup. In the simulation environment, it is possible to model important parameters of the switches. For the MOSFET switches in the transmitter, the on-resistance of the switches, the on-resistance of the diodes, and the voltage threshold of the diodes can be defined. Furthermore, in order to model the MOSFET output capacitance, an additional capacitor is placed in parallel with each MOSFET. For the simulation of the IGBT switches in the receiver, the voltage drop and on-resistance of the IGBTs and on-resistance and the voltage drop of the diodes can be defined. The resistances of the transmitter and receiver coils are modeled with R_1 and R_2 in the simulation circuit, respectively. Furthermore, C_1 and C_2 are series compensation capacitors in the transmitter and receiver, respectively. The battery and the input DC-link source are modeled only with a simple DC voltage source. The coupled inductors are implemented in a separate sub-circuit as shown in Fig. 4.2. The self-inductances of the transmitter and receiver coils are defined as L_1 and L_2, respectively. By flowing current in the coil in each side, a voltage is induced in the other side and thus, the voltage across each coil depends on the current through this coil and the induced voltage from the other coil. By having the value of the mutual inductance between the two coils and the currents of the coils, the induced voltage and consequently the coupled inductor model is implemented.

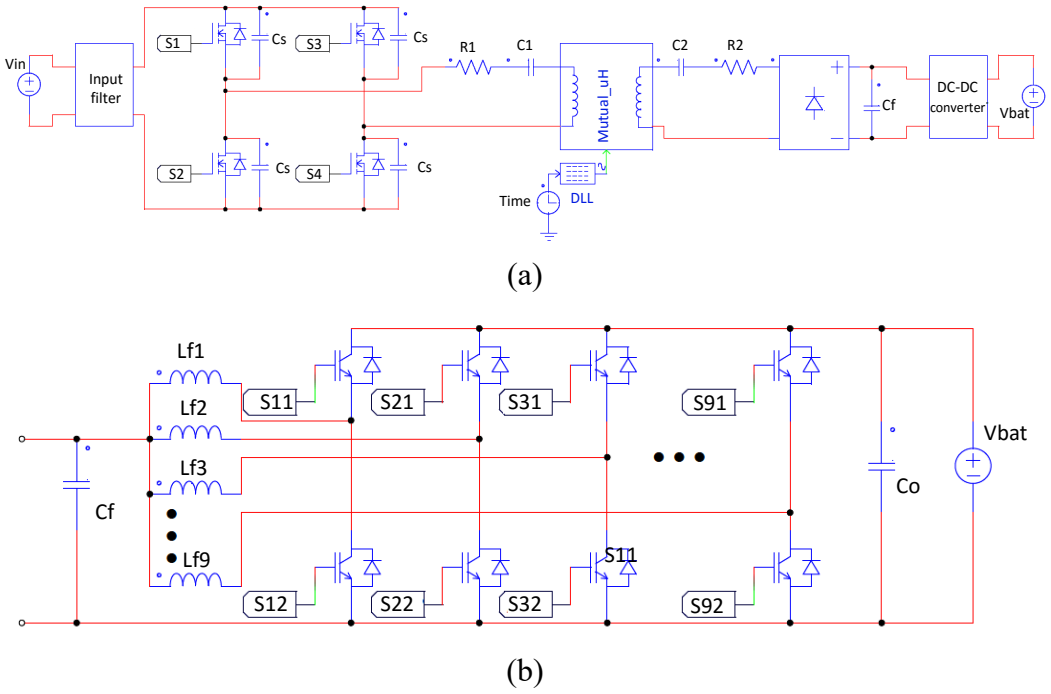

Fig. 4.1: Power circuit configuration. (a) Complete circuit, and (b) DC-DC converter power circuit.

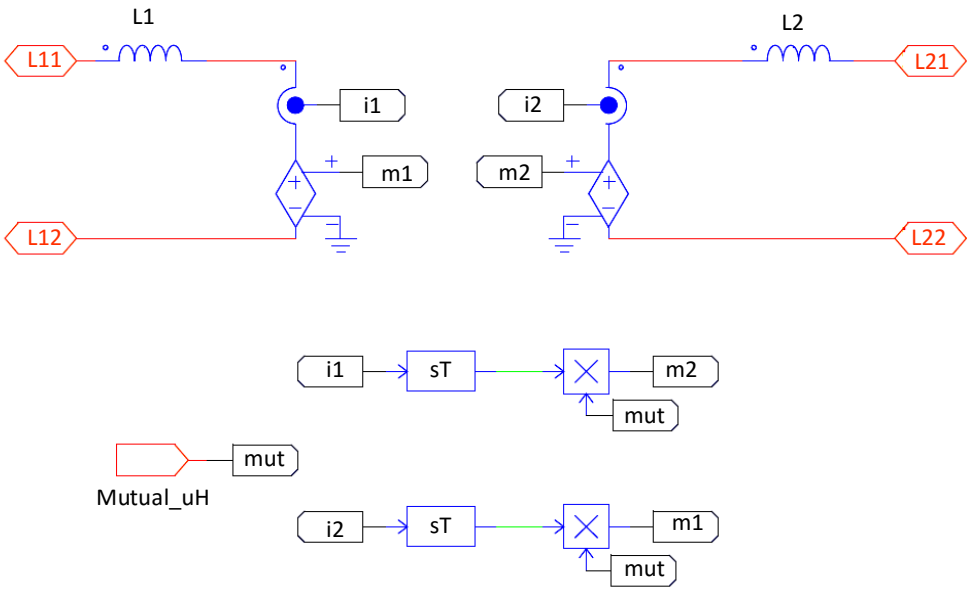

Fig. 4.2: Modeling of the coupled inductors.

The control of the WPT system is built by transmitter control and receiver control. The transmitter control is made up of the identification circuit and the current control based on the phase shift modulation scheme. The transmitter control circuit is shown in Fig. 4.3. The identification circuit is implemented in a C block in the PSIM software. The input of the C block is the phase shift angle and the output of it is the transmitter reference current. The phase shift angles for the identification of the vehicle are defined in this block. During the identification stage, the transmitter reference current is defined 3 A. When the presence of the

vehicle is identified, the reference current changes and the power transmission begins. The control circuit in the transmitter must follow the reference current generated by the detection circuit. For this purpose, a current control circuit is implemented using a PI controller. The output of this controller is the desired phase shift angle in degree according to the reference current and it is limited between 0 and 180°.

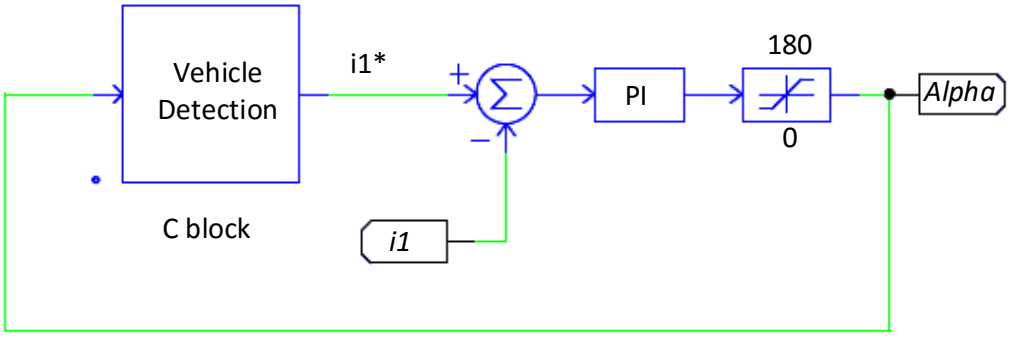

Fig. 4.3: Load detection circuit and the transmitter current controller.

The phase shift modulation circuit generates the H-bridge converter gating signals according to the phase shift angle as depicted in Fig. 4.4. The square wave source is used for the switching of the first leg of the DC-AC converter (V_{g1}). The second leg of the DC-AC converter must be shifted from the first leg according to the value of the phase shift angle. The shifted pulse is generated using two monostable multivibrators. One of the monostable multivibrators has an adjustable width which its width varies according to the phase shift angle. The other monostable multivibrator has a constant pulse width equal to the half of the switching period. The output of the second monostable multivibrator is used for the switching of the second leg of the DC-AC converter (V_{g2}).

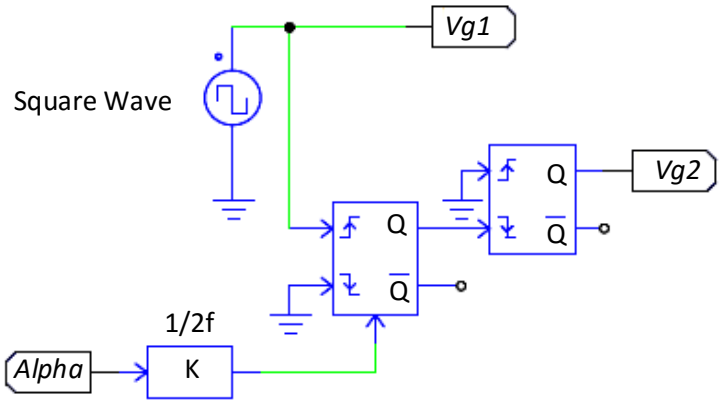

Fig. 4.4. Construction of the phase shift modulation scheme.

The generated signals from the phase shift modulation circuit are used for the switching of the H-bridge converter. For this purpose, these signals are applied to the dead time generator circuits and finally, the gating signals for all switches of the H-bridge converter are generated as illustrated in Fig. 4.5.

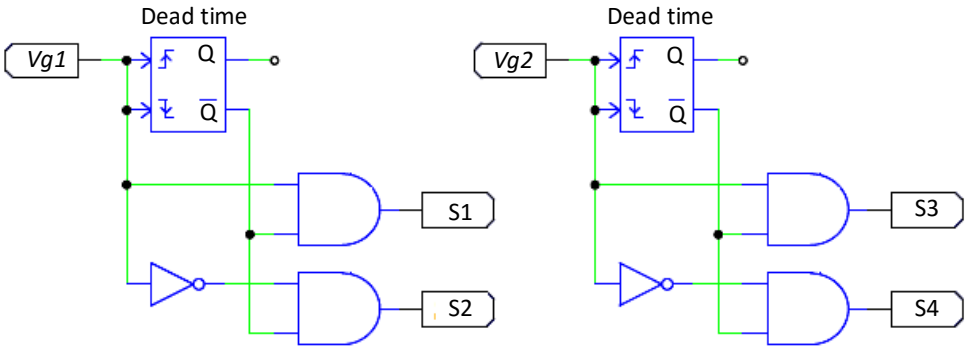

Fig. 4.5: Dead time generator circuit for the transmitter converter.

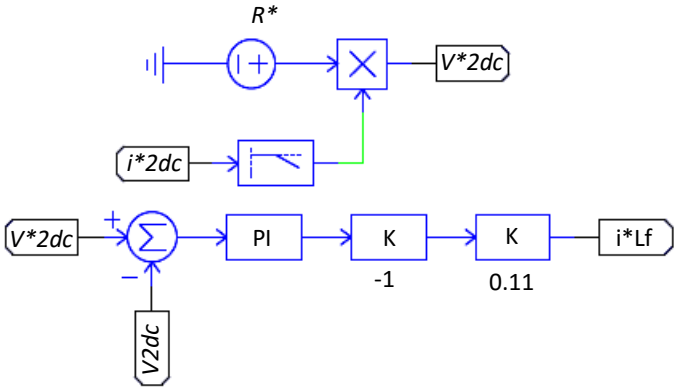

Fig. 4.6: Voltage loop circuit of the receiver control.

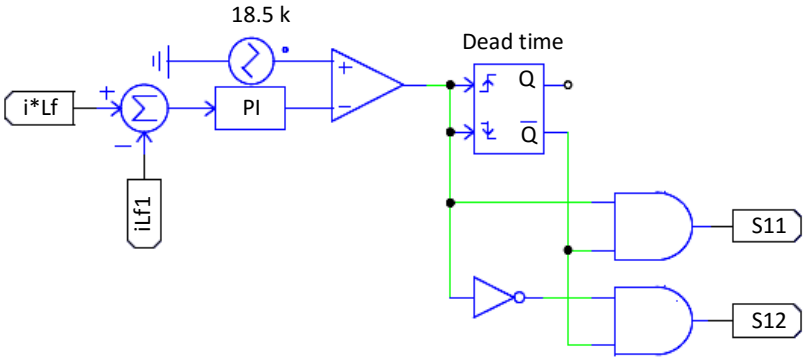

(a)

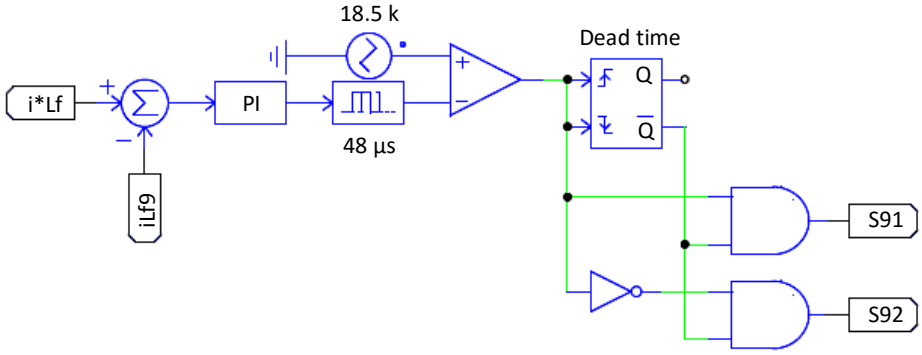

(b)

Fig. 4.7: Current loop circuit of the receiver control. (a) Control of the first leg of the DC-DC converter, (b) control of the ninth leg of the DC-DC converter.

The control in the receiver is made up of the voltage loop and the current loop. The voltage loop circuit is the outer loop of the control as illustrated in Fig. 4.6. The reference voltage is constructed by measuring the receiver DC current and multiplying it by the reference resistance. The receiver reference DC voltage is compared with the measured receiver DC voltage and the output goes to a PI controller. Finally, the reference DC current for each phase of the DC-DC converter is constructed. The current loop is presented in Fig. 4.7. Due to the limited space, only the current loops for two phases of the DC-DC converter are depicted. The difference between the reference current and the phase current is calculated and the result goes through a PI controller. The output of the PI controller is compared with the triangle source and after the dead time generator circuit, the gating signals for each phase are obtained.

The simulation parameters are shown in Table 4.1. The nominal transmitter current is 35 A. According to the control scheme, the battery power is regulated from the receiver. However, the transmitter reference current can be reduced in order to limit the transmitting power from the ground. The value of the mutual inductance at the rated air-gap of 25 cm and without any lateral misalignment is equal to 14.3 μH as calculated in chapter 3. When the air-gap changes or the lateral misalignment in x-direction and y-direction increases, the value of the mutual inductance varies. The shape of the mutual inductance during the passage of the receiver coil over two transmitter coils was obtained in chapter 3. According to this simulation, the mutual inductance behavior for the complete charging lane with several transmitter coils is built [171]. The simulation waveforms for different vehicle speeds of 10, 30 and 50 km/h are shown in Fig. 4.8. As shown in this figure, variations of the mutual inductance versus time depend on the speed of the vehicle.

Table 4.1: Specifications and parameters of the simulated circuit.

Parameter	**Value**	**Unit**
Transmitter self-inductance, L_1	280	μH
Transmitter resistance, R_1	0.78	Ω
Transmitter capacitor, C_1	12.5	nF
Receiver self-inductance, L_2	120	μH
Receiver resistance, R_2	0.53	Ω
Receiver capacitor, C_2	29.2	nF
Mutual inductance (nominal), M_n	14.3	μH
Input DC voltage, V_{in}	650	V
Battery voltage, V_{bat}	250-400	V
Transmitter maximum current, $i_{1\text{-}max}$	35	A
Operating frequency, f	85	kHz
Output filter capacitor, C_f	8	μF
Input filter inductor	2	μH
Input filter capacitor	16	μF
Boost converter inductors, L_{fi}	1	mH

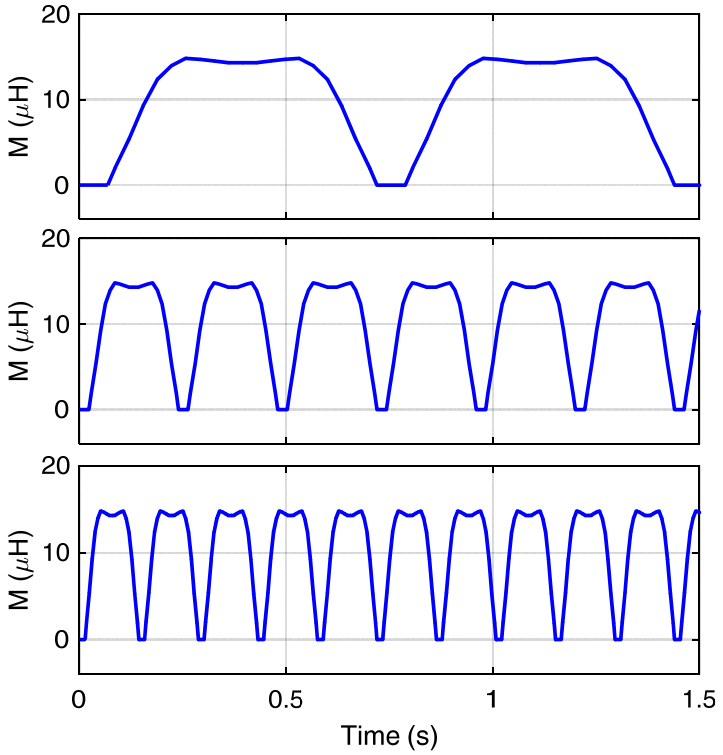

Fig. 4.8: Mutual inductance variations at different vehicle speeds. Top: 10 km/h, middle: 30 km/h, and bottom: 50 km/h.

4.2 Simulation of the dual side control

The control of the WPT system is made up of the transmitter control and the receiver control. The transmitter control duty is limiting the transmitter current during the misalignment conditions and the receiver control duty is regulating the battery power from the receiver. These controls work together but without any communication with each other. The performance of the control system during different resistances, misalignment conditions, and operating frequencies are evaluated by the simulation.

4.2.1 Operation at different resistances

The control of the output power by variations of the reference resistance R_{in} is analyzed. The simulation parameters are similar to the values of Table 4.1. In this simulation, the transmitter reference current is 35 A, the battery voltage is 400 V and the mutual inductance is constant and at the rated value of 14.3μH. The important waveforms of the system versus the variations of R_{in} are presented in Fig. 4.9. Since the input DC voltage is 650 V and the transmitter maximum current is 35 A, the reference resistance for the maximum output power can be determined according to (3.15) by

$$R_{in-Pmax} = \frac{\pi^2}{8}\left(\frac{(2\times\pi\times 85000\times 14.3\times 10^{-6})^2}{\frac{2\sqrt{2}\times 650}{\pi\times 35}-0.78}-0.53\right) = 3.86\,\Omega \quad (4.1)$$

At the rated mutual inductance and when R_{in} is smaller than 3.86 Ω, the phase shift angle and the transmitter voltage are maximum. According to Fig. 4.9(e), when R_{in} is zero, the duty cycle of the DC-DC converter is maximum and the receiver is short circuit. By increasing R_{in} from zero, the duty cycle of the DC-DC converter becomes less than one and the receiver voltage increases. Thus, the transmitter current rises and the input power and consequently the output power increase as shown in Fig. 4.9(c). By increasing R_{in} more, the transmitter current and the output power increase more. This variation is approximately linear. When R_{in} reaches 3.86 Ω, the transmitter current and the transmitter voltage values are maximum. This means that the maximum power of 16.6 kW is transferred to the output. When R_{in} is between zero and 3.86 Ω, the value of α is maximum and the DC-AC converter can operate in zero voltage switching condition which causes improving the efficiency of the transmitter. The output power reduces when R_{in} goes beyond 3.86 Ω. It is clear from Fig. 4.9(c) that the variation of the output power is not linearly but hyperbolically. When R_{in} becomes more than 3.86 Ω, the transmitter current tends to increase. However, the transmitter current cannot go beyond the maximum current and the transmitter control by reducing the transmitter voltage with the reduction of the phase shift angle keeps it at the peak level. Thus, the transmitter converter cannot operate in soft switching conditions anymore which will cause the increase of the transmitter converter losses. In this region, the transmitter current is kept constant at peak level and for this reason, the receiver voltage remains approximately constant. The efficiency waveform the system versus the variations of R_{in} is illustrated in Fig. 4.9(f). When R_{in} is very small, the system efficiency is relatively low since a great amount of the power transferred to the receiver will be dissipated in the receiver resistance R_2. As R_{in} increases, the system efficiency significantly improves. For a WPT system, in each mutual inductance and switching frequency, there is one R_{in} in which the efficiency of the system becomes maximum. At rated condition, this resistance is obtained 7.79 Ω using (2.52). If the resistance becomes more than this value, the reflected impedance to the transmitter side becomes very small and R_1 dissipates a great amount of power which results in a reduction of the efficiency.

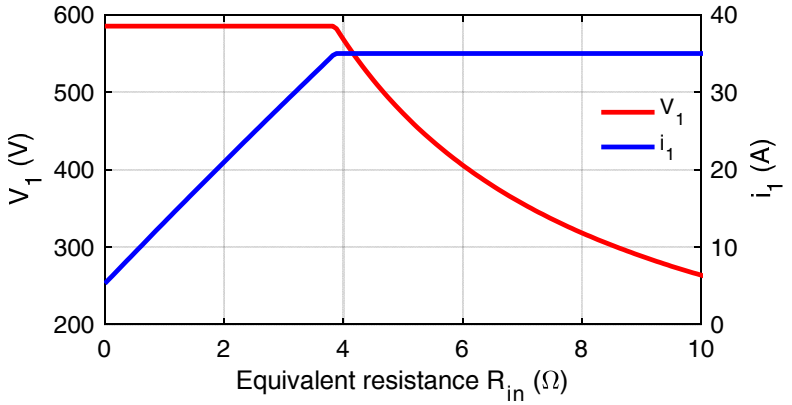
600
500
400
300
200
40
30
20
10
0
0
2
4
6
8
10
V1 (V)
i1 (A)
V1
i1
Equivalent resistance Rin (Ω)

(a)

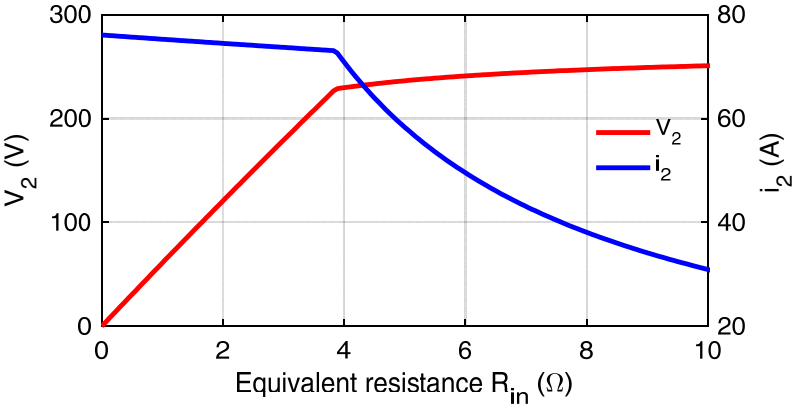
300
200
100
0
80
60
40
20
0
2
4
6
8
10
V2 (V)
i2 (A)
V2
i2
Equivalent resistance Rin (Ω)

(b)

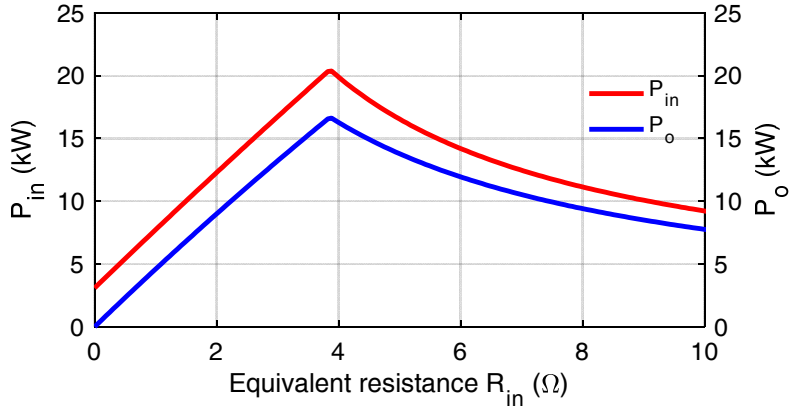
25
20
15
10
5
0
0
2
4
6
8
10
Pin (kW)
Po (kW)
Pin
Po
Equivalent resistance Rin (Ω)

(c)

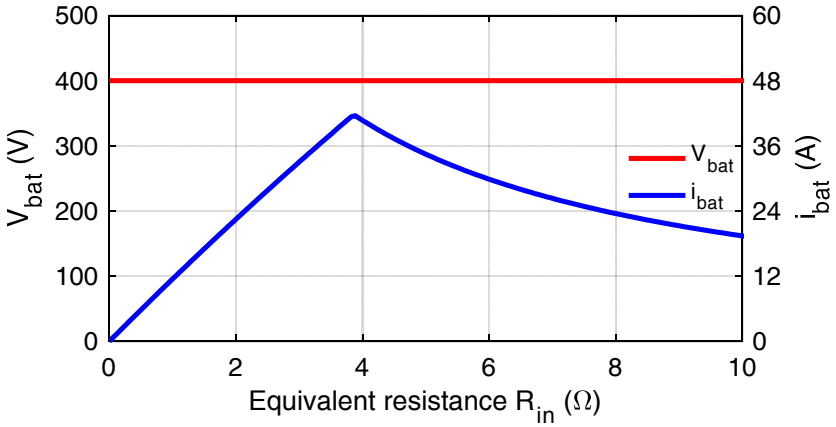
500
400
300
200
100
0
60
48
36
24
12
0
0
2
4
6
8
10
Vbat (V)
ibat (A)
Vbat
ibat
Equivalent resistance Rin (Ω)

(d)

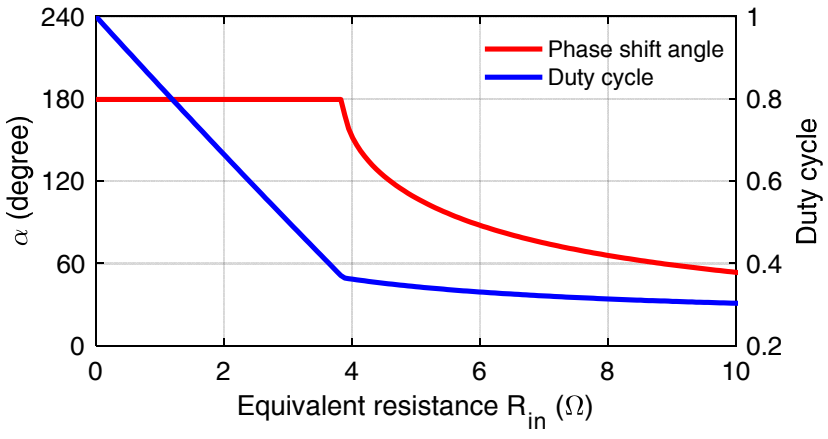

(e)

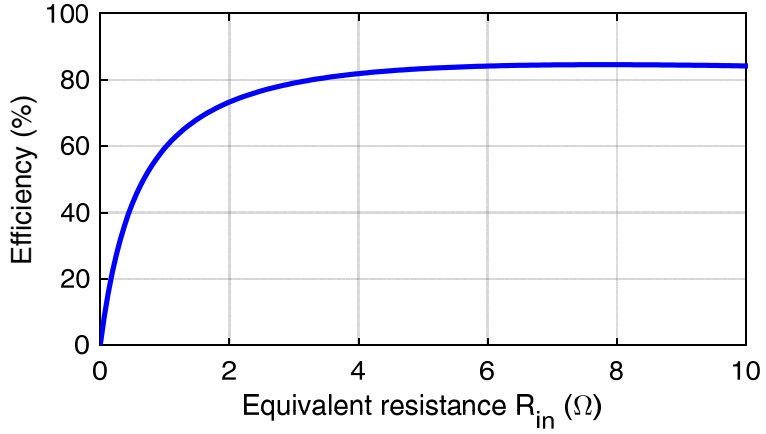

(f)

Fig. 4.9: Performance of different variables under variations of the resistance at the input of the DC-DC converter. (a) V_1 and i_1, (b) V_2 and i_2, (c) V_{bat} and i_{bat}, (d) P_{in} and P_o, (e) Phase shift angle α and duty cycle D, and (f) Efficiency.

4.2.2 Operation at different mutual inductances

The operation of the proposed control method during the variations of the mutual inductance is investigated. The simulation parameters are similar to the previous simulation. However, R_{in} has remained constant at the value of 3.86 Ω but the mutual inductance varies. The important waveforms of the system versus variations of the mutual inductance with dual side control are presented in Fig. 4.10. According to Fig. 4.10(c), when the mutual inductance is at the rated value, the maximum output power can be obtained. When the mutual inductance becomes less than the rated mutual inductance due to the misalignment or increase of the air-gap, the transmitter current becomes limited at the maximum level of 35 A by reducing the transmitter voltage as illustrated in Fig. 4.10(a). It is clear from Fig. 4.10(e) that the phase shift angle is reduced in order to control the transmitter voltage and keep the transmitter current at the maximum level. In this condition, the transmitter power and consequently the receiver power drop down.

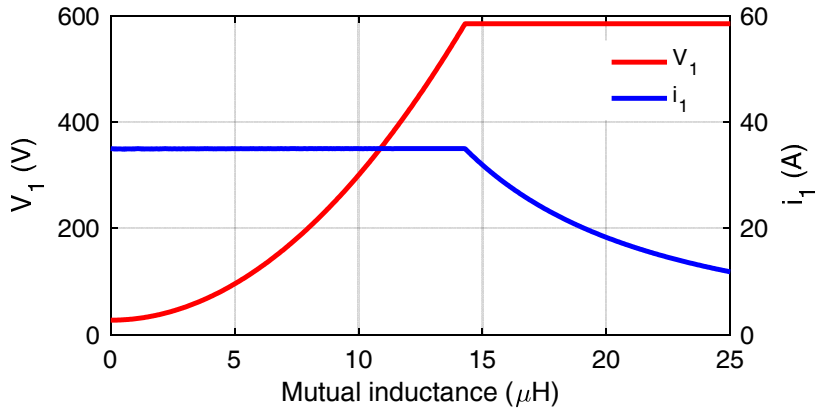
600
400
200
0
60
40
20
0
0
5
10
15
20
25
V1
i1
V1 (V)
i1 (A)
Mutual inductance (μH)

(a)

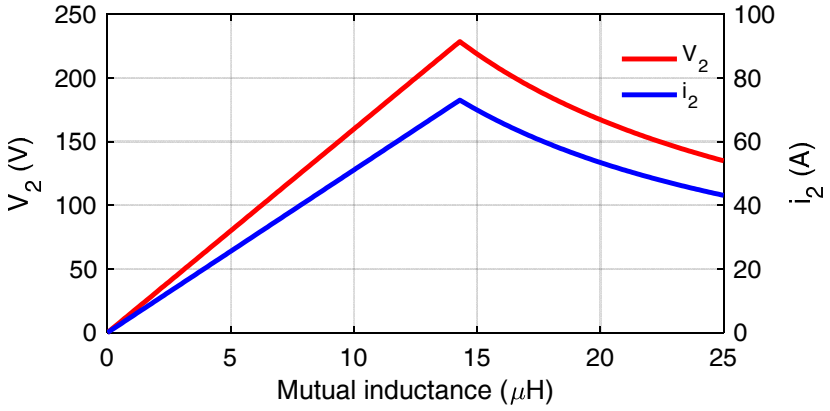
250
200
150
100
50
0
100
80
60
40
20
0
0
5
10
15
20
25
V2
i2
V2 (V)
i2 (A)
Mutual inductance (μH)

(b)

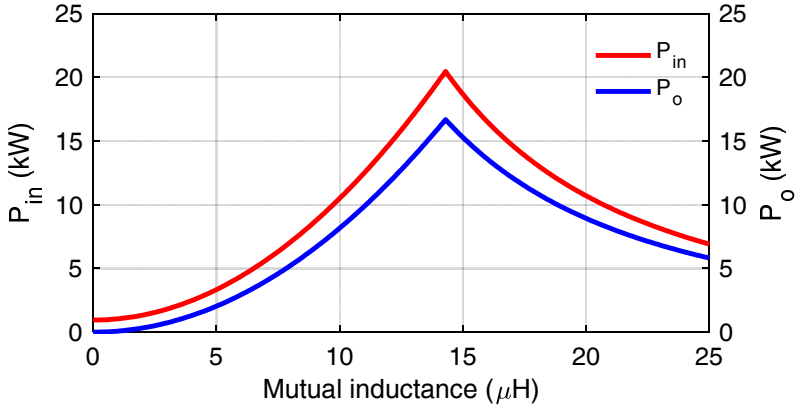
25
20
15
10
5
0
25
20
15
10
5
0
0
5
10
15
20
25
Pin
Po
Pin (kW)
Po (kW)
Mutual inductance (μH)

(c)

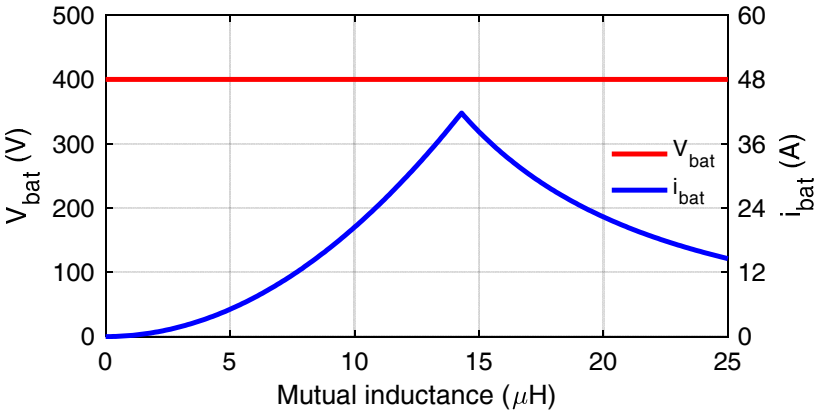
500
400
300
200
100
0
60
48
36
24
12
0
0
5
10
15
20
25
Vbat
ibat
Vbat (V)
ibat (A)
Mutual inductance (μH)

(d)

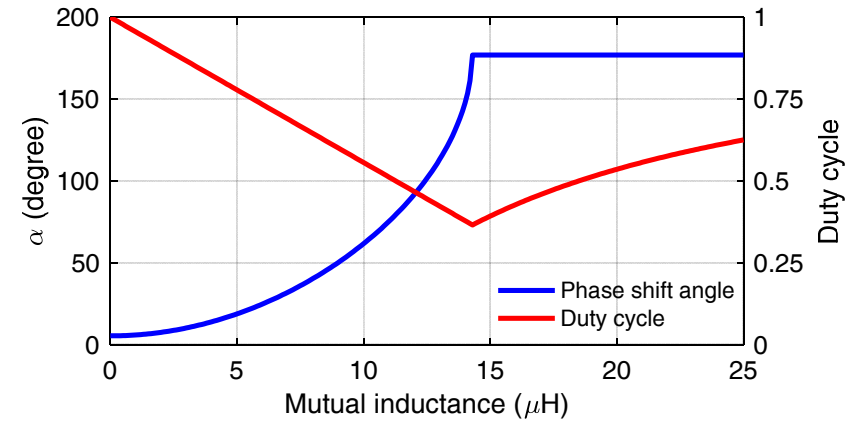

(e)

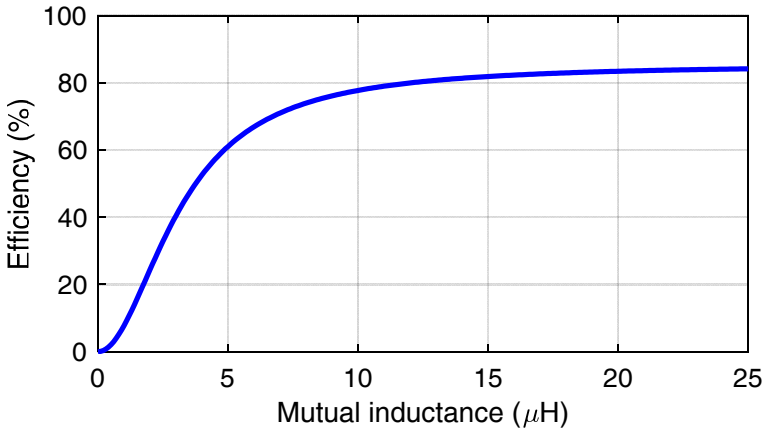

(f)

Fig. 4.10: Performance of different variables of the WPT system under variations of the mutual inductance. (a) V_1 and i_1, (b) V_2 and i_2, (c) V_{bat} and i_{bat}, (d) P_{in} and P_o, (e) Phase shift angle α and duty cycle D, and (f) Efficiency.

When the mutual inductance becomes more than the rated mutual inductance due to the reduction of the air-gap between coils, the transmitter current decreases. This reduction is due to the characteristic of series-series compensation topology where the input impedance goes up with the increase of the mutual inductance. In this condition, the phase shift angle is at the maximum level and the transmitter voltage cannot increase more. Thus, the transmitter current reduces by the increase of M. Therefore, the transmitter power reduces and consequently, P_o goes down. The efficiency waveform of the system with dual side control is presented in Fig. 4.10(f). It is clear that the efficiency goes up as the mutual inductance increases.

4.2.3 Operation at different frequencies

The operation of the control circuits at both sides with the variations of the operating frequency is analyzed.

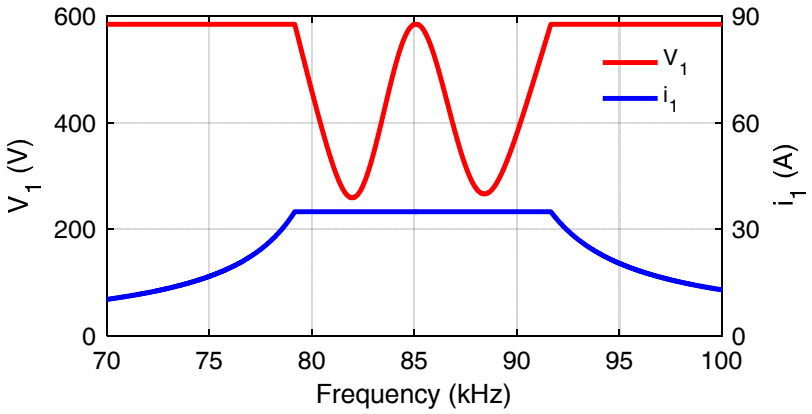
600
400
200
0
90
60
30
0
70
75
80
85
90
95
100
Frequency (kHz)
V1 (V)
i1 (A)
V1
i1

(a)

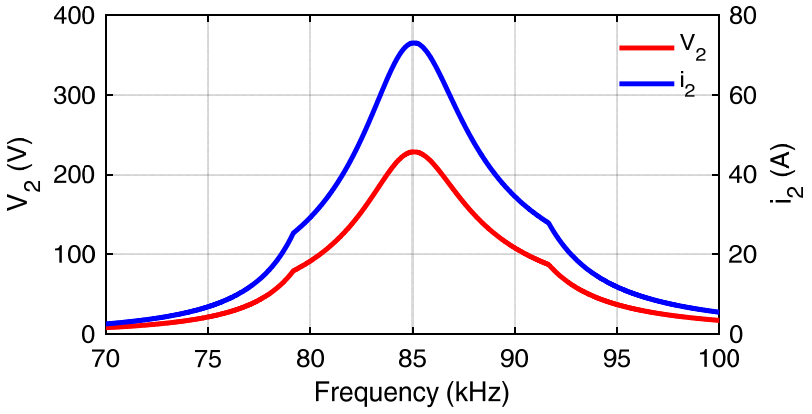
400
300
200
100
0
80
60
40
20
0
70
75
80
85
90
95
100
Frequency (kHz)
V2 (V)
i2 (A)
V2
i2

(b)

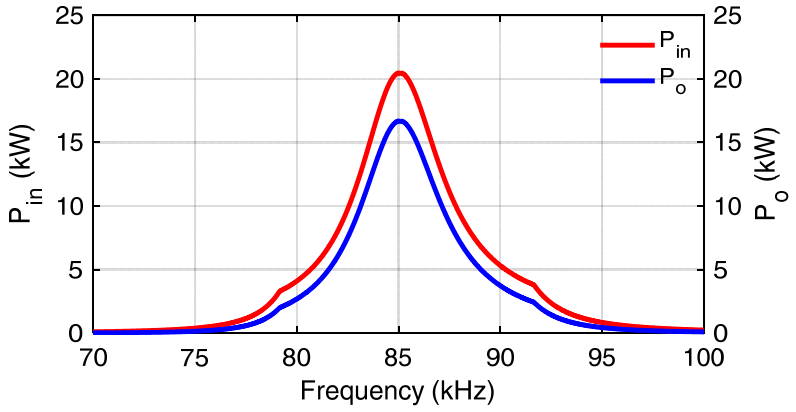
25
20
15
10
5
0
25
20
15
10
5
0
70
75
80
85
90
95
100
Frequency (kHz)
Pin (kW)
Po (kW)
Pin
Po

(c)

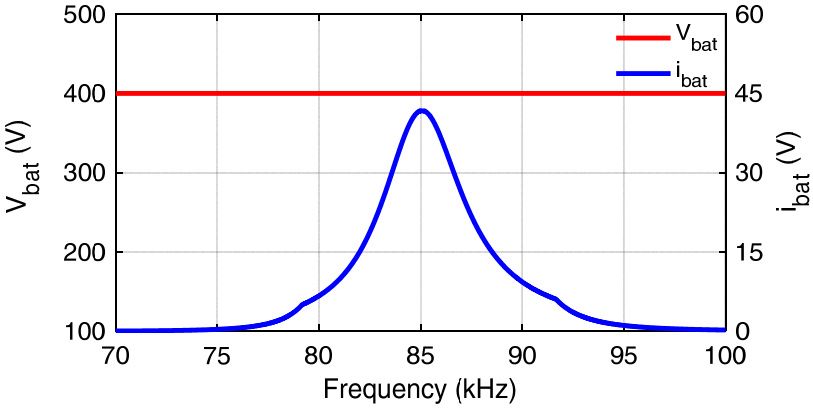
500
400
300
200
100
60
45
30
15
0
70
75
80
85
90
95
100
Frequency (kHz)
Vbat (V)
ibat (V)
Vbat
ibat

(d)

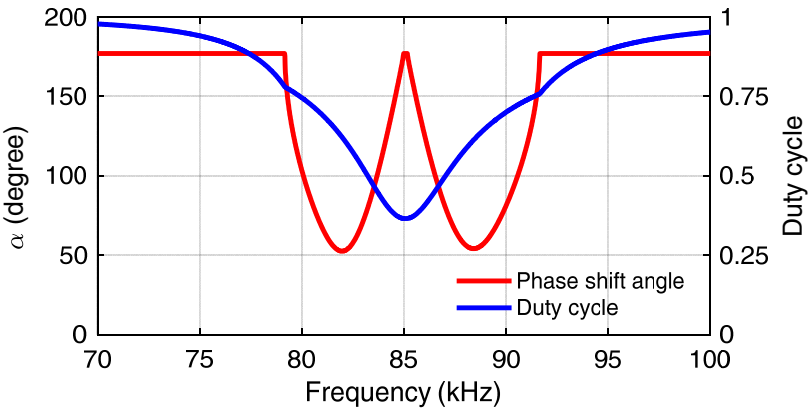

(e)

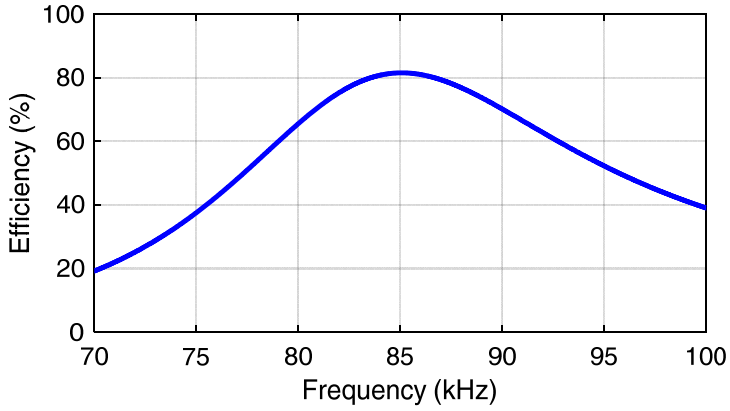

(f)

Fig. 4.11: Performance of different variables under variations of the frequency. (a) V_1 and i_1, (b) V_2 and i_2, (c) V_{bat} and i_{bat}, (d) P_{in} and P_o, (e) Phase shift angle α and duty cycle D, and (f) Efficiency.

The simulation parameters are similar to the previous simulations. R_{in} and M are remained constant at the rated values of 3.86 Ω and 14.3 μH, respectively. However, the operating frequency of the DC-AC converter changes. In the case that no control is applied to the transmitter, the voltage at the output of the DC-AC converter is always maximum. Therefore, the current of the transmitter can increase without any restriction. i_1 waveform versus frequency is similar to a double-peak waveform which is because of the system natural characteristic. The peak of the efficiency is at the resonant frequency and the DC-AC converter should operate at this frequency. But, due to the variations of the resonant elements such as coils or capacitors, the resonant frequency may change. When the operating frequency of the DC-AC converter becomes less or more than the resonant frequency, i_1 increases and becomes more than the value at the resonant frequency. Therefore, in order to keep the current of the transmitter at the peak value and protect the DC-AC converter against any overcurrent condition in case of frequency variations, control is necessary at the transmitter.

Fig. 4.11 illustrates the performance of different variables over the operating frequency variations. As shown in Fig. 4.11(a), the maximum current of the transmitter is 35 A and the transmitter current cannot increase more than this level.

It can be seen from Fig. 4.11(c) that the output power curve has one peak which is happened at the resonant frequency. The efficiency waveform versus the frequency is illustrated in Fig. 4.11(f).

4.3 Operation during the dynamic charging

The simulation results of the complete WPT system in dynamic charging and at different conditions are presented. The performance of different parameters of the system in dynamic charging at 11 kW output power is illustrated in Fig. 4.12.

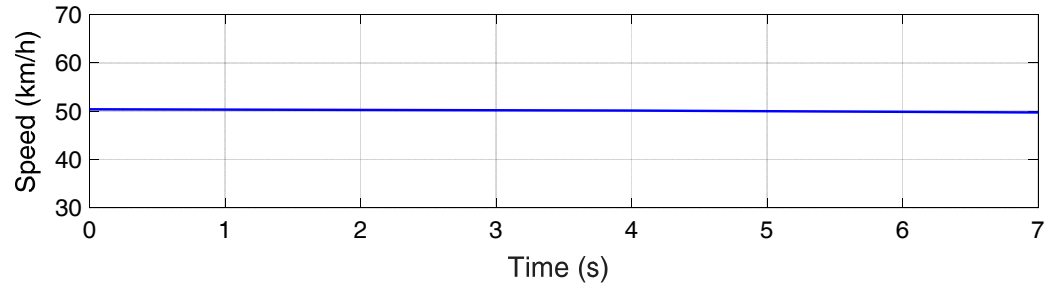

(a)

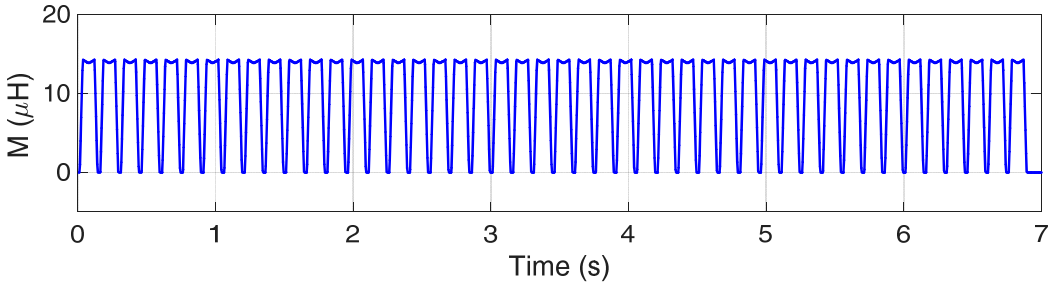

(b)

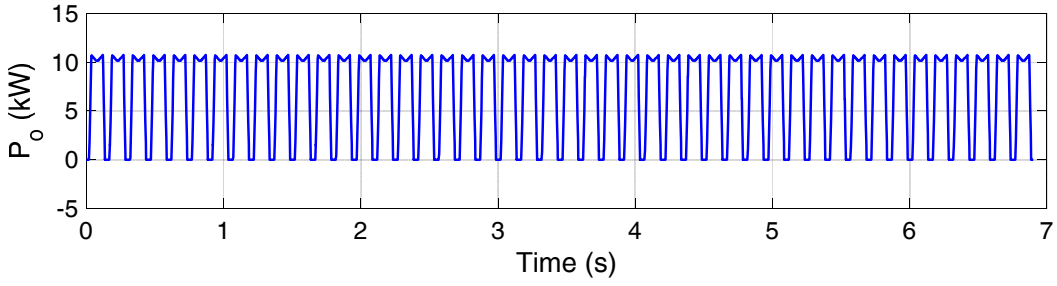

(c)

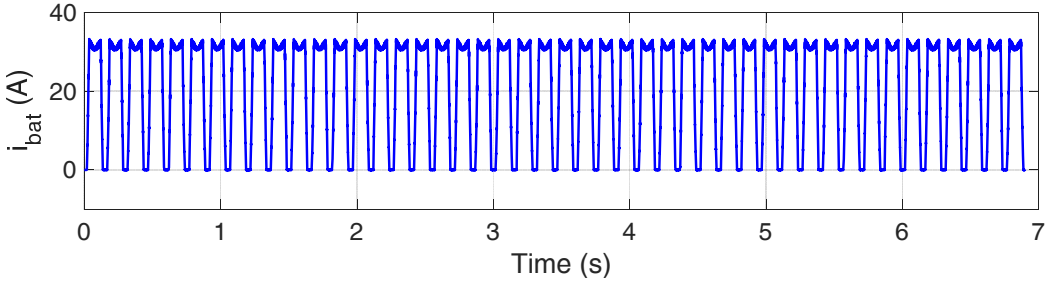

(d)

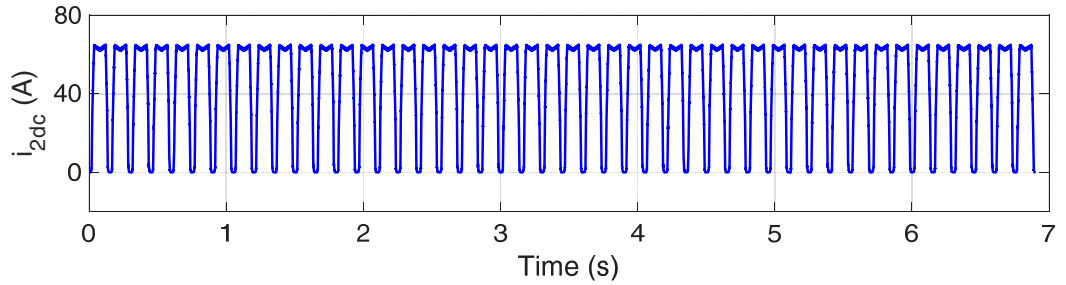

(e)

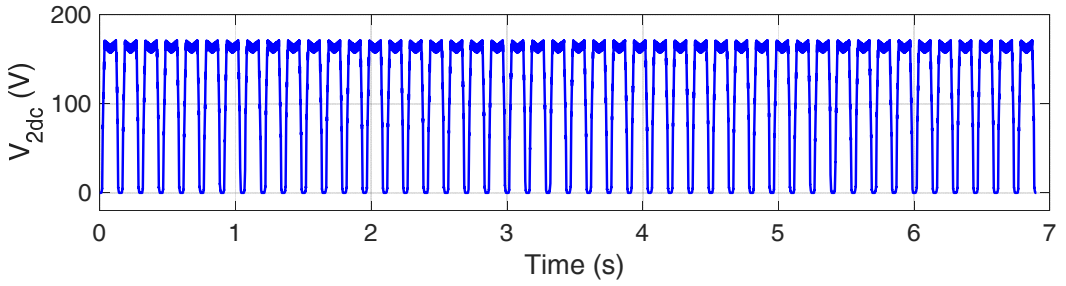

(f)

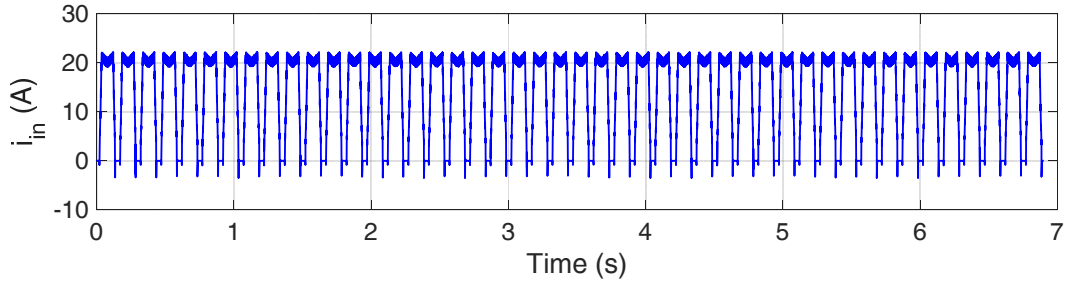

(g)

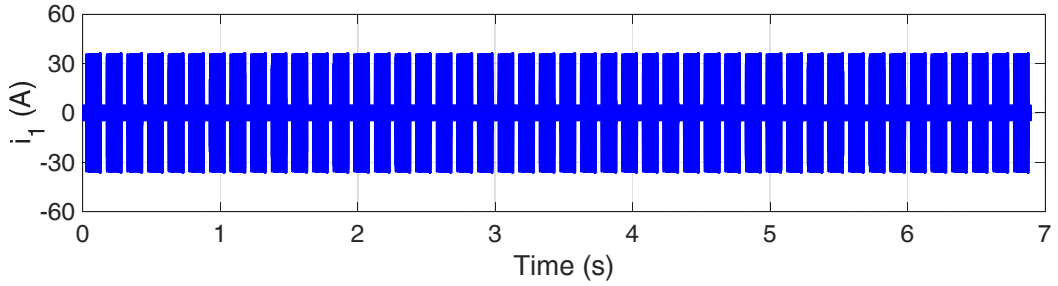

(h)

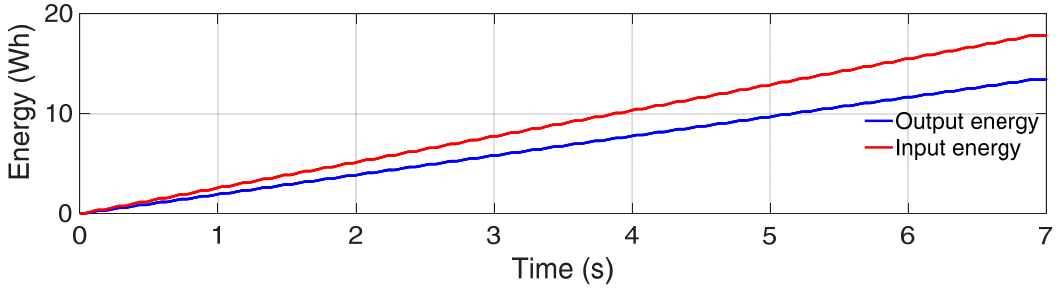

(i)

Fig. 4.12: Different quantities of the system during dynamic charging with the maximum output power of 11 kW. (a) Vehicle speed, (b) mutual inductance, (c) received power by the battery, (d) battery current, (e) receiver DC current, (f) receiver DC voltage, (g) input DC source current, (h) transmitter current, (i) received energy by the battery during the whole charging process.

The parameters of this simulation are the same as the parameters of the previous simulations but the values of i_1^* and R_{in} are set at 25 A and 2.5 Ω, respectively. In this case, the battery receives the power of 11 kW. Also in this simulation, the battery voltage is fixed at 330 V. During this test, the speed of the vehicle is kept constant at 50 km/h. Furthermore, the transmitter and receiver are perfectly aligned with the air-gap equal to 25 cm.

The waveform of the vehicle speed is presented in Fig. 4.12(a). The vehicle speed is fixed at 50 km/h. With this speed, the whole charging process takes about 7 seconds. When the vehicle passes over the transmitter coil, at first the mutual inductance increases and when the vehicle leaves the transmitter coil, the mutual inductance reduces until it reaches zero. It can be seen from Fig. 4.12(c) that the output power waveform is similar to the behavior of the mutual inductance. When the mutual inductance is maximum, power of 11 kW is received by the battery however in zero coupled region, the output power is zero. The average power received by the battery during the passage of the vehicle overall transmitter coils is approximately 7.3 kW. This value is about 66 % of the demanded power. The waveform of the receiver DC current is illustrated in Fig. 4.12(e). It is clear from this figure that the current ripple is remarkably low. The input DC current waveform at the ground side is shown in Fig. 4.12(g). Due to the input filter placed before the H-bridge converter and after the input DC source, the effect of high-frequency switching of the H-bridge converter is properly filtered. The waveform of the transmitter current is shown in Fig. 4.12(h). When M is zero, the H-bridge converter operates in detection mode and a constant current of 3 A is flowing in the transmitter coil. When the mutual inductance increases gradually, the phase shift angle changes and the transmitter control identifies the presence of the receiver coil. The transmitter reference current changes from 3 A to 25 A. In the same way, when the receiver coil leaves the transmitter coil, the transmitter control stops the power transmission and the identification for the next coil begins. It can be seen from Fig. 4.12(i) that at the beginning of the simulation, the input and output energies are zero but when the vehicle passes over the transmitter coils, the energy received by the battery and the input energy increase. When the charging process ends, the total amount of the received energy by the battery is about 13.42 Wh. Also, the amount of input energy is obtained equal to 17.84 Wh. The efficiency of the whole charging process is calculated by the ratio of the input energy and output energy. For this simulation, the total efficiency is obtained at around 75%.

The transmitter current and voltage waveforms in dynamic condition and during the passage of the EV over coils are shown in Fig. 4.13. When the coupling is zero, the transmitter current is only 3 A. This current only flows through the transmitter coil. The equivalent resistance at the output of the DC-AC converter is only the resistance of the transmitter coil. The DC link voltage is 650 V and the resistance of the transmitter is 0.78 Ω. Thus, the H-bridge output voltage must be very low in order to be able to keep the current of 3 A in the transmitter coil.

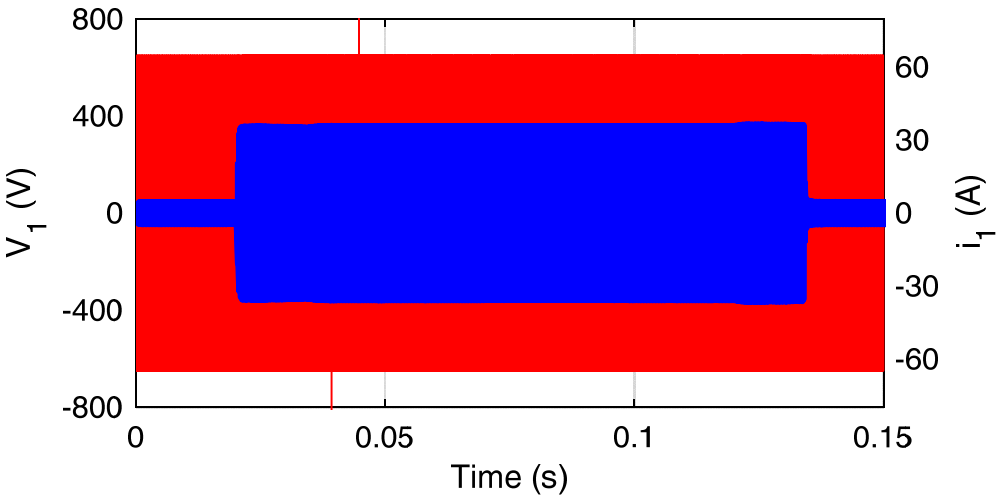

(a)

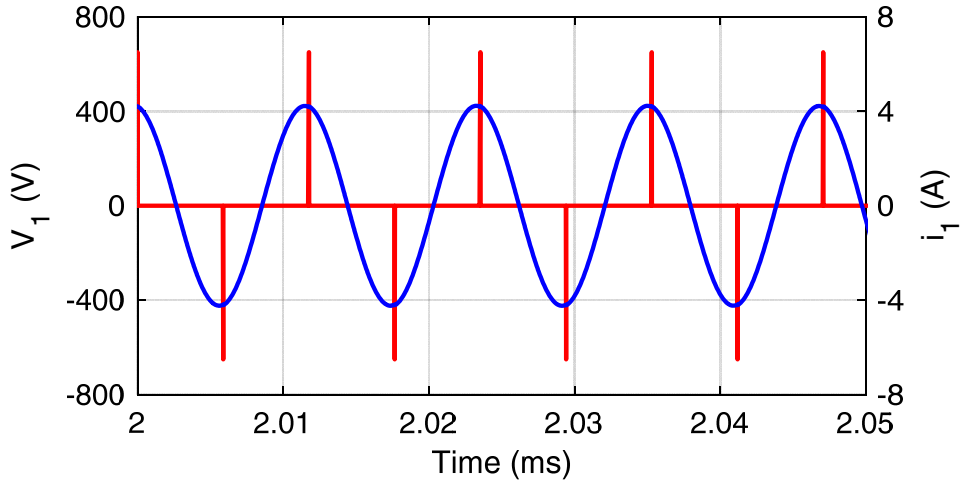

(b)

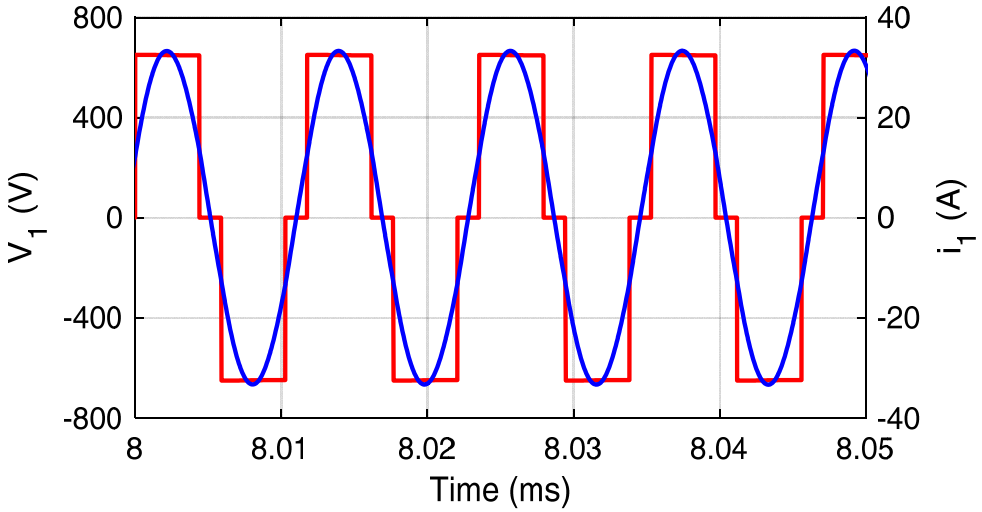

(c)

Fig. 4.13: Transmitter voltage and current with the output power of 11 kW and at the speed of 50 km/h. (a) During the passage of the vehicle, (b) during the identification process, and (c) during the power transmission.

After the vehicle detection, the transmitter reference current ramps up gradually until it reaches 25 A. The transmitter coil keeps this current constant even in case of any misalignment. When the receiver goes away, the coupling coefficient goes down and the transmitter control stops the power transmission. Then, the transmitter enters the identification mode again.

Several tests have been done in order to evaluate the performance of the WPT system in various charging conditions. The results of the tests are presented in Table 4.2, Table 4.3 and Table 4.4. Table 4.2 shows the results of the test during the dynamic charging at different vehicle speeds and different lateral misalignments when the air-gap is fixed at 25 cm. The tests have been done for two output powers of 15 kW and 7 kW. The resistance R_{in} is kept constant at 3.88 Ω which is equal to $R_{in\text{-}Pmax}$. In order to have the output power of 15 kW and 7kW, the transmitter current is fixed at 34 A and 23.3 A, respectively. The maximum efficiency is obtained by 80%. This efficiency is unchanged for different speeds of the vehicle. The average received power for the speed of 50 km/h is 10.39 kW. This power is for the condition when the demanded power for the speed of 50 km/h and without any lateral misalignment, the energy received by the battery is 19.13 Wh. This energy is proportional to vehicle speed. When the vehicle speed is reduced to 30 km/h and 10 km/h, the battery energy is increased to 31.88 Wh and 95.65 Wh, respectively. When the lateral misalignment increases, the received energy and the efficiency decrease. When the lateral misalignment is 10 cm, the efficiency variation is not significant. However if the lateral misalignment increases more, the efficiency drops rapidly. Similar tests have been done when the air-gap changes. The results for the condition when the air-gap is decreased to 20 cm are presented in Table 4.3. Furthermore, the results when the air-gap is increased to 30 cm are presented in Table 4.4. For the air-gap of 20 cm, the efficiency of the system increases. For the condition without the lateral misalignment, the efficiency has reached 81% for the 15 kW output power. This efficiency has reached to 81.3% for 7 kW output power and without any lateral misalignment. For the air-gap of 30 cm, the efficiency has dropped down to 78% when there is no lateral misalignment. Furthermore, for 20 cm of lateral misalignment, the efficiency has dropped down to 69.1 %.

The effect of vehicle speed on the received energy at two power levels when air-gap is 25 cm is illustrated in Fig. 4.14. When the vehicle speed is low, the receiver coil is above the transmitter coils in much more time and the battery can receive much more energy. For the speed of 10 km/h, the total charging process takes about 33 seconds but with the vehicle speed of 50 km/h, the total charging process takes about 6.6 seconds. The effect of lateral misalignment on the received energy by the battery for the output power of 15 kW at different vehicle speeds are illustrated in Fig. 4.15. At all vehicle speeds and in nominal air-gap, the received energy by the battery reduces as the lateral misalignment increases.

Table 4.2: Evaluation of the charging process in dynamic mode and at different conditions when air-gap is 25 cm.

Speed (km/h)	i_1 limit (A)	Misalig-nment (cm)	Battery energy (Wh)	Input energy (Wh)	Average battery power (kW)	Efficiency (%)
50	34	0	19.13	23.94	10.39	80
50	34	10	14.91	18.96	8.10	78.6
50	34	20	7.30	9.97	3.96	73
30	34	0	31.88	39.9	10.39	80
30	34	10	24.85	31.6	8.10	78.6
30	34	20	12.17	16.62	3.96	73
10	34	0	95.65	119.7	10.39	80
10	34	10	74.55	94.8	8.10	78.6
10	34	20	36.5	49.85	3.96	73
50	23.3	0	8.98	11.4	4.88	79
50	23.3	10	6.99	8.89	3.79	78.5
50	23.3	20	3.42	4.66	1.85	73.4
30	23.3	0	15.13	18.94	4.93	80
30	23.3	10	11.65	14.82	3.79	78.6
30	23.3	20	5.7	7.76	1.85	73.3
10	23.3	0	45.39	56.82	4.93	80
10	23.3	10	34.95	44.45	3.79	78.6
10	23.3	20	17.1	23.28	1.85	73.4

Table 4.3: Evaluation of the charging process in dynamic mode and at different conditions when air-gap is 20 cm.

Speed (km/h)	i_1 limit (A)	Misalig-nment (cm)	Battery energy (Wh)	Input energy (Wh)	Average battery power (kW)	Efficiency (%)
50	34	0	16.71	20.62	9.08	81
50	34	10	19.73	24.56	10.72	80.3
50	34	20	10.5	13.74	5.70	76.4
30	34	0	27.85	34.36	9.08	81
30	34	10	32.88	40.93	10.72	80.3
30	34	20	17.5	22.9	5.70	76.4
10	34	0	83.55	103.1	9.08	81
10	34	10	98.65	122.8	10.72	80.3
10	34	20	68.7	83.55	5.70	76.4
50	23.3	0	12.89	15.86	7	81.3
50	23.3	10	10.05	12.51	5.46	80.3
50	23.3	20	4.93	6.45	2.68	76.4
30	23.3	0	21.48	26.43	7	81.3
30	23.3	10	16.75	20.85	5.46	80.3
30	23.3	20	8.22	10.75	2.68	76.4
10	23.3	0	64.45	79.3	7	81.3
10	23.3	10	50.25	52.55	5.46	80.3
10	23.3	20	24.65	32.25	2.68	76.4

Table 4.4: Evaluation of the charging process in dynamic mode and at different conditions when air-gap is 30 cm.

Speed (km/h)	i_1 limit (A)	Misalig-nment (cm)	Battery energy (Wh)	Input energy (Wh)	Average battery power (kW)	Efficiency (%)
50	34	0	13.36	17.12	7.26	78
50	34	10	10.38	13.6	5.64	76.3
50	34	20	5.03	7.28	2.73	69.1
30	34	0	22.27	28.53	7.26	78
30	34	10	17.3	22.67	5.64	76.3
30	34	20	8.38	12.13	2.73	69.1
10	34	0	66.8	85.6	7.26	78
10	34	10	51.9	68	5.64	76.3
10	34	20	25.15	36.4	2.73	69.1
50	23.3	0	6.27	8.04	3.40	78
50	23.3	10	4.88	6.39	2.65	76.4
50	23.3	20	2.36	3.42	1.28	69
30	23.3	0	10.45	13.4	3.40	78
30	23.3	10	8.13	10.65	2.65	76.4
30	23.3	20	3.93	5.7	1.28	69
10	23.3	0	31.35	40.2	3.40	78
10	23.3	10	24.4	17.1	2.65	76.4
10	23.3	20	11.8	17.1	1.28	69

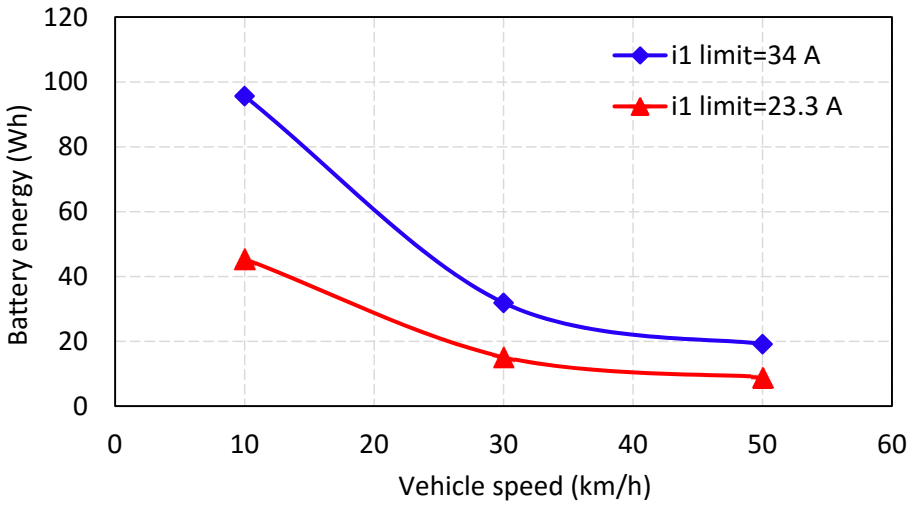

Fig. 4.14: Effect of vehicle speed on the received energy at two power levels.

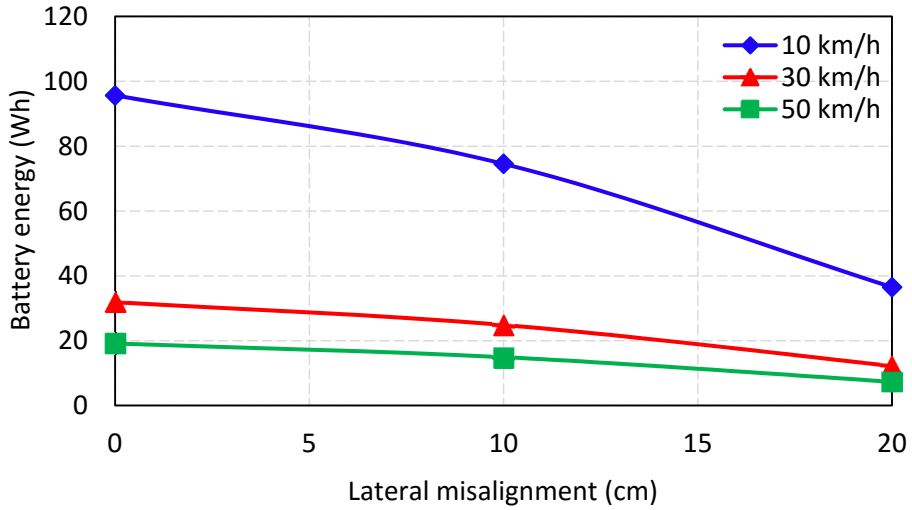

Fig. 4.15: Effect of lateral misalignment on the received energy for the transmitter current limit of 34 A at different vehicle speeds and with 25 cm air-gap.

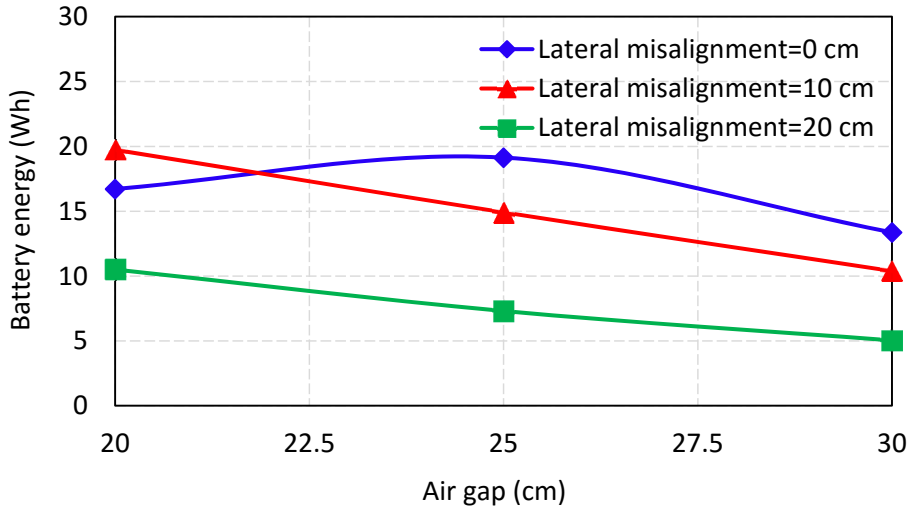

Fig. 4.16: Effect of air-gap variations on the received energy for the transmitter current limit of 34 A at different lateral misalignments.

The effect of air-gap variations on the received energy by the battery for the power limit of 15kW at different lateral misalignments is shown in Fig. 4.16. When the lateral misalignment is zero, the maximum battery energy is achieved at nominal air-gap. If the air-gap increases or decreases, the battery energy reduces. However, in the case of misalignment, the battery energy reduces if the air-gap goes up. In 20 cm of air-gap and 10 cm of misalignment, the battery energy is approximately the same as the nominal air-gap and without the lateral misalignment condition. This is due to the fact that the mutual inductance rate is near to the nominal value.

4.4 Selection of the operating frequency

The selection of the resonant frequency is so important because it has direct effects on efficiency and power transfer. There are three scenarios for the selection of the resonant frequency including the transmitter resonant frequency (composed of only L_1 and C_1), the receiver resonant frequency (composed of only L_2 and C_2) and the ZPA frequency (composed of both transmitter and receiver circuits). In an ideal WPT system, the transmitter resonant frequency, the receiver resonant frequency, and the ZPA frequency all are equal. However, due to imprecise regulation of the resonant circuits, or the variations of the coil self-inductance or capacitor value, the resonant frequency of the transmitter and receiver coils may differ from each other. The condition where the transmitter and receiver resonant frequencies are different is simulated. In this simulation, the resonant frequency of the receiver is selected 85 kHz but the resonant frequency of the transmitter is chosen 81.8 kHz. This is similar to the implemented circuits of the charging lane where the receiver resonant frequency is 85 kHz but transmitter circuits have different resonant frequencies with an average of 81.8 kHz, this results are presented in the next chapter. The output power, efficiency and the input impedance phase versus frequency variations when the frequency of the transmitter and the frequency of the receiver are not equal, are shown in Fig. 4.17.

If the operating frequency for all H-bridge converters in the charging lane is tuned at the resonant frequency of the receiver (85 kHz), in this case, the impedance for the receiver side is completely resistive and sufficient power can be transferred from the transmitter to the receiver and thus, the maximum efficiency can be achieved. The reflected impedance from the receiver to the transmitter is only a resistance. The average resonant frequency of the transmitter is less than 85 kHz and thus, the input impedance is inductive and not capacitive which would help the MOSFET switches of the transmitter converter to operate in ZVS condition. However, due to the reactive power, i_1 reaches the saturation level and the maximum power cannot be transferred. Another choice is the selection of the operating frequency different from the resonant frequency of the receiver and based on the ZPA frequency or the resonant frequency of the transmitter. In both cases, the receiver would not operate at the resonant frequency anymore. The impedance

of the receiver is not resistive and the maximum efficiency cannot be achieved. In ZPA frequency, the input impedance is resistive and the voltage and current of the DC-AC converter are in phase. However, the identification of this frequency is difficult. When working at transmitter resonant frequency, the impedance of the transmitter (composed of transmitter coil and capacitor) is resistive but the reflected impedance of the receiver to the transmitter is not a resistance and thus, the total impedance of the system is not purely resistive. Therefore, the current of the transmitter reaches the peak level and the maximum power cannot be achieved.

Fig. 4.17 is provided for two power levels. In both power levels, neither the output power nor the efficiency is maximum at the transmitter resonant frequency or ZPA frequency. On the other hand, the maximum efficiency is obtained at the resonant frequency of the receiver at both power levels. For the reduced power level, the maximum power is achieved at the receiver resonant frequency. However, for the full power case, the maximum power is obtained at a frequency different from the frequency of the transmitter, receiver or ZPA. This is due to the bifurcation effect. However, the efficiency is not maximum at the frequency. In the full power case, due to the different tuning frequencies, the waveform of the output power is not symmetrical. When the receiver frequency is greater, the right peak is greater and vice versa. It can be concluded that in a charging lane composed of several transmitter coils, the operating frequency of all H-bridge converters can be tuned at the resonant frequency of the receiver in order to transfer power at high efficiency.

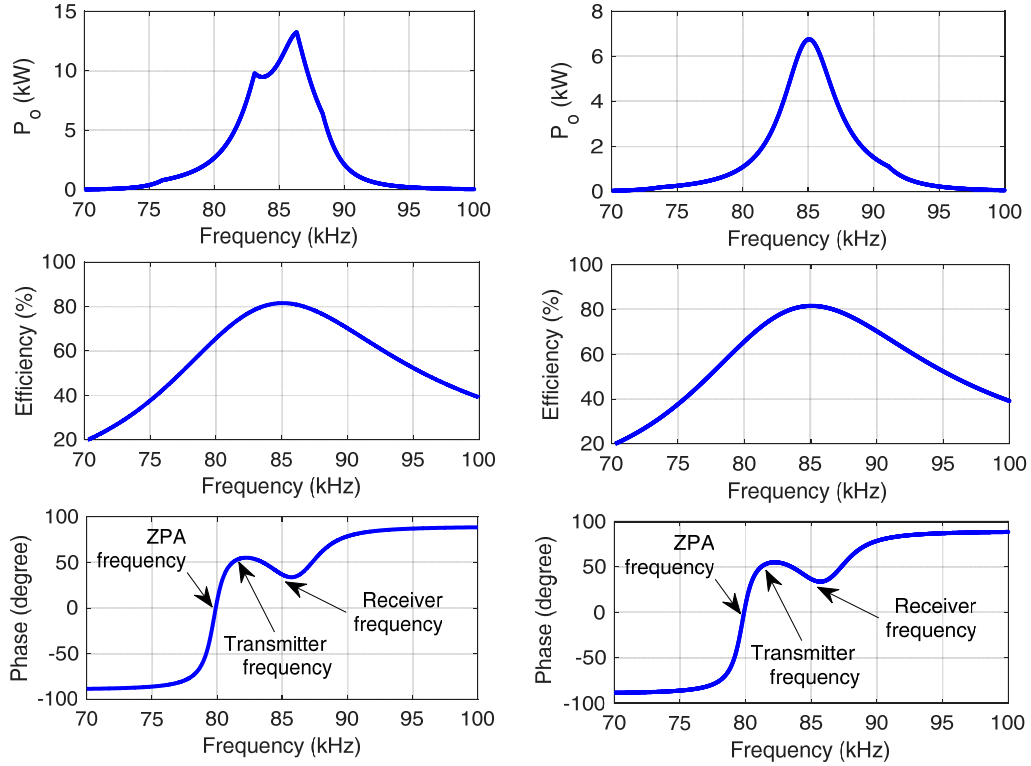

Fig. 4.17: Different variables of the system versus variations of the frequency when the resonant frequencies of the transmitter and receiver are not equal. (a) At reduced

power of 7 kW where the power is limited by the transmitter control, (b) at full power.

4.5 Conclusion

The designed wireless charging system was simulated. The performance of the charging system in both static and dynamic conditions was analyzed. In static charging mode, the behavior of the system at different operating frequencies, power levels, and mutual inductances was studied. The control system was able to control the output power at the misalignment conditions. Furthermore, the performance of the charging system during the dynamic charging at different conditions such as air-gap variations, different vehicle speeds, and various lateral misalignments was evaluated. In nominal air-gap and at a vehicle speed of 50 km/h, an efficiency of 80% and an output energy of 19.13 Wh were obtained in a 15 kW output power limit.

Chapter 5

Hardware development

The procedure for the development of the different parts of the wireless charging lane is presented in this chapter. The whole system is composed of the ground infrastructure and the onboard equipment. The ground infrastructure consists of the 650 V supply voltage, H-bridge converters, transmitter coils, and transmitter capacitors. The supply voltage is constructed using an isolating transformer and an AC-DC converter. The charging structure is composed of 46 transmitters. Thus, it is necessary to build the same number of coils, capacitors, and converters. After the development of the coils and capacitors, they are embedded inside the ground and then covered with concrete. The on-board structure consists of the receiver coil, receiver capacitor, AC-DC converter, output filter, and DC-DC converter. The receiver is mounted under the vehicle and the output of it is connected to the DC-DC converter which is the interface between the receiver and battery.

5.1 Charging system structure

The power circuit of the whole charging system is presented in Fig. 5.1. The charging line is built by 46 transmitters with the final track length of approximately 100 m. For the construction of the supply voltage, a connection from the general grid network arrives at the power room. Inside the power room, a 125 kVA isolating transformer supplies the whole charging area. This transformer is used to isolate the charging line circuit from the grid network. After the isolating transformer, an AC-DC converter is used to build the 650 voltage for supplying the coils. The 650 VDC reaches the shelter point, from the power room. After the protection circuit, the 650 VDC supply voltage is divided into two parts and each part supplies half of the charging line. The 650 VDC is used for the supply of the transmitter converter. The distribution and cabling of the 650 VDC among the H-bridge converters are like a daisy-chain form. The H-bridge converters are wired together in sequence until the final converter. The daisy-chain format is also used in the communication circuits among all power electronics converters.

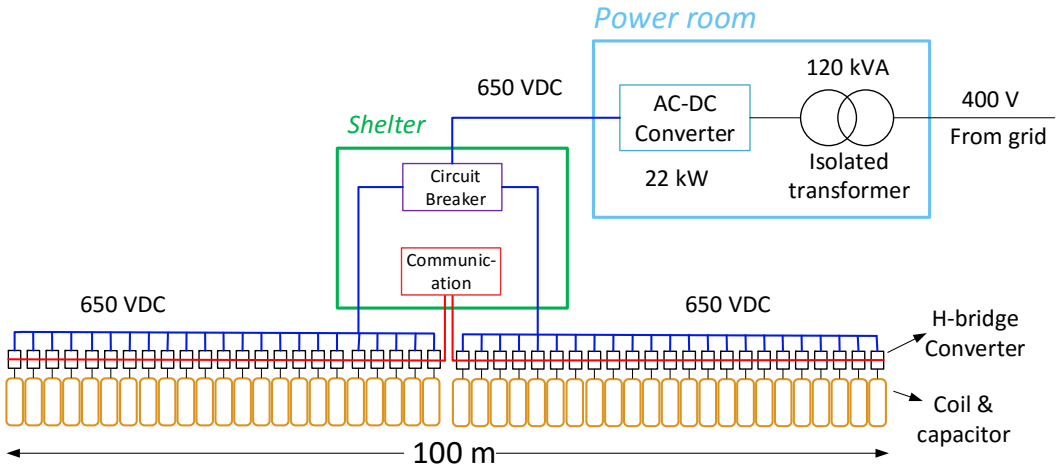

Fig. 5.1: Power circuit of the whole charging system.

Besides the 650 VDC, the supply voltage of 24 VDC is necessary for all H-bridge converters. The supply voltage is provided by two 24VDC power supplies, one for each side. Unlike the cabling of the 650 VDC and communication circuit, the cabling of the 24 VDC supply voltage was not the daisy-chain. This is due to the high voltage drop in the cabling when all 46 H-bridge converters are turned on together.

The charging line is composed of 23 manholes hosting 46 power electronics converters. The layout of the installation of the coils and the position of the manholes are presented in Fig. 5.2. The outer length of each transmitter coil is 1.6 m. Furthermore, the distance between two adjacent transmitter coils is 0.5 m. Due to this distance between the transmitter coils, the mutual coupling between them is not significant. Thus, when a transmitter coil turns on, the voltage induced to the nearby coil is negligible.

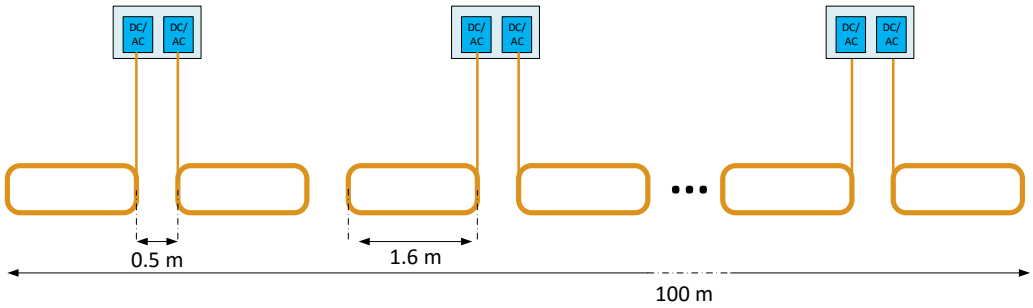

Fig. 5.2: Layout of the installation of the coils and the position of the manholes.

5.2 DC-AC converter

According to the segmented track topology adopted for the wireless charging lane, for each transmitter coil, an H-bridge converter is implemented in order to supply the coil with high-frequency current [172]. The rating power of each power converter is 20 kW. The picture of the H-bridge converter power board is presented in Fig. 5.3.

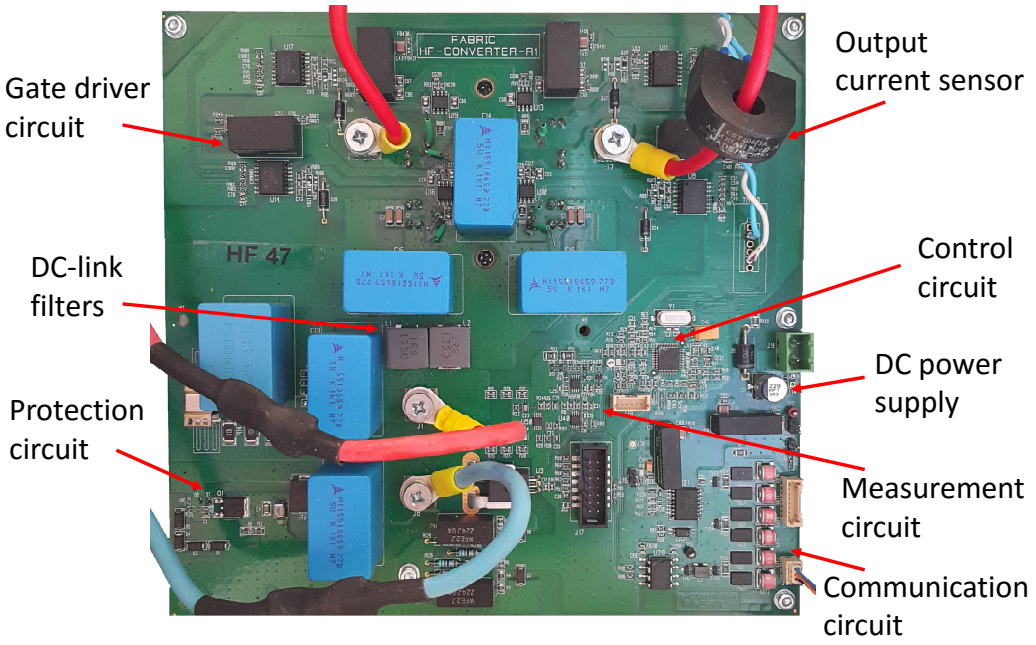

Fig. 5.3: Picture of the transmitter power electronic board.

The power electronic board is composed of the power semiconductor devices, gate driver circuits, protection circuit, measurement circuits, input filter, power supply, communication circuit and control circuit. For the power semiconductor devices, EMIPAK-2B H-bridge Silicon Carbide (SiC) MOSFET power module from Vishay is used. This power module is equipped with an integrated internal NTC thermistor. The voltage rating of this module is 1200 V and the current rating is 78 A. The MOSFET drain-source on resistance $R_{DS(ON)}$ at a current of 60 A is 24 mΩ. Furthermore, the maximum junction temperature is 175 ° C. This power module is a prototype product from Vishay and because of that, the complete datasheet with the complete features is not available.

The SiC power module is mounted under the board where it is screwed to the heatsink. Due to the SiC technology, the SiC power module has low on-resistance, high temperature, low losses, high voltage and high frequency in comparison to the silicon technology power module. Furthermore, according to the device datasheet, the variations of the on-resistance and switching losses versus temperature are very slight. Each switch of the power module is driven via IXDN614 high-speed gate drivers from IXYS and ISO5852S isolated gate driver from Texas Instruments Inc.

The role of the over-voltage protection circuit is to protect the power electronic board from voltage spikes and surges. Transient voltages spikes release a substantial amount of transient energy into the board. Thus, the over-voltage suppression circuit is necessary to clamp the voltage to a safe level. One of the common methods of voltage clamping is the application of the Zener Diodes. The protection circuit is placed in parallel with the load. The rating input DC voltage is 650 V. The input DC voltage is monitored by four series-connected 200 V Zener diodes, BZG03C200TR. When the input DC voltage is lower than 800 V, equal to the sum of the voltage rating of the Zener diodes, the Zener diodes do not conduct.

In the case of over-voltage transient, the voltage of the input DC link goes beyond the Zener diodes voltage rating and the Zener diodes start conducting. The current that flows in the Zener diodes turns on Zener-protected N-channel MOSFET STD3NK100Z and the transient energy is diverted to the ground through the MOSFET and some series resistances. Furthermore, for the protection of the power board against lightning and power surges, a gas discharge tube (GDT) device is used. This tube has two electrodes which are held inside a gas-filled. The device container is usually ceramic and it is able to divert a 1000 A pulse without destruction. The transient suppression circuit mostly consists of a gas discharge tube and a Voltage Dependent Resistor (VDR) connected in series. For the GDT, SG420 with a typical voltage rating of 420 V and for VDR, CU4032K275G2 with a maximum DC voltage of 350 V are chosen. GDT shunted across the circuit behaves like an open circuit in nominal operating voltage. When the value of the DC link voltage is higher than the sum of the voltage rating of VDR and GDT, here is 770 V, the current starts flowing. In a VDR, the characteristic of the current-voltage is not linear. If the voltage increases more, the current flowing through these components increases more and thus, the current gets away from the main components. Once the voltage returns to normal value, the flow of the current stops again.

For the input filter capacitor, three parallel capacitors, each of them 5 nF and 1100 V, were used. Furthermore, for the input filter inductor, two parallel inductors, each of them 1.8 μH and 21 A were employed.

The supply DC voltage for the power electronic boards comes from two 24 VDC power supplies. Each power supply provides DC power for 23 power electronic boards. Then, inside each board, the 24 VDC is converted to 5 V and 3.3 V by two isolated DC-DC converters MEF1S2403SP3C and MEF1S2405SP3C, respectively, in order to provide supply power for the components inside the board. Furthermore, for the protection purpose, a 24V 2.5A fuse is placed after the arrival of the 24 V to the board.

The measurement circuit is composed of the measurement of the input DC current, measurement of the input DC voltage and measurement of the output AC current. The input DC voltage and current are used in the control circuit for protection purposes. For the measurement of the input DC current of the power board, Hall-effect-based linear current sensor ACS758LCB-050U-PFF-T with a peak current of 50 A is employed. For the measurement of DC link voltage, dual channel CMOS Amplifier FAN4274IMU8X is used. In order to detect the AC current at the output of the power module, the current transformer CST206-3A is employed. The turn ratio of the transformer is 1:300 and with the maximum current of 70 A RMS. The working frequency range of this current transformer is 20-200 kHz and thus it is suitable for the operating frequency of 85 kHz. The Output AC current of the H-bridge converter is used in the control circuit in order to regulate the current of the transmitter coil. In the control circuit, the peak of the output current is necessary. In order to build the peak of the AC current, at first, the AC

current is rectified by using a diode bridge. The peak of the rectified AC current is obtained using an op-amp FAN4274IMU8X, two Shockey diodes NSR0240V2T1G, two 20 kΩ resistors, and one 4.7 nF capacitor. The schematic of the circuit is presented in Fig. 5.4. In this figure, V_{in} is the rectified voltage of the current sensor and V_o is the peak current.

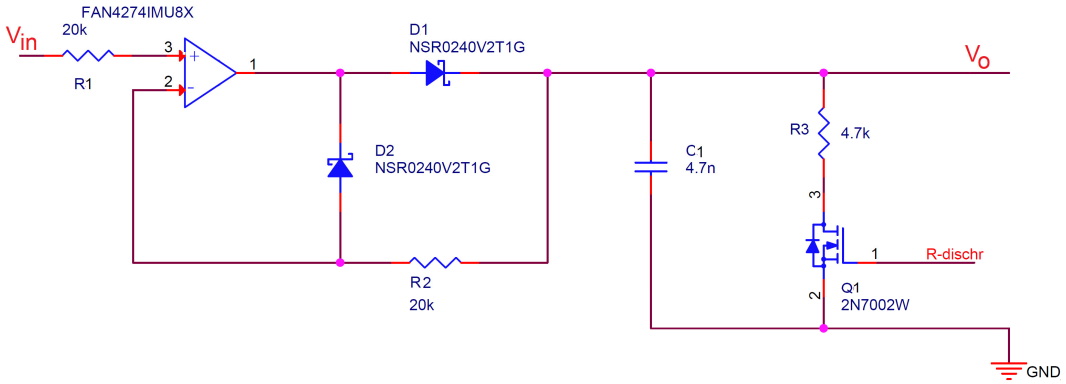

Fig. 5.4: Picture of the employed SiC MOSFET power module.

When the input signal V_{in} exceeds the V_o, the diode D_1 becomes forward biased, the circuit becomes like a voltage follower and the capacitor charges to the peak value of input signal V_o. On the other hand, when V_o is more than V_{in}, diode D_1 becomes reverse biased. Thus, the capacitor retains the voltage level until V_{in} again becomes greater than V_o. The switch Q_1 is used for resetting the peak value in each switching period.

The communication circuit consists of the CAN communication circuit. For each power board, a specific ID is defined and the microcontrollers inside all boards communicate together through this communication protocol. For the isolation of the CAN circuit, ISO1050 is employed. Through the PEAK-System CAN interface in MATLAB software it is possible to transmit and receive CAN messages. Thus, by this software, the CAN messages about the states of the power boards and different parameters of the control can be received. Furthermore, it is possible to control the power board and tune the parameters of the control via CAN massages. The role of this interface becomes more significant when it is necessary to control all the power electronics boards of the charging lane. Thanks to PEAK-System CAN interface, managing these huge CAN messages becomes feasible.

The power electronic board is controlled by the control circuit inside the board as shown in Fig. 5.3. The control circuit consists of a digital signal controller (DSC) MC56F84550 from Freescale. This DSC is based on a 32-bit DSP core with a core frequency of 80 MHz and with 96 KB flash memory. Furthermore, it includes 6 high-resolution PWM channels, high-speed 12-bit analog-to-digital controllers (ADCs) with 3.3 Msps resolution. The simplified structure of the C code inside the DSP is presented in Fig. 5.5. At first, the code starts with some initializations such as initialization of the parameters, variables, CAN module and ADC modules. Then, the program enters an infinite loop and waits for PWM interrupts. The PWM ISRs are composed of the acquisition of the data, protection, state machines, and

PWM modulations. The DSP acquires the sampling of the necessary quantities including input DC voltage, input DC current, power module temperature and the peak of the output AC current. According to the obtained data, the protection unit controls the board against input DC overvoltage, input DC under voltage, power module over temperature, and output overcurrent faults.

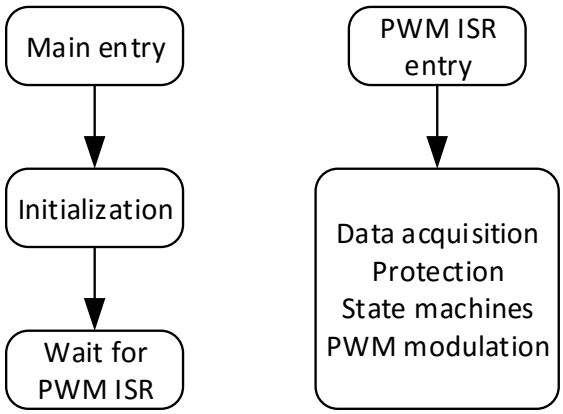

Fig. 5.5: DSP software structure.

In the case of the fault occurrence, the protection turns off the commutation of the power modules and the program goes to the Error state. Besides the Error state, the program is composed of several other states including the Parameter identification state, Static charging state, and Dynamic charging state. In the Parameter identification state, the transmitter coil (without the receiver coil) is supplied with a constant voltage and then the value of the AC current is preserved as the switching frequency changes. The frequency in which the coil has the maximum current is considered as the resonant frequency of the transmitter coil. On the other hand, if obtained AC currents are lower than a specific level, the coil is considered broken and this coil is excluded from the charging operation. In the Static charging state, a current control with PI is implemented inside the DSP. The control receives the real value of the output current and compares it with the reference value. According to these values, the control calculates the phase shift angle. The operation frequency, the reference current value and the operation time can be defined for this state. In Dynamic charging state, the control goes in identification mode and waits for the vehicle. Similar to the static charging state, also in this state a current control is implemented inside the DSP. The control supplies the transmitter coil with the identification current and monitors the phase shift angle related to this current. When the phase shift angle becomes more than the turn-on angle, the control changes the current reference from the identification reference current to the power transmission reference current. During the power transmission, the control monitors the phase angle and when the phase angle drops below to turn-off angle, control turns off the switches. The operating frequency, the reference current for the identification, phase angles (turn on and turn off) for the identification and the reference current for the power transmission can be defined for this state.

The switching of the power modules is according to the phase shift angle modulation. Thus, when the phase shift angle related to the reference current is calculated, it is possible to switch the power module. The PWM signals for the power module are implemented using the enhanced flexible pulse width modulator (eFlexPWM) module inside the DSP. This module has three PWM submodules. One PWM submodule is necessary for switching a half-bridge power stage. Here, submodule 0 (composed of PWM0A and PWM0B) and PWM submodule 1 (composed of PWM1A and PWM1B) are used for the switching of the first and second leg of the converter, respectively. The eFlexPWM module is able to generate PWM pulses according to the phase shift modulation scheme since independent control of both rising and falling edges of PWM signals is possible. For this reason, two comparators and associated registers (VAL2 and VAL2) are used for each PWM output signal. VAL2 register is used to control the turn-on edge of the PWM, and the VAL3 register is for the control of the turn-off edge of the PWM. According to the phase shift modulation, the duty cycle of each PWM signal is kept unchanged equal to a 50% duty cycle. The PWM signals of the first leg (PWM0A, PWM0B) are kept fixed but the PWM signals of the second leg (PWM1A, PWM1B) are shifted according to the phase shift modulation angle. The switching frequency of the power module is 85 kHz and the clock frequency of the DSP is 80 MHz. Thus for the phase width of each PWM signal with 50% duty cycle, approximately 470 cycles of the DSP clock are necessary. The switches of each leg of the power module are operated with the dead time of 0.5 µs.

5.3 Transmitter coils

For the whole charging lane, 46 coils are necessary. The transmitter coils are constructed by the litz wire. The wire diameter is 5 mm. The size of each transmitter coil is 1.5 m × 0.5 m and each coil has 10 turns. The picture of the transmitter coil is illustrated in Fig. 5.6. The inductance of the transmitter coil was estimated with the simulation to be 280 µH. The self-inductance of the implemented transmitter coils are measured using an LCR meter at the frequency of 85 kHz. The results of the measurement are presented in Fig. 5.7. The average value for the coils self-inductances is obtained 281.25 µH. The same measurement has been carried out for all the coils in order to obtain the resistance of each coil. The resistance measurement data are shown in Fig. 5.8. The average value for the resistance of the coil is obtained 359 mΩ.

Fig. 5.6: Picture of the transmitter coil with 10 turns.

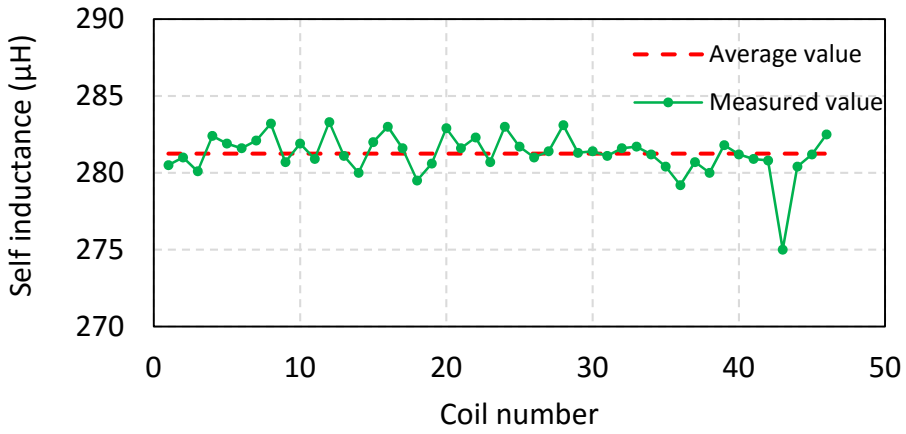

Fig. 5.7: Measured self-inductance of the coils at the frequency of 85 kHz.

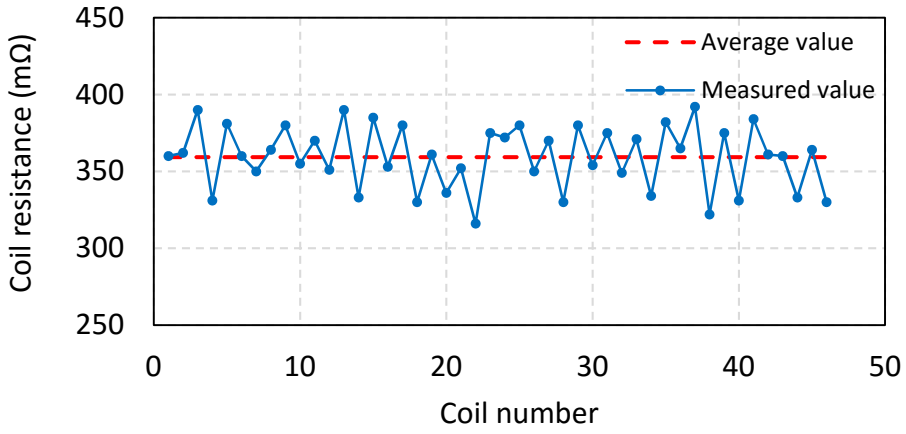

Fig. 5.8: Measurement of the resistances of coils at frequency of 85 kHz.

5.4 Transmitter capacitors

The value of the resonant capacitors must be chosen precisely in order to compensate the leakage inductances of the transformer completely, at the operating frequency. If the values of the resonant capacitors deviate from the calculated values, it effects on the power transmission capability. One of the main critical issues in SS compensated wireless charging of EVs is represented by the high voltage stress over the compensation capacitors in the transmitter and receiver side. This voltage can reach several kilowatts when the output power is in the order of decades of kilowatt [173]. For the WPT system, the transmitter current reaches 35 A when operating at the maximum power rating. Considering L_1 equal to 280 µH and C_1 equal to 12.5 nF, the voltage across the transmitter capacitor reaches 5.2 kV. The peak voltage across the transmitter capacitor is 7.4 kV. In the same way, the voltage across the receiver capacitor is calculated 4.8 kV and peak voltage of 6.8 kV. It can be seen that the resonant capacitors must tolerate very high voltage. At the present time, there are not any commercial capacitors within voltage range and operating frequency in the market. Thus, for this application, specially designed

capacitors with polyimide film were designed and developed by one of the project team members [100]. The advantage of these capacitors is that the manufacturing cost is low and because of that, they are used for the transmitter compensation circuit. The picture of the transmitter capacitor is presented in Fig. 5.9. Each transmitter capacitor is made by paralleling to polyimide film capacitors.

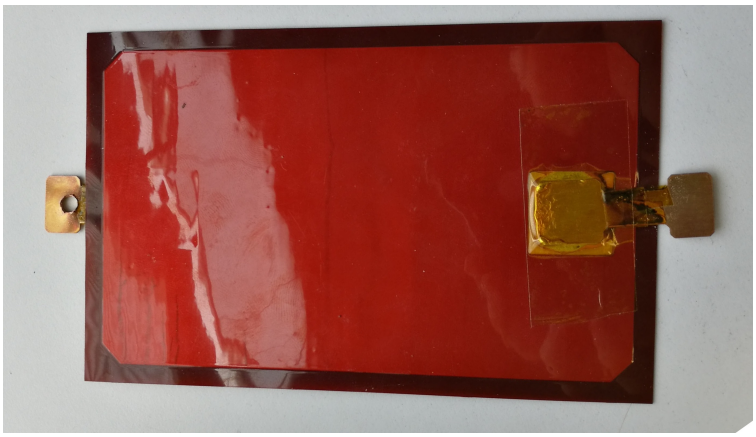

Fig. 5.9: Pictures of polyimide film capacitor for the transmitter side.

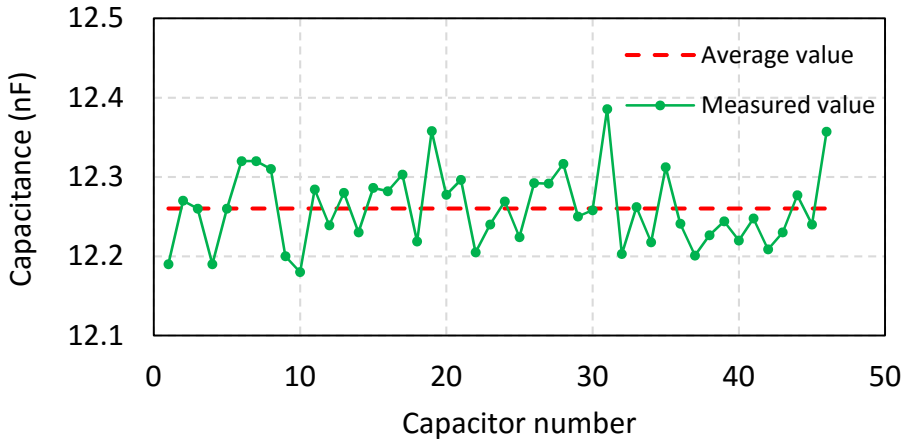

Fig. 5.10: Measured capacitance of the transmitter capacitors at 85 kHz.

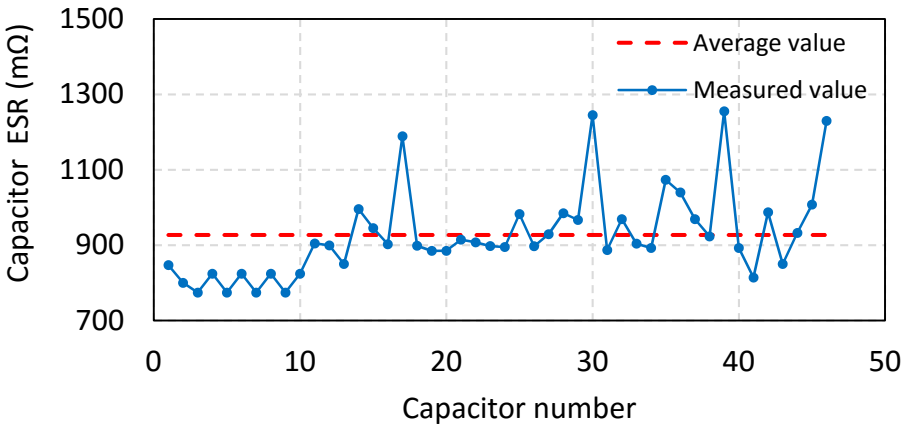

Fig. 5.11: Measured ESR of the transmitter capacitors at a frequency of 85 kHz.

The value of each capacitor set is presented in Fig. 5.10. The average value of the whole transmitter capacitors is 12.26 nF. It can be seen from this figure that the precision of the values of the capacitors is high and the deviation from the average value is not significant. The measurements for the ESR of each capacitor set is illustrated in Fig. 5.11. The mean value is 926 mΩ. The ESR of each polyimide film capacitor is around 1.8 Ω, but since each transmitter capacitor is made by paralleling two polyimide film capacitors, the total ESR is half.

After the construction of the coils and capacitors, the resonant circuit is completed. In order to build the resonant circuit, each coil is placed in series with a capacitor. The system elements are designed to resonate at the operating frequency of 85 kHz. The resonant frequency of each coil set is measured by using an LCR meter. In order to obtain the resonant frequency of the circuit, each coil set, composed of a capacitor and an inductor, is connected to the LCR meter. Then, the operating frequency of the LCR meter is changed until the impedance of the circuit becomes completely resistive. This frequency is the resonant frequency of the circuit. This measurement is carried out for all 46 coil sets. The average of the resonant frequency for all 46 coil sets is obtained 85.7 kHz which is close to the frequency of 85 kHz. The same test is carried out for the measurement of the coil resistance. At the resonant frequency, the impedance of the circuit is purely resistive and the impedance obtained by the measurement is the total resistance of the circuit. The obtained resistance is the sum of the resistance of the coil and the ESR of the capacitor. The average of the total resistance is obtained 1.28 mΩ.

5.5 Coil embedding procedure

One of the important issues in the construction of the charging lane is embedding the coil into the ground [174]–[177]. The coils have to be put inside the ground in the depth of 5 cm. After that, the coils need to be covered. Asphalt and concrete are two materials that can be used for covering the coils and paving the road. Concrete is much stronger than asphalt and avoids deforming and damaging the coils and for this reason, this material was chosen. During the first try of embedment, a coil and without the resonant capacitor was embedded into the ground and then covered with concrete. Then the impedance of the coil was measured at different frequencies. Since only the coil was embedded into the ground thus it was expecting to see the inductive behavior during the measurement. However, the phase started reducing when the frequency increased. Actually, this problem is due to the fact that when the coil is placed inside the ground, a parallel resonant circuit between the inductance of the coil and a capacitance, created between the coil and ground, forms. The parasitic capacitance between the coil and the ground is high which causes the reduction phase. The parasitic capacitance has a direct relation to the surface of the coil. Since the transmitter coil is composed of 10 turns and has a significant surface size, the value of the parasitic capacitor is big. One solution for the reduction of the parasitic capacitor is the increase of the distance between the coil and the ground similar to a conventional capacitor.

Therefore, an isolated material as the dielectric of the capacitor was placed between the coil and the ground. After the measurement, the resonant frequency between the inductor of the coil and the parasitic capacitor between the coil and concrete was moved to a frequency higher than 1 MHz and the phase of the coil was around 90° at frequencies less than this value.

The experiment demonstrated that embedding the coil in concrete caused high capacitive coupling between the concrete and coil at high frequencies (as the frequency reaches 1MHz). The study concluded that the capacitive coupling can be reduced by decreasing the capacitance between the coil and concrete. However, the WPT solutions are not expected to operate at frequencies as high as 1 MHz; therefore, it is not essential to minimize the capacitive coupling.

5.5.1 Coil embedding with the coating

The coil should be installed to a targeted depth of 5 cm below the ground surface. In order to reduce the capacitive behavior between the coil and ground, a special kind of tar is used as a non-conductive material. This material is employed to completely cover all over the coil when the coil is put inside the ground. For this reason, the empty hole is covered with the non-conductive material with a depth of 1 cm. Then, the coil is put inside the hole and again is covered with the non-conductive material with a depth of 1cm. The procedure of the coating of the coil is illustrated in Fig. 5.12.

Fig. 5.12: Coating of the coil inside the ground with isolating material.

Two different isolating materials are used for covering the coils. One isolating material (Catramina) for the first 27 coils and another isolating material (Catramix) for the rest of the coils are employed. After completely covering the coil with the isolating material, the resonant frequency of the coil is measured using an LCR meter. During the embedment, both coil and capacitor are placed inside the ground. For the measurement of the resonant frequency with LCR meter, the coil is connected to LCR meter and then the frequency of the LCR meter is changed until

the phase of the resonant circuit becomes zero. This is the resonant frequency of the coil set. After completing the test, the resonant frequencies of all coils are obtained. Unfortunately, the resonant frequency values for the first ten coils are not available. The average of the resonant frequency for the 36 coil sets is calculated 84.35 kHz. The variation of the resonant frequencies is not significant for all coils. By embedding the coil in the ground and with the help of coating material, the average of the resonant frequency is reduced by only 1.1 KHz .

5.5.2 Covering with cement:

After covering the coil with the isolation material, the next step is to pave the road. For paving the road, the concrete is chosen because it is mechanically stronger than asphalt which helps the coil not to be damaged or deformed as the vehicles move in the charging lane. The process of filling the holes and covering the coils with concrete is illustrated in Fig. 5.13.

Fig. 5.13: Covering the coil with concrete.

When the embedding the coils and covering them with concrete completed, wait for the concrete to dry. After that, another test is carried out with the LCR meter to see the variation of the resonant frequency after embedding the coil and with the presence of concrete. The measurement for the first ten coils was performed one year after the embedment and covering with concrete however, for the remaining coils, the measurement was done one week after the embedment. The adopted concrete was different and because of that, the resonant frequency is a bit lower for the first ten coils. The identification of the proper material has been a matter of long research and test and the ideal solution is not yet identified. The average of the resonant frequency for the first ten coils is 79.76 kHz and for the remaining coils is 81.83 kHz. The average of the resonant frequency for the total coils is about 81.38 kHz which is 2.5 kHz lower than the resonant frequency for the coils without the concrete. The average of the resonant frequency is still in the range of the frequency standard in static EV chargers SAE J2954.

In order to verify the accuracy of the frequency measurement with the LCR meter, a series of additional tests are carried out by connecting the transmitter coils to the power electronic converter. The H-bridge converter is supplied with 650 VDC. The coil is energized with the constant current of 5 A. The operating frequency of the H-bridge converter is changed until the transmitter voltage and current become in phase. The resonant frequencies obtained by the power electronic test is approximately the same as the measurement with LCR mater.

The comparison of the resonant frequency in different stages of embedment is presented in Fig. 5.14. This figure shows that the process of coating effects on the resonant frequency all the coils in the same manner. In fact, with coating, the resonant frequency of the coils decreases but the variation is not significant. However, a more consistent reduction of the resonant frequency is visible when covering the coils with the concrete. Although the resonant frequency of all the coils is reduced, for some coils it is reduced more than others. One reason for this spread in the resonance frequency data could be related to boundary phenomena such as weather condition during the embedment and the aging of the assemble of the coils and materials. In addition, the pressure applied to the coils and the materials during the embodiment and the passages of the vehicles contributed to deform the shape of the coils that result in a modified value of self-inductance.

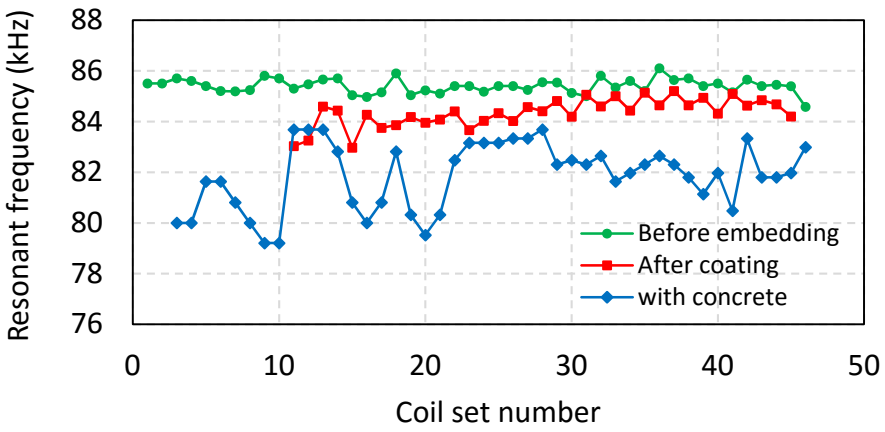

Fig. 5.14: Measured resonant frequency for each coil set before embedment, after coating and after covering with concrete.

5.6 Onboard equipment

The WPT system is supposed to charge the battery of the electric vehicle. The picture of the EV used for the test is presented in Fig. 5.15. The general on-board structure of an EV with a wireless charger is composed of the receiver structure, the DC-DC converter, the battery pack, the traction inverter, and the motor. The vehicle is equipped with a 260-400V, 19 kWh, 60 A battery pack. The DC-DC converter is for power regulation and has a power rating of 35 kW. The DC-DC converter is connected to the CAN network of the vehicle and the battery power is controlled

through the CAN messages. The traction inverter is used to supply the traction electric motor with three-phase current.

Fig. 5.15: Picture of the EV above the transmitter coils.

5.6.1 Receiver structure

The receiver structure is mounted under the vehicle and in the back of it as shown in Fig. 5.16. In order to protect the passengers and the onboard equipment against the magnetic field during the dynamic charging, under the vehicle is shielded [178], [179]. The receiver structure is composed of the receiver coil, resonant capacitor, rectifier, filter, and the protection circuit. The output of the receiver directly connects to the input of the DC-DC converter.

Fig. 5.16: Picture of the receiver structure mounted under the vehicle

The receiver coil consists of a rectangular coil made of ten turns of litz wire and two ferrite cores. The diameter of the litz wire is 5 mm. The outer size of the receiver coil is 0.4 m × 0.62 m. The picture of the receiver coil is illustrated in Fig. 5.17. The inductance of the receiver coil is measured 120 μH at the frequency of 85 kHz. Furthermore, the resistance of the receiver coil is measured 0.128 Ω. The

3F3 ferrite bars are used for the ferromagnetic elements of the receiver coil. This ferrite has reasonable permeability and low power losses at a frequency of 85 kHz.

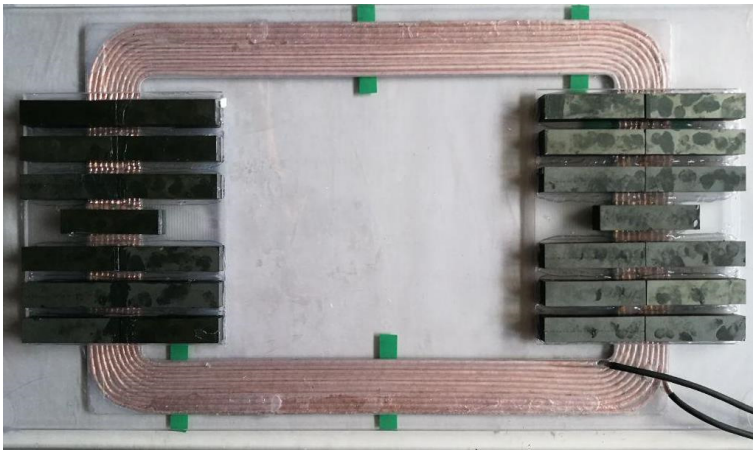

Fig. 5.17: The picture of the receiver coil and the position of the ferrite bars.

For the receiver side capacitor, the polypropylene capacitors (MKP) are employed because of low losses and operation in high frequency. The MKP capacitors in high voltage rating are not available and in order to obtain the necessary capacitance value and voltage rating, combinations of capacitors are connected in series and parallel forms. In this case, the error between the calculated and experimental values becomes minimized. The picture of the receiver capacitor bank is shown in Fig. 5.18.

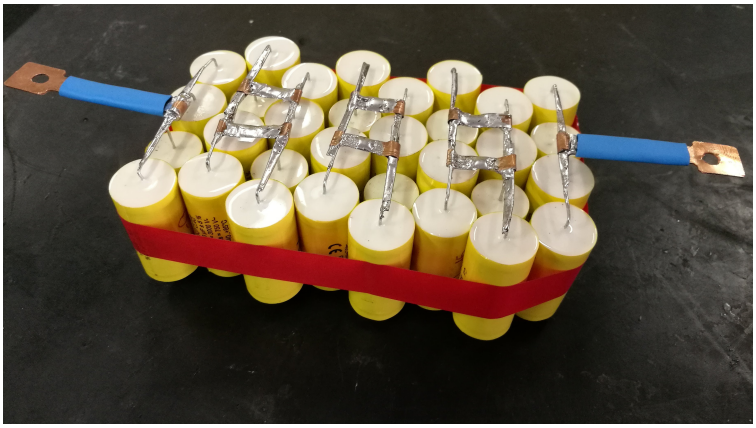

Fig. 5.18: Pictures of the MKP capacitor bank for the receiver side.

With the application of the AC-DC converter, the AC current of the receiver is converted to DC current. For the rectification stage, a passive rectifier with Diode Bridge is used. Since the output of the rectifier is connected to the DC-DC converter, it is required that the input voltage ripple of the rectifier do not exceed a specified value. The ripple can be mitigated using a filter. In the output of the rectifier, only a capacitor filter is used. The capacitor filter is implemented by three parallel film capacitors C4BSPBX4300Z. Each capacitor has the capacitance of 3

μF, the equivalent series resistance of 2.8 mΩ and the equivalent series inductance of 48 nH. Thus, the equivalent filter capacitor is 9 μF.

The behavior of the receiver current in a series-series compensated WPT system is like a current source. In the case of disconnection of the load, the current still flows through the receiver coil, rectifier, and filter. Without the load, the voltage of the filter capacitor goes up which causes severe problems in the components. When the load becomes disconnected, this fault condition cannot be handled by the transmitter side control. Thus, a protection circuit is necessary in the receiver side in order to protect the circuit in case of fault occurrence [180]. This protection circuit is placed between the capacitor filter and the DC-DC converter.

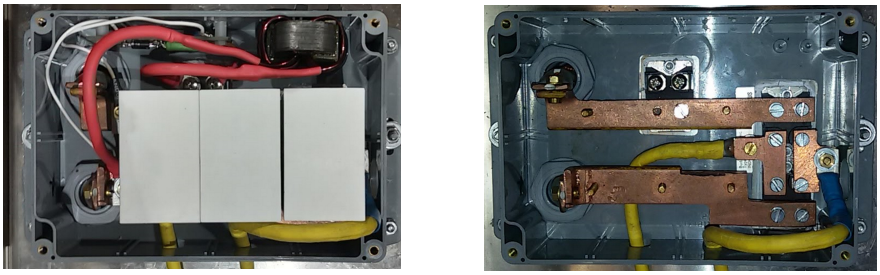

(a) (b)

Fig. 5.19: (a) Filter capacitors and over voltage fault protection, (b) rectifier.

When the voltage of the filter capacitor reaches maximum allowable voltage, defined by three Zener diodes, the receiver becomes short circuit by a thyristor and the receiver is protected against overvoltage fault. Furthermore, by short-circuiting the receiver, according to the receiver impedance referred to the transmitter, the current of the transmitter drops to zero and helps to clear the fault. With the use of some resistances, it is possible to limit the current of the Zener diodes and the thyristor. The picture of the protection circuit along with the picture of the rectifier and filter are shown in Fig. 5.19.

5.7 Conclusion

In this chapter, the development of the main components of the wireless charging system was presented. For the whole charging lane, 46 coils were implemented. The average value for the coils self-inductances was measured 281.25 μH which is close to the required value. Furthermore, the same number of capacitors was implemented. After the connection of the coil to the capacitors, the average resonant frequency of 85.7 kHz which was quite close to the desired resonant frequency. During the coil embedment and covering the coil with the concrete, the average resonant frequency of the coils reduced to 81.38 kHz. However, the resonant frequency is still in the range of the frequency standard. For the energizing transmitter coils, the power electronics board was implemented and different parts of it were described. Finally, the implementation of the different parts of the receiver structure was presented.

Chapter 6

Experimental Results

In this chapter, the results of experimental tests in static and dynamic charging modes are presented. In order to evaluate the performance of the wireless system, several tests are performed in different charging conditions. At first, the control of the battery power from the receive side by adjusting the equivalent resistance at the input of the DC-DC converter is studied. Then, the performance of the wireless charger in various coupling conditions is analyzed. During this test, the air-gap level is increased and decreased in order to have different coupling values, lower and higher than the rated coupling, and then the output power is measured at the variable coupling. Furthermore, the identification process of the vehicle at different conditions is investigated. The transmission of the power and efficiency variations at different lateral misalignments are also presented in this chapter. The final part of the chapter is dedicated to the dynamic tests with all transmitter coils. During this test, the vehicle passes over the transmitter coils with a maximum speed of 15 km/h and the energy is transferred to the battery.

6.1 Power demand control

As completely described in the third chapter, the battery power can be regulated from the receiver. In this section, the operation of the power control strategy is experimentally validated. In this test, the output of the DC-DC converter is connected to a battery emulator to provide a condition similar to the battery of the vehicle. The voltage of the battery emulator is set to 370 VDC. This test with the maximum output power of 11 kW is performed. To provide this power level at a nominal air-gap of 25 cm and a rated mutual inductance of 14.3 μH, the input DC source is set to 500 VDC and the peak of the transmitter current is set to 40 A. According to the defined input DC source voltage and the transmitter current, the $R_{in\text{-}Pmax}$ is calculated 4.2 Ω according to (3.15). At this equivalent resistance, the maximum power of 11 kW can be transferred to the output.

The operation of the system under the variations of the equivalent resistance R_{in}^{*} at nominal mutual inductance is illustrated in Fig. 6.1. In this figure, the theoretical values are compared with the experimental results. It can be seen from these waveforms that there is a good match between the experimental results and the calculated counterparts. By increasing R_{in} from zero, i_1 goes up and the output power increases. When the equivalent resistance R_{in} reaches the value of 4.2 Ω, the peak power is transferred to the battery. Thus, the control scheme is capable to regulate the output power from zero to the maximum output power just from the receiver side. The value of the equivalent resistance is increased more than 4.2 Ω to see the behavior of the control scheme in this condition. When R_{in} becomes more than 4.2 Ω, the peak of the transmitter current is kept constant at the level of 40 A by reducing the transmitter voltage. Thus, in this condition, the input power and consequently the output power are reduced. Therefore, the output power can be regulated by decreasing or increasing the equivalent resistance. When R_{in} changes from zero to 4.2 Ω, the output power varies approximately linearly.

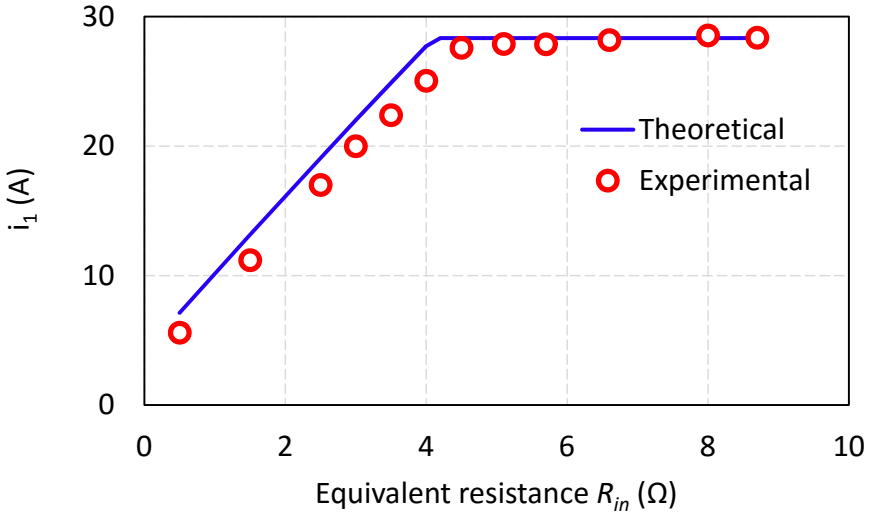

(a)

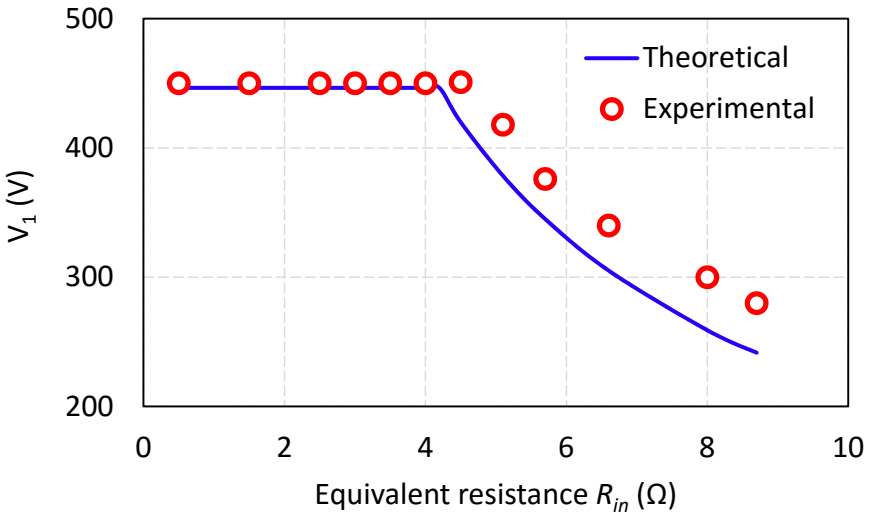

(b)

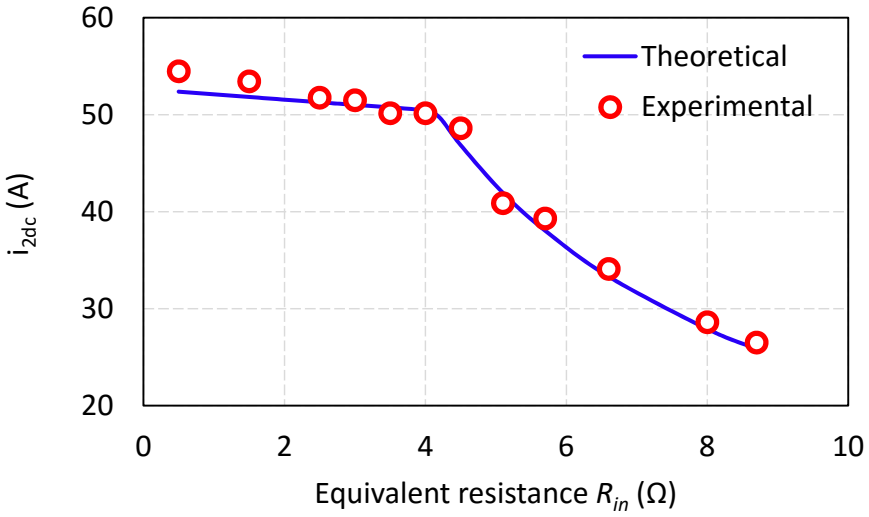

(c)

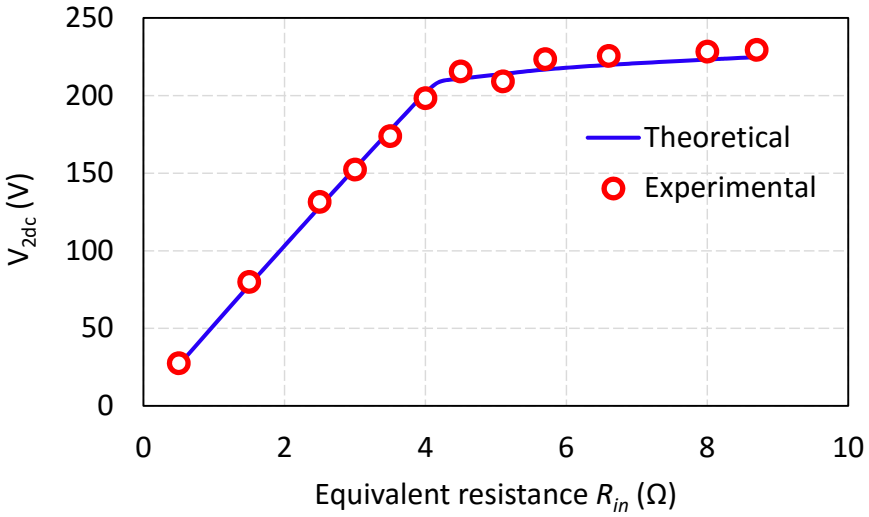

(d)

(e)

Fig. 6.1: Behavior of the system under variations of the equivalent resistance R_{in}. (a) Transmitter current i_1, (b) receiver RMS voltage V_1, (c) receiver DC current i_{2dc}, (d) receiver DC voltage V_{2dc}, (e) power at the input of the DC-DC converter P_{2dc}.

The waveforms of the transmitter and receiver for R_{in}=4.2 Ω is presented in Fig. 6.2. At this equivalent resistance, the transmitter current is at its peak level and the transmitter voltage is a full squire wave. Furthermore, the maximum power can be transferred to the receiver side. The effect of the R_{in} variations on the transmitter voltage, transmitter current, receiver DC voltage, and receiver DC current are shown in Fig. 6.3 and Fig 6.4. The output power is reduced to 6.5 kW by both increasing and decreasing R_{in}. In Fig. 6.3, the reduced output power is achieved by reducing R_{in} to 2.5 Ω. At this resistance, the transmitter current value is lower than the maximum level but the transmitter voltage is maximum. Thus, the switches of the H-bridge converter can operate at soft switching condition. The receiver DC voltage and current are approximately 130 V and 50 A, respectively.

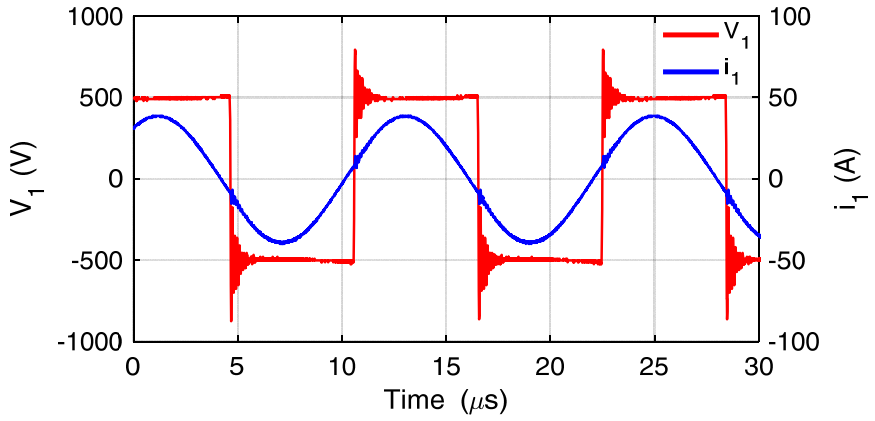

(a)

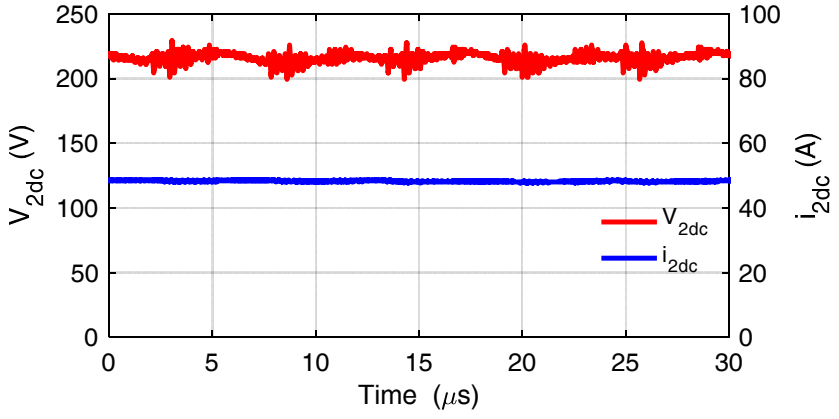

(b)

Fig. 6.2: Operation when is equal to 14.3 μH and at full power when R_{in} is 4.2 Ω. (a) Transmitter voltage V_1 and transmitter current i_1, (b) receiver DC voltage V_{2dc} and receiver DC current i_{2dc}.

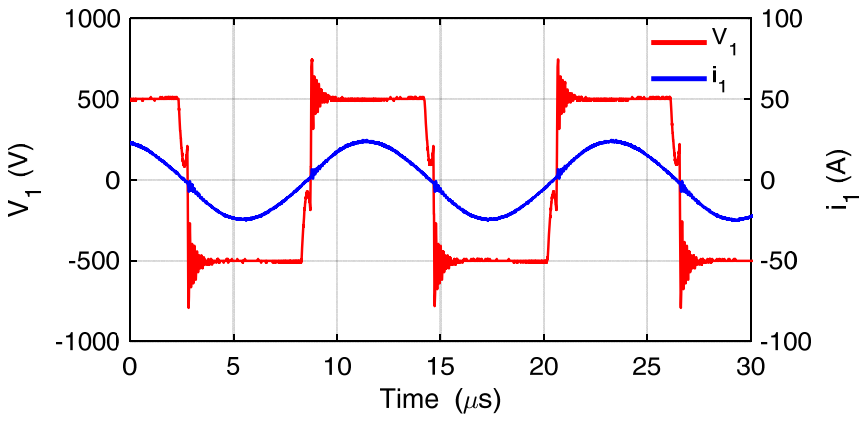

(a)

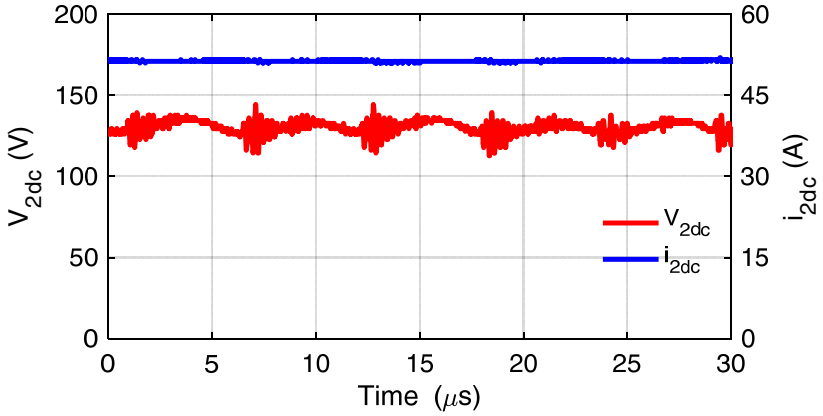

(b)

Fig. 6.3: Operation of the system at rated mutual inductance and at reduced power when R_{in} is 2.5 Ω. (a) Transmitter voltage V_1 and transmitter current i_1, (b) receiver DC voltage V_{2dc} and receiver DC current i_{2dc}.

The amount of the output power is reduced to 6.5 kW by increasing R_{in} to 8 Ω as presented in Fig. 6.4. At this point, the receiver DC voltage and current are approximately 230 V and 28 A, respectively. Furthermore, at this resistance, the transmitter current value is maximum but the transmitter voltage is reduced. Thus, the soft switching condition for all switches of the H-bridge converter cannot be achieved which could affect the losses of the H-bridge converter.

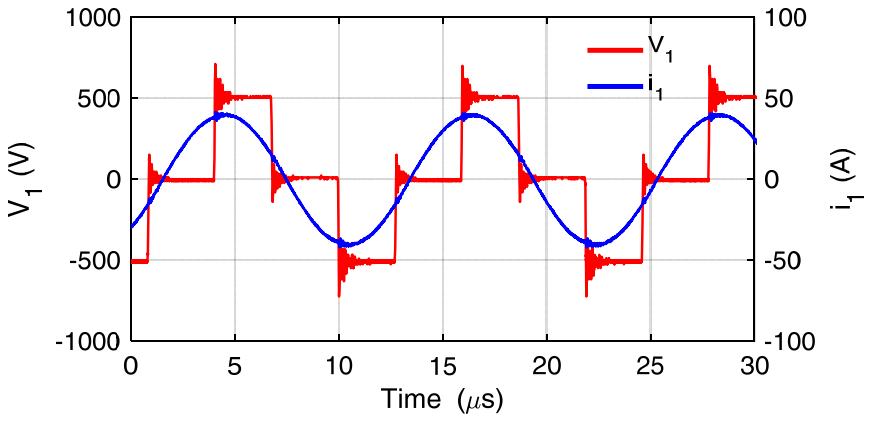

(a)

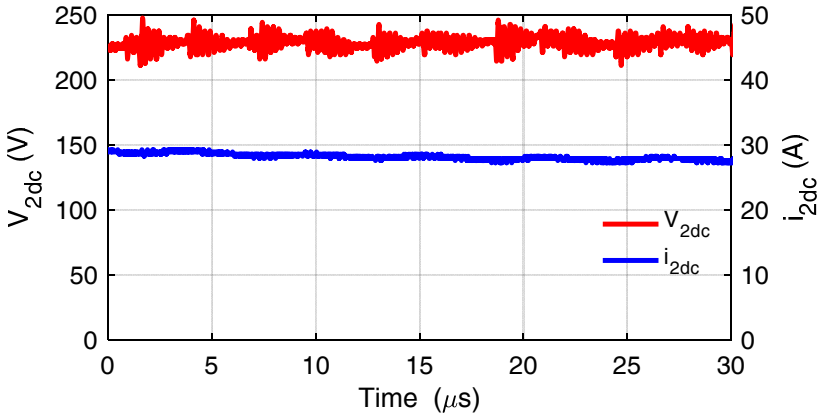

(b)

Fig. 6.4: Operation at rated mutual inductance M=14.3 μH and at reduced power when R_{in} is 8 Ω. (a) Transmitter voltage V_1 and transmitter current i_1, (b) receiver DC voltage V_{2dc} and receiver DC current i_{2dc}.

6.2 Operation at variable coupling

In this section, the operation under the variations of the mutual inductance is analyzed. The test condition is similar to the previous test in 6.1 but R_{in} is kept constant equal to 4.2 Ω. At a nominal air-gap of 25 cm, the rated mutual inductance is equal to 14.3 μH. The value of the mutual inductance changes by varying the air-gap between the transmitter and receiver coils. When the air-gap increases, the mutual inductance decreases, and vice versa.

The operation of the control scheme at the variations of the mutual inductance is illustrated in Fig. 6.5. The theoretical values are compared with experimental results in this figure. It can be seen that there is a good match between the experimental and theoretical results. The value of V_1 shown in Fig. 6.5(b) is only the fundamental harmonic of transmitter voltage. Since the oscilloscope returns the true RMS of the transmitter voltage by considering all harmonics of the waveforms, the first harmonic component is calculated separately for the measured transmitter

voltage as shown in Fig. 6.5(b). At nominal mutual inductance, the maximum power of 11 kW can be transferred to the battery. The transmitter voltage and current are maximum at this condition. When the mutual inductance is less than 14.3 μH, the transmitter current is limited at the peak value by reducing the transmitter voltage. Furthermore, by the reduction of *M*, the receiver current reduces and the output power decreases. When the mutual inductance goes up by reducing the air-gap between the coils, the transmitter voltage becomes maximum. However, the value of the input impedance seen from the transmitter side increases when mutual inductance value goes up. This will cause a reduction of the transmitter current. Thus, the output power reduces when mutual inductance increases.

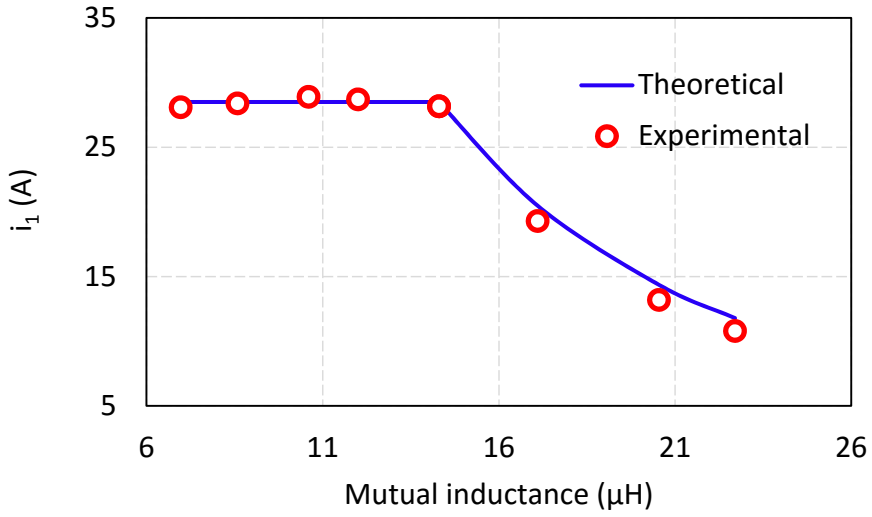

(a)

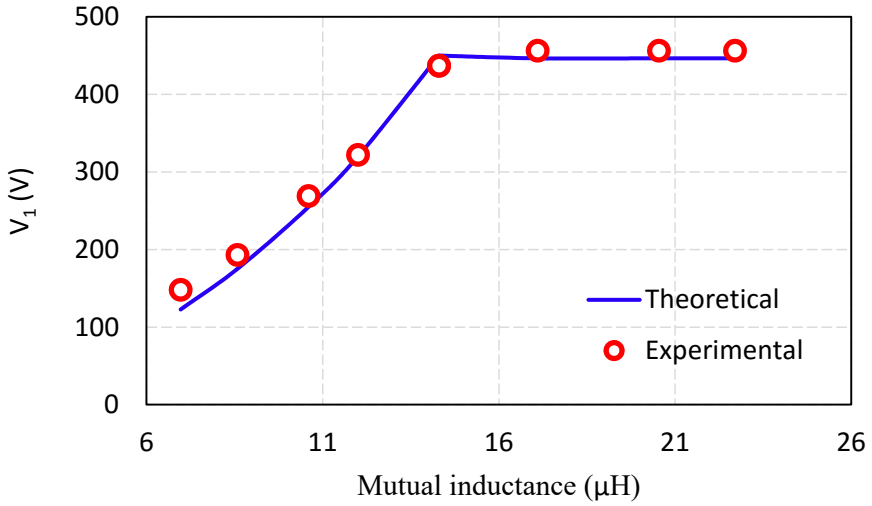

(b)

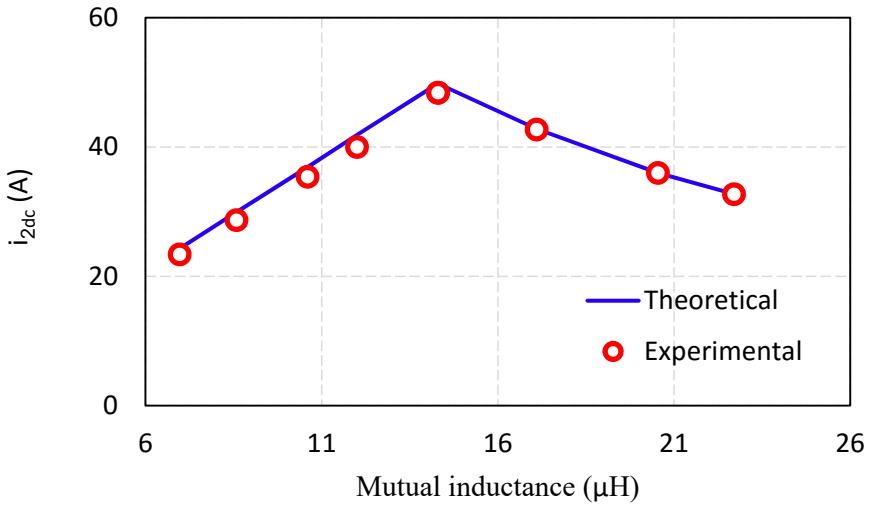

(c)

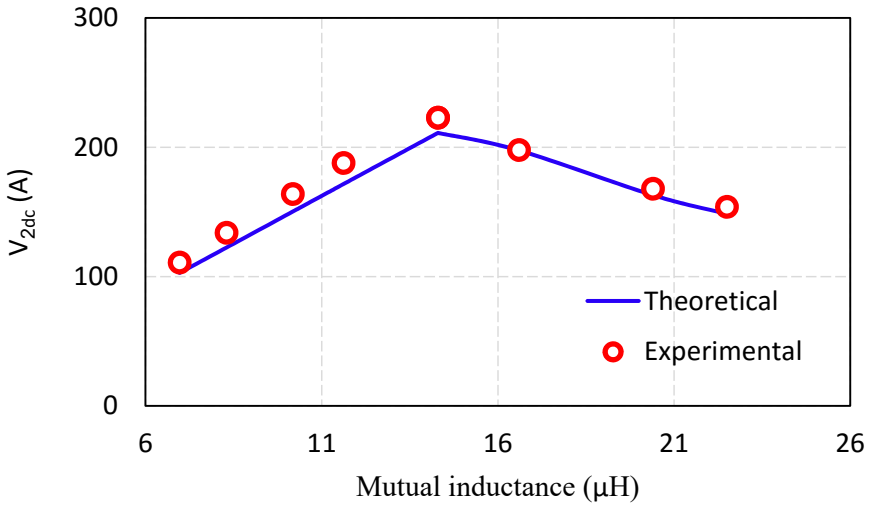

(d)

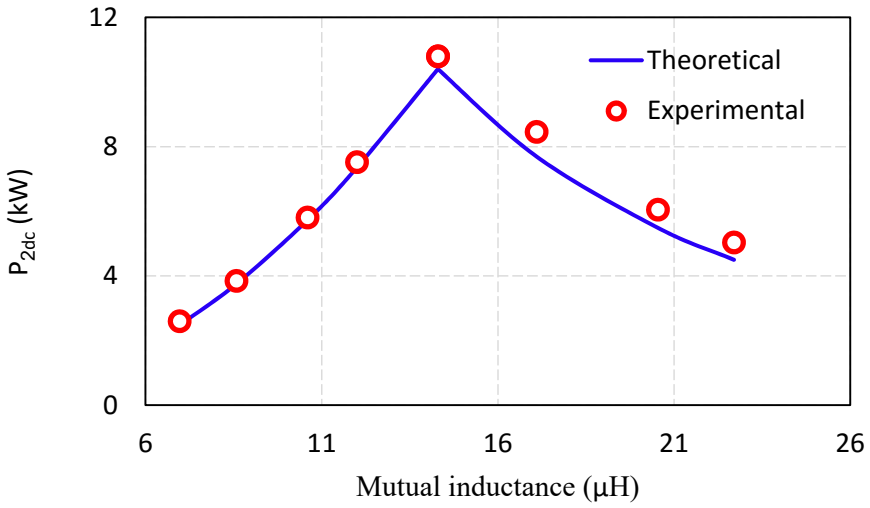

(e)

Fig. 6.5: Behavior the system under mutual inductance variations. (a) Transmitter current i_1, (b) receiver RMS voltage V_1, (c) receiver DC current i_{2dc}, (d) receiver DC voltage V_{2dc}, (e) power at the input of the DC-DC converter P_{2dc}.

The waveforms of the transmitter and receiver with the variations of the air-gap are presented in Fig. 6.6 and Fig. 6.7. When the air-gap is reduced from 25 cm to 20 cm, the transmitter current becomes lower than the nominal value. However, if the air-gap increases from 25 cm to 30 cm, the mutual inductance reduces and it causes limiting the transmitter current at the peak level with the transmitter side control.

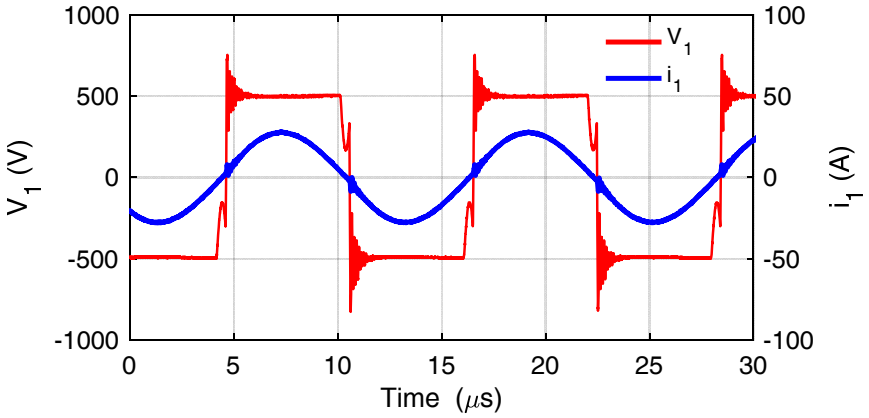

(a)

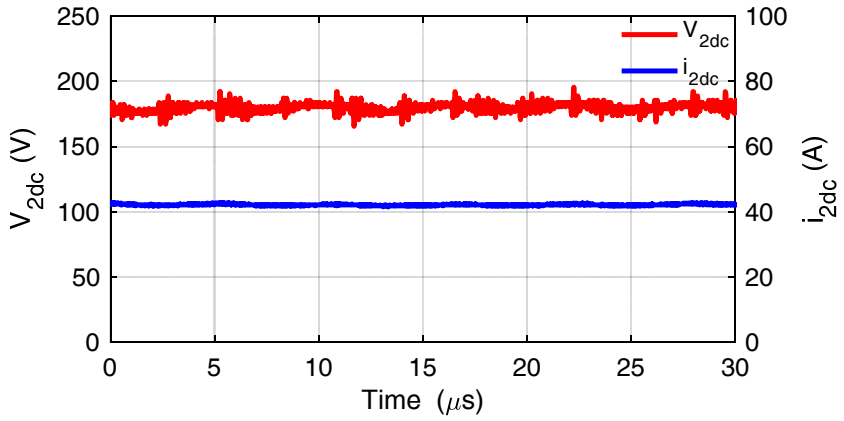

(b)

Fig. 6.6: Operation at 5 cm decrease in the air-gap and increase of the mutual inductance when R_{in} is 4.2 Ω. (a) Transmitter voltage V_1 and transmitter current i_1, (b) receiver DC voltage V_{2dc} and receiver DC current i_{2dc}.

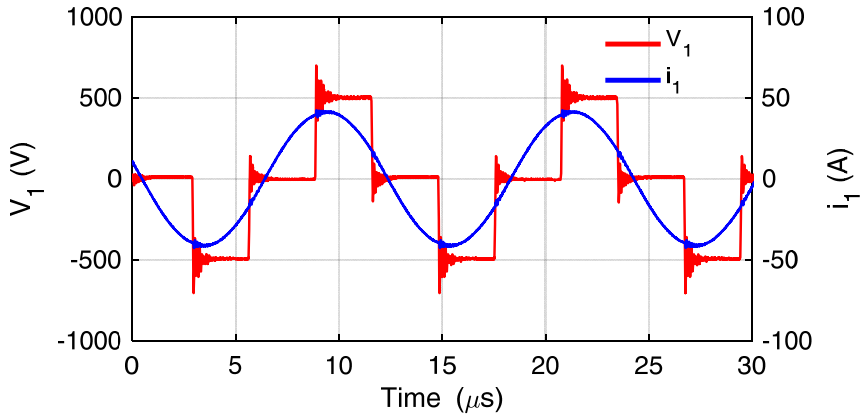

(a)

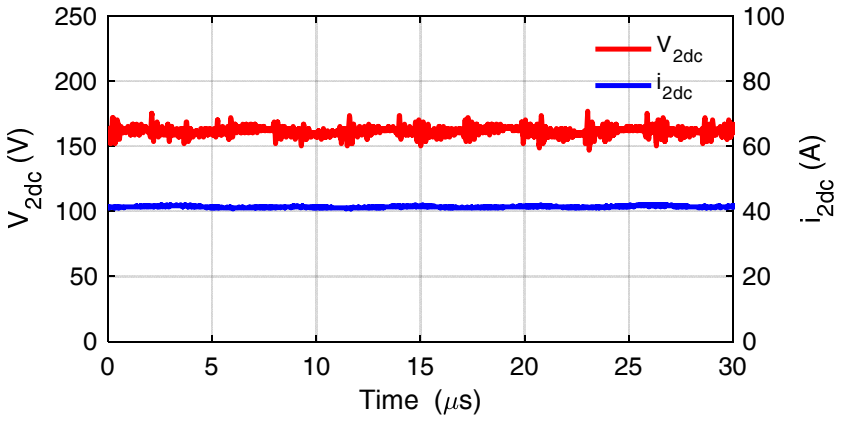

(b)

Fig. 6.7: Operation at 5 cm increase of the air-gap and the decease of the mutual inductance when R_{in} is 4.2 Ω. (a) Transmitter voltage V_1 and transmitter current i_1, (b) receiver DC voltage V_{2dc} and receiver DC current i_{2dc}.

6.3 Identification procedure

The identification method with phase shift angle monitoring described in chapter 3 is tested in this section. The parameters of the system are similar to the previous tests performed in 6.1 and 6.2. For the identification purpose, a constant peak current of 5 A is injected to the transmitter coil. When the transmitter and receiver coils become close to each other, the controller in the transmitter side increases the phase shift angle in order to maintain the current of the transmitter at 5 A peak. By performing several tests, the phase shift angle of 7° for α_{in} was selected. Thus, when the phase shift angle reaches 7°, the transmitter controller considers that the vehicle is present and mode of operation changes to power transfer mode. In this mode, the transmitter reference current changes from 5 A peak to 40 A peak. In order to increase the efficiency and avoid the problems regarding the magnetic field exposure issues, the H-bridge converter has to be turned off when the receiver leaves the transmitter coil. Again, the transmitter

controller monitors the phase shift angle and when it becomes less than 40°, the power transmission stops.

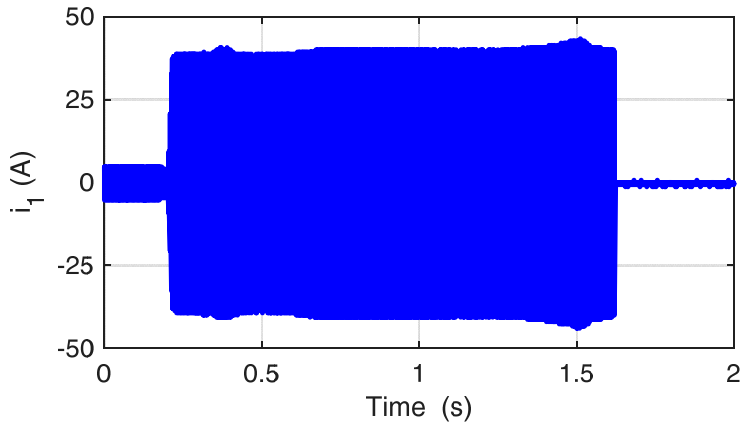

(a)

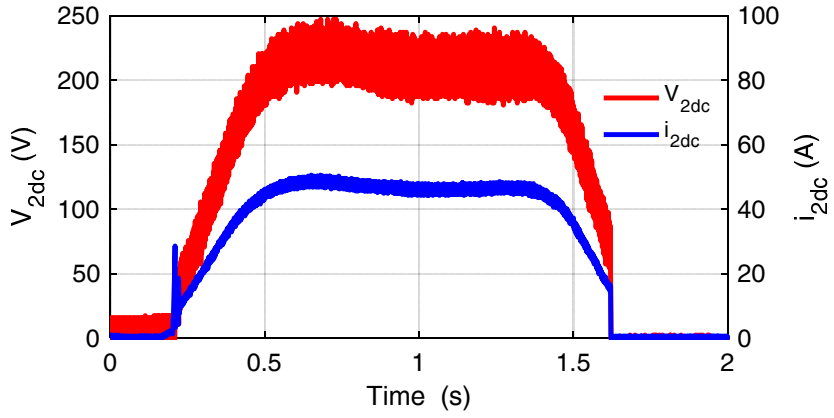

(b)

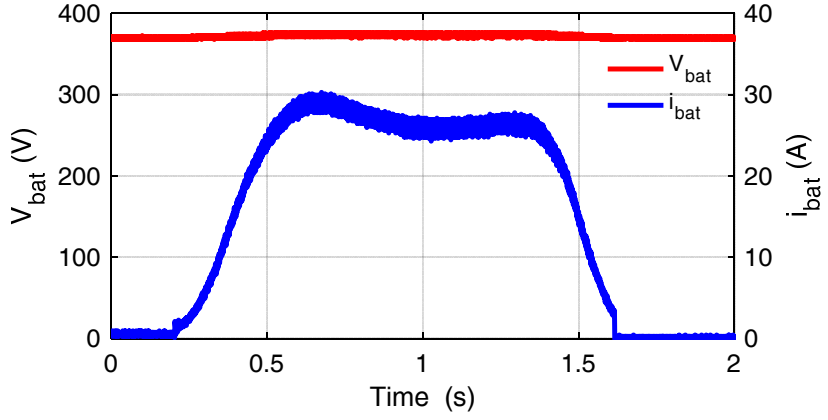

(c)

Fig. 6.8: Identification process and operation during the passage of the vehicle. (a) Transmitter current i_1, (b) receiver DC voltage V_{2dc} and receiver DC current i_{2dc}, (c) battery voltage V_{bat} and battery current i_{bat}.

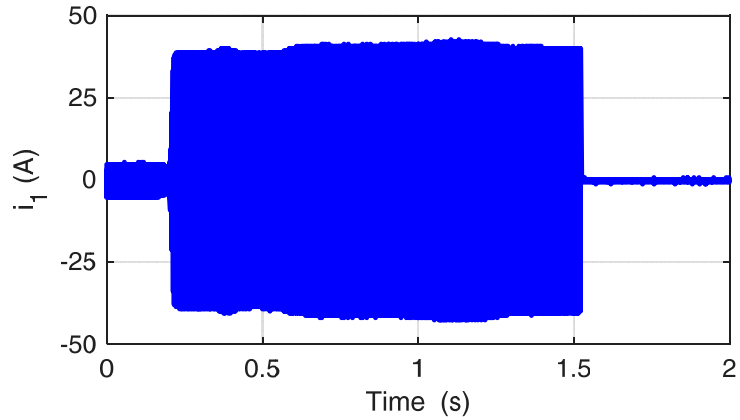

(a)

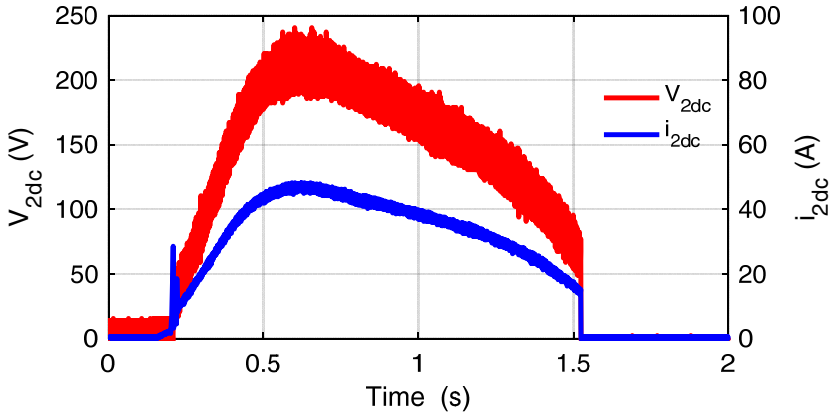

(b)

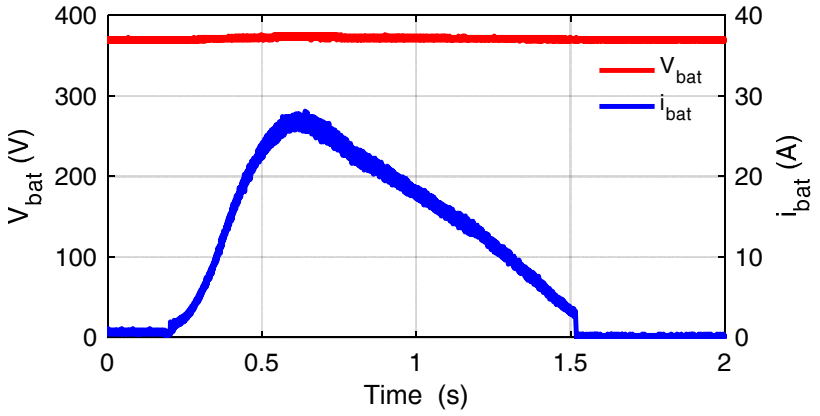

(c)

Fig. 6.9: Identification process and operation during the passage of the vehicle with gradual lateral misalignment. (a) Transmitter current i_1, (b) receiver DC voltage V_{2dc} and receiver DC current i_{2dc}, (c) battery voltage V_{bat} and battery current i_{bat}.

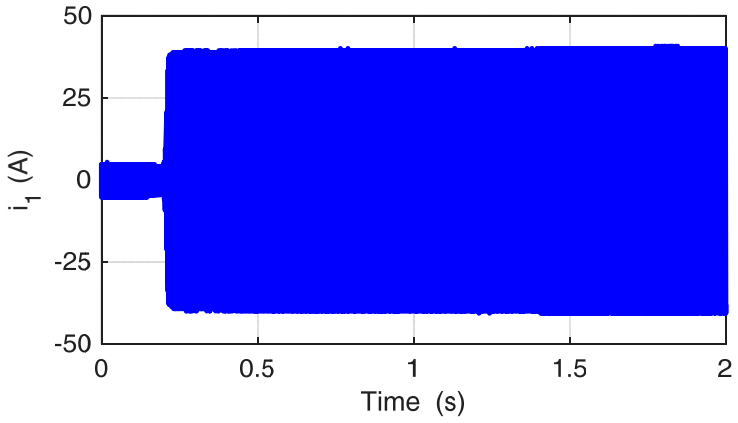

(a)

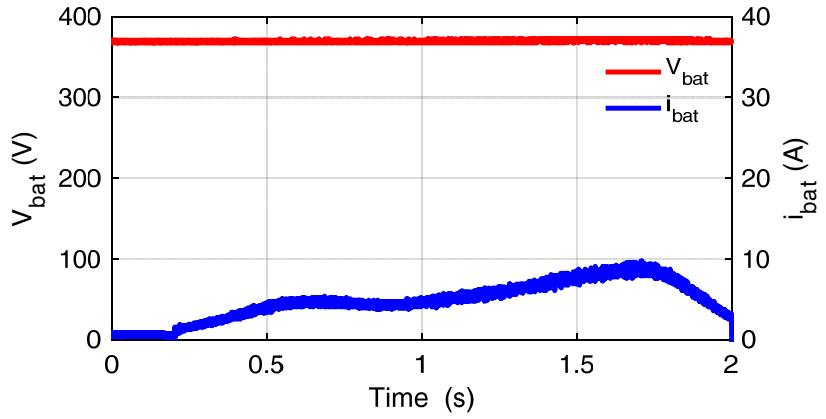

(b)

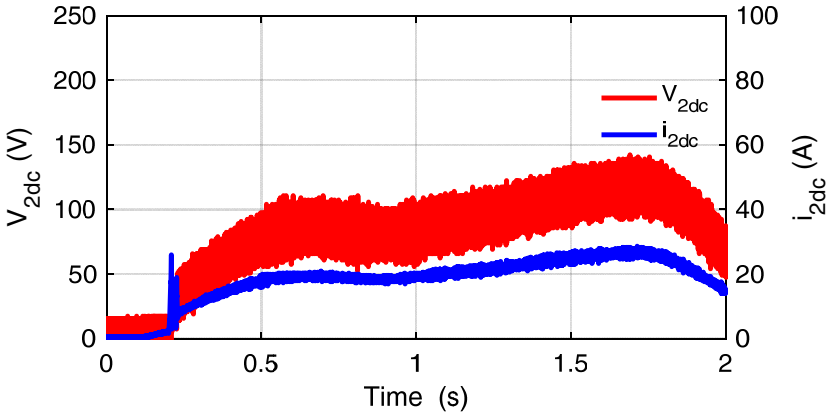

(c)

Fig. 6.10: Identification process and operation during the passage of the vehicle with high lateral misalignment. (a) Transmitter current i_1, (b) receiver DC voltage V_{2dc} and receiver DC current i_{2dc}, (c) battery voltage V_{bat} and battery current i_{bat}.

In order to emulate the passage of the vehicle, the receiver structure is moved above the transmitter coil with a speed of 4 km/h. The operation of the system during the identification process is shown in Fig. 6.8. After the presence of the receiver is identified, the transmitter current remains constant at the peak value but the receiver current and voltage follow the coupling variations. Fig. 6.9 shows the identification process when the receiver arrives properly but suddenly the lateral misalignment increases. In Fig. 6.10, the receiver arrives with a considerable lateral misalignment. The transmitter control is able to identify the presence of the receiver coil in a lateral misalignment of 30 cm. This is due to the fact that, during the identification process, the receiver is kept short circuit. In this situation, the impedance seen from the transmitter side becomes maximum. Thus, the presence of the receiver can be identified in a faster way.

The boost converter phase current and the receiver DC current during the passage of the vehicle are illustrated in Fig. 6.11. It can be seen from both figures the effect of the interleaving on the phase current ripple and input DC current ripple. Furthermore, the DC-DC converter operates at CCM during the passage of the receiver over the transmitter.

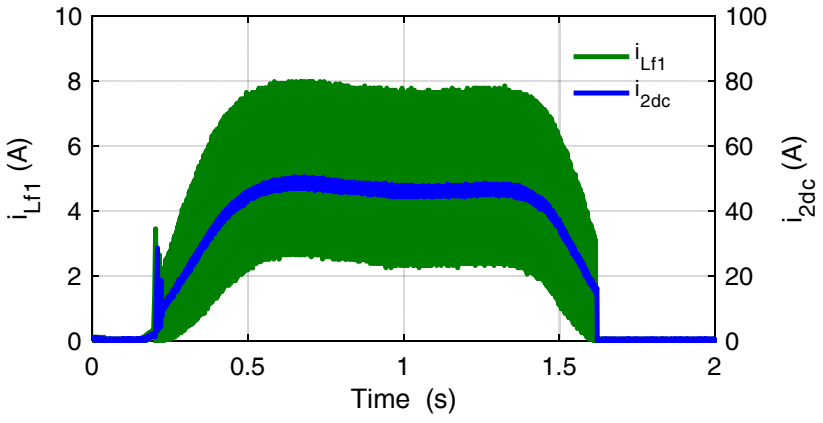

(a)

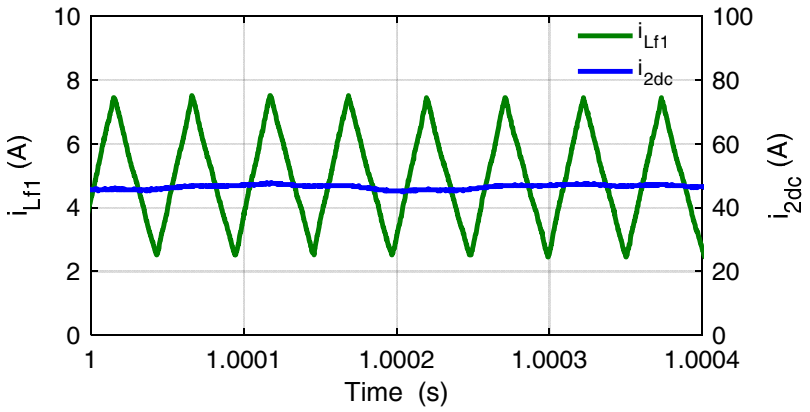

(b)

Fig. 6.11: Boost converter phase current and the receiver DC current. (a) During the passage of the vehicle, (b) zoomed waveform.

6.4 Operation with lateral misalignment

The operation of the control system during the lateral misalignment is analyzed. For this test, the air-gap is kept constant at the nominal value but the lateral misalignment in the x-direction is increased in steps of 5 cm. This test is performed with the maximum output power of 15 kW. In order to have this power level at the output of the system at the nominal condition when the lateral misalignment is zero, the input source voltage is defined 630 VDC and the transmitter RMS current is set to 35 A. Furthermore, R_{in} is defined 4.2 Ω.

The waveforms of i_1, V_1, and i_{2dc} for different lateral misalignments are presented in Fig. 6.12. When the transmitter and receiver coils are completely aligned, the mutual inductance is maximum. At this point, the transmitter current is 35 A, which is the peak of the transmitter control, the transmitter voltage is maximum and thus, the maximum power of 15 kW is transferred to the battery. At the presence of the lateral misalignment, the mutual inductance between the transmitter and receiver coils decreases. In case of misalignment, the transmitter current remains constant but the transmitter voltage reduces. Therefore, the transferred power to the battery reduces. If the lateral misalignment increases more, the transferred power reduces more.

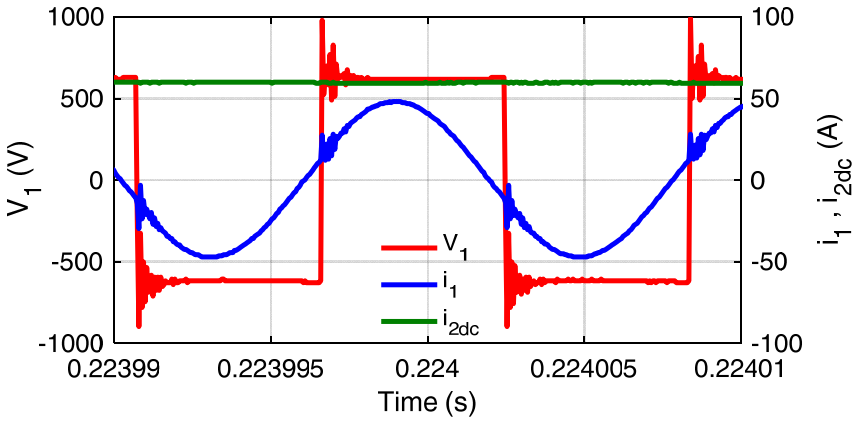

(a)

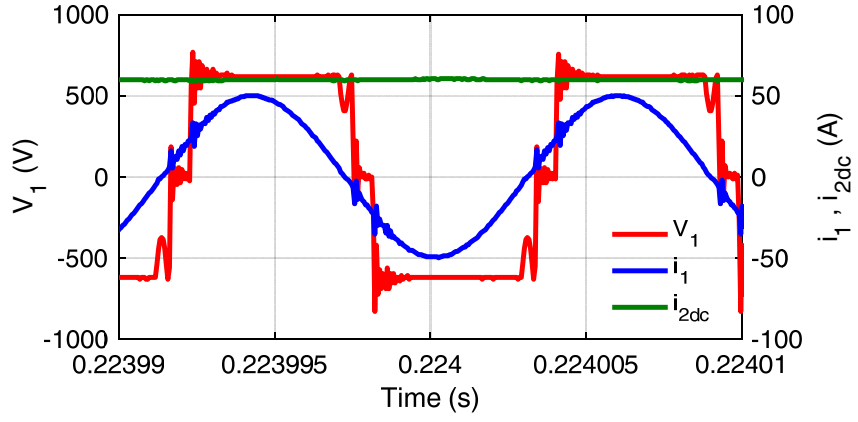

(b)

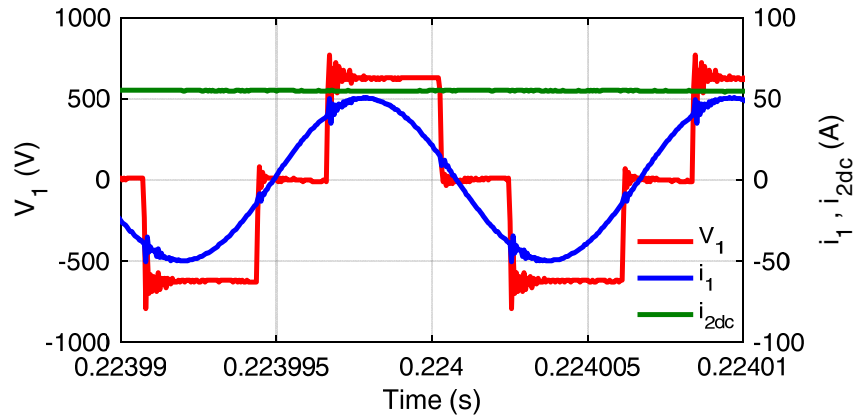

(c)

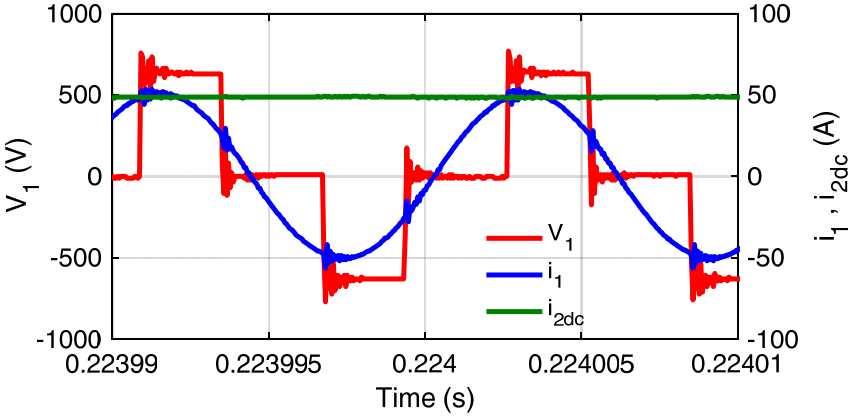

(d)

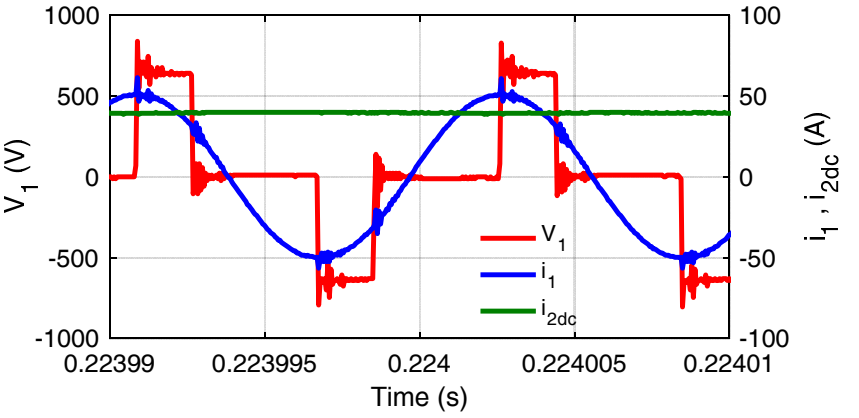

(e)

Fig. 6.12: Transmitter voltage and current and receiver DC current at different lateral misalignments. (a) Completely aligned, (b) 5 cm of misalignment, (c) 10 cm of misalignment, (d) 15 cm of misalignment, (e) 20 cm of misalignment.

The waveform of the power received by the battery versus the increase of the lateral misalignment is depicted in Fig. 6.13. For the lateral misalignment of 5 cm, theoretically, the output power must be lower than maximum power which was obtained in case of no misalignment. However, the output power is approximately constant. This is due to the fact that the transmitter current is a little more than 50 A peak and therefore, amount of the power transferred to the receiver is more. When

the lateral misalignment is equal to 20 cm, the battery receives approximately 6.7 kW.

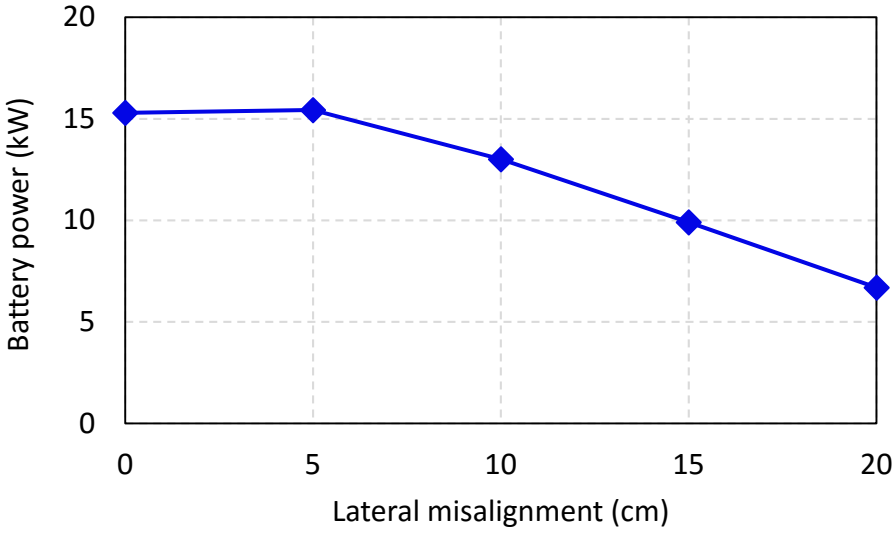

Fig. 6.13: Battery power at different lateral misalignments.

6.5 Efficiency analysis

In this section, the efficiency under the variations of the lateral misalignment in static charging mode is analyzed. The parameters of the test are similar to the previous test presented in 6.4. The efficiency is measured at different lateral misalignments with the steps of 5 cm, until a maximum of 20 cm, at the maximum output power of 15 kW. In order to calculate the total efficiency of the system, the efficiency from the input AC source at the grid side to the DC side at the battery point must be considered. However, in order to focus on the efficiency of the wireless power transfer system, only the efficiency of the input DC source to the battery is measured. Thus, the losses of the input AC-DC converter are not considered. From DC to DC efficiency point of view, the total losses of the system are composed of H-bridge converter losses, transmitter and receiver coils losses, the receiver rectifier losses and the DC-DC converter losses.

The current and voltage at the input and output side are measured and then the power and efficiency are measured using an HBM power analyzer. The measured power and efficiency for different lateral misalignments are presented in Table 6.1. DC source to battery efficiency of the system with various lateral misalignments is illustrated in Fig. 6.14. The efficiency is 88% at nominal air-gap and without any lateral misalignment. When the lateral misalignment goes beyond 5 cm, the efficiency gradually decreases. At the lateral misalignment of 20 cm, the efficiency is around 80%. The major losses of the system are coil losses. These losses are made up of the transmitter coil losses, receiver coil losses, ESR of the capacitors, core losses and losses in the aluminum shield. Thus, the efficiency of the wireless

charger can mainly be improved by redesigning the coil with higher coupling and lower resistance and employing resonant capacitors with lower ESR.

Table 6.1: Measured power and efficiency at different lateral misalignments.

Lateral misalign-ment (cm)	Power at input DC source (kW)	Power at DC-DC input (kW)	Power to the battery (kW)	DC-DC converter Efficiency (%)	DC source to battery efficiency (%)
0	17.43	15.58	15.29	98.17	87.75
5	17.52	15.73	15.43	98.08	88.07
10	14.99	13.29	13.01	97.87	86.81
15	11.78	10.19	9.904	97.18	84.11
20	8.418	6.957	6.688	96.13	79.44

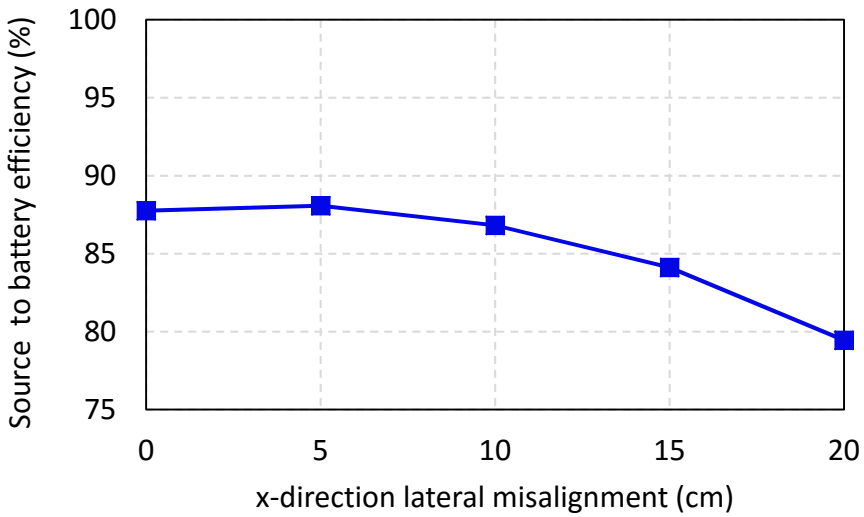

Fig. 6.14: DC source to battery efficiency at different lateral misalignments.

6.6 Analysis of common mode current

In the present WPT system, the common mode current or ground current is defined as the current that can flow from the embedded transmitter coil and cable through the ground by means of capacitive coupling. A series of tests have been carried out to evaluate the aspects of the ground currents. These currents can represent a problem when a complete WPT charging lane is active and many converters switch together in close spatial proximity. In such cases, the ground current could cause EMC problems with respect to the auxiliary electronics for the communications and the management of the charging process [173]. For this test, the transmitter H-bridge converter is supplied with 600 VDC. The H-bridge converter operates in 85 kHz and supplies the transmitter coil with 13 A. Ground

current for the system has been measured as the sum of the phase currents at the output of the insulated three-phase transformer that supplies the system. As seen in Fig. 6.15, a ground current takes place in correspondence of the H-bridge commutations. The current peak reaches 1A. This current is due to the fact that the transmitter coil has 10 turns. This number means an increase of the surface of the coil thus an increase of the capacitive coupling with respect to the ground.

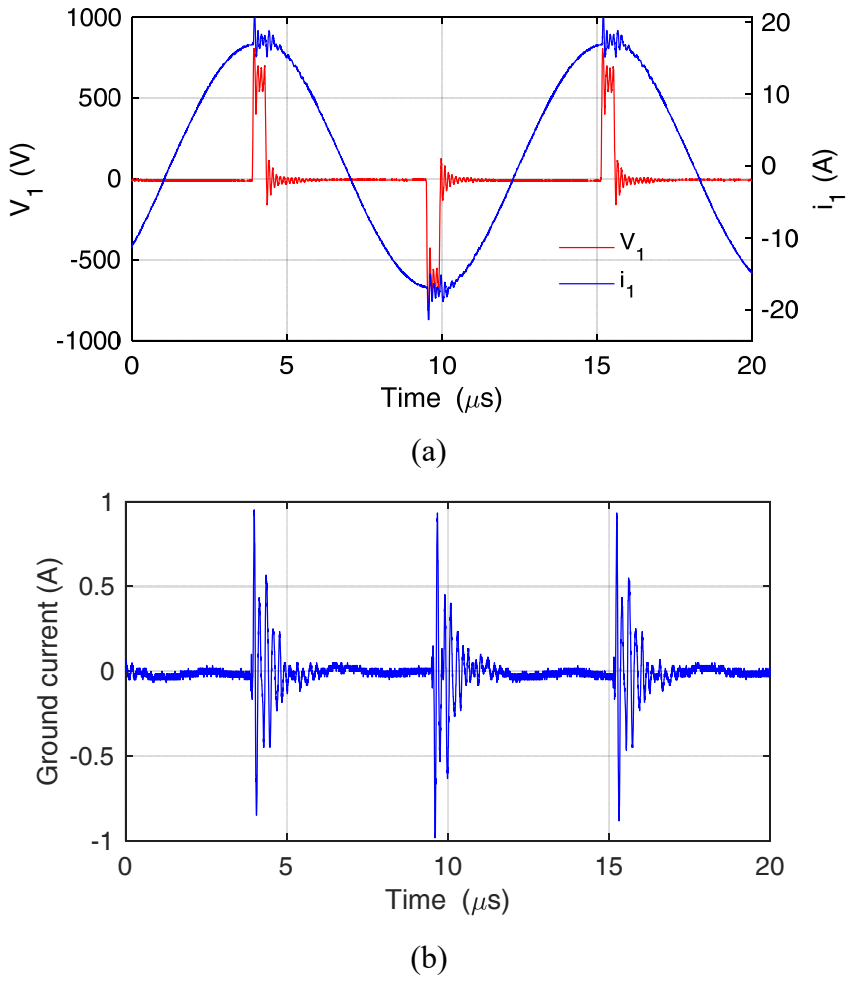

Fig. 6.15: Waveforms of the ground current test. (a) Transmitter current and voltage, (b) common mode current.

6.7 Dynamic charging

The operation of the WPT system during the dynamic charging of EV is assessed. For this test, all of the transmitter converters are connected to the transmitter coils. The transmitter converters are supplied by 650 V DC. For this test, the transmitter current is limited by the transmitter control and the maximum power that the battery received is 2 kW. This test is performed by employing 36 transmitter coils and the first ten coils are remained off. The coil number 23 is not supplied by the transmitter converter because the transmitter capacitor is broken. Since the

capacitor is buried in the ground with the transmitter coil, it is not possible to replace it with a new one. The test is performed with the rated air-gap of 25 cm and the speed of the vehicle is around 15 km/h. The presence of any misalignment at this speed of the vehicle is unavoidable.

For the identification of the vehicle, the turn-on angle and turn-off angle for each transmitter are selected independently via several tests. For the beginning of the charging process, the first transmitter coil of the charging lane goes to the identification mode. In this mode, the transmitter coil is supplied by a constant current of 5 A peak. The first transmitter coil waits for the vehicle. When the vehicle approaches the transmitter coil and the phase shift angle of the DC-AC converter reaches the turn-on angle, the converter changes the status form the identification mode to charging mode. In charging mode, the reference current of the H-bridge converter changes from 5 A peak to 18 A peak and the power transmission starts. Furthermore, at this moment a CAN message is sent to the next converter to go to the identification mode. During the passage of the receiver coil over the transmitter coil, the mutual inductance changes. At the moment the phase angle of the converter reaches the turn-off angle, the H-bridge converter detects the exit of the vehicle from the transmitter coil and the operation mode of the convert changes from the charging mode to idle mode. At this time, the second transmitter converter is waiting for the vehicle. This sequence continues until the vehicle leaves the last transmitter coil. At this moment, all of the transmitter coils become off. During the charging procedure, only one transmitter coil is in identification mode at the same time. This reduces the total power consumption of the identification process.

The important waveforms of the system during the dynamic charging of the vehicle are shown in Fig. 6.16. The main values have been obtained with a sampling time of 5ms. The speed of the vehicle is presented in Fig. 6.16(a). During the charging time, the speed of the vehicle is 15 km/h at maximum. The voltage of the battery is shown in Fig. 6.16(b). The voltage of the battery is 370 V. The battery current during the charging of the vehicle is presented in Fig. 6.16(c). The current of the battery has reached to 6 A. According to this figure, in addition to coil number 23 which was kept off, the other three coils have not participated in power transmission. This is happened due to the problem of the transmitter converters and also the communication. The variation of the peak current of the battery is due to the different resonant frequencies, different coil resistances and the misalignment between the receiver and transmitter coils. The power received by the battery is presented in Fig. 6.16(d). The battery receives approximately the power of 2 kW. It can be seen from this figure that the battery power waveform is oscillating between zero and maximum power. The amount of energy that the battery received during the passage of the vehicle is shown in Fig. 6.16(e). At this power level and vehicle speed, the battery of the vehicle has received 5.5 Wh of energy.

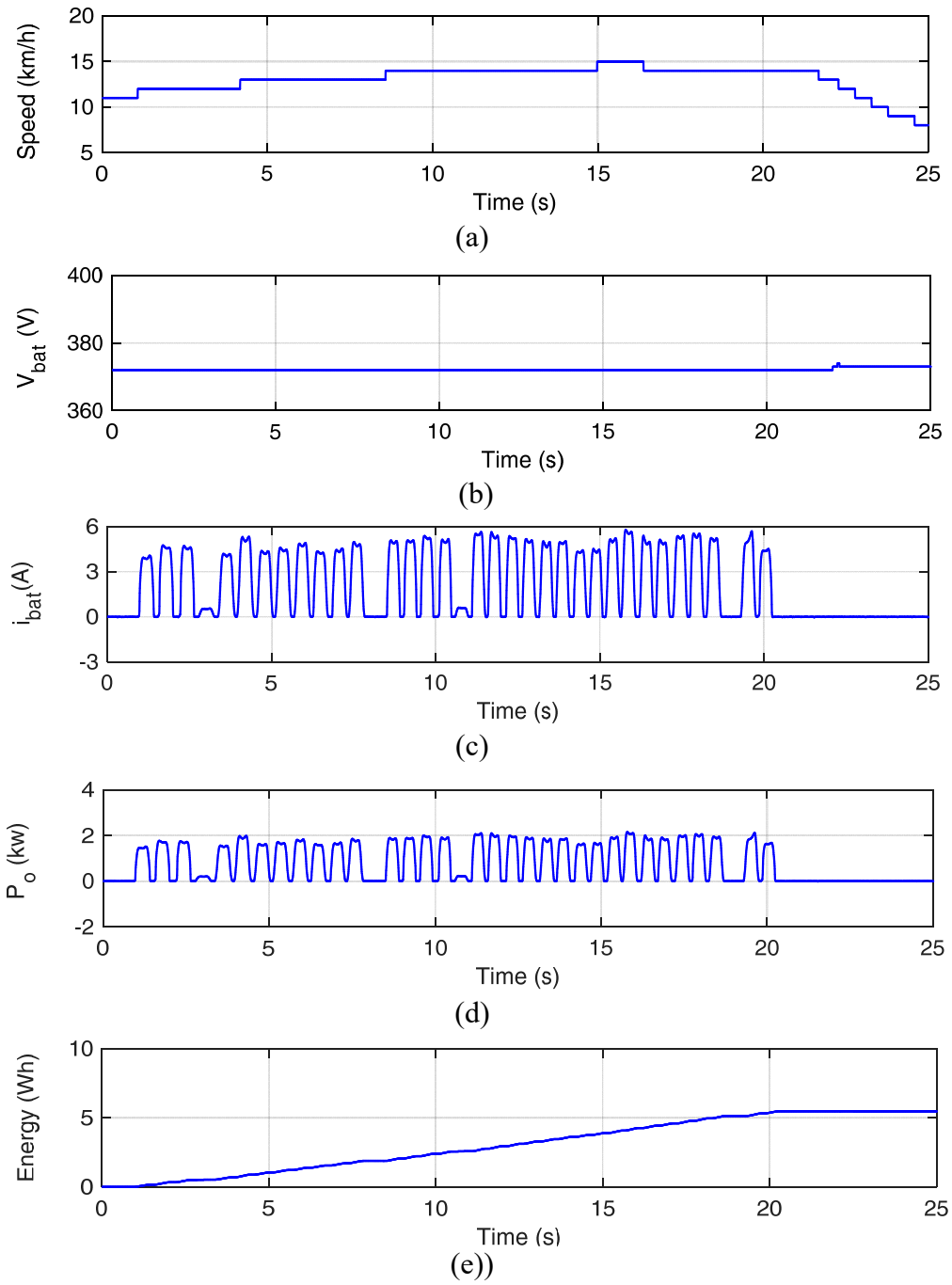

Fig. 6.16: Different quantities of the system during dynamic charging; (a) Vehicle speed, (b) battery voltage, (c) battery current, (d) received power by the battery, (e) received energy during the whole charging process.

6.8 Conclusion

In this chapter, the results of several experimental tests in static and dynamic charging modes were presented. According to the experimental results, the control was able to regulate the output power from the receiver and without any data exchange with the transmitter control for the power level from zero to the maximum

power. Due to the current control of the transmitter, the system was capable of operating with the presence of the lateral misalignment. The system was tested with the lateral misalignment of 20 cm. According to the results, the control strategy is suitable for operation in the dynamic charging of EV. Thus, the dynamic charging of the EV with 2 kW battery power and at the vehicle speed of 15 km/h was tested. With the help of the identification circuit, it was possible to identify the presence of the vehicle without any additional sensor or component. In addition, in order to reduce the identification circuit power consumption, the cascade activation of the identification circuit was used in the charging lane through the CAN messages. With this control strategy, only one transmitter coil was in identification mode at the same time and the power transmission took place only when the vehicle was above the transmitter coil.

Chapter 7

Conclusion

The application of WPT for charging an EV during movement is a feasible solution for solving the limited driving range of EVs. Starting two decades ago, many wireless charging solutions have been presented in the literature, and some of them have been developed practically for various transportation applications. However, there are still several critical issues, especially regarding the control of the charging process during the movement of the vehicle. The presented work was associated with the FABRIC project. The project goal was the construction and testing of a 100-m dynamic wireless charging prototype with a rating power of 20kW at a nominal air-gap of 25cm as well as the operating frequency of 85 kHz. This thesis provided solutions to the power control strategies limitations which have not been addressed before.

SS topology was chosen for the compensation of the coils since it has a simple structure and the values of the resonant capacitors are not dependent on the load or coupling coefficient variations during misalignment conditions. The effect of variations of frequency, load, and coupling on the system performance in SS topology was studied. It was shown that when switching frequency deviates from the resonant frequency, efficiency drops severely. Due to the lack of ferrite cores in the transmitter coil, the self-inductances of the coils were not affected very much by the misalignment. Therefore, the system can work at a fixed frequency in the presence of lateral misalignment.

For the purpose of regulating the output power, two new control strategies were proposed. In both control schemes, the transmitter limits the transmitter current in any misalignment condition, while through the receiver control, battery power can be regulated from the vehicle and without any data exchange. The lack of communication link in both control methods avoids possible delay in the charging process and makes the construction of the control simple. In addition to the control strategies, two novel methods for the identification of the vehicle in dynamic charging were introduced. In the proposed identification methods, the presence of the vehicle was identified only by the DC-AC converter of the transmitter and without any extra component. This simplifies the system and reduces the overall

cost when charging lane composed of several transmitters are necessary. The main contribution of this work is that whole charging process, including the identification and power regulation, is done without needing any additional component, sensor, or communication link.

The performance of the charging system in both static and dynamic conditions was analyzed using simulation. In static charging, the system behavior at diverse operating frequencies, power levels, and mutual inductances was studied. The control could regulate output power at the misalignment conditions. Also, the performance of the control system was investigated at different variations of the operating frequency. It was found that when the resonant frequencies of two sides are different, similar to conditions where the coils were covered by cement, in order to maximize the efficiency, the transmitter converter must operate at receiver resonant frequency. Also, the performance of the charging system during dynamic charging at different conditions, such as air-gap variations, different vehicle speeds, and various lateral misalignments, was evaluated. In nominal air-gap and at a 50 km/h vehicle speed, an efficiency of 80% and an output battery energy of 19.13 Wh were obtained.

The procedure of the construction of the charging system, including the implementation of the power electronic converter, the development of coils, and the embedding procedure was presented. The results of the power control obtained by the experimental tests showed good coherence with the simulation results, even in the presence of lateral misalignment or air-gap variations.

Some future works are suggested below:

- Because of the shape of coils and the space between the transmitter coils, the battery and the grid currents are faced with severe oscillations during the passage of the vehicle. This problem could be solved by modifying the control system and applying an additional receiver.
- The high voltage stress on the resonant capacitor in SS topology limits the power transmission capability. One solution could be the application of LCC compensation topology for the transmitter and receiver in order to reduce the voltage stress of the capacitors. In addition, the control scheme needs to be modified according to this compensation topology, since in this case, the identification circuit is not necessary.
- By implementation of the control for the active rectifier and control of phase angle between the voltage and current of the active rectifier, it will be possible to control the power transmission direction, providing more options for the system.

Published papers

- M. Khalilian, S. G. Rosu, V. Cirimele, P. Guglielmi, and R. Ruffo, “Load identification in dynamic wireless power transfer system utilizing current injection in the transmitting coil,” in *2016 IEEE Wireless Power Transfer Conference (WPTC)*, Aveiro, Portugal, 2016, pp. 1–4.
- S. G. Rosu, M. Khalilian, V. Cirimele, and P. Guglielmi, “A dynamic wireless charging system for electric vehicles based on DC/AC converters with SiC MOSFET-IGBT switches and resonant gate-drive,” in *IECON 2016 - 42nd Annual Conference of the IEEE Industrial Electronics Society*, Florence, Italy, 2016, pp. 4465–4470.
- R. Ruffo, V. Cirimele, P. Guglielmi, and M. Khalilian, “A coupled mechanical-electrical simulator for the operational requirements estimation in a dynamic IPT system for electric vehicles,” in *2016 IEEE Wireless Power Transfer Conference (WPTC)*, Aveiro, Portugal, 2016, pp. 1–4.
- R. Ruffo, M. Khalilian, V. Cirimele, P. Guglielmi, and M. Cesano, “Theoretical and experimental comparison of two interoperable dynamic wireless power transfer systems for electric vehicles,” in *2017 IEEE Southern Power Electronics Conference (SPEC)*, Puerto Varas, Chile, 2017, pp. 1–6.
- R. Ruffo, V. Cirimele, M. Diana, M. Khalilian, A. L. Ganga, and P. Guglielmi, “Sensorless Control of the Charging Process of a Dynamic Inductive Power Transfer System With an Interleaved Nine-Phase Boost Converter,” *IEEE Trans. Ind. Electron.*, vol. 65, no. 10, pp. 7630–7639, Oct. 2018.
- M. Khalilian and P. Guglielmi, “Charging Process Control of Dynamic Wireless Power Transfer System with Active Rectifier and without Wireless Communication System,” in *2018 IEEE 18th International Power Electronics and Motion Control Conference (PEMC)*, Budapest, 2018, pp. 229–235.
- M. Khalilian and P. Guglielmi, “Primary-Side Control of a Wireless Power Transfer System with Double-Sided LCC Compensation Topology for Electric Vehicle Battery Charging,” in *2018 IEEE International Telecommunications Energy Conference (INTELEC)*, Turin, Italy, 2018, pp. 1–6.
- M. Khalilian and P. Guglielmi, “A hybrid topology wireless power transfer system with constant current or constant voltage output for battery charging application,” in *2019 IEEE International Conference of Electrical and Electronic Technologies for Automotive (IEIT Automotive)*, Turin, Italy, 2019, pp. 1–6.

References

[1] A. Ahmad, M. S. Alam, and R. Chabaan, "A Comprehensive Review of Wireless Charging Technologies for Electric Vehicles," *IEEE Trans. Transp. Electrification*, vol. 4, no. 1, pp. 38–63, Mar. 2018.

[2] M. Yilmaz and P. T. Krein, "Review of Battery Charger Topologies, Charging Power Levels, and Infrastructure for Plug-In Electric and Hybrid Vehicles," *IEEE Trans. Power Electron.*, vol. 28, no. 5, pp. 2151–2169, May 2013.

[3] Z. Bi, T. Kan, C. C. Mi, Y. Zhang, Z. Zhao, and G. A. Keoleian, "A review of wireless power transfer for electric vehicles: Prospects to enhance sustainable mobility," *Appl. Energy*, vol. 179, pp. 413–425, Oct. 2016.

[4] W. Eberle and F. Musavi, "Overview of wireless power transfer technologies for electric vehicle battery charging," *IET Power Electron.*, vol. 7, no. 1, pp. 60–66, Jan. 2014.

[5] C. Qiu, K. T. Chau, C. Liu, and C. C. Chan, "Overview of wireless power transfer for electric vehicle charging," in *2013 World Electric Vehicle Symposium and Exhibition (EVS27)*, Barcelona, Spain, 2013, pp. 1–9.

[6] M. P. Kazmierkowski, R. M. Miskiewicz, and A. J. Moradewicz, "Inductive coupled contactless energy transfer systems - a review," in *2015 Selected Problems of Electrical Engineering and Electronics (WZEE)*, Kielce, Poland, 2015, pp. 1–6.

[7] C. Panchal, S. Stegen, and J. Lu, "Review of static and dynamic wireless electric vehicle charging system," *Eng. Sci. Technol. Int. J.*, vol. 21, no. 5, pp. 922–937, Oct. 2018.

[8] F. Lu, H. Zhang, H. Hofmann, and C. C. Mi, "An Inductive and Capacitive Combined Wireless Power Transfer System With LC-Compensated Topology," *IEEE Trans. Power Electron.*, vol. 31, no. 12, pp. 8471–8482, Dec. 2016.

[9] K. A. Kalwar, M. Aamir, and S. Mekhilef, "Inductively coupled power transfer (ICPT) for electric vehicle charging – A review," *Renew. Sustain. Energy Rev.*, vol. 47, pp. 462–475, Jul. 2015.

[10] D. Patil, M. K. McDonough, J. M. Miller, B. Fahimi, and P. T. Balsara, "Wireless Power Transfer for Vehicular Applications: Overview and Challenges," *IEEE Trans. Transp. Electrification*, vol. 4, no. 1, pp. 3–37, Mar. 2018.

[11] V. Cirimele, F. Freschi, and M. Mitolo, "Inductive power transfer for automotive applications: State-of-the-art and future trends," in *2016 IEEE Industry Applications Society Annual Meeting*, Portland, OR, USA, 2016, pp. 1–8.

[12] Y. J. Jang, “Survey of the operation and system study on wireless charging electric vehicle systems,” *Transp. Res. Part C Emerg. Technol.*, vol. 95, pp. 844–866, Oct. 2018.

[13] C. T. Rim and C. Mi, *Wireless power transfer for electric vehicles and mobile devices*, First edition. Hoboken, NJ: John Wiley & Sons, 2017.

[14] V. Cirimele, M. Diana, F. Freschi, and M. Mitolo, “Inductive Power Transfer for Automotive Applications: State-of-the-Art and Future Trends,” *IEEE Trans. Ind. Appl.*, vol. 54, no. 5, pp. 4069–4079, Sep. 2018.

[15] M. Yilmaz, V. T. Buyukdegirmenci, and P. T. Krein, “General design requirements and analysis of roadbed inductive power transfer system for dynamic electric vehicle charging,” in *2012 IEEE Transportation Electrification Conference and Expo (ITEC)*, Dearborn, MI, USA, 2012, pp. 1–6.

[16] S. Choi, J. Huh, W. Y. Lee, S. W. Lee, and C. T. Rim, “New Cross-Segmented Power Supply Rails for Roadway-Powered Electric Vehicles,” *IEEE Trans. Power Electron.*, vol. 28, no. 12, pp. 5832–5841, Dec. 2013.

[17] V. Cirimele, L. Pichon, and F. Freschi, “Electromagnetic modeling and performance comparison of different pad-to-pad length ratio for dynamic inductive power transfer,” in *IECON 2016 - 42nd Annual Conference of the IEEE Industrial Electronics Society*, Florence, Italy, 2016, pp. 4499–4503.

[18] S. Y. Choi, B. W. Gu, S. Y. Jeong, and C. T. Rim, “Advances in Wireless Power Transfer Systems for Roadway-Powered Electric Vehicles,” *IEEE J. Emerg. Sel. Top. Power Electron.*, vol. 3, no. 1, pp. 18–36, Mar. 2015.

[19] G. Buja, M. Bertoluzzo, and H. K. Dashora, “Lumped Track Layout Design for Dynamic Wireless Charging of Electric Vehicles,” *IEEE Trans. Ind. Electron.*, vol. 63, no. 10, pp. 6631–6640, Oct. 2016.

[20] J. M. Miller *et al.*, “Demonstrating Dynamic Wireless Charging of an Electric Vehicle: The Benefit of Electrochemical Capacitor Smoothing,” *IEEE Power Electron. Mag.*, vol. 1, no. 1, pp. 12–24, Mar. 2014.

[21] C. C. Mi, G. Buja, S. Y. Choi, and C. T. Rim, “Modern Advances in Wireless Power Transfer Systems for Roadway Powered Electric Vehicles,” *IEEE Trans. Ind. Electron.*, vol. 63, no. 10, pp. 6533–6545, Oct. 2016.

[22] S. E. Shladover, “PATH at 20—History and Major Milestones,” *IEEE Trans. Intell. Transp. Syst.*, vol. 8, no. 4, pp. 584–592, Dec. 2007.

[23] Y. D. Ko and Y. J. Jang, “The Optimal System Design of the Online Electric Vehicle Utilizing Wireless Power Transmission Technology,” *IEEE Trans. Intell. Transp. Syst.*, vol. 14, no. 3, pp. 1255–1265, Sep. 2013.

[24] J. Huh, S. W. Lee, W. Y. Lee, G. H. Cho, and C. T. Rim, “Narrow-Width Inductive Power Transfer System for Online Electrical Vehicles,” *IEEE Trans. Power Electron.*, vol. 26, no. 12, pp. 3666–3679, Dec. 2011.

[25] S. Y. Choi, S. Y. Jeong, B. W. Gu, G. C. Lim, and C. T. Rim, “Ultraslim S-Type Power Supply Rails for Roadway-Powered Electric Vehicles,” *IEEE Trans. Power Electron.*, vol. 30, no. 11, pp. 6456–6468, Nov. 2015.

[26] J. Shin *et al.*, “Design and Implementation of Shaped Magnetic-Resonance-Based Wireless Power Transfer System for Roadway-Powered Moving Electric Vehicles,” *IEEE Trans. Ind. Electron.*, vol. 61, no. 3, pp. 1179–1192, Mar. 2014.

[27] V. X. Thai, S. Y. Choi, B. H. Choi, J. H. Kim, and C. T. Rim, “Coreless power supply rails compatible with both stationary and dynamic charging of electric vehicles,” in *2015 IEEE 2nd International Future Energy Electronics Conference (IFEEC)*, Taipei, Taiwan, 2015, pp. 1–5.

[28] G. A. Covic and J. T. Boys, “Modern Trends in Inductive Power Transfer for Transportation Applications,” *IEEE J. Emerg. Sel. Top. Power Electron.*, vol. 1, no. 1, pp. 28–41, Mar. 2013.

[29] G. A. Covic and J. T. Boys, “Inductive Power Transfer,” *Proc. IEEE*, vol. 101, no. 6, pp. 1276–1289, Jun. 2013.

[30] J. T. Boys and G. A. Covic, “The Inductive Power Transfer Story at the University of Auckland,” *IEEE Circuits Syst. Mag.*, vol. 15, no. 2, pp. 6–27, 2015.

[31] A. Kamineni, G. A. Covic, and J. T. Boys, “Analysis of Coplanar Intermediate Coil Structures in Inductive Power Transfer Systems,” *IEEE Trans. Power Electron.*, vol. 30, no. 11, pp. 6141–6154, Nov. 2015.

[32] M. Budhia, G. A. Covic, and J. T. Boys, “Design and Optimization of Circular Magnetic Structures for Lumped Inductive Power Transfer Systems,” *IEEE Trans. Power Electron.*, vol. 26, no. 11, pp. 3096–3108, Nov. 2011.

[33] M. Budhia, G. Covic, and J. Boys, “A new IPT magnetic coupler for electric vehicle charging systems,” in *IECON 2010 - 36th Annual Conference on IEEE Industrial Electronics Society*, Glendale, AZ, USA, 2010, pp. 2487–2492.

[34] T.-D. Nguyen, S. Li, W. Li, and C. C. Mi, “Feasibility study on bipolar pads for efficient wireless power chargers,” in *2014 IEEE Applied Power Electronics Conference and Exposition - APEC 2014*, Fort Worth, TX, USA, 2014, pp. 1676–1682.

[35] M. Budhia, J. T. Boys, G. A. Covic, and C.-Y. Huang, “Development of a Single-Sided Flux Magnetic Coupler for Electric Vehicle IPT Charging Systems,” *IEEE Trans. Ind. Electron.*, vol. 60, no. 1, pp. 318–328, Jan. 2013.

[36] A. Zaheer, H. Hao, G. A. Covic, and D. Kacprzak, “Investigation of Multiple Decoupled Coil Primary Pad Topologies in Lumped IPT Systems for Interoperable Electric Vehicle Charging,” *IEEE Trans. Power Electron.*, vol. 30, no. 4, pp. 1937–1955, Apr. 2015.

[37] J. H. Kim *et al.*, “Development of 1-MW Inductive Power Transfer System for a High-Speed Train,” *IEEE Trans. Ind. Electron.*, vol. 62, no. 10, pp. 6242–6250, Oct. 2015.

[38] K. Ukita, “Power transfer performance verification of a non-contact power supply system for railway vehicles,” *QR RTRI*, vol. 57, no. 3, pp. 228–233, 2016.

[39] K. Throngnumchai, A. Hanamura, Y. Naruse, and K. Takeda, “Design and evaluation of a wireless power transfer system with road embedded transmitter coils for dynamic charging of electric vehicles,” in *2013 World Electric Vehicle Symposium and Exhibition (EVS27)*, Barcelona, Spain, 2013, pp. 1–10.

[40] A. Foote and O. C. Onar, “A review of high-power wireless power transfer,” in *2017 IEEE Transportation Electrification Conference and Expo (ITEC)*, Chicago, IL, USA, 2017, pp. 234–240.

[41] R. Tavakoli and Z. Pantic, “Analysis, Design, and Demonstration of a 25-kW Dynamic Wireless Charging System for Roadway Electric Vehicles,” *IEEE J. Emerg. Sel. Top. Power Electron.*, vol. 6, no. 3, pp. 1378–1393, Sep. 2018.

[42] J. M. Miller, P. T. Jones, J.-M. Li, and O. C. Onar, “ORNL Experience and Challenges Facing Dynamic Wireless Power Charging of EV’s,” *IEEE Circuits Syst. Mag.*, vol. 15, no. 2, pp. 40–53, 2015.

[43] O. C. Onar, J. M. Miller, S. L. Campbell, C. Coomer, Cliff. P. White, and L. E. Seiber, “A novel wireless power transfer for in-motion EV/PHEV charging,” in *2013 Twenty-Eighth Annual IEEE Applied Power Electronics Conference and Exposition (APEC)*, Long Beach, CA, USA, 2013, pp. 3073–3080.

[44] A. Amditis, G. Karaseitanidis, I. Damousis, P. Guglielmi, and V. Cirimele, “Dynamic Wireless Charging for More Efficient FEVs: The Fabric Project Concept,” in *MedPower 2014*, Athens, Greece, 2014, pp. 29 (6 .)-29 (6 .).

[45] C.-S. Wang, O. H. Stielau, and G. A. Covic, “Design Considerations for a Contactless Electric Vehicle Battery Charger,” *IEEE Trans. Ind. Electron.*, vol. 52, no. 5, pp. 1308–1314, Oct. 2005.

[46] V. Cirimele, S. G. Rosu, P. Guglielmi, and F. Freschi, “Performance evaluation of wireless power transfer systems for electric vehicles using the opposition method,” in *2015 IEEE 1st International Forum on Research and Technologies for Society and Industry Leveraging a better tomorrow (RTSI)*, Torino, Italy, 2015, pp. 546–550.

[47] V. Cirimele, F. Freschi, and P. Guglielmi, “Wireless power transfer structure design for electric vehicle in charge while driving,” in *2014 International Conference on Electrical Machines (ICEM)*, Berlin, Germany, 2014, pp. 2461–2467.

[48] J. L. Villa, J. Sallan, J. F. Sanz Osorio, and A. Llombart, “High-Misalignment Tolerant Compensation Topology For ICPT Systems,” *IEEE Trans. Ind. Electron.*, vol. 59, no. 2, pp. 945–951, Feb. 2012.

[49] K. Aditya and S. S. Williamson, “Comparative study of Series-Series and Series-Parallel compensation topologies for electric vehicle charging,” in *2014 IEEE 23rd International Symposium on Industrial Electronics (ISIE)*, Istanbul, 2014, pp. 426–430.

[50] M. Chinthavali, Zhiqiang Wang, and S. Campbell, “Analytical modeling of wireless power transfer (WPT) systems for electric vehicle application,” in

2016 IEEE Transportation Electrification Conference and Expo (ITEC), Dearborn, MI, USA, 2016, pp. 1–8.

[51] R. K. Jha, S. Giacomuzzi, G. Buja, M. Bertoluzzo, and M. K. Naik, "Efficiency and power sizing of SS vs. SP topology for wireless battery chargers," in *2016 IEEE International Power Electronics and Motion Control Conference (PEMC)*, Varna, Bulgaria, 2016, pp. 1014–1019.

[52] C. Fang, J. Song, L. Lin, and Y. Wang, "Practical considerations of series-series and series-parallel compensation topologies in wireless power transfer system application," in *2017 IEEE PELS Workshop on Emerging Technologies: Wireless Power Transfer (WoW)*, Chongqing, China, 2017, pp. 255–259.

[53] C. Auvigne, P. Germano, Y. Perriard, and D. Ladas, "About tuning capacitors in inductive coupled power transfer systems," in *2013 15th European Conference on Power Electronics and Applications (EPE)*, Lille, France, 2013, pp. 1–10.

[54] V. Ravikiran and R. K. Keshri, "Comparative evaluation of S-S and P-S topologies for wireless charging of electrical vehicles," in *IECON 2017 - 43rd Annual Conference of the IEEE Industrial Electronics Society*, Beijing, 2017, pp. 5324–5329.

[55] K. Okada, K. Iimura, N. Hoshi, and J. Haruna, "Comparison of two kinds of compensation schemes on inductive power transfer systems for electric vehicle," in *2012 IEEE Vehicle Power and Propulsion Conference*, Seoul, Korea (South), 2012, pp. 766–771.

[56] C. Duan, C. Jiang, A. Taylor, and K. (Hua) Bai, "Design of a zero-voltage-switching large-air-gap wireless charger with low electric stress for electric vehicles," *IET Power Electron.*, vol. 6, no. 9, pp. 1742–1750, Nov. 2013.

[57] X. Qu, Y. Jing, H. Han, S.-C. Wong, and C. K. Tse, "Higher Order Compensation for Inductive-Power-Transfer Converters With Constant-Voltage or Constant-Current Output Combating Transformer Parameter Constraints," *IEEE Trans. Power Electron.*, vol. 32, no. 1, pp. 394–405, Jan. 2017.

[58] W. Zhang and C. C. Mi, "Compensation Topologies of High-Power Wireless Power Transfer Systems," *IEEE Trans. Veh. Technol.*, vol. 65, no. 6, pp. 4768–4778, Jun. 2016.

[59] U. K. Madawala and D. J. Thrimawithana, "A Bidirectional Inductive Power Interface for Electric Vehicles in V2G Systems," *IEEE Trans. Ind. Electron.*, vol. 58, no. 10, pp. 4789–4796, Oct. 2011.

[60] S. Ge, C. Liu, H. Li, Y. Guo, and G. Cai, "Double-LCL resonant compensation network for electric vehicles wireless power transfer: experimental study and analysis," *IET Power Electron.*, vol. 9, no. 11, pp. 2262–2270, Sep. 2016.

[61] S. Li, W. Li, J. Deng, T. D. Nguyen, and C. C. Mi, "A Double-Sided LCC Compensation Network and Its Tuning Method for Wireless Power

Transfer," *IEEE Trans. Veh. Technol.*, vol. 64, no. 6, pp. 2261–2273, Jun. 2015.

[62] J. Deng, J. Deng, W. Li, S. Li, and C. Mi, "Magnetic integration of LCC compensated resonant converter for inductive power transfer applications," in *2014 IEEE Energy Conversion Congress and Exposition (ECCE)*, Pittsburgh, PA, USA, 2014, pp. 660–667.

[63] F. Lu, H. Hofmann, J. Deng, and C. Mi, "Output power and efficiency sensitivity to circuit parameter variations in double-sided LCC-compensated wireless power transfer system," in *2015 IEEE Applied Power Electronics Conference and Exposition (APEC)*, Charlotte, NC, USA, 2015, pp. 597–601.

[64] W. Li, H. Zhao, J. Deng, S. Li, and C. C. Mi, "Comparison Study on SS and Double-Sided LCC Compensation Topologies for EV/PHEV Wireless Chargers," *IEEE Trans. Veh. Technol.*, vol. 65, no. 6, pp. 4429–4439, Jun. 2016.

[65] S. Zhou and C. Chris Mi, "Multi-Paralleled LCC Reactive Power Compensation Networks and Their Tuning Method for Electric Vehicle Dynamic Wireless Charging," *IEEE Trans. Ind. Electron.*, vol. 63, no. 10, pp. 6546–6556, Oct. 2016.

[66] Q. Zhu, L. Wang, Y. Guo, C. Liao, and F. Li, "Applying LCC Compensation Network to Dynamic Wireless EV Charging System," *IEEE Trans. Ind. Electron.*, vol. 63, no. 10, pp. 6557–6567, Oct. 2016.

[67] X. Zhang, T. Kan, C. You, and C. Mi, "Modeling and Analysis of AC Output Power Factor for Wireless Chargers in Electric Vehicles," *IEEE Trans. Power Electron.*, vol. 32, no. 2, pp. 1481–1492, Feb. 2017.

[68] T. Kan, T.-D. Nguyen, J. C. White, R. K. Malhan, and C. C. Mi, "A New Integration Method for an Electric Vehicle Wireless Charging System Using LCC Compensation Topology: Analysis and Design," *IEEE Trans. Power Electron.*, vol. 32, no. 2, pp. 1638–1650, Feb. 2017.

[69] Y. Wang *et al.*, "A Double-T-Type Compensation Network and Its Tuning Method for IPT System," *IEEE Trans. Ind. Appl.*, vol. 53, no. 5, pp. 4757–4767, Sep. 2017.

[70] F. Lu, H. Zhang, H. Hofmann, W. Su, and C. C. Mi, "A Dual-Coupled LCC-Compensated IPT System With a Compact Magnetic Coupler," *IEEE Trans. Power Electron.*, vol. 33, no. 7, pp. 6391–6402, Jul. 2018.

[71] M. Khalilian and P. Guglielmi, "Primary-Side Control of a Wireless Power Transfer System with Double-Sided LCC Compensation Topology for Electric Vehicle Battery Charging," in *2018 IEEE International Telecommunications Energy Conference (INTELEC)*, Turino, Italy, 2018, pp. 1–6.

[72] V. Ravikiran, R. K. Keshri, and M. S. Trivedi, "Compound wireless power transfer topology for two stage charging of batteries," in *2017 IEEE Transportation Electrification Conference (ITEC-India)*, Pune, 2017, pp. 1–5.

[73] Fang Liu, Y. Zhang, K. Chen, Z. Zhao, and Liqiang Yuan, "A comparative study of load characteristics of resonance types in wireless transmission systems," in *2016 Asia-Pacific International Symposium on Electromagnetic Compatibility (APEMC)*, Shenzhen, China, 2016, pp. 203–206.

[74] C.-S. Wang, G. A. Covic, and O. H. Stielau, "Investigating an LCL Load Resonant Inverter for Inductive Power Transfer Applications," *IEEE Trans. Power Electron.*, vol. 19, no. 4, pp. 995–1002, Jul. 2004.

[75] Y. Su, C. Tang, S. Wu, and Y. Sun, "Research of LCL Resonant Inverter in Wireless Power Transfer System," in *2006 International Conference on Power System Technology*, Chongqing, China, 2006, pp. 1–6.

[76] C. Ma, S. Ge, Y. Guo, L. Sun, and C. Liu, "Investigation of a SP/S Resonant Compensation Network Based IPT System with Optimized Circular Pads for Electric Vehicles," *J. Power Electron.*, vol. 16, no. 6, pp. 2359–2367, Nov. 2016.

[77] H. Feng, T. Cai, S. Duan, J. Zhao, X. Zhang, and C. Chen, "An LCC-Compensated Resonant Converter Optimized for Robust Reaction to Large Coupling Variation in Dynamic Wireless Power Transfer," *IEEE Trans. Ind. Electron.*, vol. 63, no. 10, pp. 6591–6601, Oct. 2016.

[78] C.-Y. Chou, M. Tampubolon, J.-Y. Lin, Y.-C. Hsieh, and H.-J. Chiu, "Study on LCC-C Wireless Power Transfer," in *2017 IEEE Wireless Power Transfer Conference (WPTC)*, Taipei, Taiwan, 2017, pp. 1–4.

[79] Y. Wang, H. Wang, T. Liang, X. Zhang, D. Xu, and L. Cai, "Analysis and design of an LCC/S compensated resonant converter for inductively coupled power transfer," in *2017 IEEE Transportation Electrification Conference and Expo, Asia-Pacific (ITEC Asia-Pacific)*, Harbin, China, 2017, pp. 1–5.

[80] R. Mai, Y. Chen, Y. Li, Y. Zhang, G. Cao, and Z. He, "Inductive Power Transfer for Massive Electric Bicycles Charging Based on Hybrid Topology Switching With a Single Inverter," *IEEE Trans. Power Electron.*, vol. 32, no. 8, pp. 5897–5906, Aug. 2017.

[81] Y. Wang, Y. Yao, X. Liu, and D. Xu, "S/CLC Compensation Topology Analysis and Circular Coil Design for Wireless Power Transfer," *IEEE Trans. Transp. Electrification*, vol. 3, no. 2, pp. 496–507, Jun. 2017.

[82] Y. Wang, Y. Yao, X. Liu, D. Xu, and L. Cai, "An LC/S Compensation Topology and Coil Design Technique for Wireless Power Transfer," *IEEE Trans. Power Electron.*, vol. 33, no. 3, pp. 2007–2025, Mar. 2018.

[83] C. Auvigne, P. Germano, D. Ladas, and Y. Perriard, "A dual-topology ICPT applied to an electric vehicle battery charger," in *2012 XXth International Conference on Electrical Machines*, Marseille, France, 2012, pp. 2287–2292.

[84] X. Qu, H. Han, S.-C. Wong, C. K. Tse, and W. Chen, "Hybrid IPT Topologies With Constant Current or Constant Voltage Output for Battery Charging Applications," *IEEE Trans. Power Electron.*, vol. 30, no. 11, pp. 6329–6337, Nov. 2015.

[85] R. Mai, Y. Chen, Y. Li, Y. Zhang, G. Cao, and Z. He, "Inductive Power Transfer for Massive Electric Bicycles Charging Based on Hybrid Topology

Switching With a Single Inverter," *IEEE Trans. Power Electron.*, vol. 32, no. 8, pp. 5897–5906, Aug. 2017.

[86] J.-H. Lu, W.-J. Li, B. Li, and G.-R. Zhu, "Variable Compensation Network for Achieving Constant Current or Voltage Output in IPT System," in *2016 International Conference on Industrial Informatics - Computing Technology, Intelligent Technology, Industrial Information Integration (ICIICII)*, Wuhan, China, 2016, pp. 14–17.

[87] B. Li, J.-H. Lu, W.-J. Li, and G.-R. Zhu, "Realization of CC and CV Mode in IPT System Based on the Switching of Doublesided LCC and LCC-S Compensation Network," in *2016 International Conference on Industrial Informatics - Computing Technology, Intelligent Technology, Industrial Information Integration (ICIICII)*, Wuhan, China, 2016, pp. 364–367.

[88] Y. Chen, R. Mai, Y. Zhang, Y. Li, and Z. He, "Inductive power transfer for electric bicycles charging based on variable compensation capacitor," in *2017 IEEE Applied Power Electronics Conference and Exposition (APEC)*, Tampa, FL, USA, 2017, pp. 1389–1393.

[89] Y. Chen, Z. Kou, Y. Zhang, Z. He, R. Mai, and G. Cao, "Hybrid Topology With Configurable Charge Current and Charge Voltage Output-Based WPT Charger for Massive Electric Bicycles," *IEEE J. Emerg. Sel. Top. Power Electron.*, vol. 6, no. 3, pp. 1581–1594, Sep. 2018.

[90] R. Mai, Y. Chen, Y. Zhang, N. Yang, G. Cao, and Z. He, "Optimization of the Passive Components for an S-LCC Topology-Based WPT System for Charging Massive Electric Bicycles," *IEEE Trans. Ind. Electron.*, vol. 65, no. 7, pp. 5497–5508, Jul. 2018.

[91] Y. Li, Q. Xu, T. Lin, J. Hu, Z. He, and R. Mai, "Analysis and Design of Load-Independent Output Current or Output Voltage of a Three-Coil Wireless Power Transfer System," *IEEE Trans. Transp. Electrification*, vol. 4, no. 2, pp. 364–375, Jun. 2018.

[92] Y. Chen, B. Yang, Z. Kou, Z. He, G. Cao, and R. Mai, "Hybrid and Reconfigurable IPT Systems With High-Misalignment Tolerance for Constant-Current and Constant-Voltage Battery Charging," *IEEE Trans. Power Electron.*, vol. 33, no. 10, pp. 8259–8269, Oct. 2018.

[93] V. Ravikiran, R. K. Keshri, and M. S. Trivedi, "Compound wireless power transfer topology for two stage charging of batteries," in *2017 IEEE Transportation Electrification Conference (ITEC-India)*, Pune, 2017, pp. 1–5.

[94] C.-S. Wang, G. A. Covic, and O. H. Stielau, "Power Transfer Capability and Bifurcation Phenomena of Loosely Coupled Inductive Power Transfer Systems," *IEEE Trans. Ind. Electron.*, vol. 51, no. 1, pp. 148–157, Feb. 2004.

[95] S. Chopra and P. Bauer, "Analysis and design considerations for a contactless power transfer system," in *2011 IEEE 33rd International Telecommunications Energy Conference (INTELEC)*, Amsterdam, Netherlands, 2011, pp. 1–6.

[96] E. Gati, G. Kampitsis, and S. Manias, "Variable Frequency Controller for Inductive Power Transfer in Dynamic Conditions," *IEEE Trans. Power Electron.*, vol. 32, no. 2, pp. 1684–1696, Feb. 2017.

[97] Z. Li, C. Zhu, J. Jiang, K. Song, and G. Wei, "A 3-kW Wireless Power Transfer System for Sightseeing Car Supercapacitor Charge," *IEEE Trans. Power Electron.*, vol. 32, no. 5, pp. 3301–3316, May 2017.

[98] J. Sallan, J. L. Villa, A. Llombart, and J. F. Sanz, "Optimal Design of ICPT Systems Applied to Electric Vehicle Battery Charge," *IEEE Trans. Ind. Electron.*, vol. 56, no. 6, pp. 2140–2149, Jun. 2009.

[99] D. Barth, B. Klaus, and T. Leibfried, "Litz wire design for wireless power transfer in electric vehicles," in *2017 IEEE Wireless Power Transfer Conference (WPTC)*, Taipei, Taiwan, 2017, pp. 1–4.

[100] V. Cirimele, "Design and integration of a dynamic IPT system for automotive applications," *Politec. Torino*, 2017.

[101] Howard W. Sams & Co, Ed., *Handbook of electronics tables and formulas*, 6th ed. Indianapolis, IN, USA: H.W. Sams, 1986.

[102] A. Van den Bossche and P. Sergeant, "Inductive coupler for contactless power transmission," *IET Electr. Power Appl.*, vol. 2, no. 1, pp. 1–7, Jan. 2008.

[103] R. Bosshard, U. Badstubner, J. W. Kolar, and I. Stevanovic, "Comparative evaluation of control methods for Inductive Power Transfer," in *2012 International Conference on Renewable Energy Research and Applications (ICRERA)*, Nagasaki, Japan, 2012, pp. 1–6.

[104] A. De Alwis, Z. Harris, D. J. Thrimawithana, and U. K. Madawala, "Control of Inductive Power Transfer systems: A comparison," in *2014 IEEE International Conference on Industrial Technology (ICIT)*, Busan, South Korea, 2014, pp. 379–384.

[105] B. Peschiera, K. Aditya, and S. S. Williamson, "Asymmetrical voltage-cancellation control for a series-series fixed-frequency inductive power transfer system," in *IECON 2014 - 40th Annual Conference of the IEEE Industrial Electronics Society*, Dallas, TX, USA, 2014, pp. 2971–2977.

[106] K. Aditya and S. S. Williamson, "Advanced controller design for a series-series compensated inductive power transfer charging infrastructure using asymmetrical clamped mode control," in *2015 IEEE Applied Power Electronics Conference and Exposition (APEC)*, Charlotte, NC, USA, 2015, pp. 2718–2724.

[107] J.-H. Lee, B.-S. Lee, S.-H. Lee, and K.-P. Yi, "A study on the control of output current to respond to the load changes of the wireless power transfer," in *2015 IEEE Transportation Electrification Conference and Expo (ITEC)*, Dearborn, MI, USA, 2015, pp. 1–4.

[108] J. Tritschler, B. Goeldi, S. Reichert, and G. Griepentrog, "Comparison of different control strategies for series-series compensated inductive power transmission systems," in *2015 17th European Conference on Power*

Electronics and Applications (EPE'15 ECCE-Europe), Geneva, 2015, pp. 1–8.

[109] K. Hata, T. Imura, and Y. Hori, "Dynamic wireless power transfer system for electric vehicles to simplify ground facilities - power control and efficiency maximization on the secondary side," in *2016 IEEE Applied Power Electronics Conference and Exposition (APEC)*, Long Beach, CA, USA, 2016, pp. 1731–1736.

[110] W. Zhong and S. Y. R. Hui, "Charging Time Control of Wireless Power Transfer Systems Without Using Mutual Coupling Information and Wireless Communication System," *IEEE Trans. Ind. Electron.*, vol. 64, no. 1, pp. 228–235, Jan. 2017.

[111] R. Tavakoli, A. Jovicic, N. Chandrappa, R. Bohm, and Z. Pantic, "Design of a dual-loop controller for in-motion wireless charging of an electric bus," in *2016 IEEE Energy Conversion Congress and Exposition (ECCE)*, Milwaukee, WI, USA, 2016, pp. 1–8.

[112] P.-A. Gori, D. Sadarnac, A. Caillierez, and S. Loudot, "Sensorless inductive power transfer system for electric vehicles: Strategy and control for automatic dynamic operation," in *2017 19th European Conference on Power Electronics and Applications (EPE'17 ECCE Europe)*, Warsaw, 2017, p. P.1-P.10.

[113] I. Karakitsios, F. Palaiogiannis, A. Markou, and N. D. Hatziargyriou, "Optimizing the Energy Transfer, With a High System Efficiency in Dynamic Inductive Charging of EVs," *IEEE Trans. Veh. Technol.*, vol. 67, no. 6, pp. 4728–4742, Jun. 2018.

[114] U. K. Madawala and D. J. Thrimawithana, "New technique for inductive power transfer using a single controller," *IET Power Electron.*, vol. 5, no. 2, p. 248, 2012.

[115] I. I. Nam, R. A. Dougal, and E. Santi, "Novel Unity-Gain Frequency Tracking Control of Series–Series Resonant Converter to Improve Efficiency and Receiver Positioning Flexibility in Wireless Charging of Portable Electronics," *IEEE Trans. Ind. Appl.*, vol. 51, no. 1, pp. 385–397, Jan. 2015.

[116] H. Li, J. Li, K. Wang, W. Chen, and X. Yang, "A Maximum Efficiency Point Tracking Control Scheme for Wireless Power Transfer Systems Using Magnetic Resonant Coupling," *IEEE Trans. Power Electron.*, vol. 30, no. 7, pp. 3998–4008, Jul. 2015.

[117] D. J. Thrimawithana and U. K. Madawala, "A primary side controller for inductive power transfer systems," in *2010 IEEE International Conference on Industrial Technology*, Vi a del Mar , Chile, 2010, pp. 661–666.

[118] H. H. Wu, A. Gilchrist, K. D. Sealy, and D. Bronson, "A High Efficiency 5 kW Inductive Charger for EVs Using Dual Side Control," *IEEE Trans. Ind. Inform.*, vol. 8, no. 3, pp. 585–595, Aug. 2012.

[119] T. Diekhans and R. W. De Doncker, "A Dual-Side Controlled Inductive Power Transfer System Optimized for Large Coupling Factor Variations and

Partial Load," *IEEE Trans. Power Electron.*, vol. 30, no. 11, pp. 6320–6328, Nov. 2015.

[120] Z. Li, K. Song, J. Jiang, and C. Zhu, "Constant Current Charging and Maximum Efficiency Tracking Control Scheme for Supercapacitor Wireless Charging," *IEEE Trans. Power Electron.*, vol. 33, no. 10, pp. 9088–9100, Oct. 2018.

[121] J. M. Miller, O. C. Onar, and M. Chinthavali, "Primary-Side Power Flow Control of Wireless Power Transfer for Electric Vehicle Charging," *IEEE J. Emerg. Sel. Top. Power Electron.*, vol. 3, no. 1, pp. 147–162, Mar. 2015.

[122] D. J. Thrimawithana and U. K. Madawala, "A Generalized Steady-State Model for Bidirectional IPT Systems," *IEEE Trans. Power Electron.*, vol. 28, no. 10, pp. 4681–4689, Oct. 2013.

[123] U. K. Madawala, M. Neath, and D. J. Thrimawithana, "A Power–Frequency Controller for Bidirectional Inductive Power Transfer Systems," *IEEE Trans. Ind. Electron.*, vol. 60, no. 1, pp. 310–317, Jan. 2013.

[124] P. Wu, L. Shi, H. Cai, and Y. Li, "An inductively coupled power transfer system based power control for motor drives of rail transit vehicle," in *2014 17th International Conference on Electrical Machines and Systems (ICEMS)*, Hangzhou, China, 2014, pp. 202–205.

[125] Z. Li, Y. Wang, Y. Zhang, and X. Yuan, "Output voltage control of inductive power transfer system based on extremum seeking control," *IET Power Electron.*, vol. 8, no. 11, pp. 2290–2298, Nov. 2015.

[126] Y. Huang, N. Shinohara, and T. Mitani, "Impedance Matching in Wireless Power Transfer," *IEEE Trans. Microw. Theory Tech.*, vol. 65, no. 2, pp. 582–590, Feb. 2017.

[127] G. Lovison, M. Sato, T. Imura, and Y. Hori, "Secondary-side-only simultaneous power and efficiency control for two converters in wireless power transfer system," in *IECON 2015 - 41st Annual Conference of the IEEE Industrial Electronics Society*, Yokohama, 2015, pp. 004824–004829.

[128] M. Debbou and F. Colet, "Interleaved DC/DC charger for wireless power tranfer," in *2017 IEEE International Conference on Industrial Technology (ICIT)*, Toronto, ON, 2017, pp. 1555–1560.

[129] D. Bui, T. M. Mostafa, A. P. Hu, and R. Hattori, "DC-DC Converter Based Impedance Matching for Maximum Power Transfer of CPT System with High Efficiency," in *2018 IEEE PELS Workshop on Emerging Technologies: Wireless Power Transfer (Wow)*, Montréal, QC, Canada, 2018, pp. 1–5.

[130] Yao-Ching Hsieh, Te-Chin Hsueh, and Hau-Chen Yen, "An Interleaved Boost Converter With Zero-Voltage Transition," *IEEE Trans. Power Electron.*, vol. 24, no. 4, pp. 973–978, Apr. 2009.

[131] D.-Y. Jung, Y.-H. Ji, S.-H. Park, Y.-C. Jung, and C.-Y. Won, "Interleaved Soft-Switching Boost Converter for Photovoltaic Power-Generation System," *IEEE Trans. Power Electron.*, vol. 26, no. 4, pp. 1137–1145, Apr. 2011.

[132] M. Pahlevaninezhad, P. Das, J. Drobnik, P. K. Jain, and A. Bakhshai, "A ZVS Interleaved Boost AC/DC Converter Used in Plug-in Electric Vehicles," *IEEE Trans. Power Electron.*, vol. 27, no. 8, pp. 3513–3529, Aug. 2012.

[133] A. Khosroshahi, M. Abapour, and M. Sabahi, "Reliability Evaluation of Conventional and Interleaved DC–DC Boost Converters," *IEEE Trans. Power Electron.*, vol. 30, no. 10, pp. 5821–5828, Oct. 2015.

[134] Y.-S. Lin, K.-W. Hu, T.-H. Yeh, and C.-M. Liaw, "An Electric-Vehicle IPMSM Drive With Interleaved Front-End DC/DC Converter," *IEEE Trans. Veh. Technol.*, vol. 65, no. 6, pp. 4493–4504, Jun. 2016.

[135] H.-B. Shin, J.-G. Park, S.-K. Chung, H.-W. Lee, and T. A. Lipo, "Generalised steady-state analysis of multiphase interleaved boost converter with coupled inductors," *IEE Proc. - Electr. Power Appl.*, vol. 152, no. 3, p. 584, 2005.

[136] Gyu-Yeong Choe, Byoung-Kuk Lee, Jin Hur, and Dong-Wook Yoo, "Comparative analysis of CCM and DCM modes of interleaved boost converters for fuel cell electric vehicles," in *2009 IEEE Vehicle Power and Propulsion Conference*, Dearborn, MI, 2009, pp. 686–690.

[137] P. Magne, Ping Liu, B. Bilgin, and A. Emadi, "Investigation of impact of number of phases in interleaved dc-dc boost converter," in *2015 IEEE Transportation Electrification Conference and Expo (ITEC)*, Dearborn, MI, USA, 2015, pp. 1–6.

[138] G. R. Chandra Mouli, J. H. Schijffelen, P. Bauer, and M. Zeman, "Design and Comparison of a 10-kW Interleaved Boost Converter for PV Application Using Si and SiC Devices," *IEEE J. Emerg. Sel. Top. Power Electron.*, vol. 5, no. 2, pp. 610–623, Jun. 2017.

[139] J. S. Batchvarov, J. L. Duarte, and M. A. M. Hendrix, "Interleaved converters based on hysteresis current control," in *2000 IEEE 31st Annual Power Electronics Specialists Conference. Conference Proceedings (Cat. No.00CH37018)*, Galway, Ireland, 2000, vol. 2, pp. 655–661.

[140] R. Redl and N. O. Sokal, "Current-mode control, five different types, used with the three basic classes of power converters: Small-signal AC and large-signal DC characterization, stability requirements, and implementation of practical circuits," in *1985 IEEE Power Electronics Specialists Conference*, Toulouse, France, 1985, pp. 771–785.

[141] G. Calderon-Lopez, S. K. K. R. Todd, A. J. Forsyth, P. Kakosimos, and A. Villarruel-Parra, "Comparison of Digital PWM Control Strategies for High Power Interleaved DC-DC Converters," in *8th IET International Conference on Power Electronics, Machines and Drives (PEMD 2016)*, Glasgow, UK, 2016, pp. 6 .-6 .

[142] H. Higure, N. Hoshi, and J. Haruna, "Inductor current control of three-phase interleaved DC-DC converter using single DC-link current sensor," in *2012 IEEE International Conference on Power Electronics, Drives and Energy Systems (PEDES)*, Bengaluru, Karnataka, India, 2012, pp. 1–5.

[143] D. Schumacher, P. Magne, M. Preindl, B. Bilgin, and A. Emadi, “Closed loop control of a six phase interleaved bidirectional dc-dc boost converter for an EV/HEV application,” in *2016 IEEE Transportation Electrification Conference and Expo (ITEC)*, Dearborn, MI, USA, 2016, pp. 1–7.

[144] Y. Tang, Y. Chen, U. K. Madawala, D. J. Thrimawithana, and H. Ma, “A New Controller for Bidirectional Wireless Power Transfer Systems,” *IEEE Trans. Power Electron.*, vol. 33, no. 10, pp. 9076–9087, Oct. 2018.

[145] K. Colak, E. Asa, M. Bojarski, D. Czarkowski, and O. C. Onar, “A Novel Phase-Shift Control of Semibridgeless Active Rectifier for Wireless Power Transfer,” *IEEE Trans. Power Electron.*, vol. 30, no. 11, pp. 6288–6297, Nov. 2015.

[146] M. Moghaddami, A. Sundararajan, and A. I. Sarwat, “A Power-Frequency Controller With Resonance Frequency Tracking Capability for Inductive Power Transfer Systems,” *IEEE Trans. Ind. Appl.*, vol. 54, no. 2, pp. 1773–1783, Mar. 2018.

[147] D. J. Thrimawithana, U. K. Madawala, and M. Neath, “A Synchronization Technique for Bidirectional IPT Systems,” *IEEE Trans. Ind. Electron.*, vol. 60, no. 1, pp. 301–309, Jan. 2013.

[148] R. Mai, Y. Liu, Y. Li, P. Yue, G. Cao, and Z. He, “An Active-Rectifier-Based Maximum Efficiency Tracking Method Using an Additional Measurement Coil for Wireless Power Transfer,” *IEEE Trans. Power Electron.*, vol. 33, no. 1, pp. 716–728, Jan. 2018.

[149] Yiming Zhang, Fanbo He, Fang Liu, Kainan Chen, Zhengming Zhao, and Liqiang Yuan, “Comparison of two bidirectional wireless power transfer control methods,” in *2016 Asia-Pacific International Symposium on Electromagnetic Compatibility (APEMC)*, Shenzhen, China, 2016, pp. 68–70.

[150] A. A. S. Mohamed, A. Berzoy, and O. A. Mohammed, “Experimental Validation of Comprehensive Steady-State Analytical Model of Bidirectional WPT System in EVs Applications,” *IEEE Trans. Veh. Technol.*, vol. 66, no. 7, pp. 5584–5594, Jul. 2017.

[151] Y.-C. Hsieh, Z.-R. Lin, M.-C. Chen, H.-C. Hsieh, Y.-C. Liu, and H.-J. Chiu, “High-Efficiency Wireless Power Transfer System for Electric Vehicle Applications,” *IEEE Trans. Circuits Syst. II Express Briefs*, vol. 64, no. 8, pp. 942–946, Aug. 2017.

[152] A. Berger, M. Agostinelli, S. Vesti, J. A. Oliver, J. A. Cobos, and M. Huemer, “Phase-shift and amplitude control for an active rectifier to maximize the efficiency and extracted power of a Wireless Power Transfer system,” in *2015 IEEE Applied Power Electronics Conference and Exposition (APEC)*, Charlotte, NC, USA, 2015, pp. 1620–1624.

[153] A. A. S. Mohamed and O. Mohammed, “Physics-Based Co-Simulation Platform With Analytical and Experimental Verification for Bidirectional IPT System in EV Applications,” *IEEE Trans. Veh. Technol.*, vol. 67, no. 1, pp. 275–284, Jan. 2018.

[154] M. Khalilian and P. Guglielmi, “Charging Process Control of Dynamic Wireless Power Transfer System with Active Rectifier and without Wireless Communication System,” in *2018 IEEE 18th International Power Electronics and Motion Control Conference (PEMC)*, Budapest, 2018, pp. 229–235.

[155] T.-S. Lee, S.-J. Huang, C.-C. Tai, R.-Y. Chen, and B.-R. Jiang, “Design of wireless power transfer for dynamic power transmission with position-detection mechanism,” in *2015 IEEE International Conference on Industrial Technology (ICIT)*, Seville, 2015, pp. 976–981.

[156] N. Hasan, H. Wang, T. Saha, and Z. Pantic, “A novel position sensorless power transfer control of lumped coil-based in-motion wireless power transfer systems,” in *2015 IEEE Energy Conversion Congress and Exposition (ECCE)*, Montreal, QC, Canada, 2015, pp. 586–593.

[157] F. Liu, Z. Zhao, Y. Zhang, K. Chen, F. He, and L. Yuan, “A selection method of mutual inductance identification models based on sensitivity analysis for wireless electric vehicles charging,” in *2016 IEEE Energy Conversion Congress and Exposition (ECCE)*, Milwaukee, WI, USA, 2016, pp. 1–6.

[158] C. Jiang, Y. Sun, Z. Wang, and L. Xiang, “State identification of Evs’ wireless power supplying based on inverter voltage detection,” in *2017 IEEE PELS Workshop on Emerging Technologies: Wireless Power Transfer (WoW)*, Chongqing, China, 2017, pp. 1–4.

[159] M. Moghaddami, A. Sundararajan, and A. I. Sarwat, “Sensorless electric vehicle detection in inductive charging stations using self-tuning controllers,” in *2017 IEEE Transportation Electrification Conference (ITEC-India)*, Pune, 2017, pp. 1–4.

[160] T. Loewel, C. Lange, and F. Noack, “Identification and positioning system for inductive charging systems,” in *2013 3rd International Electric Drives Production Conference (EDPC)*, Nuremberg, Germany, 2013, pp. 1–5.

[161] Chen Shuwei, Liao Chenglin, and Wang Lifang, “Research on positioning technique of wireless power transfer system for electric vehicles,” in *2014 IEEE Conference and Expo Transportation Electrification Asia-Pacific (ITEC Asia-Pacific)*, Beijing, China, 2014, pp. 1–4.

[162] K. Lee, Z. Pantic, and S. M. Lukic, “Reflexive Field Containment in Dynamic Inductive Power Transfer Systems,” *IEEE Trans. Power Electron.*, vol. 29, no. 9, pp. 4592–4602, Sep. 2014.

[163] A. Dominguez, A. Otin, I. Urriza, L. A. Barragan, D. Navarro, and J. I. Artigas, “Load identification of domestic induction heating based on Particle Swarm Optimization,” in *2014 IEEE 15th Workshop on Control and Modeling for Power Electronics (COMPEL)*, Santander, Spain, 2014, pp. 1–6.

[164] Z.-H. Wang, Y.-P. Li, Y. Sun, C.-S. Tang, and X. Lv, “Load Detection Model of Voltage-Fed Inductive Power Transfer System,” *IEEE Trans. Power Electron.*, vol. 28, no. 11, pp. 5233–5243, Nov. 2013.

[165] G. R. Nagendra, L. Chen, G. A. Covic, and J. T. Boys, “Detection of EVs on IPT Highways,” *IEEE J. Emerg. Sel. Top. Power Electron.*, vol. 2, no. 3, pp. 584–597, Sep. 2014.

[166] G. R. Nagendra, L. Chen, G. A. Covic, and J. T. Boys, “Detection of EVs on IPT highways,” in *2014 IEEE Applied Power Electronics Conference and Exposition - APEC 2014*, Fort Worth, TX, USA, 2014, pp. 1604–1611.

[167] Q. Deng *et al.*, “edge position detection of on-line vehicles with segmental wireless power supply,” *IEEE Trans. Veh. Technol.*, pp. 1–1, 2016.

[168] A. Kamineni, M. J. Neath, A. Zaheer, G. A. Covic, and J. T. Boys, “Interoperable EV Detection for Dynamic Wireless Charging With Existing Hardware and Free Resonance,” *IEEE Trans. Transp. Electrification*, vol. 3, no. 2, pp. 370–379, Jun. 2017.

[169] M. Khalilian, S. G. Rosu, V. Cirimele, P. Guglielmi, and R. Ruffo, “Load identification in dynamic wireless power transfer system utilizing current injection in the transmitting coil,” in *2016 IEEE Wireless Power Transfer Conference (WPTC)*, Aveiro, Portugal, 2016, pp. 1–4.

[170] R. Ruffo, V. Cirimele, M. Diana, M. Khalilian, A. L. Ganga, and P. Guglielmi, “Sensorless Control of the Charging Process of a Dynamic Inductive Power Transfer System With an Interleaved Nine-Phase Boost Converter,” *IEEE Trans. Ind. Electron.*, vol. 65, no. 10, pp. 7630–7639, Oct. 2018.

[171] R. Ruffo, V. Cirimele, P. Guglielmi, and M. Khalilian, “A coupled mechanical-electrical simulator for the operational requirements estimation in a dynamic IPT system for electric vehicles,” in *2016 IEEE Wireless Power Transfer Conference (WPTC)*, Aveiro, Portugal, 2016, pp. 1–4.

[172] S. G. Rosu, M. Khalilian, V. Cirimele, and P. Guglielmi, “A dynamic wireless charging system for electric vehicles based on DC/AC converters with SiC MOSFET-IGBT switches and resonant gate-drive,” in *IECON 2016 - 42nd Annual Conference of the IEEE Industrial Electronics Society*, Florence, Italy, 2016, pp. 4465–4470.

[173] R. Ruffo, M. Khalilian, V. Cirimele, P. Guglielmi, and M. Cesano, “Theoretical and experimental comparison of two interoperable dynamic wireless power transfer systems for electric vehicles,” in *2017 IEEE Southern Power Electronics Conference (SPEC)*, Puerto Varas, Chile, 2017, pp. 1–6.

[174] F. Chen, N. Taylor, R. Balieu, and N. Kringos, “Dynamic application of the Inductive Power Transfer (IPT) systems in an electrified road: Dielectric power loss due to pavement materials,” *Constr. Build. Mater.*, vol. 147, pp. 9–16, Aug. 2017.

[175] F. Chen, R. Balieu, E. Córdoba, and N. Kringos, “Towards an understanding of the structural performance of future electrified roads: a finite element simulation study,” *Int. J. Pavement Eng.*, vol. 20, no. 2, pp. 204–215, Feb. 2019.

[176] Feng Chen and N. Kringos, “Towards new infrastructure materials for on-the-road charging,” in *2014 IEEE International Electric Vehicle Conference (IEVC)*, Florence, Italy, 2014, pp. 1–5.

[177] N. Sakai, D. Itokazu, Y. Suzuki, S. Sakihara, and T. Ohira, “Single-seater vehicle prototype experiment powered by high frequency electric field on an asphalt-paved roadway,” in *2016 6th International Electric Drives Production Conference (EDPC)*, Nuremberg, Germany, 2016, pp. 101–104.

[178] V. Cirimele, F. Freschi, L. Giaccone, L. Pichon, and M. Repetto, “Human exposure assessment in dynamic inductive power transfer for automotive applications,” in *2016 IEEE Conference on Electromagnetic Field Computation (CEFC)*, Miami, FL, 2016, pp. 1–1.

[179] V. Cirimele, F. Freschi, L. Giaccone, L. Pichon, and M. Repetto, “Human Exposure Assessment in Dynamic Inductive Power Transfer for Automotive Applications,” *IEEE Trans. Magn.*, vol. 53, no. 6, pp. 1–4, Jun. 2017.

[180] A. L. Ganga, V. Cirimele, R. Ruffo, and P. Guglielmi, “Fast hardware protection for a series-series compensated inductive power transfer system for electric vehicles,” in *2017 IEEE Southern Power Electronics Conference (SPEC)*, Puerto Varas, Chile, 2017, pp. 1–6.